Dynamic behavior under fluid flow of wire-wrapped fuel pins and associated dimensioning method

Xiaoshu Ma

École Doctorale 353

CEA/DES/IRESNE/DEC/SESC/Laboratoire de Modélisation Multi-échelle des Combustibles
Laboratoire de Mécanique et d'Acoustique de Marseille

THÈSE DE DOCTORAT

pour obtenir le grade de

DOCTEUR de l'ÉCOLE CENTRALE de MARSEILLE

Discipline : Sciences pour l'ingénieur : Mécanique, Physique, Micro et Nanoélectronique

Dynamic behavior under fluid flow of wire-wrapped fuel pins and associated dimensioning method

Par

MA Xiaoshu

Directeur de thèse : COCHELIN Bruno, BOURGEOIS Stéphane

Soutenue le 01/06/2022

devant le jury composé de :

Jacquet-Richardet Géorges	Professeur/ INSA Lyon	Président
Cadou Jean Marc	Maitre de Conférence HdR/ Université Lorient	Rapporteur
Acary Vincent	Directeur de Recherche HdR/ Inria Grenoble	Rapporteur
Terrien Soizic	Chargée de Recherche/ CNRS	Examinatrice
Gatt Jean-marie	Directeur de Recherche/ CEA	Encadrant
Ricciardi Guillaume	Directeur de Recherche/ CEA	Encadrant
Bourgeois Stéphane	Maitre de Conférence HdR/ ECM	Co-directeur
Cochelin Bruno	Professeur/ ECM	Directeur

Abstract

Understanding the dynamic behavior of fuel pins subjected to seismic loading is one of the major concerns for the design of SFRs (Sodium-cooled Fast Reactors) and in particular for the design of the ASTRID prototype. In this field, two physical aspects are important: the strong non-linearity due to the contacts (between the fuel pins and between the pins and the wrapper tube) and the fluid-structure interaction with the coolant.

These phenomena are taken into consideration with the fluid-elastic force model proposed by Paidoussis and a penetration impact law. Several parameters engaged with these models are to be determined with experiments. To this end, a test bench CARNEAU equipped with a fast camera as measurement is designed to capture the motion history of the fuel pins in water flow of different velocities and under sine sweep excitation. It is anticipated to identify the global parameters lumping the effects of the detailed physics with modal analysis, unfortunately the experiments were not carried out.

With the parameters decided with the inspiration from the previous experiments and theoretic works, two numeric methods have been used to exploit the model: the traditional method using implicit Newmark integration and the global periodic time integration (GPTI) method. The modelling enables us to have a phenomenal analysis on the nonlinear dynamics of the fuel pins: the relatively simple global vibration and the local impact-related chatters of much smaller time scale, which is the origin of the complexity of the dynamic behavior. The two methods have both their advantages and limits with the impact-related problem. The direct time-integration is quite direct and can be applied for any contact rigidity, but it is difficult to cover the coexisting regimes led by the nonlinearity as it is sensible to the initial condition. The GPTI method allows to unfold the solution branch for a varying parameter and each solution point corresponds to a vibration regime, but the difficulty with the continuation leads to a limited range of contact stiffness and excitation amplitude. With an increasing amplitude, more and more solution branches coexist for the periodic dynamic responses of the fuel pin resulting in a great complexity, the GPTI method does not neither guarantee the observation of all the possible periodic solutions, the direct time-integration can be complementary but not exhaustive.

The fluid-structure coupling is also an essential element for the correct modeling of the system. The effects of the fluid on the structure have been taken into account in the previous model. To go further, it is necessary to take into account the effects of the structure on the flow. To this end, a spatial averaging method considering the space-and-time dependent RVEs has been proposed. It makes it possible to establish the equations of motion of the fluid by averaging the Navier Stockes equation in the form of Arbitrary Lagrangian Eulerian (ALE). The coupling with the structure is accounted for by using the hydraulic model of Paidoussis.

Résumé

La compréhension du comportement dynamique des aiguilles combustibles soumises à un chargement sismique est une des préoccupations majeures pour la conception des RNR (Réacteurs à Neutrons Rapides) et notamment pour la conception du prototype ASTRID. Dans ce domaine, deux aspects physiques sont importants : la forte non-linéarité due aux contacts (entre les aiguilles combustibles et entre les aiguilles et le tube hexagonal) et l'interaction fluide-structure avec le caloporteur.

Ces phénomènes sont pris en compte en utilisant le modèle de la force fluide-élastique proposé par Paidoussis et une loi de contact par pénalisation. Plusieurs paramètres associés à ces modèles sont à déterminer expérimentalement en utilisant la méthode d'analyse modale. A cet effet, un banc d'essai CARNEAU équipé d'une caméra rapide a été conçu pour visualiser la vibration des aiguilles sous écoulement d'eau à différentes vitesses et sous sollicitation dynamique de type balayage sinusoïdal. Malheureusement, les essais visagés n'ont pas pu être réalisés dans le cadre de ce travail.

En utilisant les paramètres déterminés dans la littérature (expérimentalement ou bien par des approches théoriques), le modèle numérique développé dans ce travail a pu être exploité en mettant en œuvre deux méthodes : la méthode traditionnelle en utilisant l'intégration de Newmark implicite et la méthode GPTI (global periodic time integration). Ces modélisations nous permettent d'avoir une analyse phénoménologique de la dynamique non linéaire des aiguilles combustible : la vibration globale, qui reste relativement simple, et les vibrations parasites liées aux contacts se produisant sur des échelles de temps beaucoup plus petites, d'où la complexité du comportement dynamique. Les deux méthodes ont leurs propres avantages et limites pour les problèmes de contacts. La première méthode est assez directe et utilisable avec n'importe quelle rigidité de contact, mais des difficultés apparaisent pour obtenir les régimes coexistants sensibles aux conditions initiales choisies et générés par la non-linéarité. La méthode GPIT permet de déployer une branche de solution pour un paramètre variable (fréquence, amplitude de la sollicitation, ...) et chaque point solution correspond à un régime de vibration. Cependant la difficulté induite par la continuation conduit à une plage limitée de la raideur de contact et de l'amplitude de sollicitation. Avec l'augmentation de l'amplitude, de plus en plus de branches de réponses périodiques coexistent pour la dynamique de l'aiguille et présentent une grande complexité pour l'analyse. Par ailleurs, la méthode GPIT ne garantit pas l'observation de toutes les branches, et donc la méthode d'intégration directe peut être une solution complémentaire mais ne permet pas de trouver toutes les solutions correspondantes aux comportements dynamiques des aiguilles.

La prise en compte du couplage fluide structure est aussi un élément essentiel à la bonne modélisation du système. Les effets du fluide sur la structure ont bien été pris en compte dans le cadre du modèle précédent. Pour aller plus loin, une prise en compte des effets de la structure sur l'écoulement est nécessaire. Pour cela, une approche par moyenne spatiale, sur chaque Volume Elémentaire Représentative dépendante de l'espace et du temps, a été proposée. Elle permet d'établir les équations du mouvement du fluide en moyennant l'équation de Navier-Stokes sous une forme ALE (Arbitrary Lagrangian Eulerian). Le couplage avec la structure est pris en compte en utilisant le modèle hydraulique de Paidoussis.

Contents

Introduction

The nuclear industry has very demanding safety requirements. A new prototype must undergo a risk analysis involving several disciplines. The CEA launched a Sodium Fast Reactor project ASTRID in 2008 and even though suspended in 2019, the numeric modelling of the design phase is always in progress. This thesis work makes a part of it.

The fuel sub-assembly of the ASTRID reactor is wrapped by a hollow hexagonal tube, which allows the passage of the axial coolant flow of about 20 kg/s. Inside is inserted a bundle of 217 fuel pins arranged in a hexagonal configuration. The claddings of the fuel pins are closed tubes of about one centimeter in diameter and two meters in length, containing the fuel in the form of pellets. A wire helically wound around the cladding will make it possible to maintain the spacing between the pins, improve the heat exchanges and also guard the pin bundle against the flow induced vibrations (FIV). The fuel pins are only held on the lower part by a grid and left free on the upper part, so as not to be thermally stressed. As a result, they are relatively mobile inside the wrapper tube especially at the start of life when the clearance between them is not closed. Under external loads like an earthquake, the fuel pins will have collisions with the wrapper tube and among themselves. The significant number of shocks is a challenge to the integrity of the fuel claddings, which constitute the first barrier against the release of radioactive products. In order to estimate the impact forces, it is of great importance to understand the dynamic behaviors of the fuel pins. And this has proved to be a challenging task, as the multi-physics setup involving fluid-structure interaction with turbulent flow and impact-induced strong non-linearity, is quite complex.

The purpose of this work is to describe accurately the dynamic responses of the fuel pins to an excitation, of which the amplitude and the frequency varies in the range of an earthquake-induced load. In fact, the aspect of numerous potential impacts in air has been studied both experimentally and numerically in the thesis work by Catterou [12], our goal is thus to take the fluid aspect into consideration. Similarly, both the experiments and the numeric modellings are in plan. Basing on the experiences from the earlier test projects, a bench is designed to carry out the sweep sine excited experiments under different flow velocity and a guaranteed measurement is anticipated to calibrate the parameters engaged in the numerical models.

As for the simulation part, a model incorporating globally the effect of axial flow on the fuel pin is firstly constructed, different numerical methods are proposed to exploit it. Given that the flow acts as a damper under a critical velocity of fluid-elastic instability, dynamic responses more regular than those in air can be expected. The traditional approach, which consists in using implicit time-integration, is used to have an overview on the contact related phenomena. It is able to predict the history of motions of the system under an excitation with a given combination of amplitude and frequency. As it is well known that some parameter combinations lead to coexisting vibration regimes when non-linearity is involved, the different initial conditions are to be searched and it is difficult to fully cover the possible outcomes. Therefore, a periodic response searching method is developed, which combined with the continuation allows to unfold the solution branch for a varying parameter and associate each of the solution point to a particular dynamical behavior. The methods of this type are known to have a good performance in the weakly nonlinear problem, hence their performances in the impact problems are evaluated and then applied to study the model of the fuel pin.

The model firstly constructed is more suited to the study of the single fuel pin, in order to be able to simulate the coupling motion of several fuel pins, an improved model is proposed basing on a modified spatial averaging method. Equations of motion for an equivalent fluid is established by spatially averaging the Navier–Stokes equation written with an arbitrary Lagragian Eulerian (ALE) approach. Structure related effects on the fluid are accounted for by a body force, which is also defined from the fluid forces acting on a beam subjected to an axial flow. The fuel pins are modelled as a porous medium subjected to the opposite of the body force.

The manuscript is organized into five chapters. The first one gives firstly a description of the ASTRID reactor and offers a literature overview on the experiments and the numerical models on the physical phenomena involved our problem, such as the impact and nonlinear damping for the structures, the hydraulic characteristics and the fluid-structure interaction.

The second chapter is dedicated to the design of a test bench CARNEAU. It is anticipated to perform the dynamic experiments of one single fuel pin and a row of pins in air, in still water and in water flow of different speed, in order to determine with modal analysis the empirical parameters associated with the numerical models used and to give a reference to validate the modelling. Unfortunately, we were not able to perform the experiments as a result of the budget limitation and the difficulty arising from the health crisis.

The third chapter establishes the model for analyzing the dynamics of the fuel pin in fluid with contact points and under earthquake. Due to the lack of experiments, an estimation of the coefficients in our model has been performed based on the previous theoretical and experimental studies. With the direct time-integration method, the qualitative description not thorough of the phenomenon relative to impact will be given with some particular cases.

The forth chapter gives an overview on the existing periodic response searching methods. The classical Harmonic Balance Method (HBM) is found to have limitations in the context of our study with a simplified fuel pin model with less contact points. A global periodic time integration method is therefore developed and its performance with the impact problems is firstly evaluated with the vibro-impact problem. Then it is applied to the study of the fuel pin with some compromises.

The final chapter is dedicated to the formulation of an improved model, which is able to take into consideration the coupling of the motions of several fuel pins. It is based on a modified spatial averaging method by considering a deformable Representative Volume Element (RVE). The hypothesis used for deriving the model are presented.

Chapter 1 State of the Art

This chapter offers a literature overview on the physical phenomena involving our problem. Firstly, a SFR reactor ASTRID is introduced as the context of our study. In fact, many topics are discussed. From the structural aspect, the models and experiments regarding the impact and nonlinear damping are presented. The experimental and numerical studies on the hydraulics characteristics under SFR fuel assembly configurations give us an insight on the flow pattern. Finally, a detailed summary of researches done on date on the fluid-structure interaction is given.

1.1 Industry context

1.1.1 Sodium Fast reactors in France

The sodium-cooled fast reactor (SFR) concept is one of the four fast neutron concepts selected by the Generation IV International Forum (GIV). Contrary to a large majority of Nuclear Reactors in the world cooled by water, the SFR is a concept cooled by sodium which may play an important role in the future of nuclear energy production because of the excellent potential for natural resource utilization and ability to reduce the volume and lifetime of nuclear waste.

The schematic diagram of an SFR is presented in Figure 1.1. The core, where the chain reaction and the production of energy occur, is immersed in a main vessel filled with sodium. The sodium circulates both around and in the fuel assembly. Its temperature at the inlet of the core is approximately 400°C and reaches 550°C on an average at core outlet. The hot primary sodium then flows into an intermediate exchanger which transfers the heat of the primary sodium to the sodium of a second independent system called “secondary system”. The main vessel is topped by a slab used as a cover. The slab includes a rotating plug above the core to allow insertion and removal of the sub-assemblies, and to allow the penetration of the core control rod mechanisms and the core measuring devices.

France launched its first SFR project RAPSODIE in 1958, only 24 years after the discovery of artificial radioactivity. The power of this reactor reached 20 MW during its first divergence in 1967 and was then increased to 40 MW. The project was not aimed at generating electricity, but for data collection on core material, especially the irradiation swelling, and verification on the selection of fuel, providing experience for the research of PHENIX reactor.

PHENIX is a prototype with electric power of 250 MW which operated from 1973 to 2010. It was initially designed to generate electricity, and then after the halt of SUPERPHENIX, its goal extended to the study of the transmutation of long-lived radioactive waste. The operation of PHENIX was punctuated by several shutdowns due to sodium leaks in secondary circuit before 1989. Thanks to the knowledge gained from the incidents, SUPERPHENIX experienced only 3 leaks during its 10 years of operation.

SUPERPHENIX, launched in 1974 under cooperation of Italy, Germany and France, was designed to generate a power comparable to that of a conventional nuclear power plant: 1200 MW. On the consequence of the Chernobyl disaster, the lack of transparency and communication has led to the mistrust of the public on nuclear security. SUPERPHENIX was forced to suspend operations several times by the demonstrations (53 months of operation in 10 years), and finally out of service in 1997 due to politics and financial problem.

The most recent project ASTRID was launched in 2008. The designed electric power was initially 600 MW and it was reduced to 100 – 200 MW due to the financial concern in 2018. Until its suspension in 2019, ASTRID was always under detailed design phase.

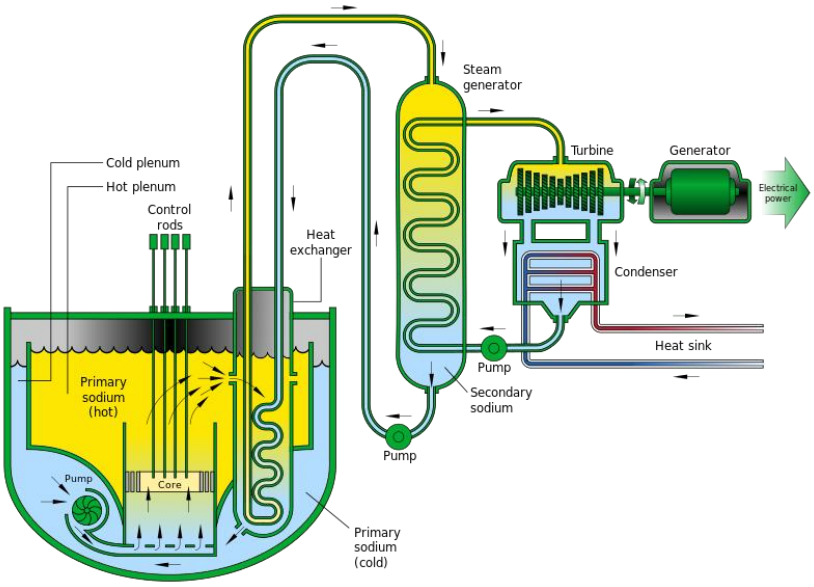

Figure 1.1. Schematic diagram of a sodium-cooled fast reactor

1.1.2 Description of ASTRID reactor

The core of ASTRID is made up of a large number of hexagonal tubes, called assemblies of about 17cm wide and 4.5m high. Several types of sub-assemblies exist. As is shown in Figure 1.2, the fuel sub-assemblies, in the center of the core in yellow and red, contain 217 thin pins in which the fuel is in the form of pellets. The absorber devices are distributed among the fuel sub-assemblies, making it possible to regulate the reactivity. At the periphery, the lateral reflector in blue and shielding arrangement in gray surround the fuel sub-assemblies in order to reduce neutron leaks.

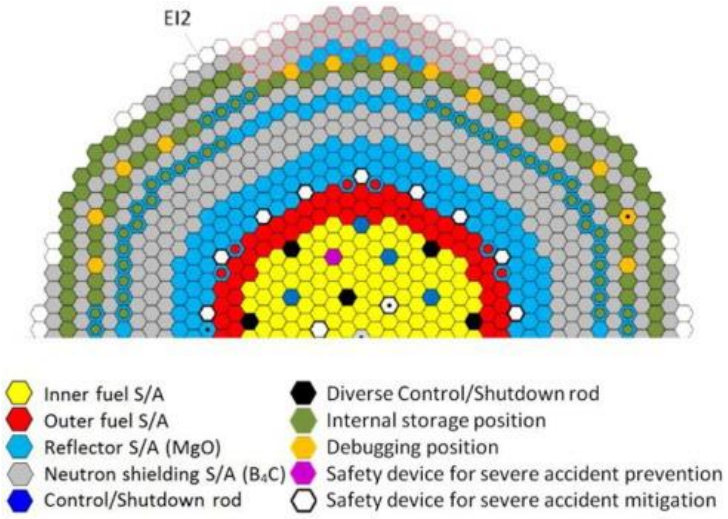

Figure 1.2. Representation of the core of ASTRID

A representation of a fuel sub-assembly is given in Figure 1.3. The spike is inserted into a support with a key system that does not interfere with the core assemblies. On the upper part of the spike, contact occurs between its spherical part and a conical area of the support.

The sub-assembly consists of 217 fuel pins with a 9.70 mm outer diameter separated by a 1 mm-diameter spacer wire helically wound around the pins. The spacer wire guard the pin bundle against the flow induced vibrations (FIV). It also acts as a mixing device to avoid the trapping of the coolant so that the heat transfer can be enhanced and the pressure loss is increased.

The pin's lower plugs are mounted on the rails of a stainless-steel single-part grid to form a bundle that is vertically held within the hexagonal wrapper tube. To ensure suitable clearance between the sub-assemblies in the core, a rectangular spacer pad is stamped through each side of the hexcan just above the fuel pins. The pads play a central role in the mechanical equilibrium of the core, they also enhance safety by preventing reactivity increases due to a core compaction that follows a flowering, which may occur when core is subjected to dynamic stresses such as earthquake or internal pulse load release.

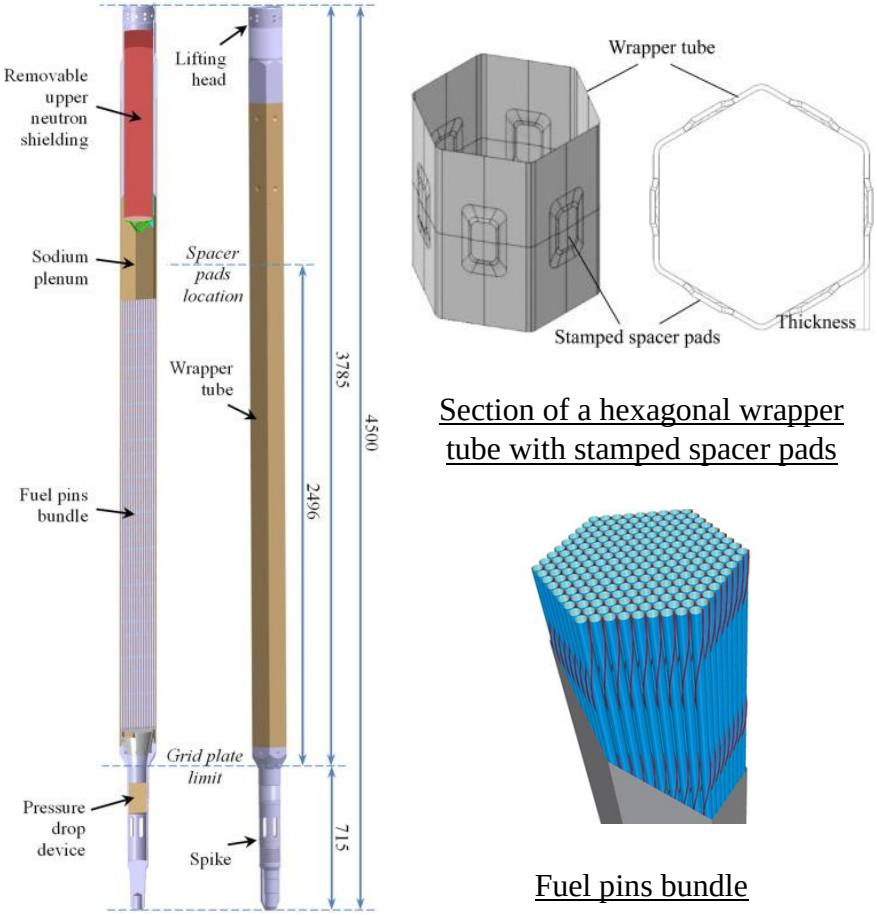

Figure 1.3. ASTRID fuel sub-assembly

The inner core fuel pin is axially heterogeneous with fertile zone sandwiched between the two fissile zones, as we can see in Figure 1.4. The fissile zone in the inner part of the core is made of UPuO2 pellets that undergo nuclear chain reaction producing energy. The thick fertile zone contains fertile material that becomes fissile with neutron bombardment. Two plugs close the

pin at its ends and hold the spacer wire in position. The fuel pellets are inserted into the sheath about half the height, leaving a plenum to contain the gases released by the fission reaction. The clearance between the pellets and the cladding initially exists and evolves during the life of the pin under irradiation. The fuel column is held by a spring at the top and a crimped spacer at the bottom. Fuel pellets are so heavy elements that the distribution of the mass will therefore be extremely heterogeneous, 75% of the total mass is concentrated in its upper half. In addition, during the life of the sub-assembly, the cladding of the pin will swell under irradiation. This swelling is very heterogeneous in the height of the pin and influences the distribution of clearances in the fuel pin bundle.

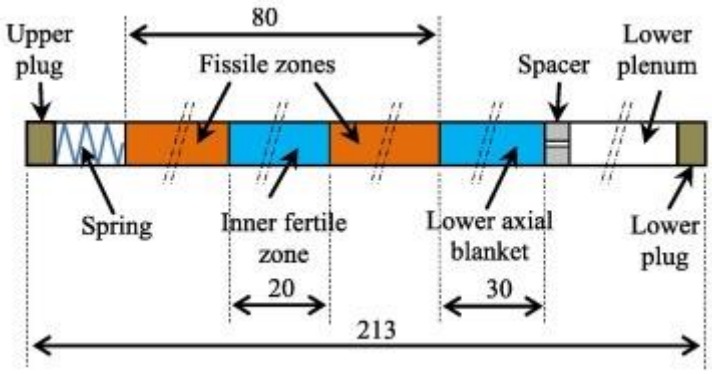

Figure 1.4. Configuration of inner core fuel pin

1.1.3 Dynamic behavior under seismic loading

The sub-assembly, formed by pin bundle, is susceptible to accidental scenario during its service life. An earthquake generates relative movements between the components during the functioning of the core, thus causing chocks that could lead to structural cracking and system failure. Therefore, the characterization of the dynamics of fuel pins is one of the major safety issues.

In the following, we will describe the different physical phenomena involved in the problem, and a literature overview of the previous studies and models on these phenomena will be carried out.

1.2 Nonlinear dynamics of fuel pins

The fuel pins have a rich dynamic behaviors because of strong nonlinearities. It typically means a nonlinear stiffness and a nonlinear damping, which is due to the impacts and friction between the components. For all these stresses, of very different duration, amplitude and frequency, it is necessary to determine criteria not to be exceeded in order to guarantee the good mechanical strength of the pins and to avoid sheath breakage.

1.2.1 Impact modelling

All the pins in the bundle are oriented in the same direction. The impacts happen at the altitudes predetermined by the pitch of spacer wire, whether between a wire and a clad (Figure 1.5a) or a wire and one surface of the wrapper tube (Figure 1.5b). Therefore, there is a plan with contact points every $1/12^{th}$ of the helical pitch noted Lp. In a fuel subassembly of ASTRID, with a helical pitch of 180 mm and a pin length of 2.136 m, the subassembly contains approximately 15,000 potential contact points.

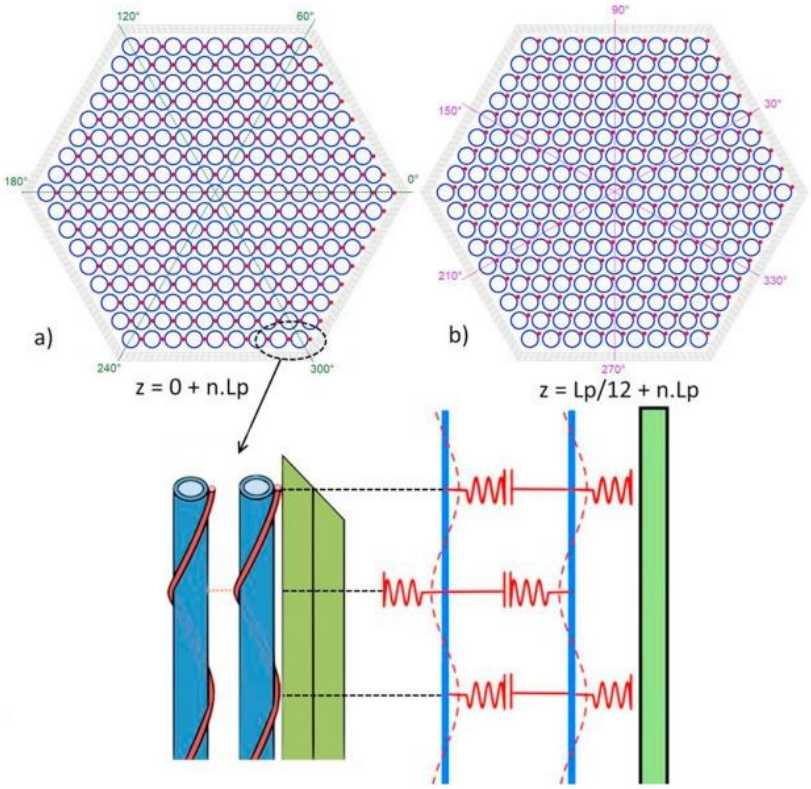

Figure 1.5. Sub assembly sections and schematic representation of contacts [2]

Due to the great number of collisions, the numeric implementation of contacts remains challenging. Fadaee and Yu [3] has proposed the linear complementarity problem (LCP) formulation for handling the frictional contact problem. The study is conducted on an array of 37 rods of CANDU type inside a tube. The rod-to-rod contact is supposed to be frictionless and the multiple unilateral frictional constraints between rod and the outer tube are reduced through a coordinate transformation and an auxiliary incremental displacement variable. Several frictional models were applied by Hassan and Rogers [4] to understand the effect of tube-support clearance and preload on the predicted work rate.

There are several ways to model the normal contact in structural dynamics [5]. There are two major categories: non-smooth laws for which the contact is instantaneous and the velocity is discontinuous, and smooth laws for which solids in contact will be able to interpenetrate each other. In non-smooth dynamics, a restitution parameter, which refers to the ratio between absolute values of velocity before and after the shock, is introduced to model the damping [6]. The discontinuity of velocity represents a challenge for the usual time-stepping integration schemes. As a consequence, specialized methods have been devised to treat such problems [7]. In smooth dynamics, the support exerts a restoring force F_c on the structure for the duration of contact, which occurs over a finite time interval rather than instantaneously. The non-linear force is introduced with a penalty formulation depending on the distance δ between reference points of solids in contact [8]:

$$F_c(\delta) = \begin{cases} 0 & if\ \delta > 0 \\ g(\delta) + h(\delta, \dot{\delta}) & if\ \delta \leq 0 \end{cases} \tag{1.1}$$

The simplest impact law is “linear spring dashpot” [9] where $g(\delta)$ represents a linear spring of stiffness k_c and $h(\dot{\delta})$ a linear impact damper to account for energy losses resulting from impacts, which is analogous to the role of a restitution coefficient. In comparison with the non-smooth

laws, besides enhanced ease for numerical simulations, this approach has the advantage of being physically significant, as the parameter k_c is a measurable quantity which represents the cross-section deformation during impact. Catterou [12] has proposed a non-linear contact law by taking into account all the possible phenomena, as schematized in Figure 1.6. The contact forces generated by the ovalization of clad and spacer wire are computed by using Fourier series decomposition and solving a fourth order system of equation [10], which are proportional to δ and the contact force generated by the spacer wire-to-clad or spacer wire-to-wrapper tube local deformation is modeled by the Hertz theory [11], which is non-linear whatever the surface in contact. The spring combination is quasi-linear, but Hertz stiffnesses add a substantial flexibility to the contact point [2], so that equation (1.1) can be applied.

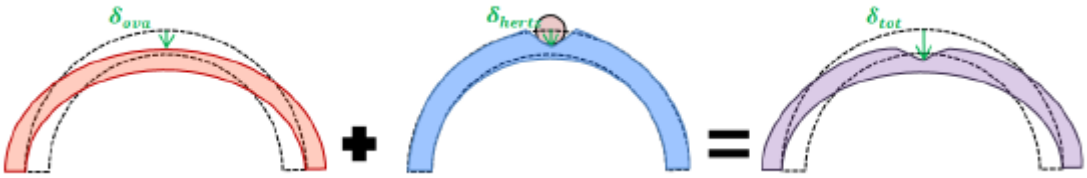

Figure 1.6. Ovalization and local deformation

1.2.2 Nonlinear damping

Catterou [12] performed bending release tests on pins of two different pellet materials. Three different phases of damping are identified, as shown in Figure 1.7. A phenomenological model is proposed and reveals that the high damping for large oscillations is due to friction between pellets and the phases for smaller oscillations are due to the viscous damping of the clad and of the pellets. The nonlinear aspect due to the presence of pellets has been studied for the first time by Lee [13] who computed the displacement of the pellets column introduced inside a clad with clearance. His work has been extended by Choi [14]. Then recently, several papers discussed about nonlinear damping on fuel rod, particularly the increase of damping due to loading magnitude and the effect of the pellets/clad clearance [15]-[17].

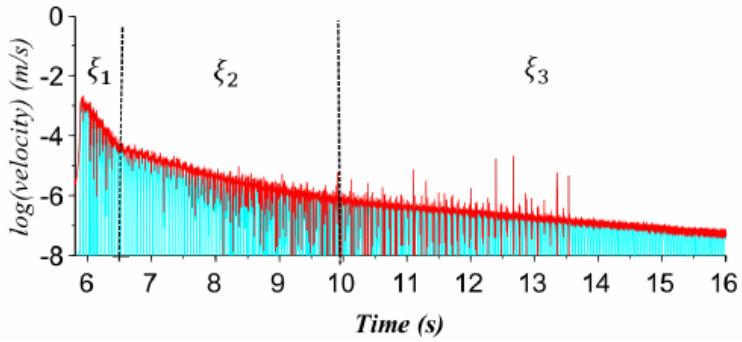

Figure 1.7. Three phases of damping for a lead-antimony pin [12]

1.3 Hydraulics in fuel sub-assembly

The study on the flow pattern in wire-wrapped fuel bundle is of interest since the prediction of the thermo-hydraulics characteristics is vital to estimate the performance and safety of SFR reactors.

1.3.1 Experiments

Few experiments with sodium as the coolant in forced convection regime were conducted in the 1970s and 1980s [18][23]. Many experiments have been performed in earlier reactor design stages to measure the pressure drop due to friction in a channel with length L and hydraulic diameter D_h :

$$\Delta p = \frac{1}{2} f_D \frac{L}{D_h} \rho v^2 \tag{1.2}$$

with f_D the Darcy friction factor.

Novendstern developed a semi-empirical model to predict pressure losses in a hexagonal array of wire-wrapped pins in the turbulent flow regime [24]. Rehme, who performed a vast number of experiments, proposed a model based on an effective velocity, taking into account the swirl motion. Additionally, a parameter was incorporated to take into account the influence of the number of pins [25]. Cheng and Todreas introduced their hydrodynamic models for sub-channel friction factors and mixing parameters in a 37-pin fuel bundle, which covered the laminar, transition and turbulent flow regimes [26]. In the detailed correlation (CTD), the friction factor in all three types of subchannels are computed. In the edge and corner subchannels pressure drop is mainly caused by skin friction due to a swirling, induced by the wire, while in the interior subchannels the pressure drop originates from a combination of wire drag and skin friction. As the evaluation of this correlation is quite tedious, the same authors also gave a simplified correlation (CTS), lumping the effect of the three types of subchannels in one global coefficient. A summary [27] of pressure-drop correlations and their application range are given in Table 1.1. These correlations are then evaluated by more experiments with different geometrical parameters and pin numbers [28][30].

Table 1.1. Summary of pressure-drop correlations and their application range (The geometrical parameters are indicated on Figure 1.8)

Model	Number of pins	P/D	Helical pitch/D	Flow type	Re
NOV	19 - 217	1.06 – 1.42	8 - 96	Trans. / Turb.	$2600 – 2.10^5$
Rehme	7 - 217	1.1 – 1.42	8 - 50	Trans. / Turb.	$1000 – 3.10^5$
CTD	19 - 217	1.0 – 1.42	4 - 52	All	$50 - 10^6$
CTS	19 - 217	1.025 – 1.42	8 - 50	All	$50 - 10^6$

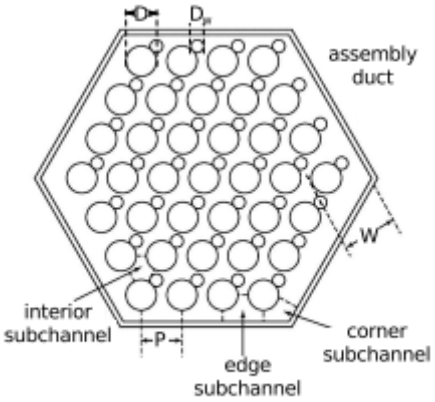

Figure 1.8. Typical wire-wrapped triangular rod bundle with some common notation: P - pitch, D - rod diameter, Dw - wire diameter, W – edge pitch diameter [27]

More detailed flow characteristics are also studied by some experiments. Roidt [31] investigated the pressure drops and hydraulic velocity field inside a 217-pin wire-spacer assembly with the probes. More recently, the high spatial and temporal resolution measurements of the pressure and velocity fields at different locations in a 61-pin fuel bundle of MYRRHA-reactor have been performed by employing the matched-index-of-refraction (MIR) technique to allow laser diagnostic velocity measurement techniques, especially, particle image velocimetry (PIV) [32][33]. The recent experiments offer the validation of numeric simulations [34].

1.3.2 Numeric studies

Modeling the flow in wire-wrapped pin bundles is still a challenging problem. Large uncertainties exist in the treatment of wire spacers and drag models used for momentum transfer in current low resolution (lumped parameter) models. Some traditional subchannel codes treat the wire effects solely as an enhancement of turbulent mixing but ignore the directional cross flow between subchannels [35][36]. Others, such as COBRA-IV [37], ASFRE [38], and MATRA-LMR-FB [39], apply "forcing function" type models to account for the diversion flow but are limited in their applications to certain validated conditions (flow regime, channel geometry, or operating conditions) and rely on complex coefficients which were derived from fitting certain sets of experimental data.

In most of the cases, the insight of the flow characteristics in wire-wrapped pin bundles is offered by Computational Fluid Dynamics (CFD) tools. These simulations have received extensive interest. There are three CFD approaches of different levels of accuracy for modelling the turbulent flow: Reynolds Averaged Navier Stokes (RANS), Large Eddy Scale (LES) and Direct Numerical Simulation (DNS). In DNS, the meshing size should be of the Kolmogorov scales, which is proportional to $1/Re^{9/4}$. Therefore, the simulation with DNS for high Re number is very time consuming.

RANS Studies

The principal of RANS method is to decompose the variables in to a time averaged part and a fluctuating part, which is considered as the influence of turbulence. The main advantage of this method is its low computational cost and time taken to have average steady state results.

Taking the velocity $\boldsymbol{v}$ for example of decomposition:

$$\boldsymbol{v} = \frac{1}{\Delta t}\int_{t}^{t+\Delta t} \boldsymbol{v}dt + \boldsymbol{v}' = \overline{\boldsymbol{v}} + \boldsymbol{v}' \tag{1.3}$$

with Δt the time step of the temporal discretization. The Reynolds averaged Navier-Stokes equations for incompressible flow are as follows:

$$\nabla\overline{\boldsymbol{v}} = 0 \tag{1.4}$$

$$\frac{\partial\overline{\boldsymbol{v}}}{\partial t} + (\overline{\boldsymbol{v}}\cdot\nabla)\overline{\boldsymbol{v}} = -\frac{1}{\rho}\nabla\bar{p} + \nu\nabla^2\overline{\boldsymbol{v}} - \frac{\partial(\overline{v_i'v_j'})}{\partial x_j} \tag{1.5}$$

The Reynolds decomposition of variables into time averaged and fluctuating quantities leads to additional term – product of fluctuating velocities called as Reynolds stresses. Only the equations for time averaged variables are simulated while the Reynolds stresses are modelled. There are two major categories of RANS turbulence model – Eddy Viscosity Model (EVM) and Reynolds Stress Models (RSM). The EVM is a first order turbulence model that uses the Boussinesq hypothesis. The RSM is the second order turbulence model that solves a separate differential transport equations for each component of Reynolds stress.

EVMs are the common used model to simulate the flow pattern in wire-wrapped fuel bundle. Depending on the way the eddy viscosity is modelled, there exists: zero equation model like mixing length model, one equation model based on equation for turbulent kinetic energy k, two equations model like k-ε model, k-ω model [40], Shear Stress Transport (SST) model [41].

Ahmad and Kim [42] and De Ridder [43] performed RANS simulations of 7- and 19-pin bundles using the k-ω SST turbulent model. Natesan [44] studied with several turbulence models (k-ε, k-ω and RSM) in a range of Reynolds numbers between 50000 and 150000, while Rolfo's work [45] is a complementary by decreasing the interested range of Reynolds numbers. Gajapathy performed RANS simulations on 7-pin bundles using the k-ε model [46]. RANS calculations for 37-pin fuel bundle using k-ε and k-ω turbulence models were presented in Rasu [47] and Jeong [48].

LES Studies

In LES, only the large scales of motions which are carriers of energy are simulated, and the smaller scales of motion which undergo energy dissipation are modelled using sub-grid model. A filtering operation G is defined to filter out the turbulent scales, taking the velocity v for example:

$$v = \int_{-\infty}^{+\infty} G(x-\xi)v(\xi)d\xi + v'' = \langle v\rangle + v'' \tag{1.6}$$

v'' denotes the sub-grid value for the small isotropic scales, which is considered as the turbulent effect. The LES space filtered equations for incompressible flow are as follows:

$$\nabla\langle\boldsymbol{v}\rangle = 0 \tag{1.7}$$

$$\frac{\partial\langle\boldsymbol{v}\rangle}{\partial t} + (\langle\boldsymbol{v}\rangle\cdot\nabla)\langle\boldsymbol{v}\rangle = -\frac{1}{\rho}\nabla\langle p\rangle + \nu\nabla^2\langle\boldsymbol{v}\rangle + \frac{\partial}{\partial x_j}(\langle v_i\rangle\langle v_j\rangle - \langle v_i v_j\rangle) \tag{1.8}$$

$$\tau_{ij} = \langle v_i\rangle\langle v_j\rangle - \langle v_i v_j\rangle \tag{1.9}$$

The new term τ is the sub-grid-scale stress tensor, which represents the transfer of momentum due to sub-grid viscous forces. The sub-grid-scale turbulence models employ the Boussinesq hypothesis as in the RANS models, computing sub-grid-scale turbulent stresses as shown below:

$$\tau_{ij} - \frac{1}{3}\tau_{kk}\delta_{ij} = -2\nu_t\langle S_{ij}\rangle \tag{1.10}$$

$$\langle S_{ij}\rangle = \frac{1}{2}\left(\frac{\partial\langle v_i\rangle}{\partial x_j} + \frac{\partial\langle v_j\rangle}{\partial x_i}\right) \tag{1.11}$$

where ν_t is the sub-grid viscosity, $\langle S_{ij}\rangle$ is the filtered rate of deformation. Smagorinsky supposed that there is no production and dissipation of energy in the sub grid and model the eddy-viscosity by [49]:

$$\nu_t = (C_s\Delta)^2\sqrt{2\langle S_{ij}\rangle\langle S_{ij}\rangle} \tag{1.12}$$

where C_s is the Smagorinsky constant and Δ is the filter length.

The application of LES to the geometry of sub-assembly with spacer-wire is limited. Fischer performed hydraulic calculation using LES method on central local region of fuel pin with a part of neighboring pins and axial periodicity [50]. In the work of Saxena [51], the RANS method is used at first to give information about the steady state velocity, pressure and temperature field in the complete sub-assembly with 217 fuel pins of ASTRID type. The information about higher order statistics of these physical quantities is then obtained by performing LES calculation on the local region of the sub-assembly, which is of the similar geometry as that used by Fischer.

With all the above experiments and CFD simulations, the main flow characteristics can be concluded. As shown in Figure 1.9, the flow has two distinct region: the central flow and the peripheral flow. In the central part, the sodium follows a helical movement along the spacer wire whereas in the periphery the fluid rotates around the hexagonal duct wall, which is called swirl flow. Close to the wire a wake exists, arising from the flow crossing the wire. When the wire passes through an inter-channel connection a steady vortex is shed from the wake of the wire. The wire additionally causes axial flow velocity variations, with a low flow velocity in the gap between the rod and its wire, in the wake of the wire and in the vortex shed from it. To ensure continuity the axial flow velocity is higher directly outside these regions. The increased flow velocity zones cause coherent and steady pressure differences across the bundle.

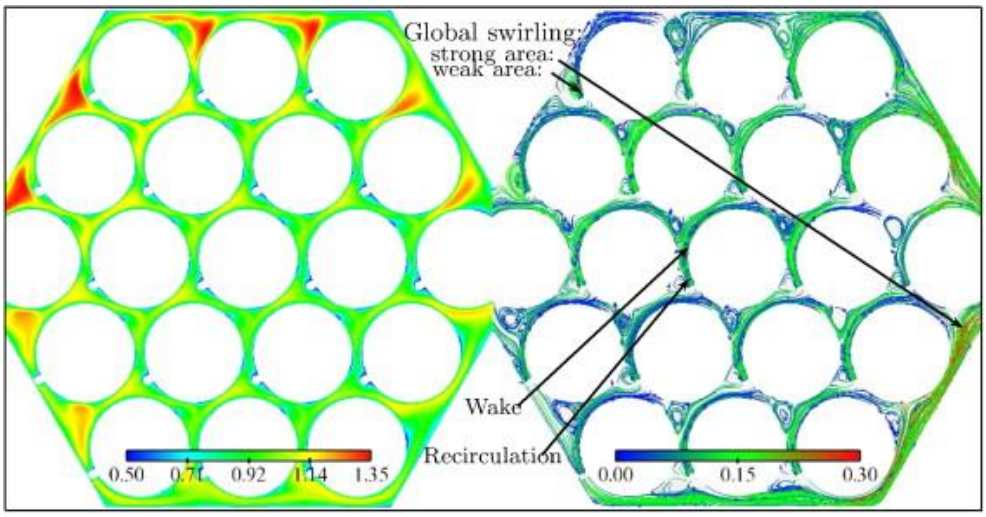

Figure 1.9. The velocity distribution for 19 pin sub-assembly showing (a) dimensionless streamwise velocity and (b) transverse velocity [45]

1.4 Fluid-Structure Interaction

Understanding and modelling the interaction forces is of fundamental importance in order to be capable of predicting the dynamic behaviors of the fuel pins under seismic loading. As the flow described in the previous section is mainly aligned with the fuel pin bundle and the remaining cross-flow is changing direction multiple times along the full height, the investigation of fluid-structure interaction of the system consists of flexible cylinders in axial flow.

1.4.1 Solitary cylinder in axial flow

Many of the analytical models for slender cylinders or related structures in axial flow that are used nowadays are mainly based on motion-induced hydraulic forces, by assuming that the axial flow is steady and uniform, and are thus not based on the full Navier-Stokes equations. Paidoussis [52] built a dynamic theory for a single flexible slender cylinder in axial flow, based on Lighthill's theory [53] which was used to deal with the inviscid force, and Taylor's theory [54] which was applied to get the viscous force imposed on cylinder. Later on, Paidoussis modified his theory [55] by taking gravity into account and modifying frictional force.

The inviscid force derived F_A from potential flow theory is related to the added mass M:

$$F_A = M\left(\frac{\partial^2}{\partial t^2} + 2\frac{\partial^2}{\partial t \partial x} + U^2\frac{\partial^2}{\partial x^2}\right)w \tag{1.13}$$

where U the bulk velocity of the axial flow and w is the centerline displacement of the cylinder. The added mass is equal to ρA for unconfined flow, with ρ the density of fluid and A the cross section area of the cylinder, while for a confined flow it increases as the diameter of the flow channel decreases [56][57]. A parameter related to confinement is introduced and $M = \chi\rho A$.

$$\chi = (D_{ch}^2 + D^2)/(D_{ch}^2 - D^2) \tag{1.14}$$

with D_{ch} the diameter of confining channel. Experiments [55][56] demonstrate clearly that the cylinder is greatly destabilized by confinement, which means a smaller critical velocity for the divergence (buckling around the cylinder's static equilibrium) of the cylinder.

The viscous forces based on Taylor's theory, respectively in normal and longitudinal direction, can be linearized for the small displacement by:

$$F_N = \frac{1}{2}\rho D U C_N \left(\frac{\partial w}{\partial t} + U\frac{\partial w}{\partial x}\right) + \frac{1}{2}\rho D C_D \frac{\partial w}{\partial t} \tag{1.15}$$

$$F_L = \frac{1}{2}\rho D U^2 C_T \tag{1.16}$$

In the expression for the normal forces, C_D governs the friction due to the movement in a viscous medium without flow. C_N and C_T are the friction drag coefficients corresponding to normal and tangential frictions. The values used for the coefficients of these forces have been studied by many experiments, as summarized in the works of Paidoussis ([58] Appendix D and [59] Appendix A).

However, more recent combined experimental and numerical work by Divaret [60] has found that, contrary to expectations, (i) the normal force on a yawed cylinder is dominated by lift rather than drag; (ii) for small yaw angles, damping depends linearly, rather than quadratically on the yaw angle; (iii) the damping rate increases linearly with axial flow velocity. These important new results cast doubt on the validity of Taylor's model. This work was pursued by Joly [61], both numerically and experimentally. One important finding is that C_N has a much larger value, thus 0.11 is reported rather than 0.0125, which is habitually used [57][62].

The dynamic behavior of a cantilevered cylinder is affected strongly by the velocity of fluid along the cylinder, as well as by the boundary condition at free end. Assuming that the cross-sectional area is tapered smoothly from A to zero over a distance l sufficiently short over the total length L and the lateral velocity of cylinder to be considered constant, the boundary condition on tapered end, if frictional and gravity effects are neglected, can be expressed as [52][63]:

$$EI\frac{\partial^3 w}{\partial x^3} + fMU\left(\frac{\partial w}{\partial t} + U\frac{\partial w}{\partial x}\right) - (m + fM)\chi_e \frac{\partial^2 w}{\partial t^2} = 0 \tag{1.17}$$

where EI is the flexural rigidity, m is the mass per unit length of the cylinder and $\chi_e = \frac{1}{A}\int_{L-l}^{L} A(x)dx$. Considerably more elaborate forms of Eq. (1.17), taking into account friction and gravity effects, are available in the works of Lopes [58][64]. f is the parameter dealing with the shape of the free end. For a well streamlined end, f tends to 1 and for blunter ends, f tends to 0. Experiments [52],[65][66] have been conducted to study the effect of end shape on the cylinder dynamics. For a cylinder with a fairly well streamed end, the onset of divergence occurred at a certain flow velocity and when the flow velocity was increased further, a second-mode flutter developed (oscillatory instability), while for less well-streamlined free-end shapes, the system is more stable, i.e. the critical flow velocities for both divergence and flutter are higher. Numerical studies [65][67] on the parametric effect on the dynamics of cantilevered cylinder shows a reasonable agreement with the experimental observations. For most theoretical calculations, the base drag at free end, expressed as $\frac{1}{2}\rho D^2 U^2 C_b$, is related to its shape and $C_b = \frac{\pi}{4}(1 - f)$ was taken arbitrarily due to the lack of refinement in dealing with the free-end boundary conditions [58]. These works are in the context that the cylinder is of length relatively short, de Langre [68] has then extended the similar studies into the case of a very long cantilevered cylinder.

Studies have also been conducted on the dynamics of a cylinder in axial flow by means of numerical simulations, utilizing CFD-CSM (computational fluid dynamics and solid mechanics) methodologies. Liu [69] obtained solutions utilizing the arbitrary Lagrange–Euler (ALE) framework to solve the Navier–Stokes equations. A more extensive study was conducted by De

Ridder [43]. In the CFD part, the Reynolds-averaged Navier–Stokes (RANS) equations were solved, with turbulence modelled by the k-ω model. They obtained values for the critical flow velocities for static divergence and flutter comparable to those of experiments [70] for cylinders with clamped ends. More recently, Ter Hofstede [71] deployed SST k-ω and RSM model and found that dominant vibration frequency of the cylinder in turbulent flow matched reasonably well with the experimental data reported in Lillberg [72]. The random pressure fluctuations resulting from the main flows were found to be the main factor responsible for the vibration of the cylinder. However, these two models could only capture large-scale flow structures which were responsible for low frequency pressure fluctuations. De Santis [73], based on the SST turbulence model, studied the dependence of the modal characteristics of a cylinder from that of experiments. Another study was made by Lu [74] on the dynamics of a clamped–clamped cylinder in axial flow, with special emphasis on the effect of turbulence intensity on the dynamics.

1.4.2 Clustered cylinders in axial flow

It is obvious that there exists coupling in the motions within a cluster: when one cylinder moves laterally, the fluid is accelerated and transverse forces are generated on the moving cylinder and on all other cylinders.

The earliest studies have been performed by Chen [75], Paidoussis [76][77] and many others. The hydrodynamic normal inviscid force is, instead of one added mass for each cylinder, generalized into an added mass matrix. For a cluster of K cylinders under axial flow, it has been shown that free motions are coupled, so that the different modes of the system are characterized not only by the axial modal shapes of each cylinder, but also by the cross-sectional patterns of motion involving all cylinders in the cluster, i.e. $2K$ modes with each flexural mode shape, differing from one another by different cross-sectional patterns of motion. The viscous coupling matrix was first presented by Lin [78]. The expressions of the forces are given in [58].

The modal and spectral characteristics and flow-induced vibration of four-cylinder clusters were studied both theoretically and experimentally by Paidoussis and Gagnon [79][80][81]. Good agreement was found. The works revealed that the clustered cylinders in close spacing lost stability by buckling and flutter at high flow velocities, similarly to isolated cylinder in an unbounded flow, however, the critical flow velocities were much lower.

A great deal of works are devoted to the small-amplitude vibrations of clusters excited by turbulence in the flow, in which case the flow velocity is below the threshold of fluid-elastic instabilities, they are synthesized by Paidoussis and Curling [82]. Stochastic analytical equations for obtaining the vibratory response of bundles of cylinders in turbulent axial flow are presented [83]. The cross-spectral densities (CSDs) of wall-pressure fluctuations around the circumferences of the cylinders are necessary for characterizing the excitation field (lateral CSD of the turbulent fluid force-per-unit-length), thus the calculation of the spectral densities of the random vibration response of the cylindrical structures. Measurements [81][84][85] of the pressure field have been performed.

Numerical studies on a cluster of cylinders, utilizing CFD-CSM have been conducted. Liu [86] studied the fluid–structure interaction of two- and four-cylinder clusters in axial flow with the arbitrary ALE framework to solve the Navier–Stokes equations. De Ridder [87] generalized his work [43] into the study of the modal characteristics of a 7-rod bundle. De Santis [88]

subsequently studied the dynamics of two- and seven-cylinders cluster with SST k-ω turbulent model.

While the works above depict the dynamics of each cylinder in the cluster, Ricciardi [89] proposed a homogenization method, based on the Paidoussis theory, to study the global dynamics of a Pressurized Water Reactor (PWR) fuel assembly (a cluster of cylinders with two ends clamped). Then this work is extended to the simulations of a row of 3 fuel assemblies separated by by-passes with axial flow [90], utilizing the model proposed in a precedent work [91]. It is found that the coupling between the assemblies by the flow appears to be significant.

It is noted that the numerical studies are concerned with the cluster of cylinders with two ends fixed, but the methods can be applied to the studies on the cluster of cantilevered cylinders.

Chapter 2 Test bench CARNEAU

The fuel pin bundle in axial turbulent flow is a complex system, involving several potential contact zones and fluid-structure interaction. In order to take all these physical phenomena into consideration when characterizing the dynamics of fuel pins, the models discussed in the precedent chapter will be applied. Therefore, many empirical parameters are to be determined. The design of our test bench is inspired by the earlier experiments conducted in CEA.

2.1 Earlier impact tests on SFR fuel pins

2.1.1 Experiments of Pelloux

Pelloux was interested in the dynamics of a row of fuel pins under earthquake [92]. The tests were conducted with fuel pin sections hung by strings on a fixed frame and enclosed in a carriage filled with air or water. The number of the fuel pin sections and the clearance between them are adjustable. The instrumentation consisted of two accelerometers and force sensors at the plates on the wall of carriage, which measure the impact between fuel pins and wrapper tube. The stiffness and damping of impact have been identified by release tests of one hanged fuel pin section, considering it as the Newton's pendulum. Forcing tests have also been done with the carriage solicited by a frequency-adjustable vibrant.

In order to study the effect of clearance, experimental results have been compared with the numerical results from a simplified mass-spring model, where the spring models the bending of fuel pins. Numerical calculations seemed to show that the low clearance results in a greater impact force (from 10 to 25%), but the experimental tests, due to the low acquisition frequency and parameter uncertainties, have the difficulty in proving this phenomenon. Therefore, the model is not representative of the real system, complete models such as the BELIER test bench had to be conducted.

2.1.2 BELIER test bench

The BELIER tests are the impact tests on a truncated PHENIX sub-assembly in air or water carried out between the 1989 and 1995 [93][94][95]. The impacts are measured with the release tests against a fixed stopper stiffened in bending and in torsion by braces, making it possible to obtain the shocks on the plates. A device consisting of a pull rod and a trigger is used to impose the initial arc of the sub-assembly. The foot is embedded in a pedestal (instead of a ball joint and a sliding pivot connection) and its diameter has been adjusted to obtain an equivalent stiffness close to that of the PHENIX sub-assembly at the level of the mid-plan. The mass of the lead sinker at the head of sub-assembly has been adjusted to have the frequency of the first mode close to that of the actual assembly. A sensor measuring the force and displacement at the head make it possible to quantify the energy of the impact and the deformation gauges on fuel pins make it possible to estimate the stresses during the test.

The experimental campaign showed the very strong sensitivity of the sub-assembly to the smallest defects, especially on the conditions of alignment of the components and on the fuel pin clearances and the parasitic vibrations, which result in the dynamic behaviors of the model not representative of the real system. It was difficult to conclude with the experimental results which configuration (free or compacted) is the most restrictive.

2.1.3 CARNAC test bench

In general, the precedent experiments confirmed the order of magnitude of the theoretical and numerical results, they were found to be imperfect or incomplete on the instrumentation used or on the configurations tested. A new test bench CARNAC was developed by Catterou [2] in order to precisely understand the dynamic behavior of a fuel pin isolated from the bundle. It was intended to carry out the release and the forcing tests with the fuel pin of different geometries, in particular of ASTRID or PHENIX type, and with adaptable impact clearances. As shown in Figure 2.1, the fuel pin cantilevered at its foot is placed in a vertical position in a rigid frame. The forces of different frequencies and amplitudes are applied on the head of the pin using a shaker. Stoppers are placed on either side of the pin to represent the pin-to-wrapper tube and pin-to-pin contacts. The forces at each stopper are measured with force sensors and the velocity of fuel pin are measured at pre-defined points with laser vibrometers. The experiments conducted allowed to obtain the parameters of the impact force and also the non-linear damping of the vibration, as explained in section 1.2.

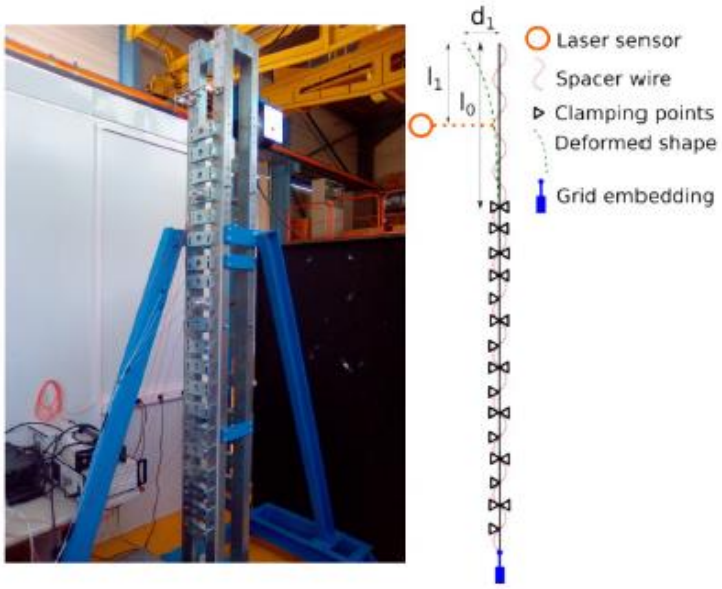

Figure 2.1. CARNAC test bench and schematic representation of bending release

However, only the experiments in air can be carried out with the CARNAC test bench. In order to obtain not only the parameters of impact force in flow, but also the coefficients characterizing the hydraulic forces, a new test bench combing the hydraulic part should be developed. Some earlier experiments on fluid-structure interaction can give us some inspirations.

2.2 Earlier experiments on fluid-structure interaction

Until now, the hydraulic experiments carried out in CEA are all with the PWR assemblies. The experimental campaigns began from 1991 by observing this strong fluid damping on the full-scale fuel assemblies [96]. The release tests were carried out and measured the assembly displacement through plexiglass front face by camera. The confinement were adjustable by screwing the PVC plates into the test section.

Later on, the difficulties are observed in determining the damping by the classical logarithmic decrement method: the damping being so strong that the oscillations disappear in less than one period. These difficulties of the release tests lead to the installation of a new experimental device: one assembly will henceforth be subjected to a quasi-harmonic excitation thanks to a

hydraulic jack [97], as shown in Figure 2.2. The force measurement at the level of this jack and the laser velocimetry measurements make it possible to obtain the transfer function and therefore fitting with the least square method to identify the fluid damping, for the first mode [98], and even for higher modes [99].

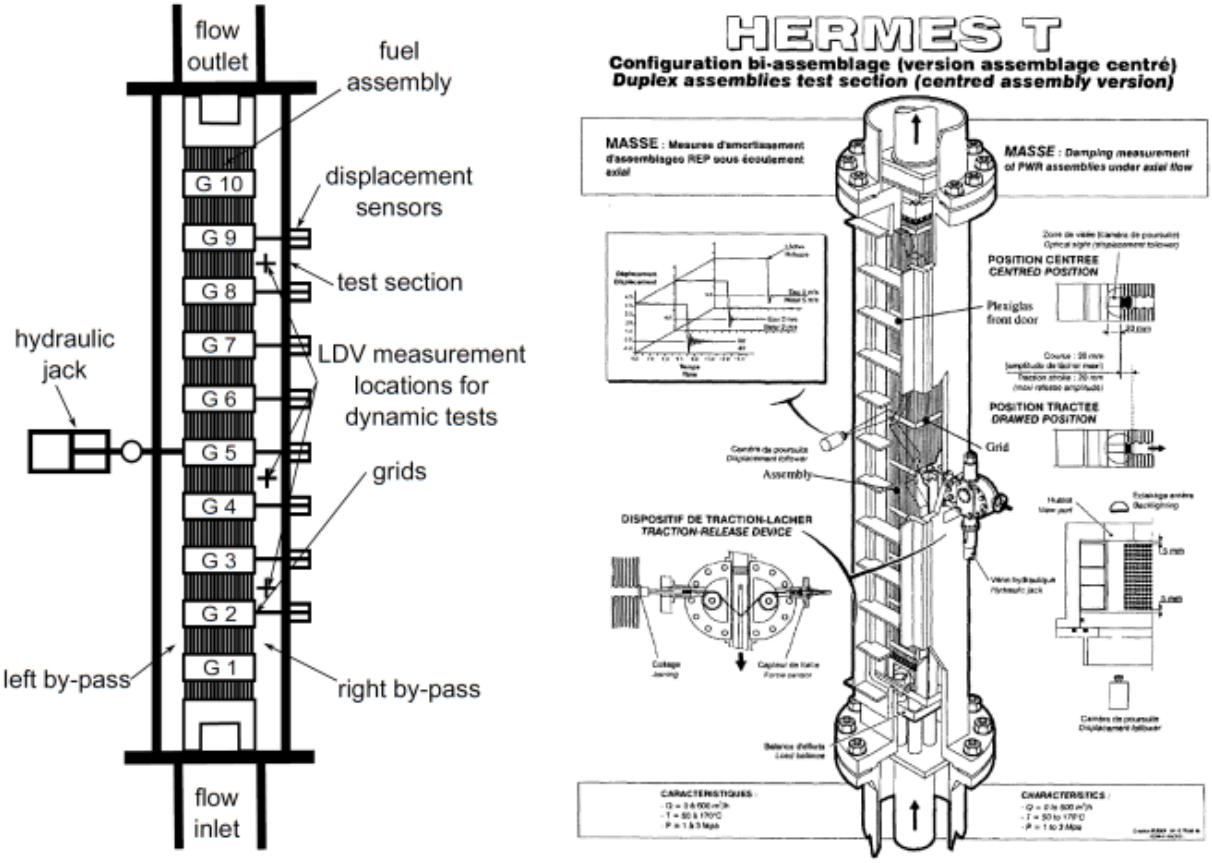

Figure 2.2. Schematic representation and configuration of Hermes test bench

Further experiments were conducted with the array of reduced fuel assemblies. The COUPLAGE experiments, made of 3*3 highly reduced fuel assemblies, allowed to study coupling force between the fuel assemblies and to outline the presence of non-negligible interaction forces between assemblies placed on different rows [89]. To be more representative, the ICARE facility has been designed [100]. Experimental results related to dynamical response of one excited assembly are presented and the coupling effects between different fuel assemblies are analyzed.

2.3 CARNEAU test bench development

Inspired by the previous experiments, a new test bench dedicated to estimate the impact forces under axial flow and the coupling between the fuel pins will be developed. The objective of the CARNEAU test bench is on one hand to identify a certain number of model parameters and on the other hand to give an experimental basis to validate the modeling of fuel pins under axial flow.

2.3.1 General description of CARNEAU test bench

The CARNEAU test bench is made up of the following main components:

1) A test vein to accommodate one, three or six pins in a row. This vein is a rectangular case with plexiglass portholes and entry/ exit connections.
2) A row of fake pins with fixed pellets, which were used in CARNAC tests, embedded in the foot of the vein.
3) A hydraulic loop supplying the water flow in the vein: a pump, the flexible supplying pipes and a temperature regulator.
4) A sliding rail allowing the horizontal mobility of the vein in the plane of the row of pins.
5) A shaker soliciting the vein in the direction of the sliding rail.
6) A spring for release tests.
7) Guidance at the top of the vein.
8) Instrument for measuring the displacement of the vein and the pins.

Experimental studies on the dynamic behaviors of SFR fuel pins have already been carried out in air on CARNAC test bench. The CARNEAU bench will be installed on the frame of the already existing CARNAC bench. We have carried out a preliminary design of the CARNEAU bench, which is shown in Figure 2.3. Even though this preliminary draft does not necessarily represent the ideal design to meet all the needs, it has offered an example to the enterprises and to this end, the holders have proposed other technical solutions and gave a price estimation.

In this preliminary draft, six pins are connected at the foot of the test vein by a mounting rail, this is representative of a row of fuel pins in the bundle with the wrapper tube being simulated by the right and left walls of the vein. The number of pins applied can also be reduced to one or three pins by screwing the blocks. The water flow, of which the temperature can be controlled, is supplied by a pump and circulates in the vein from the bottom to the top. In this way, an asymmetry on the water distribution can be imposed and the turbulence is well developed at the entrance. A sliding rail is used to connect the vein to the frame so that the movement is always in the x-z plane. The guiding pads will be installed on the upper part of the vein to prevent out-of-plane movements.

Two types of tests will be performed: release tests with the spring, and forced vibration tests for which the solicitation is exerted at the level of the connection between the vein and the pins. The shaker can provide the sinusoidal signals, of which the frequency and the amplitude are adjustable, to be representative of an earthquake.

A displacement measurement will be made through the plexiglass portholes by a fast camera supplied by CEA. To this end, the pins will be painted black with white dots every 2 cm in the axial direction and the displacements on these dots can be recorded and then analyzed by the existing software to obtain the parameters for different modes.

2.3.2 Demands on different components

The CARNEAU test bench have the objective of performing hydraulic tests in water, it will therefore be exposed to the water and to the atmosphere of the test hall. To this end, all the components will need to resist oxidation and corrosion.

2.3.2.1 Hydraulic vein

The test duct will be integrated into the CARNAC frame, therefore the constraints on the size and on the mechanical aspect must be respected, as detailed below. A schematic representation of the vein is shown in Figure 2.4.

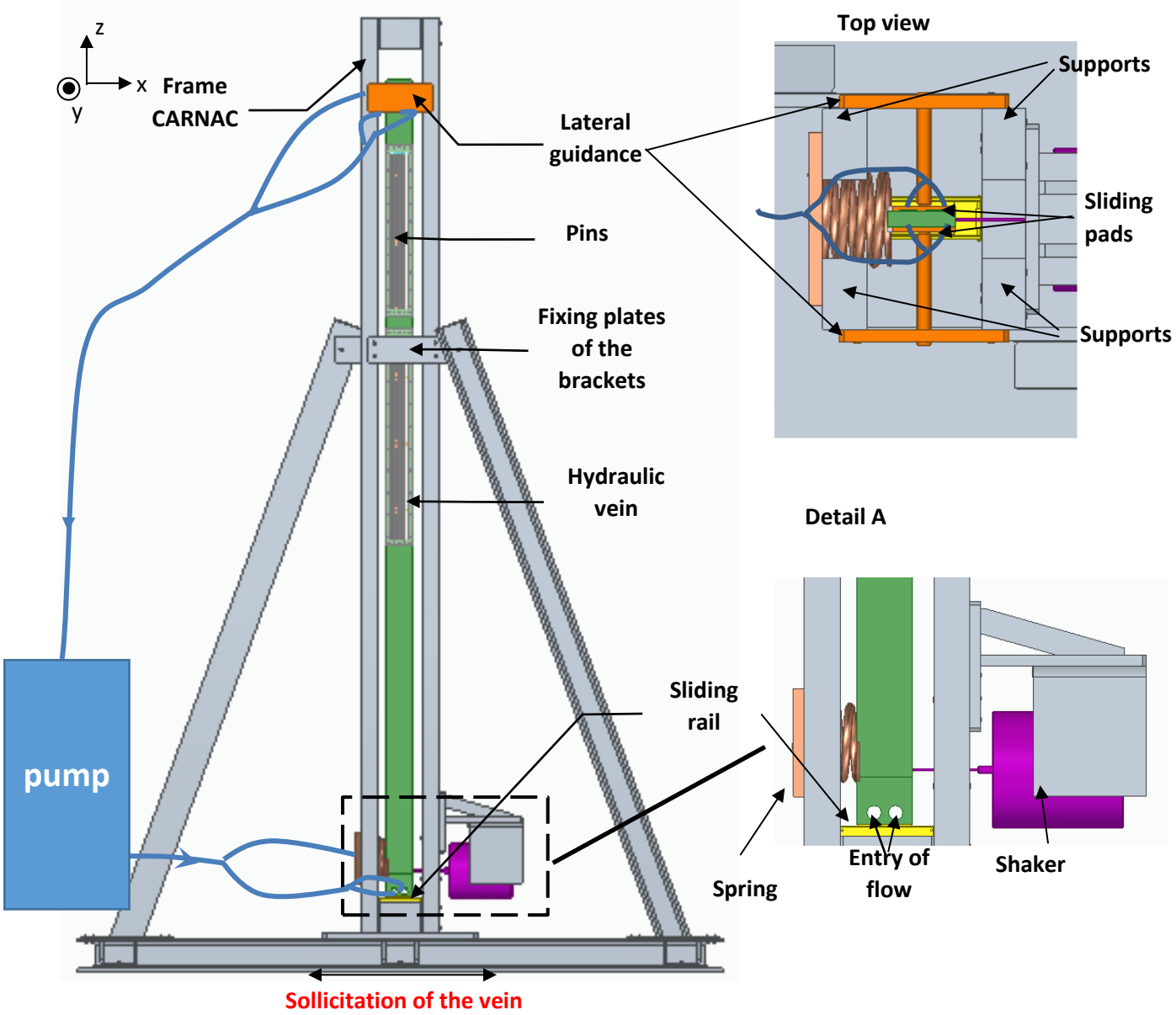

Figure 2.3. Preliminary design of the CARNEAU test bench

As the vein contains water, it must be sealed up to the maximum operating pressure, 3 bar. We propose a stainless steel case with symmetrical holes, equipped with 4 plexiglass portholes allowing optical measurements with cameras. The portholes must be flush with the internal face of the vein so as not to disturb the hydraulic channel. In order to have the vein enough rigid, the number and size of the portholes should be determined by the enterprises. But it should be guaranteed that the total height of the portholes allows the visualization of 90% the length of pins and the width allow visualizing the displacement of six fuel pins (Lx > 65.9mm).

The displacement of pins will be measured using a fast camera through the portholes at front face. The portholes will be installed on both the front and back faces so as to respect the symmetry to avoid twisting movements of the vein. The maximum amplitude of the displacement of the vein at the level of the sliding rail is of +/- 1 cm. The camera must be able to visualize through the portholes the interior of the vein between the supports of the CARNAC frame, the spacing of which in the direction x is 130 mm.

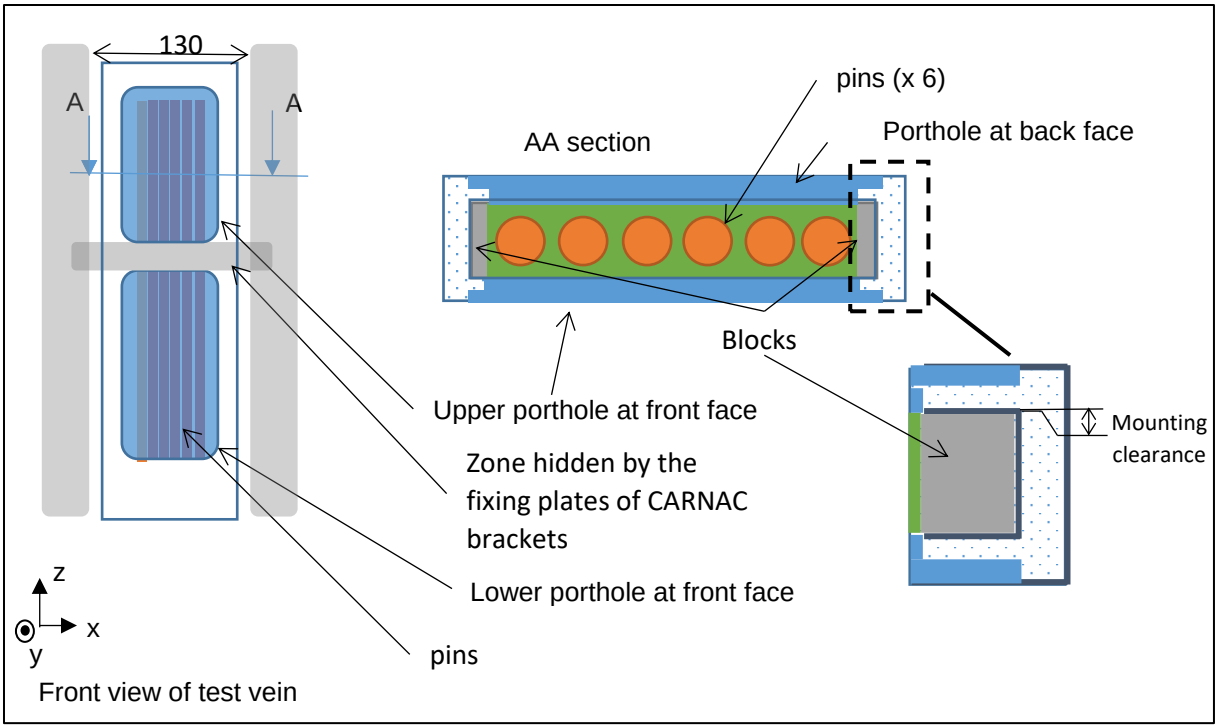

Figure 2.4. Schematic representation of the vein

The vein will be designed to contain, for the purposes of the tests, different numbers of pins (1, 3 or 6) with a clearance of 0.1 mm (clearance between the spacer wire and the clad of the neighboring pin). The maximum internal dimensions of the vein will therefore be imposed by the maximum number of pins to be integrated (see Figure 2.5). To perform the tests with a smaller number of pins (1 or 3), the internal dimension of the vein should be able to be reduced via removable blocks. For the sake of contact properties, the blocks will also be incorporated for the 6-pin configuration. The blocks and their means of fixing, whether from the top or from the side of the vein, will be designed in order to be capable of the manual operation when changing the test configuration. They must be fixed parallel to the internal walls of the vein, with an ignorable clearance to avoid the disturbance on the fuel pin vibration during tests. In all cases, the seal of the vein must be ensured.

In order to stabilize the flow, it will be necessary to maximize the distance d1 between the supplies and the foot of fuel pins and the distance d2 between the top of fuel pins and the outlets, as shown in Figure 2.5. The total height of the vein is however limited by the CARNAC frame: the CARNAC supports are 2700 mm long, and the lower and upper fixing pieces are 90 mm high, the total height of the vein with the sliding rail is therefore limited at 2520 mm.

The thickness of the stainless steel vein will be designed in order to guarantee the rigidity of the vein during dynamic tests. The displacement at the head of the vein along the x axis is expected to remain less than 3 mm for an acceleration of 0.5 g.

2.3.2.2 Mounting rail of the fuel pins

In a real fuel assembly, the connection is carried out by inserting the rails into a groove at the lower plug of the pins. The rail is used for mounting the fuel pin bundle, since it makes possible to join the pins of the same row. The embedding of the pins, being representative of the real rail, at the foot of the vein ensures their positioning in the vein. It will be designed to be

removable for the ease of changing the fuel pin number. Letting the pass by of the flow, the connection with the vein will be made at the ends of the rail (in red in Figure 2.6). Respecting the dimensions, the enterprises will be asked to make the propositions in order to guarantee the rigidity of the mounting rail.

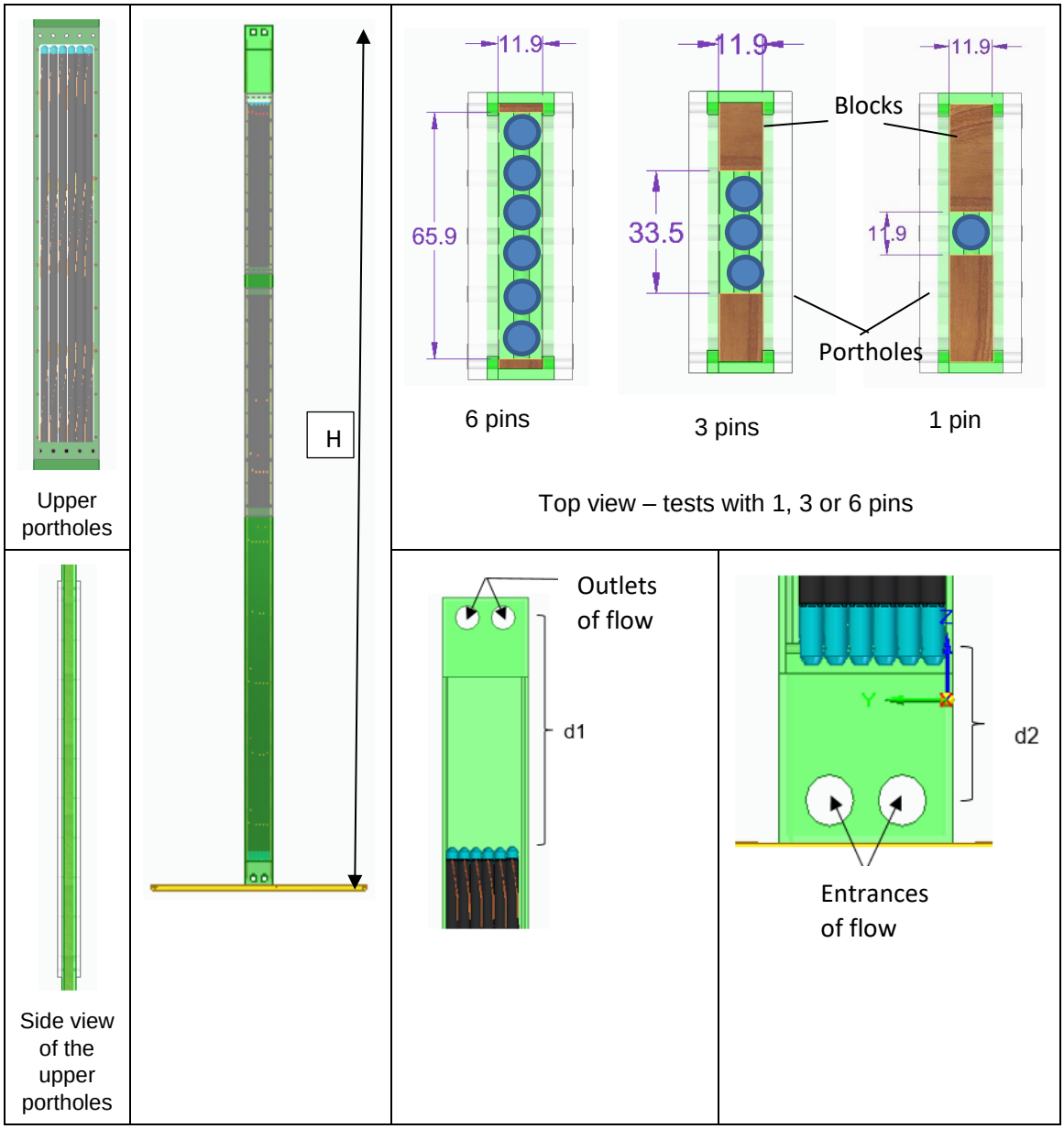

Figure 2.5. Detailed views of the pre-project CARNEAU vein

2.3.2.3 Sliding connections

The vein must be free in translation in the x direction, it will therefore be connected in its lower part to the CARNAC frame via a sliding rail (see Figure 2.3). In these pre-project studies, we consider a ball bearing slide, shown in Figure 8. As explained in section 2.3.2.1, the amplitude of the displacement during the dynamic tests is limited by the distance between the two supports of the CARNAC frame (130 mm). The length of the slide must make it possible to guide the vein in vibration in the desired frequency range (0-50 Hz) and amplitude (+/- 1 cm). If necessary, the slide can be extended to allow removing the vein from the frame and facilitate the mounting of the various components (pins, mounting rail and blocks). The clearance in the directions

perpendicular to the displacement must be minimal, ideally zero, in order to limit parasitic vibrations.

For dimensioning of the sliding rail, a force, equal to the product of the total mass (vein, pins and water) by an acceleration of 0.5 g, is applied to the center of gravity of the vein in a 6-pin configuration and filled with water. The force will result in a moment around the y axis. The rotation of the vein due to deformation of the slide is expected to remain negligible compared to the maximum deflection of the pins (0.6 mm), and therefore that the rotation of the vein around the y axis does not induce a displacement of the pins at the level of the upper plug greater than 0.06 mm.

The guidance will be installed at the top of the vein to limit its deflection in axis y. As shown in Figure 2.3, they are adjustable in y and z directions. Two sliding pads will be glued to the vein to reduce friction with the guidance.

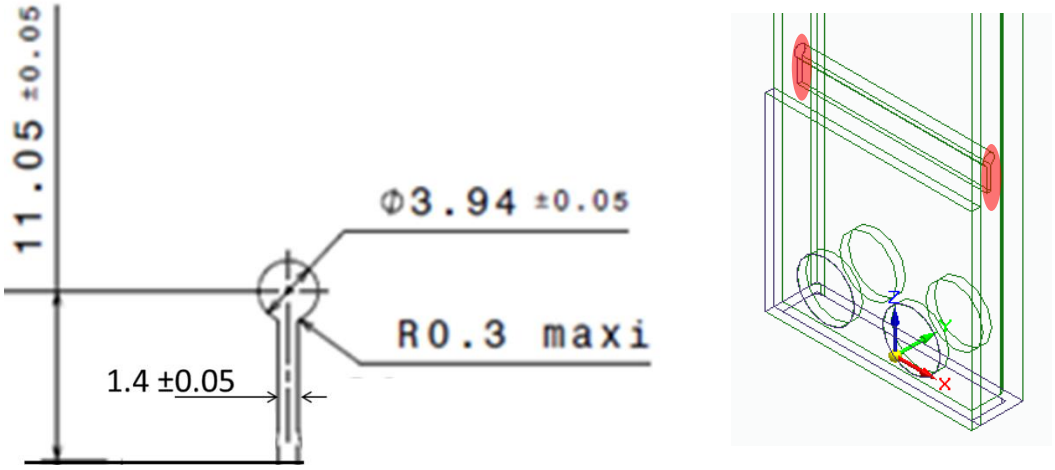

Figure 2.6. Pre-project mounting rail

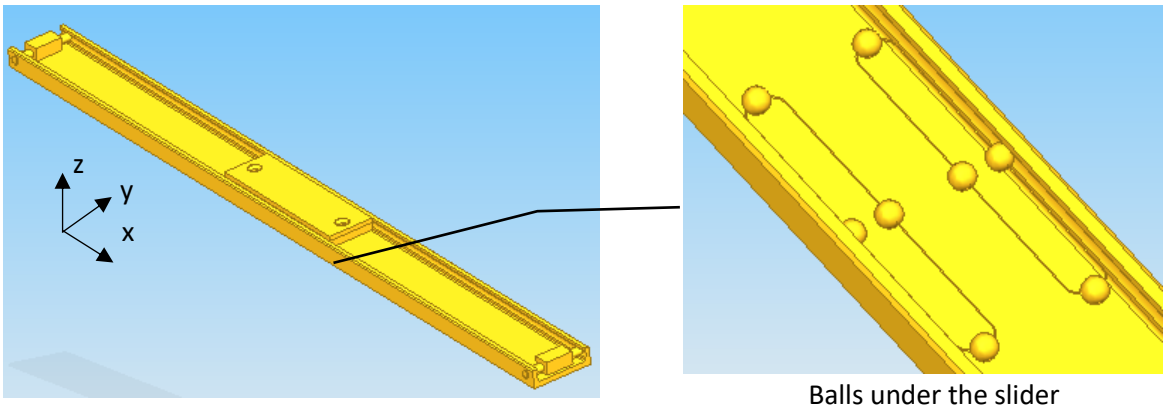

Figure 2.7. Ball bearing slide

2.3.2.4 Spring

To perform release tests with free oscillations of the vein, a spring will be placed at the lower part of the vein, as close as possible to the sliding rail, cf. Figure 2.8. The spring should be able to be tensioned by hand, thus a maximum spring stiffness of 15,000 N/m. For the forced vibration tests, the spring will be removed and replaced by a shaker.

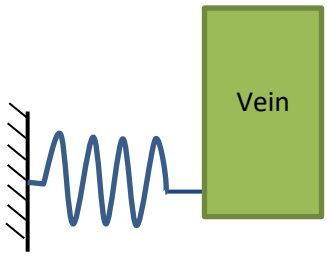

Figure 2.8. Schematic representation of the release test

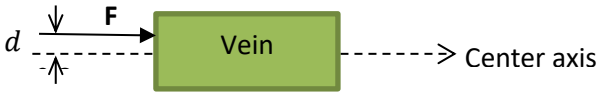

Figure 2.9. Position of the extension rod of the shaker

2.3.2.5 Shaker

The forced vibration tests are performed by stimulating the vein with a sinusoidal signal of variable frequency and amplitude using a shaker associated with an amplifier. The frequency range will be between 0 and 50 Hz, the maximum amplitude of the displacement will be +/- 5 mm and the maximum acceleration will be 0.5g. The shaker must withstand the dynamic forces imposed by the vein.

The rod of the shaker will be connected to the vein along the x axis at the level of the mounting rail. Drills must be made on the CARNAC frame supports to fix the shaker, as shown in Figure 2.3. The connection between the shaker and the vein is to be well defined. The strain on the vein should be minimized to avoid the flexion and torsion outside the xOz plane. Therefore, the force must be directed in the x direction and centered in relation to the thickness of the vein. The deviation of the position of the rod from the axis of symmetry of the vein should be less than 0.2 mm, as shown in Figure 2.9.

2.3.2.6 Hydraulic loop

A hydraulic loop will be installed to perform the tests under axial flow. It consists of a pump, a temperature regulator and symmetrical pipes at the inlet and outlet of the vein as shown in Figure 11. In order to guarantee the symmetry of the flow distribution, the vein is here supplied with water via four nozzles in the lower part. The water flow comes out of the vein through 4 nozzles in the upper part to go back into the pump. The inlet tapings must have an identical pressure of +/- 0.1 bar. Sensors are installed at upper and lower part of the vein to measure the pressure drop along the fuel pins.

The water temperature will be limited so that the components are not damaged. To approximate the properties of sodium in a reactor, the water temperature should be adjustable between 40 and 60 ° C. Two temperature sensors will be installed respectively at the inlet and outlet of the test vein.

The fuel sub-assembly in ASTRID reactor will experience an axial flow of approximately 25 kg/s of liquid sodium at 400℃ from bottom to top [1], thus the coolant speed is around 4.56 m/s. The flow velocity of the test bench can therefore be estimated according to the Burgreen criterion:

$$\frac{U_w}{U_{Na}} = \frac{{\rho_{Na}}^{0.5} \times {\mu_{Na}}^{-0.33} \times {E_{SFR}}^{-0.33} \times {M_{SFR}}^{0.165}}{{\rho_w}^{0.5} \times {\mu_w}^{-0.33} \times {E_{exp}}^{-0.33} \times {M_{exp}}^{0.165}} \quad (2.1)$$

where U_w is the water flow speed and U_{Na} is the sodium coolant speed. At a given temperature, ρ_{Na} and ρ_w are the respective densities while μ_{Na} and μ_w are the dynamic viscosities. Finally E_{SFR}/E_{exp} and M_{SFR}/M_{exp} are the ratios at SFR operation and test temperature of the Young moduli and the mass per unit length, respectively.

The resulting water flow speed in the testing temperature range is as shown in Figure 2.10, which yields a lower Reynolds number (around 3×10^4) comparing to that in the ASTRID fuel sub-assembly (5×10^4). It is not of much significance on the turbulence intensity, since we are working in a fully developed turbulent flow region. A flow meter will be installed in the circuit to control the flow velocity according to the temperature.

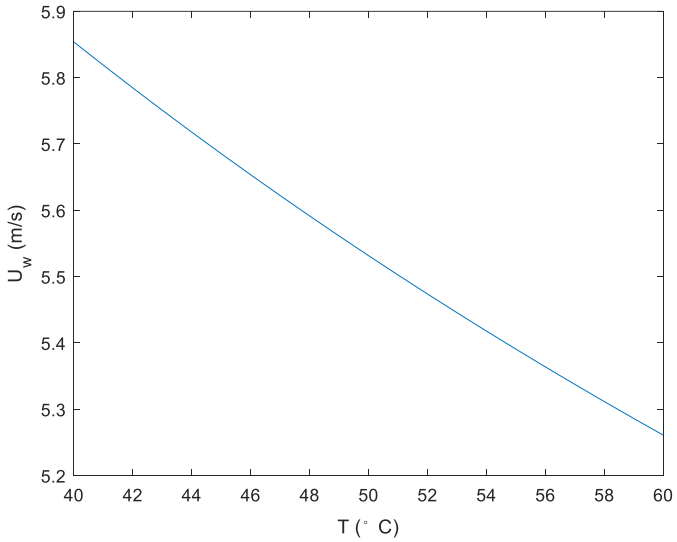

Figure 2.11. Water flow speed at test bench temperature

2.3.3 Experiments anticipated and difficulties encountered

As described in Section 1.3, the flow is mainly aligned with the fuel pin. However, the existence of spacer wire complicates the flow pattern: the remaining cross-flow is changing direction multiple times along the full height. This arises the difficulty in the investigation of local fluid-structure interaction of the fuel pin. However, the global parameters associated with the numerical model, which will be introduced in the following chapter, can be determined with the experiments.

In order to obtain the empiric parameters of the hydraulic forces and of the impacts, it is anticipated to perform the experiments in air, in still water and in water flow of different speed. As inspired by the previous experiments [97], the quasi-static (very low frequency) and sweep sine excitation are applied by the shaker. The modal analysis [101] is performed in each case to obtain the respective eigen frequencies and damping ratios. This allows to identify the global parameters, which take the effect of spacer wire on hydraulics into consideration.

Unfortunately, we were not able to perform the experiments as a result of the budget limitation and the difficulty arising from the health crisis.

Chapter 3 Dynamics of fuel pins: direct time-integration analysis

3.1 Numerical model

The objective of this section is to establish a numerical model to better understand the effect of fluid-structure interaction and of the impacts on the dynamics of the fuel pin.

The numerical simulation with finite element method for modelling the impacts in air has been discussed by Catterou [2]. Errors with different types of elements have been estimated with the static calculation of the displacement at the center of a pipe placed on four supports subjected to a distributed loading. With the dimensions of the ASTRID fuel pin, the choice of using Bernouilli beam elements associated with particular impact laws, which takes the ovalization into account is satisfying.

Given that the fuel pin can be modelled as the Euler-Bernouilli beam, the fluid related effects can be integrated as the hydraulic forces that the axial flow exerts on the slender body, whose expressions are proposed by Paidoussis [58]. The local phenomena are globally accounted for in the coefficients of the fluid-elastic model.

3.1.1 General formulation of a cantilevered cylinder in confined axial flow

Under the assumption that the flow velocity is perfectly axial, uniform and steady, the random excitation by turbulence is neglected as *the fluctuations from turbulent fields introduce perturbations on the limit cycles of the system, without altering its underlying dynamics* [102]. This means that, for fixed parameter values, the number and nature of coexisting attractors is unchanged by turbulence. A summary of the Païdoussis model for a vertical hanging cylinder is given below, focusing on the force balance which leads to write the equation of motion for a cylinder in axial flow.

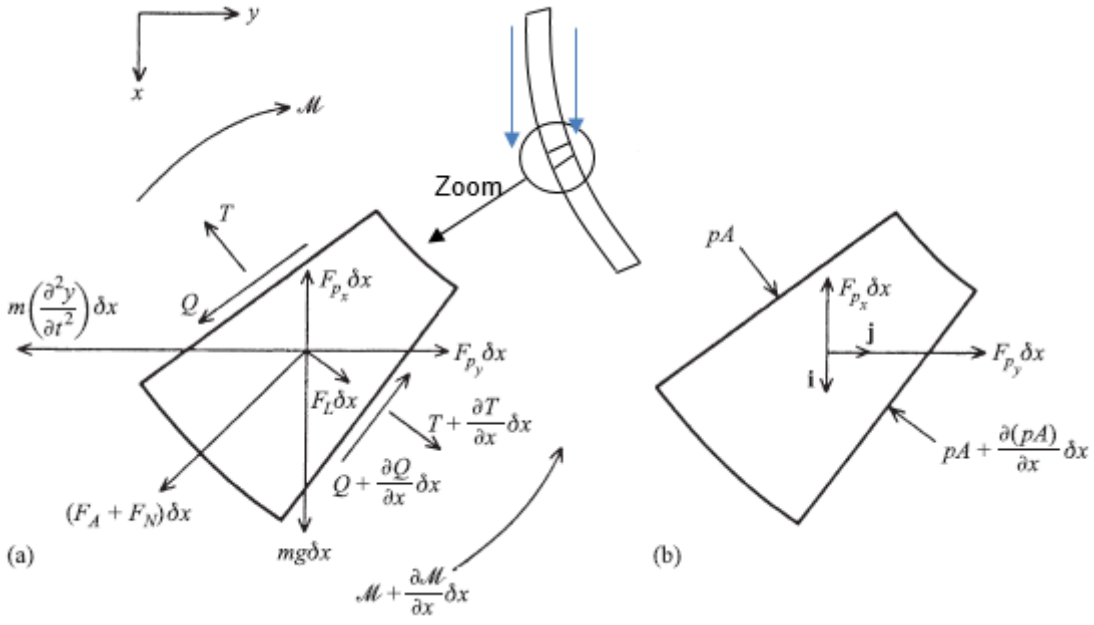

Figure 3.1. (a) An element δx of the cylinder showing forces and moments acting on it; (b) an equivalent rigid element surrounded by fluid

The forces and moments acting on an element δx of the cylinder undergoing small oscillations, w(x, t) are shown in Figure 3.1(a), where F_A represents the inviscid hydrodynamic force, F_N and

F_L are the viscous forces per unit length in the normal and longitudinal direction respectively. F_{px} and F_{py} are the hydrostatic forces in the x and y direction, Q is the lateral shear force, $\mathcal{M}$ the bending moment, T the axial tension, and m the mass of the cylinder per unit length. Hence, the equations of motion in the x and y directions may be written as:

$$\frac{\partial T}{\partial x} + mg + F_L + (F_N + F_A)\frac{\partial w}{\partial x} - F_{px} = 0 \tag{3.1}$$

$$\frac{\partial Q}{\partial x} - (F_N + F_A) + F_{py} + \frac{\partial}{\partial x}\left(T\frac{\partial w}{\partial x}\right) + F_L\frac{\partial w}{\partial x} = m\frac{\partial^2 w}{\partial t^2} \tag{3.2}$$

where the fact that w and its derivatives are small has been utilized; the inertial forces in the axial direction are of second order of magnitude for small lateral motions of large wavelength and have been neglected. Similarly, the effects of angular acceleration of the element are neglected and, by elementary Euler–Bernoulli beam theory, we have:

$$Q = -\frac{\partial \mathcal{M}}{\partial x} = -\frac{\partial}{\partial x}\left(EI\frac{\partial^2 w}{\partial x^2}\right) \tag{3.3}$$

Where EI is the flexural rigidity. In order to determine the forces F_{px} and F_{py} (resultants of the mean pressure p acting on the external surface of the element), we can consider Figure 3.1(b) which represents the element of the cylinder momentarily frozen and immersed in fluid on all sides. The resultant of all the forces is known to be the buoyancy force and, by assuming that the pressure is a linear function of x, we can write:

$$\left[-\frac{\partial(pA)}{\partial x} - F_{px}\right]\delta x\boldsymbol{i} + \left[F_{py} - \frac{\partial}{\partial x}\left(pA\frac{\partial w}{\partial x}\right)\right]\delta x\boldsymbol{j} = -\oint p\boldsymbol{n}dA = -\iiint \boldsymbol{\nabla}pdV = -\frac{\partial p}{\partial x}A\delta x\boldsymbol{i}$$

Where A denotes the cross section area. Hence,

$$F_{px} = \frac{\partial p}{\partial x}A - \frac{\partial(pA)}{\partial x}, \quad F_{py} = \frac{\partial}{\partial x}\left(pA\frac{\partial w}{\partial x}\right) \tag{3.4}$$

For a cylinder of uniform cross section, $F_{px} = 0$.

Substituting now equation (3.4) into equations (3.1) and (3.2), one obtains:

$$\frac{\partial}{\partial x}(T + pA) + (mg - \frac{\partial p}{\partial x}A) + F_L + (F_N + F_A)\frac{\partial w}{\partial x} = 0 \tag{3.5}$$

$$\frac{\partial Q}{\partial x} - (F_N + F_A) + \frac{\partial}{\partial x}\left((T + pA)\frac{\partial w}{\partial x}\right) + F_L\frac{\partial w}{\partial x} = m\frac{\partial^2 w}{\partial t^2} \tag{3.6}$$

By integrating (3.5) from x to L, which denotes the total length of the cylinder, and combining it with equations (3.6) and (3.3), one obtains:

$$EI\frac{\partial^4 w}{\partial x^4} + F_N + F_A - [(T + pA)_L + mg(L - x) - \frac{\partial p}{\partial x}A(L - x) + \int_x^L F_L dx]\frac{\partial^2 w}{\partial x^2} + (mg - \frac{\partial p}{\partial x}A)\frac{\partial w}{\partial x} + m\frac{\partial^2 w}{\partial t^2} = 0 \tag{3.7}$$

For a cylinder in confined flow, the pressure drop is closely related to friction forces exerted on the cylinder and on the flow channel. Considering a fluid element δx of overall flow area A_{ch}, one has approximately:

$$-A_{ch}\frac{\partial p}{\partial x} = F_L\frac{\sum_j S + S_{ch}}{S} - A_{ch}\rho g \tag{3.8}$$

Where the lateral surface of the cylinder is S and the lateral surface of flow channel is S_{ch}, ρ is the density of fluid. Recalling the expressions of the hydraulic forces for small lateral motions (1.13) – (1.16):

$$F_A = \chi\rho A(\frac{\partial}{\partial t} + U\frac{\partial}{\partial x})^2 w$$
$$F_N = \frac{1}{2}\rho DUC_N\left(\frac{\partial w}{\partial t} + U\frac{\partial w}{\partial x}\right) + \frac{1}{2}\rho DC_D\frac{\partial w}{\partial t}$$
$$F_L = \frac{1}{2}\rho DU^2C_T$$

Consider next the term $(T + pA)_L$ in equation (3.7), for the case where the cylinder is free at $x = L$. Recalling that the pA terms arise from the pressure on the sides of the cylinder, and considering a slice of the cylinder at $x = L$, one obtains $T_L = -p_bA$, where p_b is the base pressure, hence $(T + pA)_L = (p_L - p_b)A$. Since $p_b < p_L$ generally, this is something like form drag, more accurately referred to as base drag, which may be expressed as:

$$(T + pA)_L = \frac{1}{2}\rho D^2U^2C_b \tag{3.9}$$

Therefore, by substituting equations (3.9), and (1.13) – (1.16) into equation (3.7), after some manipulation the equation of small lateral motions of the cantilevered cylinder is obtained as:

$$\begin{aligned} EI\frac{\partial^4 w}{\partial x^4} &+ \chi\rho A(\frac{\partial}{\partial t} + U\frac{\partial}{\partial x})^2 w \\ &- \left\{\left[(m - \rho A)g + \frac{1}{2}\rho DU^2C_T\left(1 + \frac{D}{D_h}\right)\right]\cdot(L - x) + \frac{1}{2}\rho D^2U^2C_b\right\}\frac{\partial^2 w}{\partial x^2} \\ &+ \frac{1}{2}\rho DUC_N\left(\frac{\partial w}{\partial t} + U\frac{\partial w}{\partial x}\right) + \frac{1}{2}\rho DC_D\frac{\partial w}{\partial t} + \left[(m - \rho A)g + \frac{1}{2}\rho DU^2C_T\frac{D}{D_h}\right]\frac{\partial w}{\partial x} \\ &+ m\frac{\partial^2 w}{\partial t^2} = 0 \end{aligned} \tag{3.10}$$

Where $D_h = \frac{4A_{ch}}{\sum_j S + S_{ch}}$ is the hydraulic diameter.

3.1.2 Boundary conditions

For a cantilevered cylinder fixed at $x = 0$, there is no displacement nor rotation, the boundary condition can be expressed as:

$$w(0,t) = w'(0,t) = 0 \tag{3.11}$$

At the free end, it is assumed that the cross sectional area tapers smoothly from A to zero over a distance l sufficiently short over the total length L, so that w and the lateral velocity $(\frac{\partial}{\partial t} + U\frac{\partial}{\partial x})w$ may be considered constant. This requirement allows the forces acting on the tapered end to be lumped and considered in appropriate boundary conditions [63]. Equating the lateral shear and inertial forces to the rate of change of lateral momentum over the tapered end ($L - l < x < L$), and neglecting frictional and gravity effects, the boundary condition can be expressed as:

$$EI\frac{\partial^3 w}{\partial x^3} + fMU\left(\frac{\partial w}{\partial t} + U\frac{\partial w}{\partial x}\right) - (m + fM)\chi_e\frac{\partial^2 w}{\partial t^2} = 0 \tag{3.12a}$$

Where $\chi_e = \frac{1}{A}\int_{L-l}^{L} A(x)dx$ and $M = \chi\rho A$. The parameter f, which is equal to unity for slender-body inviscid flow theory, has been introduced because the theoretical lateral force at the free end may not be fully realized as a result of boundary-layer effects. Accordingly, f will normally be less than unity [63].

Lopes [64] has then gave a more careful deviation, taking into account gravity and friction effects:

$$EI\frac{\partial^3 w}{\partial x^3} + fMU\left(\frac{\partial w}{\partial t} + U\frac{\partial w}{\partial x}\right) - \left[m\frac{\partial^2 w}{\partial t^2} + fM\left(\frac{\partial^2 w}{\partial t^2} + U\frac{\partial^2 w}{\partial t\partial x}\right)\right]\chi_e - \left[(m-\rho A)g + \frac{1}{2}\rho DU^2 C_T\frac{D}{D_h}\right]\frac{\partial w}{\partial x}\chi_e - \frac{1}{2}\rho DUC_N\left(\frac{\partial w}{\partial t} + U\frac{\partial w}{\partial x}\right)\overline{\chi_e} = 0 \quad (3.12b)$$

Where $\overline{\chi_e} = \frac{1}{D}\int_{L-l}^{L} D(x)dx$.

It is understood, of course, that $l/L \ll 1$, so that the boundary conditions may be considered to apply at $x = L$. Furthermore, to first order, it may be assumed that the bending moment at the free end is zero, so that:

$$w''(L,t) = 0 \quad (3.13)$$

3.1.3 Model for ASTRID fuel pin subjected to an earthquake

The earthquake is often taken into account as a sinusoidal acceleration imposed on the reactor. Transforming to the non-inertial reference frame which follows the global vibration, the fuel pins are considered to be subjected to an acceleration opposite to the sinusoidal acceleration induced by the earthquake, thus the fictitious inertial force is modelled by a load uniformly distributed along the cylinder's span $q(t)$. The external force results in the relative displacement between the fuel pins and between the fuel pin and the wrapper tube, as described in section 1.2.1, and thus generates the impact forces at all potential contact points, of which the set of coordinates is defined as $\boldsymbol{x_c} = \{x_{c1}, x_{c2}, \cdots, x_{c_{nc}}\}$. The impact at each contact point is computed as:

$$\forall i \in [\![1, nc]\!], F_c(x_{ci}) = \begin{cases} \max(k_c(w(x_{ci}) - d), 0) & if\ i\ is\ pair \\ \min(k_c(w(x_{ci}) + d), 0) & if\ i\ is\ odd \end{cases} \quad (3.14)$$

Where k_c denotes the contact stiffness and d is the clearance between the fuel pin and the contact point. The energy losses resulting from impacts and the squeeze film effect [103] is difficult to be quantified. The damper is lumped with that of the pellets and will be accounted for by a structural viscous damping, often modelled as a Rayleigh damping.

Therefore the fuel pin is subjected to a total external force expressed as:

$$F_{ext}(x,t) = q(t) + F_c(w)\delta_{\boldsymbol{x_c}}(x) \quad (3.15)$$

Where $\delta_{\boldsymbol{x_c}}(x) = \begin{cases} 1 & if\ x \in \boldsymbol{x_c} \\ 0 & if\ x \notin \boldsymbol{x_c} \end{cases}$

Furthermore, the axial flow circulates from bottom to top in ASTRID fuel assembly, small modifications on the equation of motion (3.10) should be made to adapt to the studied case:

$$EI\frac{\partial^4 w}{\partial x^4}+\left\{\chi\rho AU^2-\left[\frac{1}{2}\rho DU^2C_T\left(1+\frac{D}{D_h}\right)-(m-\rho A)g\right]\cdot(L-x)-\frac{1}{2}\rho D^2U^2C_b\right\}\frac{\partial^2 w}{\partial x^2}$$
$$+\left[\frac{1}{2}\rho DU^2C_N+\frac{1}{2}\rho DU^2C_T\frac{D}{D_h}-(m-\rho A)g\right]\frac{\partial w}{\partial x}+2\chi\rho AU\frac{\partial^2 w}{\partial x\partial t} \tag{3.16}$$
$$+\left(\frac{1}{2}\rho DUC_N+\frac{1}{2}\rho DC_D\right)\frac{\partial w}{\partial t}+(m+\chi\rho A)\frac{\partial^2 w}{\partial t^2}=F_{ext}$$

3.1.4 Method of solution

The equations of motion to be solved in structural vibrations result from the finite-element discretization of the continuous expression of dynamical equilibrium. They are sets of nonlinearly-coupled, second-order, ordinary differential equations whose analytical solutions are generally impossible to find. Hence, numerical methods are fundamental in investigating their dynamic behavior. The finite element formulation of (3.16) is developed with the principle of virtual work:

$$\int_0^L \delta w\left(EI\frac{\partial^4 w}{\partial x^4}+\left\{\chi\rho AU^2-\left[\frac{1}{2}\rho DU^2C_T\left(1+\frac{D}{D_h}\right)-(m-\rho A)g\right]\cdot(L-x)-\frac{1}{2}\rho D^2U^2C_b\right\}\frac{\partial^2 w}{\partial x^2}\right.$$
$$+\left[\frac{1}{2}\rho DU^2C_N+\frac{1}{2}\rho DU^2C_T\frac{D}{D_h}-(m-\rho A)g\right]\frac{\partial w}{\partial x}+2\chi\rho AU\frac{\partial^2 w}{\partial x\partial t} \tag{3.17}$$
$$\left.+\left(\frac{1}{2}\rho DUC_N+\frac{1}{2}\rho DC_D\right)\frac{\partial w}{\partial t}+(m+\chi\rho A)\frac{\partial^2 w}{\partial t^2}\right)dx=\int_0^L \delta wF_{ext}dx$$

Applying integration by parts on the first term of (3.17):

$$\int_0^L \delta wEIw''''dx=[\delta wEIw''']_0^L-[\delta w'EIw'']_0^L+\int_0^L \delta w''EIw''dx$$

We denotes the deviation with respect to x by $'$ and that with respect to t by $\dot{}$. Since we have the boundary conditions $\delta w(0)=\delta w'(0)=0$ and $w''(L)=0$, hence

$$\int_0^L \delta wEIw''''dx=\int_0^L \delta wEIw'''\delta(x-L)dx+\int_0^L \delta w''EIw''dx \tag{3.18}$$

Where $\delta(x-L)$ is the Dirac's delta function. By combining (3.12b) and (3.18) into (3.17), the weak formulation becomes:

$$\int_0^L \delta w''EIw''dx+\int_0^L \delta w\left(\left\{\chi\rho AU^2-\left[\frac{1}{2}\rho DU^2C_T\left(1+\frac{D}{D_h}\right)-(m-\rho A)g\right]\cdot(L-x)\right.\right.$$
$$\left.-\frac{1}{2}\rho D^2U^2C_b\right\}\frac{\partial^2 w}{\partial x^2}+\left[\frac{1}{2}\rho DU^2C_N+\frac{1}{2}\rho DU^2C_T\frac{D}{D_h}-(m-\rho A)g\right]\frac{\partial w}{\partial x}$$
$$+2\chi\rho AU\frac{\partial^2 w}{\partial x\partial t}+\left(\frac{1}{2}\rho DUC_N+\frac{1}{2}\rho DC_D\right)\frac{\partial w}{\partial t}+(m+\chi\rho A)\frac{\partial^2 w}{\partial t^2}\Big)dx$$
$$+\int_0^L \delta w\left(-fMU\left(\frac{\partial w}{\partial t}+U\frac{\partial w}{\partial x}\right)+\left[m\frac{\partial^2 w}{\partial t^2}+fM\left(\frac{\partial^2 w}{\partial t^2}+U\frac{\partial^2 w}{\partial t\partial x}\right)\right]\chi_e\right. \tag{3.19}$$
$$\left.+\left[\frac{1}{2}\rho DU^2C_T\frac{D}{D_h}-(m-\rho A)g\right]\frac{\partial w}{\partial x}\chi_e+\frac{1}{2}\rho DUC_N\left(\frac{\partial w}{\partial t}+U\frac{\partial w}{\partial x}\right)\overline{\chi_e}\right)\delta(x-L)dx$$
$$=\int_0^L \delta wF_{ext}dx$$

The equation (3.19) is discretized with Bernouilli beam element of two nodes by cubic Hermite interpolation. Applying the procedure detailed in appendix A, and take into the structural damper modelled by the Rayleigh damping:

$$\boldsymbol{C_R} = \alpha \boldsymbol{M_s} + \beta \boldsymbol{K_s} \tag{3.20}$$

we obtain the following general form of the second order ordinary differential equation:

$$(\boldsymbol{M_s} + \boldsymbol{M_f})\ddot{\boldsymbol{X}} + (\boldsymbol{C_R} + \boldsymbol{C_f})\dot{\boldsymbol{X}} + (\boldsymbol{K_s} + \boldsymbol{K_f})\boldsymbol{X} + \boldsymbol{F_c} = F_{ext}(t)\boldsymbol{Q} \tag{3.21}$$

Where $\boldsymbol{X}$ is the generalized coordinates.

3.1.5 Assessment of the finite element method with a stability analysis

In the literatures [58][64][68], the stability analysis is usually performed with the dimensionless formulation.

In order to render the linear partial differential equation (3.16) and the boundary conditions (eq. (3.12b) and eq. (3.13)) dimensionless, the following relations are used:

$$\begin{gathered}\eta = \frac{w}{L}, \xi = \frac{x}{L}, \tau = \left(\frac{EI}{m+\rho A}\right)^{\frac{1}{2}} \frac{t}{L^2}, u = \left(\frac{\rho A}{EI}\right)^{\frac{1}{2}} LU, \beta = \frac{\rho A}{m+\rho A}, \gamma = \frac{(m-\rho A)gL^3}{EI}, \\ \varepsilon = \frac{L}{D}, h = \frac{D}{D_h}, c_N = \frac{4}{\pi} C_N, c_T = \frac{4}{\pi} C_T, c_b = \frac{4}{\pi} C_b, c = \frac{4}{\pi}\left(\frac{\rho A}{EI}\right)^{\frac{1}{2}} LC_D, \chi_e = \frac{\chi_e}{L}, \overline{\chi_e} = \frac{\overline{\chi_e}}{L}\end{gathered} \tag{3.22}$$

The equation of motion and the boundary conditions for a cantilevered cylinder are thus

$$\begin{gathered}\eta'''' + \left(\chi u^2 - \left[\frac{1}{2}\varepsilon c_T u^2 (1+h) - \gamma\right](1-\xi) - \frac{1}{2}u^2 c_b\right)\eta'' + 2\chi\beta^{\frac{1}{2}} u\dot{\eta}' + (1 + (\chi - 1)\beta)\ddot{\eta} \\ + \left(\frac{1}{2}\varepsilon c_T u^2 h + \frac{1}{2}\varepsilon c_N u^2 - \gamma\right)\eta' + (\frac{1}{2}\varepsilon c_N \beta^{\frac{1}{2}} u + \frac{1}{2}\varepsilon c \beta^{\frac{1}{2}})\dot{\eta} = 0\end{gathered} \tag{3.23}$$

$$\eta(0) = \eta'(0) = 0 \tag{3.24}$$

$$\begin{gathered}\text{At } \xi = 1, \quad \eta'' = \eta''' + \left(\chi f - \tfrac{1}{2}\overline{\chi_e}\varepsilon c_N\right)\left(\beta^{\frac{1}{2}} u\dot{\eta} + u^2\eta'\right) - \chi_e\left[(1 + (\chi f - 1)\beta)\ddot{\eta} + \chi f \beta^{\frac{1}{2}} u\dot{\eta}'\right] - \\ \chi_e\left(\tfrac{1}{2}\varepsilon c_T u^2 h - \gamma\right)\eta' = 0\end{gathered} \tag{3.25}$$

The dimensionless form of equation (3.21) can be obtained with the same procedure. The stability analysis is performed by converting it into a set of first order ordinary differential equations $\dot{\boldsymbol{Y}} = \boldsymbol{A}\boldsymbol{Y}$ with $\boldsymbol{Y} = \begin{bmatrix}\boldsymbol{X} \\ \dot{\boldsymbol{X}}\end{bmatrix}$ and $\boldsymbol{A}$ written as:

$$\boldsymbol{A} = \begin{bmatrix}\boldsymbol{0} & \boldsymbol{I} \\ -\boldsymbol{M^{-1}K} & -\boldsymbol{M^{-1}C}\end{bmatrix}$$

The eigenvalue problem is finally solved using MATLAB code for eigenvalues λ of matrix $\boldsymbol{A}$, which correspond to the dimensionless complex frequencies ω ($i\omega = \lambda$) of the cantilevered cylinder. The imaginary part of ω, $Im(\omega)$ represents the damping, whereas the real part $Re(\omega)$ represents the dimensionless oscillation frequency.

Implementing the dimensionless parameters used by Paidoussis [55], which are $\beta = 0.5$, $\varepsilon c_N = \varepsilon c_T = 1$, $f = 0.8$, $\chi = 1$, $\chi_e = 0.01$ and $\varepsilon c = c_b = h = \gamma = 0$, the Argand diagram for the first three modes at dimensionless velocity, u ranging from 0 to 9 is as shown in Figure 3.2. The calculation with our code is in good agreement with the results obtained with the so called 'extended Galerkin method' by Paidoussis.

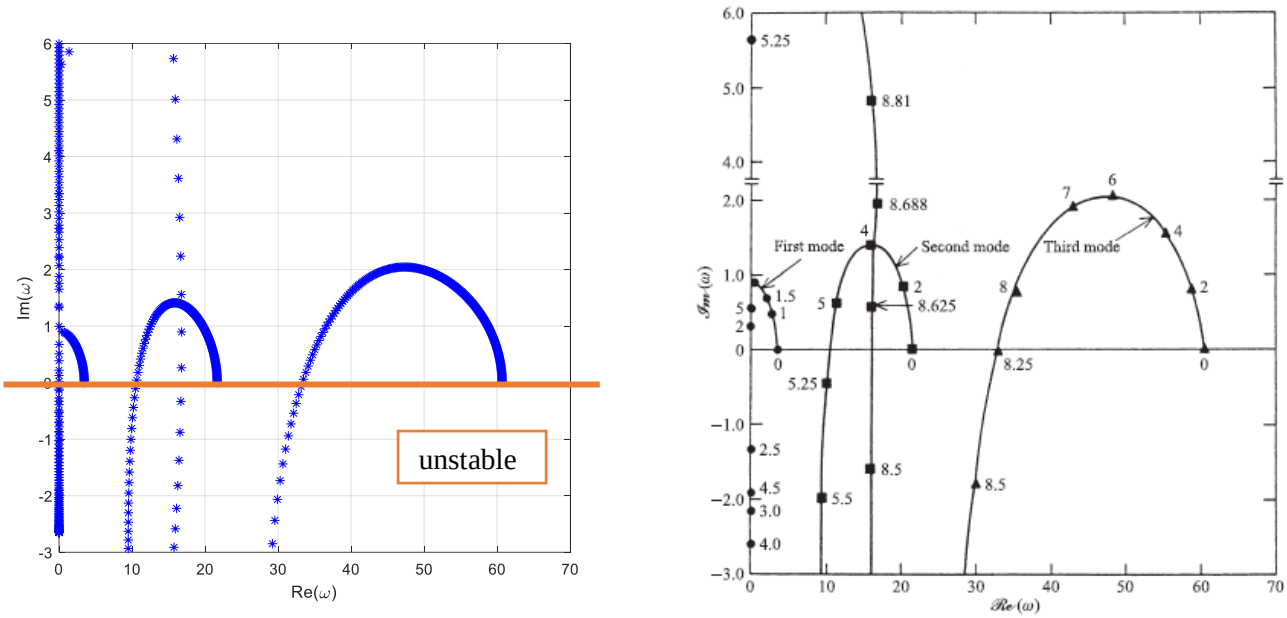

(a) (b)

Figure 3.2. Argand diagram of the complex frequencies of the first three modes (a) discretization using cubic Hermite polynomials as shape functions; (b) discretization with extended Galerkin method [55]

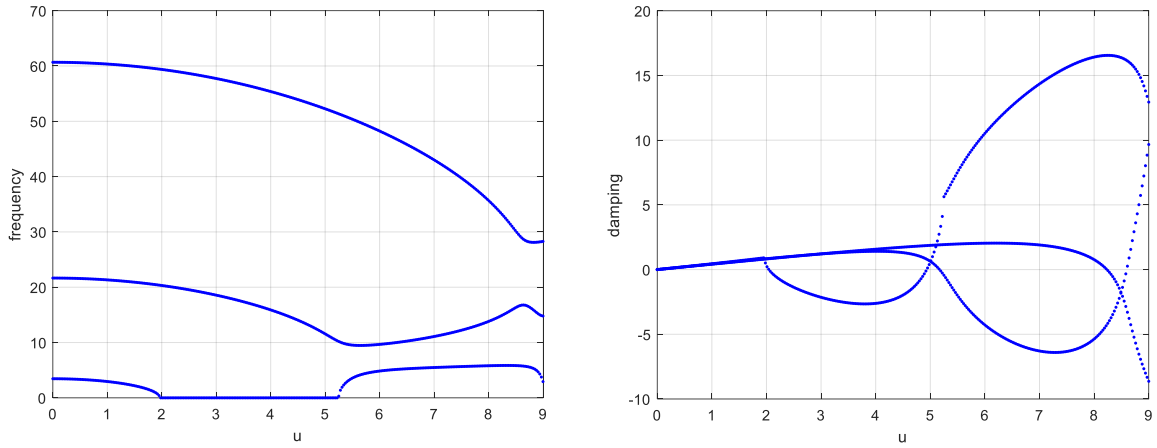

Figure 3.3. Dimensionless oscillation frequency and damping of the first three modes as function of u

From Figure 3.3, it is observed that cylinder motions caused by perturbation are damped at small u. At sufficiently high u, the cylinder first loses stability by divergence in its first mode, via a pitchfork bifurcation, at $u_{cr,d1} = 2.042$. The symbol cr represents the critical value for the onset of instability, d stands for static divergence and 1 represents the first mode shape. The system then re-stabilizes at $u_{r1} = 4.965$, and then loses stability by second mode flutter, via a Hopf bifurcation, at $u_{cr,fl2} = 5.173$ with a corresponding dimensionless frequency 10.47.

3.1.6 Time integration scheme

Numerical time-integration techniques are fundamental in capturing transient behavior of dynamical systems. There are two categories of integration schemes: the explicit schemes for which the position at moment t depends only on the data at the preceding moments, and the implicit schemes, for which the calculation of the position at moment t is carried out by iteration

until a convergence criterion is reached. In general, explicit schemes are more suitable for dealing with contact problems because they allow faster calculations and turn out to be stable when the calculation time step is small enough. But implicit schemes are sometimes used to solve contact problems when it is preferable to use a larger time step [104][105].

The most widely-used method in structure mechanics is the Newmark family:

$$\begin{aligned} \dot{\boldsymbol{X}}_{n+1} &= \dot{\boldsymbol{X}}_n + \Delta t\left[(1-\gamma)\ddot{\boldsymbol{X}}_n + \gamma\ddot{\boldsymbol{X}}_{n+1}\right] \\ \boldsymbol{X}_{n+1} &= \boldsymbol{X}_n + \Delta t\dot{\boldsymbol{X}}_n + \frac{\Delta t^2}{2}\left[\,(1-2\beta)\ddot{\boldsymbol{X}}_n + 2\beta\ddot{\boldsymbol{X}}_{n+1}\right] \end{aligned} \tag{3.26}$$

Catterou [2] in his study has taken $\beta = 0$ and $\gamma = \frac{1}{2}$ to obtain an explicit Newmark scheme, called 'centered difference'. This scheme is conditionally stable, a calculation time step too large or a non-linearity too strong can lead to accumulating errors.

It is unconditionally stable by choosing $\frac{1}{2} \leq \gamma \leq 2\beta$. When $\beta = \frac{1}{4}$ and $\gamma = \frac{1}{2}$, we obtain the implicit scheme called "average acceleration". Therefore, a larger time step compared to the explicit one can be used thanks to the Newton-Raphson iteration. By defining the notation (k) as the iteration counter, the position of the next iteration is calculated by adding the difference between successive iterations ΔX:

$$^{t+\Delta t}X^{(k)} = \Delta X^{(k)} + {}^{t+\Delta t}X^{(k-1)} \tag{3.27}$$

The acceleration and velocity of the next iteration $^{t+\Delta t}\ddot{X}^{(k)}$ and $^{t+\Delta t}\dot{X}^{(k)}$ can therefore be calculated by replacing (3.27) into (3.26):

$$\begin{aligned} {}^{t+\Delta t}\ddot{X}^{(k)} &= \frac{2}{\Delta t}\left({}^{t+\Delta t}\dot{X}^{(k)} - {}^{t}\dot{X}\right) - {}^{t}\ddot{X} = \frac{2}{\Delta t}\left[\frac{2}{\Delta t}\left({}^{t+\Delta t}X^{(k)} - {}^{t}X\right) - {}^{t}\dot{X} - {}^{t}\dot{X}\right] - {}^{t}\ddot{X} \\ &= \frac{4}{\Delta t^2}\left({}^{t+\Delta t}X^{(k)} - {}^{t}X\right) - \frac{4}{\Delta t}\,{}^{t}\dot{X} - {}^{t}\ddot{X} \\ &= \frac{4}{\Delta t^2}\Delta X^{(k)} + \frac{4}{\Delta t^2}\left({}^{t+\Delta t}X^{(k-1)} - {}^{t}X\right) - \frac{4}{\Delta t}\,{}^{t}\dot{X} - {}^{t}\ddot{X} \\ &= \frac{4}{\Delta t^2}\Delta X^{(k)} + {}^{t+\Delta t}\ddot{X}^{(k-1)} \end{aligned} \tag{3.28}$$

$$\begin{aligned} {}^{t+\Delta t}\dot{X}^{(k)} &= \frac{2}{\Delta t}\left({}^{t+\Delta t}X^{(k)} - {}^{t}X\right) - {}^{t}\dot{X} = \frac{2}{\Delta t}\Delta X^{(k)} + \frac{2}{\Delta t}\left({}^{t+\Delta t}X^{(k-1)} - {}^{t}X\right) - {}^{t}\dot{X} \\ &= \frac{2}{\Delta t}\Delta X^{(k)} + {}^{t+\Delta t}\dot{X}^{(k-1)} \end{aligned} \tag{3.29}$$

By replacing (3.28) and (3.29) into (3.21), we obtain:

$$\begin{aligned} M\,{}^{t+\Delta t}\ddot{X}^{(k-1)} + C\,{}^{t+\Delta t}\dot{X}^{(k-1)} + K\,{}^{t+\Delta t}X^{(k-1)} + F_c\left({}^{t+\Delta t}X^{(k-1)}\right) + \left(\frac{4}{\Delta t^2}M + \frac{2}{\Delta t}C + K + \widehat{K}\right)\Delta X^{(k)} \\ = {}^{t+\Delta t}F_{ext} \end{aligned}$$

Where $\widehat{K} = \frac{\partial F_c}{\partial X}$, and the residue is evaluated by:

$$R\left({}^{t+\Delta t}X^{(k)}\right) = {}^{t+\Delta t}F_{ext} - M\,{}^{t+\Delta t}\ddot{X}^{(k)} - C\,{}^{t+\Delta t}\dot{X}^{(k)} - K\,{}^{t+\Delta t}X^{(k)} - F_c\left({}^{t+\Delta t}X^{(k)}\right) \tag{3.30}$$

$\Delta X^{(k)}$ can be calculated by solving the linear equation:

$$\left(\frac{4}{\Delta t^2}M + \frac{2}{\Delta t}C + K + \widehat{K}\right)\Delta X^{(k)} = R\left({}^{t+\Delta t}X^{(k-1)}\right) \tag{3.31}$$

There exist three convergence criterions, respectively on displacement, on impact force and on energy, as listed in Table 3.1. We adopt the criterion on impact force in our study.

Table 3.1. Convergence criterions and respective comments

	Criterion	Comment
Displacement	$\frac{\left\|\Delta X^{(k)}\right\|_2}{\left\|{}^{t+\Delta t}X^{(k)}\right\|_2} \leq \epsilon_D$	For the cases where the displacement evolves slowly during the iteration, the criterion could be satisfied with a bad result.
Impact force	$\left\|R\left({}^{t+\Delta t}X^{(k)}\right)\right\|_2 \leq \epsilon_F \left\|{}^{t+\Delta t}F_{ext} - F_c\left({}^{t}X\right) - M\ {}^{t}\ddot{X} - C\ {}^{t}\dot{X} - K\ {}^{t}X\right\|_2$	In the case where the contact point is soft, a small error in the force could lead to a large deviation in the displacement.
Energy	${\Delta X^{(k)}}^T R\left({}^{t+\Delta t}X^{(k)}\right) \leq \epsilon_E \left[{\Delta X^{(1)}}^T \left({}^{t+\Delta t}F_{ext} - F_c\left({}^{t}X\right) - M\ {}^{t}\ddot{X} - C\ {}^{t}\dot{X} - K\ {}^{t}X\right)\right]$	This criterion is complex but the most commonly used, since it contains information on the displacement and also on the force.

3.2 Parametric study

As explained in Section 2.3.3, the investigation of the fluid-structure interaction of ASTRID fuel pin can be performed, basing on the model of bare cylinder in axial flow introduced above, since the effect of spacer wire on the hydraulics is lumped into the global coefficients determined by the experiments. In consequence, the spacer wire is considered only as the potential contact points.

Without the results from experiments, the coefficients can be estimated with some models previously derived [52][106] and empirical findings [66][107][27]. In order to understand the effect of hydraulic forces, studies of the force coefficients on the eigenfrequencies and damping of the ASTRID fuel pin will be carried out. The eigenfrequencies of fuel pin in air are calculated as a reference.

3.2.1 Flexion of fuel pin in air

By neglecting the flow density ($\rho = 0$), equation (3.16) is reduced to the motion equation of the flexion of fuel pin in air. The effect of pellets are taken into consideration by an added mass in the pellet span and also by a viscous damping, modelled by eq. (3.20).

With an eigenvector ϕ_i of $M_s^{-1}K_s$ and the associated eigenvalue ${\omega_{0,i}}^2$, the corresponding damping ratio ξ_i is calculated by:

$$2\xi_i\ \omega_{0,i} = \frac{\phi_i^T C_R \phi_i}{\phi_i^T M_s \phi_i} = \frac{\alpha \phi_i^T M_s \phi_i + \beta \phi_i^T K_s \phi_i}{\phi_i^T M_s \phi_i} = (\alpha + \beta\ {\omega_{0,i}}^2) \tag{3.32}$$

By taking the damping ratio for the first two modes equal to 3% [2], the eigenfrequencies $f_i = f_{0,i}\sqrt{1-\xi_i^2}$ and damping ratios of the first six modes are listed in Table 3.2. It shows that the effect of damping become more important with higher modes.

Table 3.2. Eigenfrequencies and damping ratios of the first six modes of flexion of ASTRID fuel pin in air

N° mode	*1*	*2*	*3*	*4*	*5*	*6*
Frequency (Hz)	*0.89*	*6.65*	*22.87*	*44.20*	*67.32*	*98.18*
Damping ratio ξ	*3%*	*3%*	*9.23%*	*17.91%*	*27.89%*	*43.31%*

3.2.2 Flexion of fuel pin in still water

According to equation (3.14), the only coefficients engaged are the coefficient related to the confinement χ and the zero-flow normal coefficient C_D. The end-shape parameter f also plays a role on the boundary condition. Hannoyer [66] proposed the expression of f as:

$$f = \frac{4{\chi_e}^2}{4{\chi_e}^2 + D^2} \tag{3.33}$$

With the geometrical parameters of ASTRID fuel pin, we obtain $f \approx 0.3$.

The drag coefficient for a long cylinder oscillating in quiescent viscous fluid has been discussed [58]. The viscous force per unit length is found to be given by:

$$F = -C_d \omega \rho A \dot{w} \tag{3.34}$$

Where C_d is a drag coefficient. Comparing with $F = \frac{1}{2}\rho D C_D \dot{w}$, a correlation between C_d and C_D is obtained:

$$C_D = \left(\frac{\pi}{2}\right) D \omega C_d \tag{3.35}$$

Sinyavskii [106] derived the expression for Cd as:

$$C_d = \frac{2\sqrt{2}}{\sqrt{St}} \frac{1+{\gamma_c}^3}{(1-{\gamma_c}^2)^2} \tag{3.36}$$

Where $\gamma_c = \frac{D}{D_e}$ is a confinement parameter, being related with χ by $\chi = \frac{1+{\gamma_c}^2}{1-{\gamma_c}^2}$. And St is the Stokes number expressed as:

$$St = \frac{D^2 \omega}{4\nu} \tag{3.37}$$

Where ν is the kinematic viscosity. ω can be determined as in the previous sections. Therefore, The iterative solution starts by considering an initial guess for C_D equal to zero. ω is calculated and then substituted in eq. (3.37) to calculate *St*. Hereafter, eqs. (3.36), (3.35) are used in order to get the new value of C_D. The iteration is repeated until a converged value of C_D is obtained.

Preliminary parametric study has been carried out with the linear model by taking the parameters of ASTRID fuel pin. The effect of confinement on the zero-flow normal coefficient is as shown in Figure 3.4. When the system becomes more confined, C_D increases, leading to

an increasing damping. The increasing confinement also results in a more important added mass. In this case, the effect of C_D on the eigenfrequencies and corresponding damping ratios is illustrated in Figure 3.5. The eigenfrequencies of the first two modes decrease and the damping ratios increase, while the damping ratio of for the third mode can decrease with an increasing eigenfrequency. It means that the effect of added mass is more important.

In our study, the confinement parameter $\chi \approx 3$ and $C_D \approx 0.11$, which results in a $c = \frac{4}{\pi}\left(\frac{\rho A}{EI}\right)^{\frac{1}{2}} LC_D \approx 0.01$. Paidoussis [58] recommended that for metal cylinders $c \approx 0.008$, of the same order of the magnitude with our result. The resulting eigenfrequencies and the damping ratios are as listed in Table 3.3.

Table 3.3. Eigenfrequencies and damping ratios of the first six modes of flexion of ASTRID fuel pin in confined still water ($f \approx 0.3, \chi \approx 3$ and $C_D \approx 0.11$)

N° mode	*1*	*2*	*3*	*4*	*5*	*6*
Frequency (Hz)	*0.76*	*5.33*	*16.68*	*30.99*	*50.72*	*74.01*
Damping ratio ξ	*9.86%*	*3.69%*	*7.25%*	*12.73%*	*20.78%*	*31.60%*

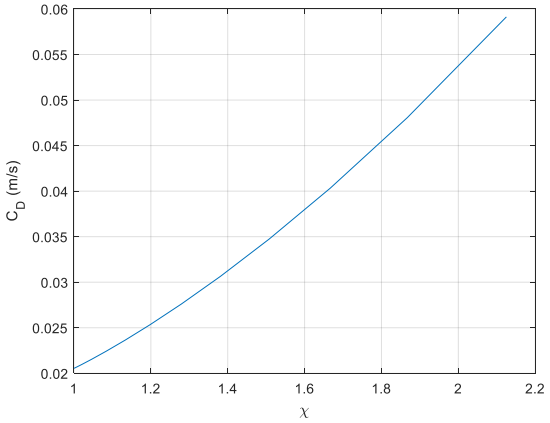

Figure 3.4. Effect of confinement on zero-flow normal coefficient C_D

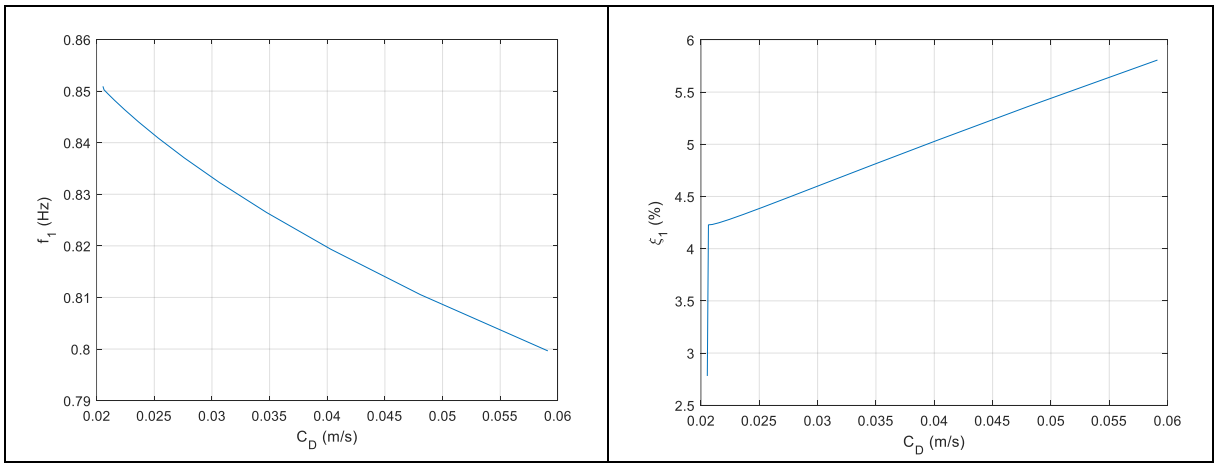

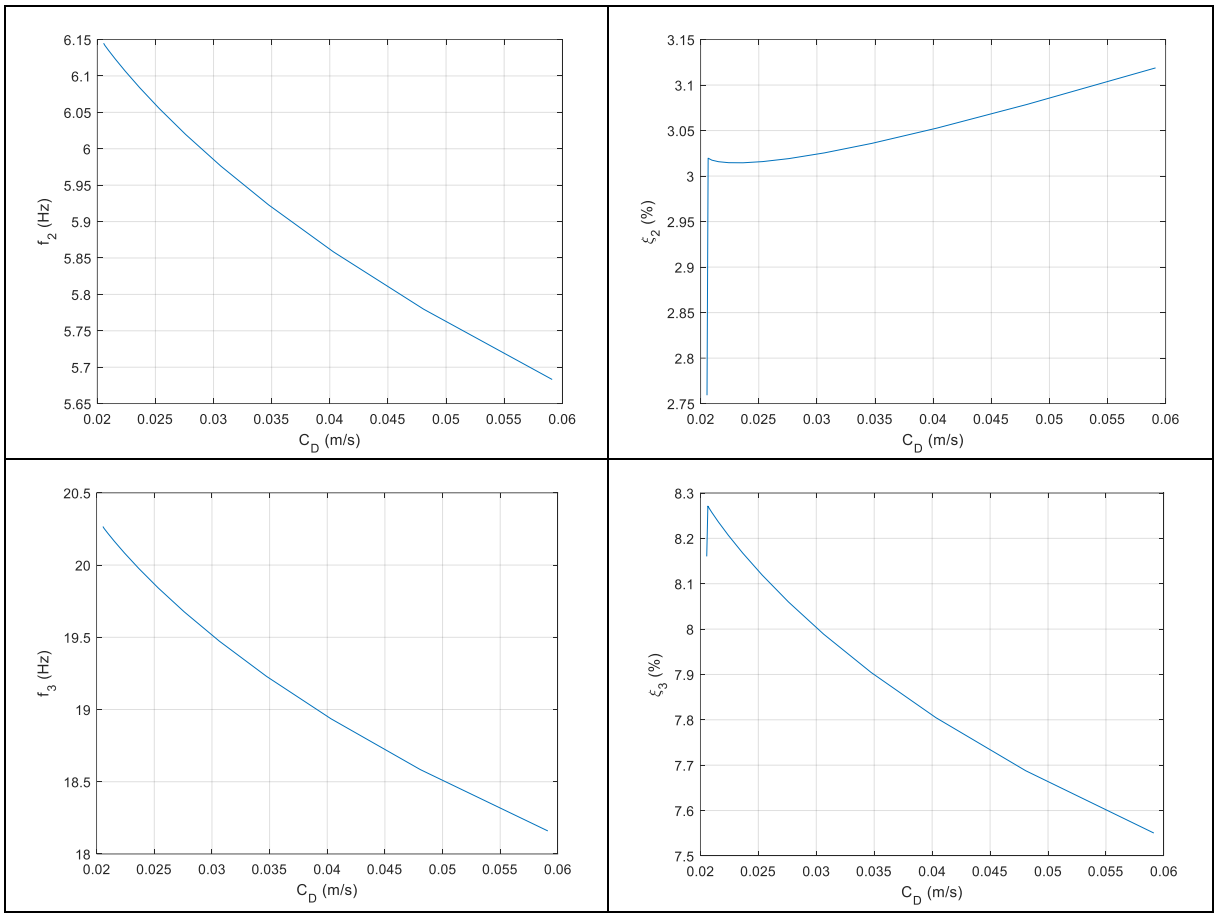

Figure 3.5. Effect of C_D on the eigenfrequencies and damping ratios of the first three modes of flexion of ASTRID fuel pin in still water

3.2.3 Flexion of fuel pin in water flow

By fixing the value of f, χ and C_D, the longitudinal and normal viscous coefficients C_T and C_N along with the base drag coefficient C_b are to be discussed in the case of water flow.

In many previous works [64][68], $c_b = \frac{4}{\pi} C_b$ is roughly estimated to be equal to $1 - f$ in the case of tapered end. Paidoussis [65] has conducted further experiments by having part of the tapered end lopped off, and found that f was only slightly reduced but c_b became substantially higher as a result of the flat end, which is the case of the ASTRID fuel pin. Therefore, c_b should be greater than 0.7 in our case, which proposed by Hoerner [107] is approximately 0.82.

The estimation of C_T is carried out with the empiric formulation of the pressure drop along the flow channel. The pressure drop due to friction is expressed as:

$$\Delta p = \frac{1}{2} \rho U^2 f_{fric} \frac{L}{D_h} \tag{3.38}$$

Where L is the tube length, D_h the hydraulic diameter of the flow channel. Relating with eq. (3.8), where if the gravity is neglected $\Delta p = \frac{1}{2} \rho D U^2 C_T \frac{4L}{D_h(\pi D)}$, a correlation between f_{fric} and C_T is obtained:

$$C_T = \frac{\pi}{4} f_{fric} \tag{3.39}$$

Friction factor for the wire-wrapped fuel bundle in the simplified Cheng-Todreas model [26] is calculated based on the following correlations:

$$f_{fric} = \frac{C_{fT}}{Re^{0,18}}$$
$$C_{fT} = (0.8063 - 0.9022\log\left(\frac{H}{D}\right) + 0.3526(log\left(\frac{H}{D}\right))^2) \times (\frac{P}{D})^{9.7}\left(\frac{H}{D}\right)^{1.78-2\frac{P}{D}} \quad (3.40)$$

Where H is the helical pitch and P is the fuel pin pitch. With the geometrical parameters, f_{fric} is estimated to be equal to 0.023, which is in the range proposed by Paidoussis (0.01-0.025).

The estimation of C_N is quite difficult, and the uncertainty on C_D is also transferred to it as we adopt the estimation procedure in the previous section while the flow patterns for an oscillating cylinder in quiescent fluid and in axial flow cannot be very similar [58]. Ortloff [108] suggested that the physically realizable range for c_N is governed by $1/2 \leq c_N/c_T \leq 2$, where c_N/c_T = 2 holds for smooth cylinders and $c_N/c_T = 1/2$ for very rough ones. Some very careful experiments have been conducted [57], using clamped-clamped and cantilevered rods in axial water-flow, excited electromagnetically, with the vibration being sensed optically and c_N was found to range between 0.025 and 0.103. The effect of C_N is studied by taking its value of different order of magnitude. The results are as listed in Table 3.4, it is observed that the effect of C_N is noticeable for the first mode and becomes much less important for the higher modes. Given the results, even though it is not usually realistic, it is acceptable to suppose $C_N = C_T$ as in some previous works [52][55].

Table 3.4. Eigenfrequencies and damping ratios of the first four modes of flexion of ASTRID fuel pin in confined water flow of 5 m/s with different C_N

C_N	f_1(Hz)/ ξ_1	f_2(Hz)/ ξ_2	f_3(Hz)/ ξ_3	f_4(Hz)/ ξ_4
0.004	0.81/ 27.6%	5.40/ 7.93%	16.75/ 8.82%	31.06/ 13.56%
0.01	0.82/ 28.9%	5.40/ 8.25%	16.75/ 8.95%	31.05/ 13.63%
0.02	0.84/ 31.6%	5.40/ 8.95%	16.74/ 9.25%	31.05/ 13.79%
0.04	0.86/ 35.0%	5.41/ 9.86%	16.74/ 9.64%	31.04/ 14.00%
0.1	0.91/ 45.5%	5.41/ 13.05%	16.73/ 11.02%	31.01/ 14.73%

3.2.4 Summary

In this part, due to the lack of experimental data, an estimation of the coefficients in our model based on the previous theoretical and experimental studies has been performed. Their effects on the eigenfrequencies and the damping ratios of the cylinder have been estimated in air and in water.

A first study in air showed that Rayleigh damping, which accounts for the energy losses due to the impacts and the existence of pellets, acts mainly on higher modes with a weak effect on lower modes. This implies that bending waves that can be generated by the impacts will be damped quickly. In still water, the main influence on the system is brought by the added mass of fluid. The study in water flow showed that the effect of the viscous hydraulic forces is mainly on the first mode of the system.

3.3 Temporal results

In the following, the temporal simulations will be conducted with the parameters determined in the above section. The effect of contact will be taken into consideration. The dynamic responses of the fuel pin to the sinusoidal external accelerations of different frequencies and amplitudes a_{ext} are studies. The range of amplitude for an ASTRID reactor with seismic isolator is $0 \leq a_{ext} \leq 3\ m/s^2 (0.3g)$and we are interested in the range of frequency which includes the first two eigenfrequencies, thus $0.4\ Hz \leq f_{ext} \leq 6\ Hz$.

3.3.1 Fuel pin with one contact point at half-length

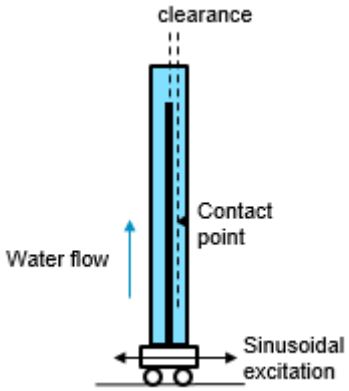

Figure 3.6. Fuel pin with one contact point at half-length under flow

In order to understand the effect of the impact, the study starts with a less strong nonlinear case, where only one contact point is introduced at the half length of the fuel pin, as schematized in Figure 3.6.

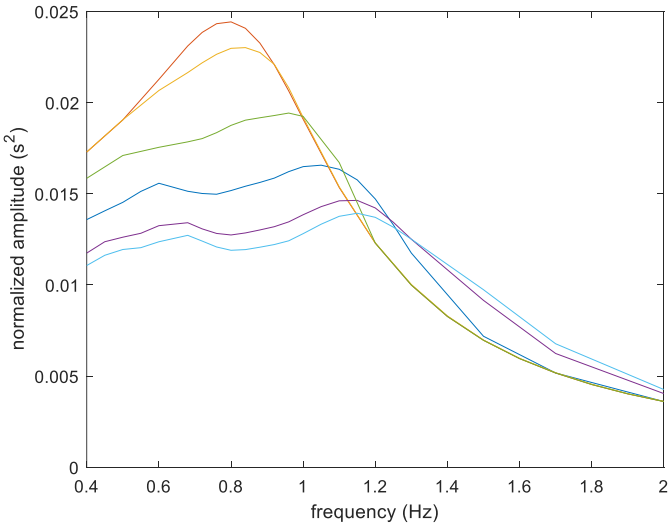

Figure 3.7. Motional spectrum of the fuel pin with one contact point with different amplitudes of the external acceleration (a_{ext} = 0.02, 0.03, 0.05, 0.1, 0.3 and 1 m/s^2).

When the fuel pin is subjected to an external acceleration, it finally reaches a steady-state vibration after the transient behavior dies out. Figure 3.7 shows the variation of the normalized amplitude, which is defined as the ratio between the amplitude of the steady-state vibration and

the amplitude of the external acceleration, with the external frequency. When the external acceleration is too small to have the impact happens, we are in the linear case. A resonance peak is observed on the motional spectrum. The first impact happens with an acceleration equal to 0.03 m/s^2, a slight offset of the resonance peak is observed. Going beyond this value, the resonance peak splits into two peaks around the resonance frequency. As is shown in Figure 3.8, multiples of f_{ext} occurs in the temporal response in the two-peak region. Similarly for the second resonance peak corresponding to the second eigenfrequency of the fuel pin, the nonlinearity is interpreted by this vibration pattern.

Another type of nonlinear response due to a bifurcation of period-doubling is observed in Figure 3.9 with f_{ext} between the two resonance frequencies. The period-doubling cascade was reported in many literatures [109] as a common route by which nonlinear dynamical systems develop chaos, even though in the range studied of a_{ext} the temporal response of the fuel pin is always periodic.

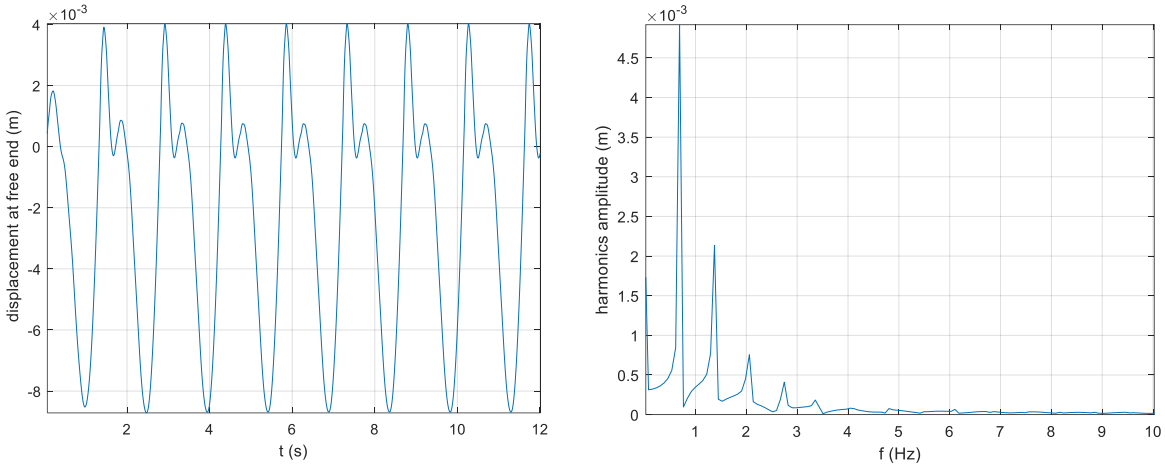

Figure 3.8. Temporal response and corresponding Fourier transformation of the fuel pin with one contact point ($a_{ext} = 1m/s^2$and $f_{ext} = 0.68\ Hz$)

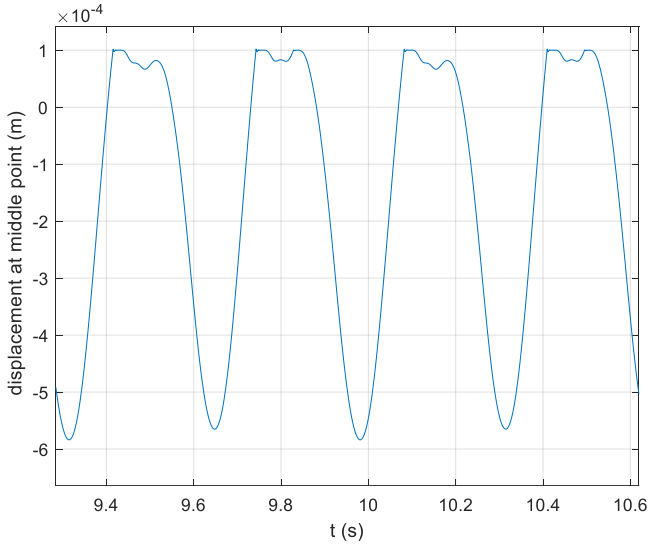

Figure 3.9. Periodic response of the fuel pin with one contact point ($a_{ext} = 3\ m/s^2$ and $f_{ext} = 3\ Hz$)

3.3.2 Fuel pin with several contact points

In this section, we are interested in a more realistic case. The spacer wire is taken into account as a periodically distributed contact points along the fuel pin span. The schematic contacts between a fuel pin and the wrapper tube is as shown in Figure 3.10.

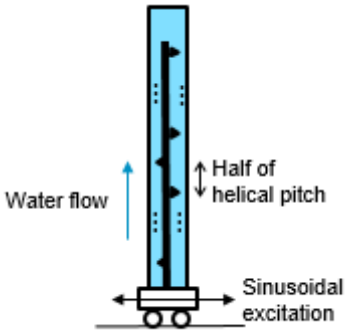

Figure 3.10. Fuel pin with contact points modelling the spacer wire

As there are more potential contact points, the nonlinearity of the system is stronger and we observe more complex dynamic behaviors of the fuel pin. Besides the linear zone where no contact happens during steady-state vibration, two types of nonlinear periodic responses are observed. A rough classification of the responses to the excitation of different accelerations and different frequencies is as shown in Figure 3.11. It is "rough" because the computation is not exhaustive (the separation lines are obtained with some sample points) and the transition between the periodic response and the chaotic response is quite vague. We distinguish them by the Fast Fourier Transform of the temporal evolution of the displacement at free end: the periodic response presents clear spectral peaks, like the cases shown in Figure 3.14 and Figure 3.15a, whereas the chaotic response presents a large bandwidth of the peaks due to noises and even the occurrence of a peak at $f \approx 0$ Hz, as shown in Figure 3.15c. The change is sometimes not that sudden at an exact value, but sometimes it is with noises of greater and greater level that the periodicity becomes less and less obvious. Anyway, we can have a fair idea of the different dynamic responses.

In fact, the dynamic response of a fuel pin against repeated impacts is composed of a global behavior, of which the period is of the order of that of the excitation, and the local chatters in much smaller time scale. Here, the local chatters mean the repeated impacts and rebounds in a short time interval. The local behavior is very sensitive to the choice of the impact law and numerically sensitive to the time integration scheme and the time step. As a result, the strict periodicity is only observed in a very limited range (a_{ext} not much greater than the linear level), in most cases what we obtain is a "globally periodic" response, where the periodicity of the global vibration is clear but the chatters can differ from period to period. These chatters are the origin of the noises observed in the spectrum. It is concluded that the global dynamic behavior of the fuel pin under excitation is relatively simple in our studied range and the complexity is mainly due to the local vibrations. In the following, the qualitative description of the phenomenon relative to impact will be given with some particular cases.

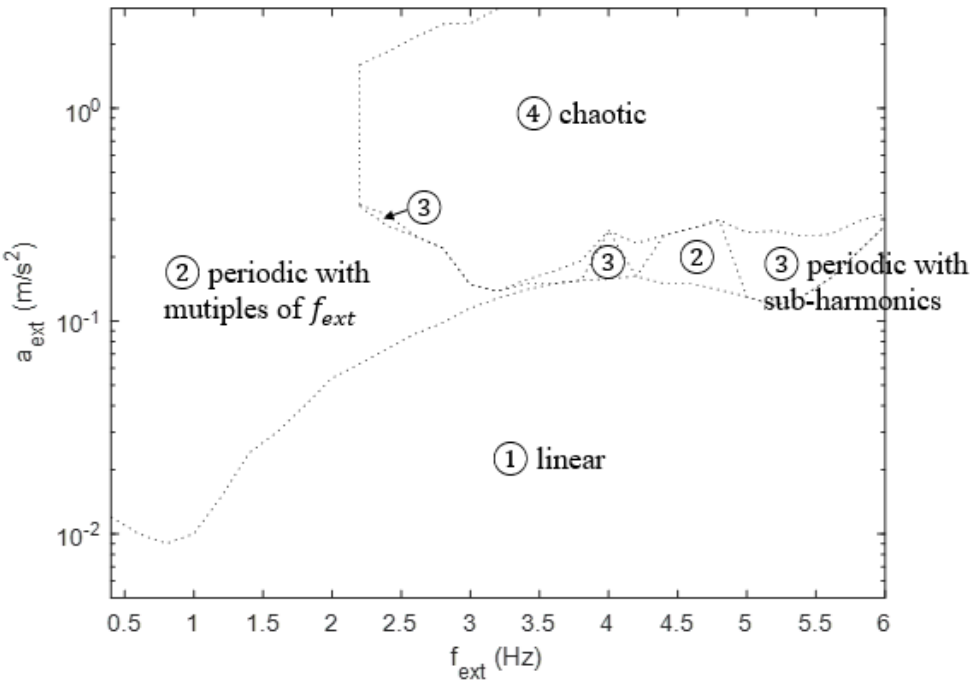

Figure 3.11. Classification of the vibration patterns in the investigated range of a_{ext} and f_{ext}

It is observed that with a low external frequency ($f_{ext} < 2Hz$), the dynamic responses are always globally periodic. In this case, the fuel pin vibrates from right to left remaining "stuck" with the contact points (see Figure 3.16(a)), the chatters generated by the impacts are damped during the "sticking" procedure. With an increasing a_{ext}, the chatters become more and more important and result in the non-periodicity due to numeric sensitivity. Analyzed with the Fourier transform, the temporal responses contain the multiples of f_{ext}. The odd multiples are generally more weighted, as shown in Figure 3.12.

When the frequency becomes higher, the periodic vibrations with sub-harmonics happen, as for example shown in Figure 3.13. Apart from the imposed frequency and its multiples, a sub-harmonics of half the imposed frequency along with its multiples occur. There exists also periodic vibrations with sub-harmonics of other frequencies, like one third the imposed frequency, as shown in Figure 3.14. In this case besides the "sticking" contact with chatters, alternately during separation at free end, the impact-induced flexural wave travelling along the beam is strong enough to cause another contact at the points around half-length and results in a rebound (see Figure 3.16(b)) at free end without being stuck. This appears to be the origin of the sous-harmonics, thus results in the period-doubling bifurcation.

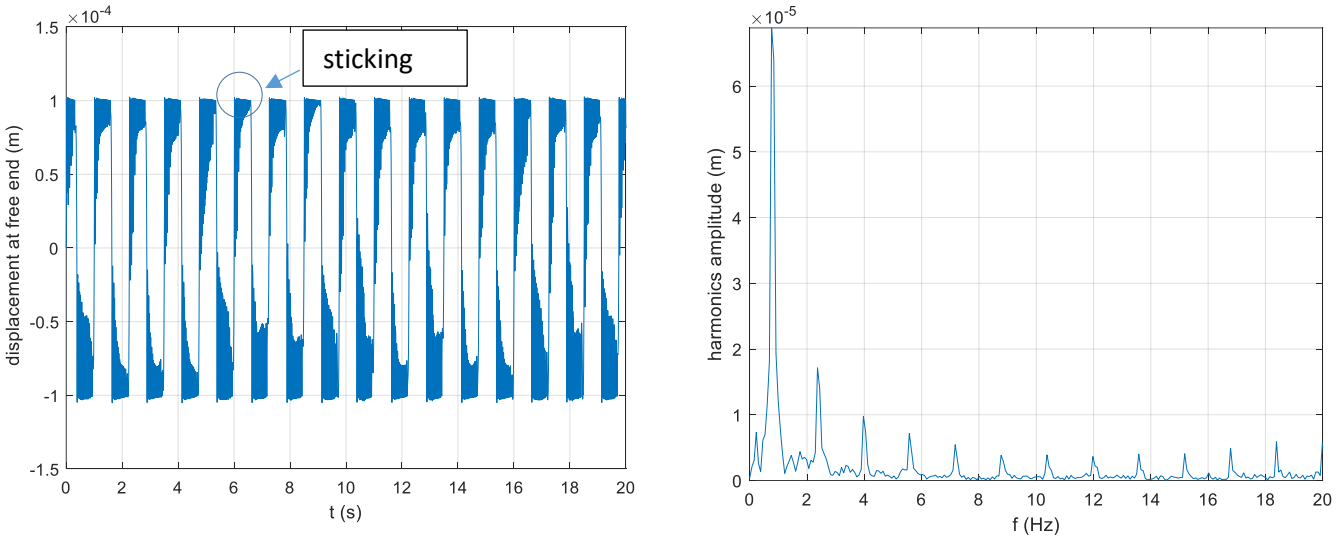

Figure 3.12. Temporal response and corresponding Fourier transformation of the fuel pin with contact points modelling the spacer wire ($a_{ext} = 3\ m/s^2$and $f_{ext} = 0.8\ Hz$)

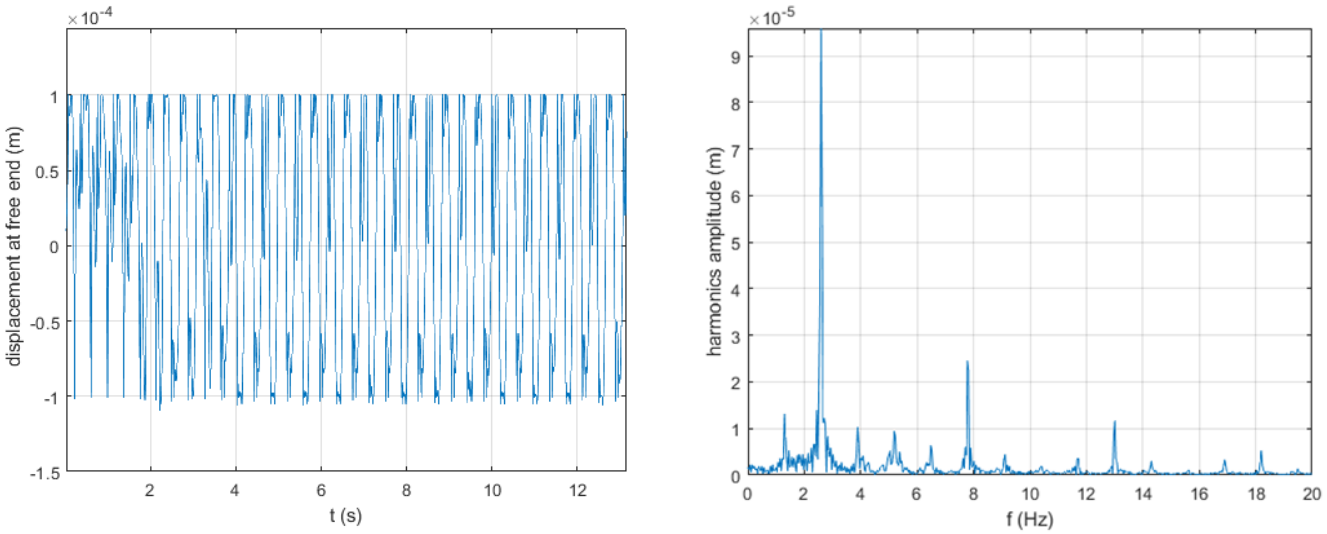

Figure 3.13. Temporal response and corresponding Fourier transformation of the fuel pin with contact points modelling the spacer wire ($a_{ext} = 0.25m/s^2$and $f_{ext} = 2.6\ Hz$)

With the case where the frequency was imposed at 3 Hz, the transition between the periodic behavior (Figure 3.15a) and chaotic behavior (Figure 3.15b) can be observed. The chaotic behavior results from a random alternation of the two mechanisms, “sticking” and “rebound”, at contact points. With a_{ext} increases, the dynamic behavior of the fuel pin is chaotic due to the sub-harmonics and their multiples (Figure 3.15c). As for the phenomenon of the vibration, the chaotic behavior is mainly caused by the mixing of different “rebounds”. Finally, a re-stabilization is observed beyond the chaotic zone (Figure 3.15d). This phenomenon can only be observed at an external frequency relatively low.

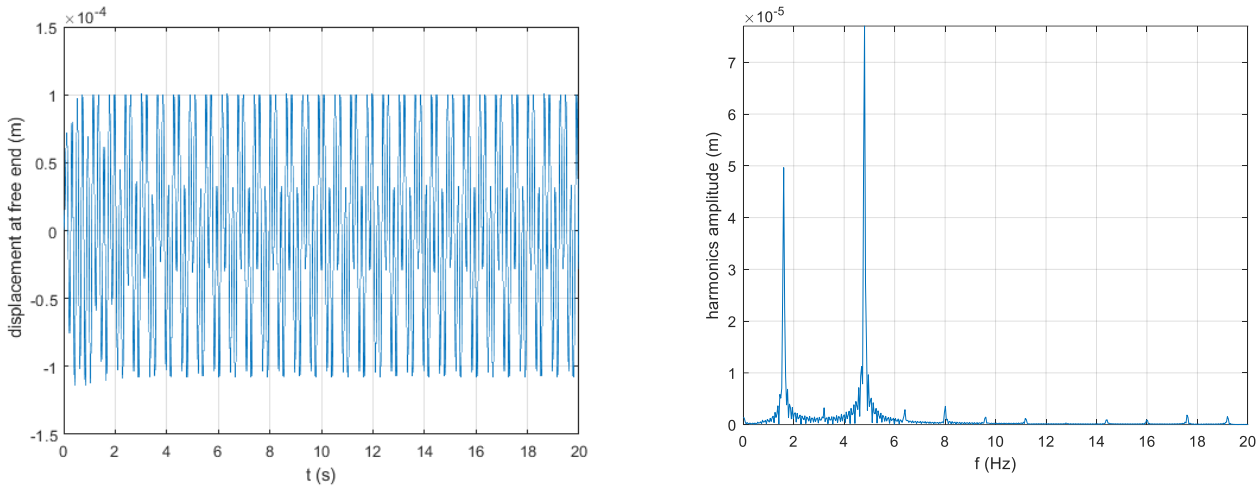

Figure 3.14. Temporal response and corresponding Fourier transformation of the fuel pin with contact points modelling the spacer wire ($a_{ext} = 0.145m/s^2$and $f_{ext} = 4.8\ Hz$)

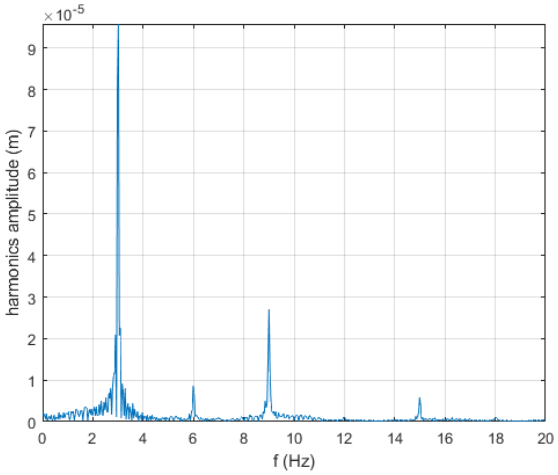

a) Periodic with $a_{ext} = 0.148m/s^2$

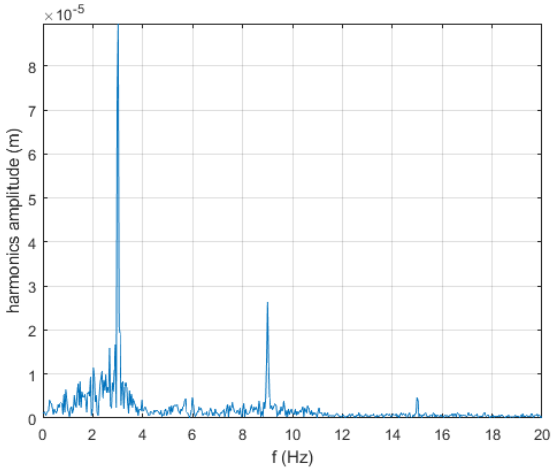

b) Chaotic with $a_{ext} = 0.149m/s^2$

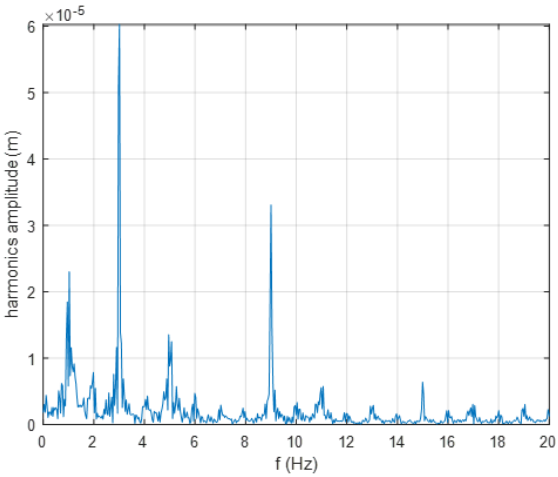

c) Chaotic with $a_{ext} = 0.2\ m/s^2$

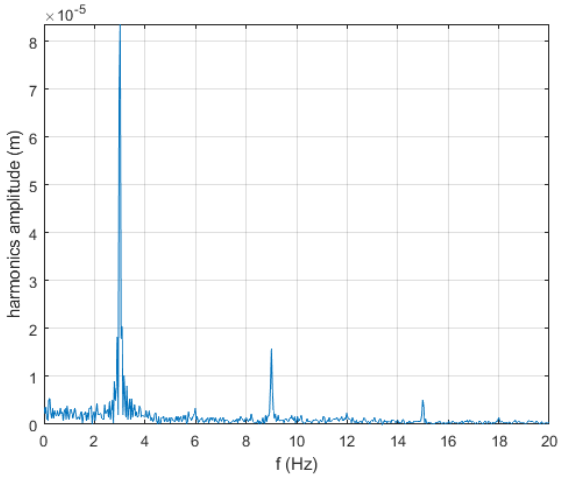

d) Periodic with $a_{ext} = 3\ m/s^2$

Figure 3.15. Fourier transformation of the temporal responses of the fuel pin with contact points modelling the spacer wire when $f_{ext} = 3\ Hz$ and different amplitudes

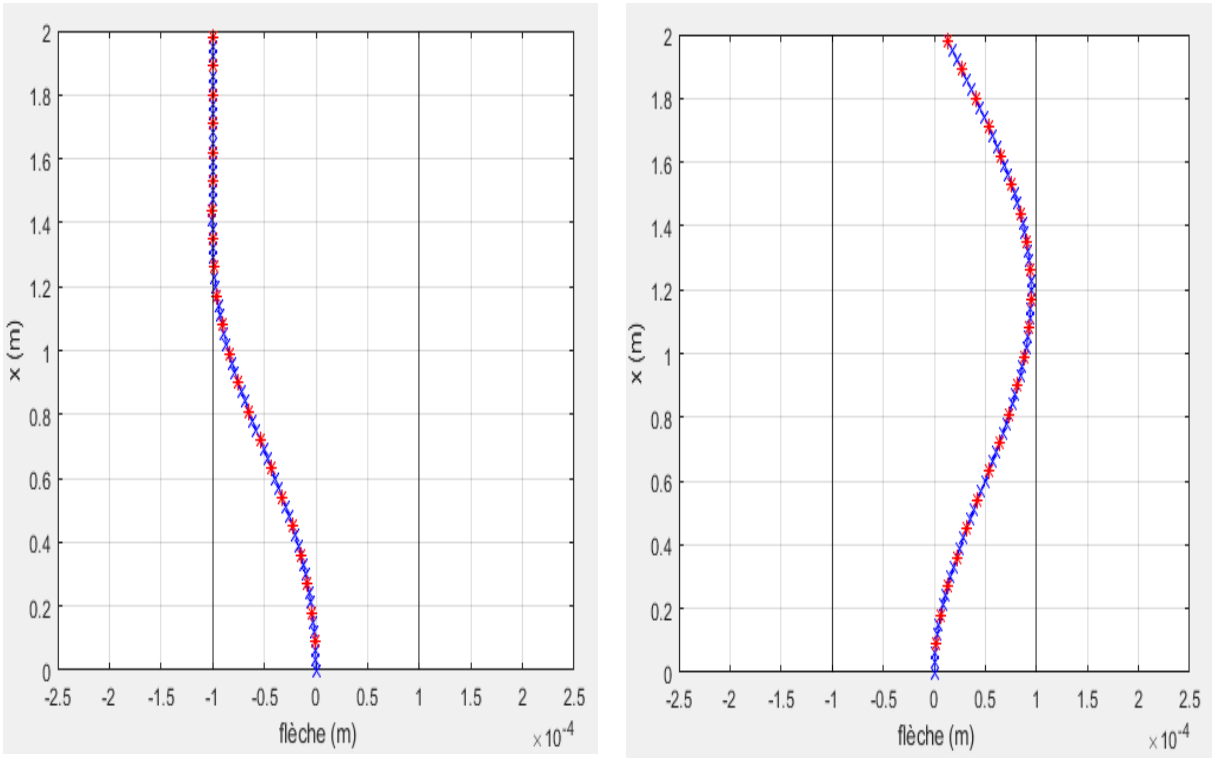

(a) "sticking" contact (b) "rebound"

Figure 3.16. Vibration patterns of (a) "sticking" contact; (b) "rebound"

3.3.3 Six fuel pins in a row

The study now involves a row of 6 fuel pins with 120 pin-to-pin contact points and 24 pin-to-wrapper tube contact points, as schematized in Figure 3.17. This preliminary simulation does not take into consideration the coupling by the flow between the fuel pins, which means that the motion equation of each fuel pin is the same and only the impacts due to the relative displacements are modelled.

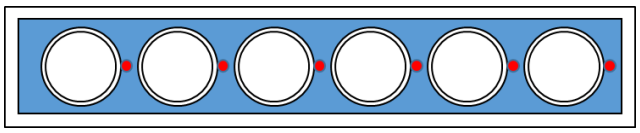

Figure 3.17. Schema of a row of six fuel pins with 144 contact points

We can observe that the dynamic responses to an imposed frequency equal to 4 Hz are always globally periodic in the investigated range of the amplitude, the periodic response with $a_{ext} = 3\ m/s^2$ is shown in Figure 3.18(a). Furthermore, when the frequency of the excitation is 6 Hz, the periodic behavior can be observed until $a_{ext} = 1.5\ m/s^2$(Figure 3.18(b)). In the sense that the chaotic response arrives with a greater amplitude and a higher frequency of the excitation, it can be concluded that this system is less nonlinear comparing with the fuel pin with several contacts. This difference of behavior can probably be explained by the fact that a row of fuel pins is less constrained in space than a single pin.

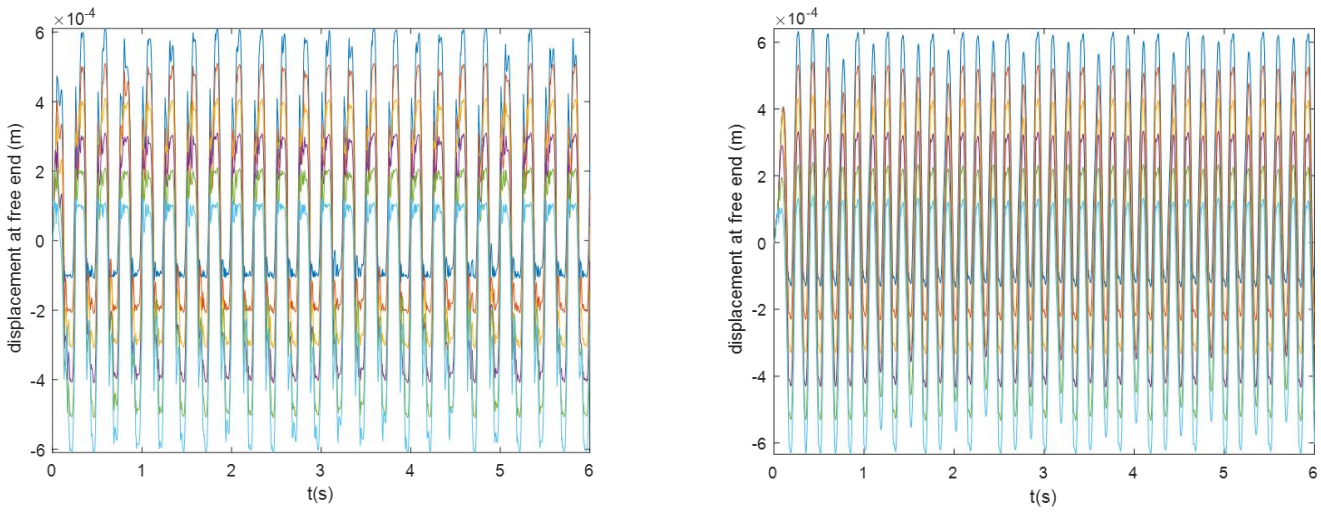

a) b)

Figure 3.18. Temporal responses of six fuel pins in a row: a) globally periodic response with $f_{ext} = 4Hz$ and $a_{ext} = 3\ m/s^2$; b) periodic response with $f_{ext} = 6Hz$ and $a_{ext} = 1.5\ m/s^2$

3.4 Conclusion

In this chapter, the model for analyzing the dynamics of the fuel pin with contact points and under earthquake has been constructed, basing on the model of hydraulic forces in axial flow proposed by Paidoussis [58] and the impact law taking the ovalization into account [2]. The numeric method consists in the finite element method with the 2-node element of Bernouilli beam with the cubic Hermite interpolation, the implicit Newmark scheme which is carried out by Newton-Raphson iteration until a convergence criterion on force is reached.

Due to the lack of experiments, an estimation of the coefficients in our model has been performed based on the previous theoretical and experimental studies [27][52][66][106][107]. Their effects on the eigenfrequencies and the damping ratios of the fuel pin have been evaluated in air, in still water and in water flow.

With these parameters, the analyses on the nonlinear responses of the fuel pin have been performed. For the fuel pin with one contact at half-length, the motional spectrum with different excitation amplitudes is obtained, and the different nonlinear vibration patterns, of multiples of imposed frequency and of period-doubling, have been identified.

For the fuel pin with several contacts modelling the spacer wire, a rough classification of the vibration behaviors has been conducted in the investigated range of the acceleration and frequency. It is found that the global dynamic behavior of the fuel pin under excitation is relatively simple in our studied range and the complexity is mainly due to the local chatters in much smaller time scale. The periodic behavior composed of multiples of the imposed frequency, which corresponds to the “sticking” contact, and the one identifying the sub-harmonics, which corresponds to the “rebound” are observed. The transition to chaotic response has been figured out, being due to the random alternation of the “sticking” contacts and the “rebounds”. Another type of chaotic response caused by the mixing of different sub-harmonics is also observed with our simulations.

It is found that the chaotic response of the system of six fuel pins in a row arrives with a greater amplitude and a higher frequency of the excitation, comparing with the fuel pin with several

contacts. The nonlinearity is weaker, even with a greater number of contact points, is possibly due to the greater space for the vibration.

In conclusion, the complexity of the nonlinear responses for the impact problems is mainly due to the interaction between the impact-induced transient waves and the contact points. The simulation of the local vibrations due to the repeated impact is sensitive to the choice of the impact law and the time-integration scheme.

Chapter 4 Dynamics of fuel pins: periodic solution finding

4.1 Introduction

As the steady-state responses of the fuel pin determine the long-term behavior, the search for periodic solutions is of particular importance. Again, it is reasonable to assume that the random excitation of turbulence is negligible, since after an initial transient period, turbulent flows become statically steady, in the sense that mean flow features do not vary over time. The focus is therefore to search the periodic solutions of the model developed in section 3.1.

In the previous chapter, the time-integration method is adopted to observe the vibration patterns. Nevertheless, it is inefficient as computations have to be performed over a large-enough interval to ensure that the transient response has faded, thus require considerable resources both in terms of computation time and data storage.

As an alternative, the methods for searching directly the periodic responses have been developed. They are usually subdivided into two main groups: those relying on the frequency-domain formulation and those relying on the time-domain formulation. The first group corresponds to the so-called harmonic balance method (HBM) [110] where the unknown variables are decomposed into truncated Fourier series. The second group consists of methods where a time integration algorithm or a collocation approach, which is generally limited to a single period, is used to transform the original differential system into a system of algebraic equations, in which the unknowns are the values of the original unknown variables at grid points along the periodic orbit.

With these methods, once one periodic solution is found, a whole branch of solutions can be unfolded by the continuation method, which consists in treating one of the system's parameters as a new unknown and following the equilibrium path. Different approaches for path-following have been employed over the years, with the most popular variants being arc-length continuation [111] and the Asymptotic Numerical Method (ANM) [112]. The former consists in taking a step along the tangent direction to the path at a given solution, followed by orthogonal corrections until convergence. The latter, on the other hand, uses a series expansion to locally represent the path in the vicinity of the initial solution, iteratively solving for the expansion coefficients. Arc-length continuation can be seen as a first-order truncation of the corresponding series expansion.

In this chapter, the periodic solution searching methods are explored in the context of the study of dynamics of fuel pins. Different methods have been evaluated and compared. All the calculations are performed with the software *Manlab* [113]. It is an interactive software program developed in LMA (Laboratoire de Mécanique et d'Acoutique) for the continuation and bifurcation analysis of algebraic systems, based on ANM continuation.

4.2 Harmonic Balance Method

4.2.1 State of the art

Krylov and Bogoliubov [114] were probably the first to have proposed a semi-analytic method whose principle was to look for periodic solutions in the form of truncated Fourier series. A Galerkin projection of the differential equations of motion onto a base of trigonometric functions, which are mutually orthogonal, transforms the initial problem into a system of nonlinear algebraic equations whose unknowns are the Fourier coefficients up to a certain

harmonic component. The estimation of the number of terms required to correctly capture periodic motion is seldom possible [109]. The study by Nakhla and Vlach [115] is often said to be a milestone in the modern formulation of HBM as they succeeded in circumventing this issue. Dynamical equilibrium is formulated as a minimization problem for an error function, and the number of harmonics is adjusted accordingly. Although the classical HBM is simple in its principle, the Fourier expansion of the nonlinear force can be cumbersome or even impracticable, when the system contains complex nonlinearities and when a large number of harmonics is required, i.e. more than 5 or 10 [116].

To overcome these shortcomings, many variations of the basic algorithm have been proposed. Lau [117] introduced the Incremental HB method (IHBM) to study geometrically-nonlinear systems with one or several degrees of freedom. This method balances the harmonics only for the linearized problems that appear in the continuation process. This approach was followed by Pierre [118] and Ferri [119] for the study of friction-damped systems. Another approach is the Alternating Frequency-Time (AFT) procedure proposed by Cameron and Griffin [120]. The main idea is to transfer the "most nonlinear" unknowns to the time domain using the inverse fast Fourier transform (IFFT) at each iteration in the continuation procedure so as to compute the nonlinear force in the time domain. Then using fast Fourier transform (FFT) the nonlinear force is switched back to the frequency domain. This technique has been used, for instance, to analyze nonlinear vibrations in mechanical systems with contact and dry friction [102][121]. Finally, Cochelin and Vergez [110] proposed a high-order frequency-based HB method which recasts the nonlinearities present in the original system into purely polynomial quadratic terms. A very large class of systems with smooth equations can indeed be transformed in quadratic form by making a few algebraic manipulations and a few additions of equations and auxiliary variables. In comparison with the AFT procedures, no problems of convergence, which can be difficult with AFT [122], arise with the quadratic recast method and the computational cost is fairly rather low.

With the quadratic recast HBM, the Jacobian can be calculated analytically. But on the other hand, for very nonlinear systems, the error introduced in the Jacobian estimation results in inaccurate updates of the unknowns and a large number of iterations and possibly no convergence. Therefore, an outstanding performance can be expected for inherently smooth systems, whereas it is less suited to treat regularized nonsmooth nonlinearities like impacts or friction. Works are still done for the systems with impact. Karkar [123] searched for the periodic solutions of a vibro-impact with exponential regularization. A very high number (1000) of harmonics in the HBM is used in the case of a stiff regularization (a ratio of 200 between the contact stiffness and the stiffness of the oscillator). Moussi [124] computed the nonlinear normal modes of a clamped simply supported linear elastic beam connected to a bilateral nonlinear elastic contactor. Unlike the local method [125] which consider an individual number of harmonics for each algebraic equation, he partitioned the linear and nonlinear equations as with the AFT. A low number of harmonics is applied for the linear part whereas a high number of harmonics for the strongly nonlinear part of the model.

4.2.2 Formulation of HBM for the fuel pin with contact points

Recalling the formulation of the forced fuel pin with potential contact points constructed in Section 3.1.4:

$$\boldsymbol{M\ddot{X}} + \boldsymbol{C\dot{X}} + \boldsymbol{KX} + \boldsymbol{F_c} = F_e \cos(\omega t)\boldsymbol{Q} \tag{4.1}$$

Where $\boldsymbol{X}$ is the generalized coordinates, which is expressed as:

$$\boldsymbol{X}^T = [\, w_2 \; \varphi_2 \; \dots \; w_{N+1} \; \varphi_{N+1}]$$

The impact forces locate only at the potential contact points, coinciding with the nodes numbered c_i ($i \in [\![1, nc]\!]$) and they are alternatively situated at left and right side of the fuel pin. The not-zero elements of the vector $\boldsymbol{F_c}$ are therefore:

$$\forall i \in [\![1, nc]\!], \boldsymbol{F_c}(2c_i - 1) = \boldsymbol{F_c}\big(\boldsymbol{X}(2c_i - 1)\big) = \begin{cases} \max\big(k_c\big(w_{c_i} - d\big), 0\big) \;\; if \; i \; is \; pair \\ \min\big(k_c\big(w_{c_i} + d\big), 0\big) \; if \; i \; is \; odd \end{cases}$$

The nonsmooth nonlinear force is regularized into the polynomial form:

$$\forall i \in [\![1, nc]\!], \boldsymbol{F_c}(2c_i - 1) = \begin{cases} \frac{k_c}{2}\big(w_{c_i} - d\big) + \sqrt{\left[\frac{k_c}{2}\big(w_{c_i} - d\big)\right]^2 + \varepsilon} \;\; if \; i \; is \; pair \\ \frac{k_c}{2}\big(w_{c_i} + d\big) - \sqrt{\left[\frac{k_c}{2}\big(w_{c_i} + d\big)\right]^2 + \varepsilon} \;\; if \; i \; is \; odd \end{cases} \tag{4.2}$$

Where ε is an adjustable regularization parameter. An example of the regularized nonlinear impact law is as shown in Figure 4.*1*.

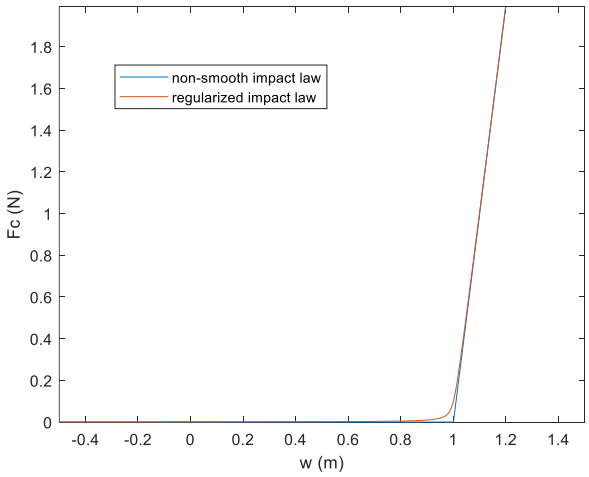

Figure 4.1. Regularized impact force with respect to displacement ($k_c = 10\ N/m$, $d = 1\ m$, $\varepsilon = 0.01$)

Three auxiliary variables $\boldsymbol{u}$, $\boldsymbol{r}$ and $\boldsymbol{z}$ are used to recast the system quadratic, for $\forall i \in [\![1, nc]\!]$, they are written as:

$$u_i = \begin{cases} \frac{k_c}{2}\big(w_{c_i} - d\big) \; if \; i \; is \; pair \\ \frac{k_c}{2}\big(w_{c_i} + d\big) \; if \; i \; is \; odd \end{cases} \tag{4.3}$$

$$r_i{}^2 = u_i{}^2 + \varepsilon$$

$$r_i = z_i{}^2$$

The third equation is to guarantee that the elements of $\boldsymbol{r}$ are always positive. Therefore, equation (4.1) can be rewritten into the quadratic form if the forcing pulsation is chosen as the continuation parameter λ, for $\forall i \in [\![1, nc]\!]$:

$$\begin{cases} \dot{\boldsymbol{X}} = & & \boldsymbol{Y} & & \\ \boldsymbol{M}\dot{\boldsymbol{Y}} = & F_e\cos(\lambda t)\boldsymbol{Q} & -\boldsymbol{C}\boldsymbol{Y} - \boldsymbol{K}\boldsymbol{X} - \boldsymbol{F_C} & & \\ 0 = & & \boldsymbol{F_c}(2c_i - 1) - u_i - r_i & & if\ i\ is\ pair \\ 0 = & & \boldsymbol{F_c}(2c_i - 1) - u_i + r_i & & if\ i\ is\ odd \\ 0 = & \frac{k_c}{2}d & -\frac{k_c}{2}\boldsymbol{X}(2c_i - 1) + u_i & & if\ i\ is\ pair \\ 0 = & -\frac{k_c}{2}d & -\frac{k_c}{2}\boldsymbol{X}(2c_i - 1) + u_i & & if\ i\ is\ odd \\ 0 = & -\varepsilon & & +{r_i}^2 - {u_i}^2 & \\ 0 = & & r_i & -{z_i}^2 & \end{cases} \tag{4.4}$$

It is also possible to carry out the continuation by varying the amplitude of the external force F_e, then the forcing pulsation should be fixed and the constant term in the second line of eq. (4.4) becomes $\lambda\cos(\omega t)\boldsymbol{Q}$. There are in total $N_e = 4N + 4nc$ algebraic equations, which can be globally expressed with an extended variable $\boldsymbol{Z} = [\boldsymbol{X}; \boldsymbol{Y}; \boldsymbol{F_C}(2c_i - 1); \boldsymbol{u}; \boldsymbol{r}; \boldsymbol{z}]$ ($i \in [\![1, nc]\!]$):

$$d(\dot{\boldsymbol{Z}}) = c(\lambda, t) + l_1(\boldsymbol{Z}) + l_2(\boldsymbol{Z}, \boldsymbol{Z}) \tag{4.5}$$

Where c is the constant (in blue case) related to the continuation parameter λ, d (terms at the left side) and l_1 (in red case) are linear operators and l_2 (in green case) is a bilinear operator. Applying the HBM to equation (4.5), the extended variable is decomposed into Fourier series with H harmonics:

$$\boldsymbol{Z}(t) = \boldsymbol{Z_0} + \sum_{k=1}^{H} \boldsymbol{Z_{c,k}}\cos(k\omega t) + \sum_{k=1}^{H} \boldsymbol{Z_{s,k}}\sin(k\omega t) \tag{4.6}$$

The number of harmonic coefficients is selected on the basis of the number of significant harmonics expected in the non-linear dynamical response. Generally speaking, harmonic components become less significant when H increases. The forcing frequency is related to the response frequency by putting $\lambda = \omega$, then this formulation includes only harmonic and super-harmonic responses of the system. The sub-harmonics are taken into account by choosing $\lambda = p\omega$ with p an integer. As a result, $c(\lambda, t)$ can be expanded into $c_0 + c_{c,p}\cos(p\omega t)$.

In order to determine the value of the $N_e \times (2H + 1)$ unknown coefficients, eq. (4.6) is introduced into eq. (4.5), and balancing the harmonics a new quadratic system is obtained:

$$\omega D(\boldsymbol{U}) = (C_0 + C_{c,p}) + L_1(\boldsymbol{U}) + L_2(\boldsymbol{U}, \boldsymbol{U}) \tag{4.7}$$

where $\boldsymbol{U}$ regroups the unknowns:

$$\boldsymbol{U} = [\boldsymbol{Z_0}; \boldsymbol{Z_{c,1}}; \boldsymbol{Z_{s,1}}; \boldsymbol{Z_{c,2}}; \boldsymbol{Z_{s,2}}; \cdots \boldsymbol{Z_{c,H}}; \boldsymbol{Z_{s,H}};] \tag{4.8}$$

and the new operators D, $C_0 + C_{c,p}$, L_1 and L_2 that apply to $\boldsymbol{U}$ depend only on the operators d, c, l_1 and l_2 of Eq. (4.5) and on the number of harmonics H [110].

If the continuation is performed with respect to ω, the algebraic equations to be solved is therefore:

$$\begin{aligned} R(\widehat{\boldsymbol{U}}) &= C + L_1(\widehat{\boldsymbol{U}}) + \widehat{L_2}(\widehat{\boldsymbol{U}}, \widehat{\boldsymbol{U}}) = 0 \\ \widehat{L_2}(\widehat{\boldsymbol{U}}, \widehat{\boldsymbol{U}}) &= L_2(\boldsymbol{U}, \boldsymbol{U}) - \omega D(\boldsymbol{U}) \end{aligned} \tag{4.9}$$

with $\widehat{\boldsymbol{U}} = [\boldsymbol{U}, \omega]$. For each solution of eq. (4.9), and provided it is not a bifurcation point, the implicit function theorem guarantees the existence of a locally unique one-dimensional continuum of periodic solutions called a solution branch (or solution family) [126]. The ANM relies on a high-order Taylor series expansion of the solution branch with respect to the pseudo-arclength parameter $s = (\widehat{\boldsymbol{U}} - \widehat{\boldsymbol{U}}_{\boldsymbol{0}})\widehat{\boldsymbol{U}}_{\boldsymbol{1}}^{\boldsymbol{T}}$, where $\widehat{\boldsymbol{U}}_{\boldsymbol{0}}$ is a solution point and $\widehat{\boldsymbol{U}}_{\boldsymbol{1}}$ is the tangent vector at $\widehat{\boldsymbol{U}}_{\boldsymbol{0}}$ [110]:

$$\widehat{\boldsymbol{U}}(s) = \widehat{\boldsymbol{U}}_{\boldsymbol{0}} + s\widehat{\boldsymbol{U}}_{\boldsymbol{1}} + s^2\widehat{\boldsymbol{U}}_{\boldsymbol{2}} + \cdots + s^n\widehat{\boldsymbol{U}}_{\boldsymbol{n}} \tag{4.10}$$

Replacing the series (4.10) into eq. (4.9), and each power of *s* should be equated to zero:

$$\begin{aligned} R\left(\widehat{\boldsymbol{U}}(s)\right) &= C + L_1\left(\sum_{k=0}^{n} s^k\widehat{\boldsymbol{U}}_{\boldsymbol{k}}\right) + \widehat{L_2}\left(\sum_{k=0}^{n} s^k\widehat{\boldsymbol{U}}_{\boldsymbol{k}}, \sum_{k=0}^{n} s^k\widehat{\boldsymbol{U}}_{\boldsymbol{k}}\right) \\ &= C + \sum_{k=0}^{n} s^k L_1(\widehat{\boldsymbol{U}}_{\boldsymbol{k}}) + \sum_{k=0}^{n} s^k\left(\sum_{i+j=k} \widehat{L_2}(\widehat{\boldsymbol{U}}_{\boldsymbol{i}}, \widehat{\boldsymbol{U}}_{\boldsymbol{j}})\right) \\ &= R(\widehat{\boldsymbol{U}}_{\boldsymbol{0}}) + \sum_{k=1}^{n} s^k\left(L_1(\widehat{\boldsymbol{U}}_{\boldsymbol{k}}) + \sum_{i+j=k} \widehat{L_2}(\widehat{\boldsymbol{U}}_{\boldsymbol{i}}, \widehat{\boldsymbol{U}}_{\boldsymbol{j}})\right) \end{aligned} \tag{4.11}$$

$$J_{\widehat{U}_{\boldsymbol{0}}}(\widehat{\boldsymbol{U}}_{\boldsymbol{k}}) = L_1(\widehat{\boldsymbol{U}}_{\boldsymbol{k}}) + \widehat{L_2}(\widehat{\boldsymbol{U}}_{\boldsymbol{0}}, \widehat{\boldsymbol{U}}_{\boldsymbol{k}}) + \widehat{L_2}(\widehat{\boldsymbol{U}}_{\boldsymbol{k}}, \widehat{\boldsymbol{U}}_{\boldsymbol{0}}) = -\sum_{i=1}^{k} \widehat{L_2}(\widehat{\boldsymbol{U}}_{\boldsymbol{i}}, \widehat{\boldsymbol{U}}_{\boldsymbol{k-i}}) \tag{4.12}$$

with $J_{\widehat{U}_{\boldsymbol{0}}}$ the Jacobian matrix of R evaluated at $\widehat{\boldsymbol{U}}_{\boldsymbol{0}}$. The range of utility of the truncated power series is the interval $[0, s_{max}]$ for limiting the residual inferior to a given tolerance.

4.2.3 Analysis with simple model

In this section, a preliminary study on the advantages and the limits of the HBM method will be conducted with a simple model, as schematized in Figure 4.2, where one cantilevered beam with a totally blunt end is immersed in water flow. Four contact points with two on each side are located in the beam's span with a uniform pitch.

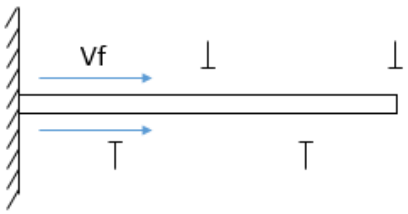

Figure 4.2. Cantilevered beam with four contact points

Without the contact points, the effect of the existence of fluid and the velocity of fluid flow can be observed in Figure 4.3. The existence of fluid brings an added mass into the system so that the natural frequency diminishes. With the added stiffness and the supplementary damping generated by the flow velocity, the amplitude of deformation diminishes and the resonance peaks are shifted a little bit.

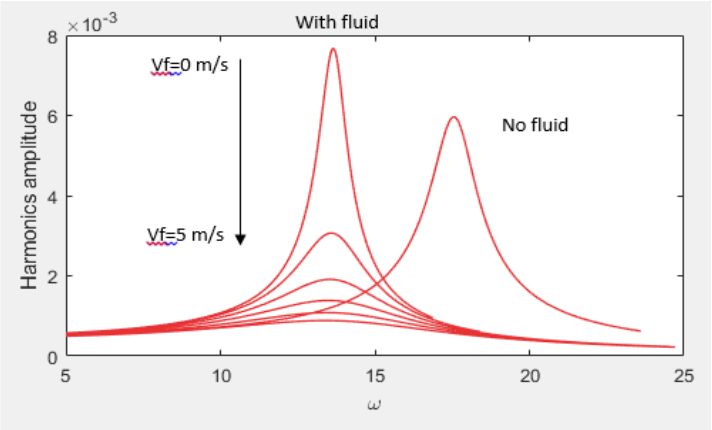

Figure 4.3. Effect of the existence of fluid and the velocity of fluid flow (without contact)

The effect of the potential contact points on the motional spectrum will be studied with both the HBM method and the temporal calculations. Recalling equation (4.2), the impact force is regularized into a polynomial form and it brings a supplementary stiffness of about $\varepsilon/k_c d^2$ (as the regularization parameter $\varepsilon \ll 1$) to the system when the beam is not deformed. The force existing before contact happens could have a physical meaning of the film effect. The supplementary stiffness should be negligible before the bending stiffness of the cantilevered beam, which is estimated by $3EI/L^3$ ≈10 N/m, however a too small value can pose a numeric problem in continuation.

4.2.3.1 First result with a hard stiffness contact

For the particular case with representative values of fuel pin ($k_c = 2.46 \times 10^6\ N/m$ and $d = 0.1\ mm$), analysis has been done by choosing $\varepsilon/k_c d^2 = 0.1$. The continuation with respect to the imposed pulsation $\lambda = 2\omega$ is performed with a very low acceleration of amplitude equal to 0.001g. Variation of the amplitude of the first harmonic ($\cos(\omega t)$ and $\sin(\omega t)$) of the displacement at free end is obtained with different numbers of harmonics, as shown in Figure 4.4. It is observed that a number not enough (H = 32) may generate fluctuations on the branch and the difficulty in continuation (the branch can go no longer further at $\lambda = 6.15$). The unexpected (with temporal calculation) bifurcation points occur on the solution branches as a result of the misrepresented contact, which is detailed in Figure 4.5. Taking the temporal calculation as a reference, it is observed that with H = 32, the "sticking" contact is not well represented and a fake period-doubling bifurcation is observed. Even with H = 96, the result does not perfectly correspond to that of the temporal calculation. It is logic that the representation of the sticking contact demands a Fourier expansion of great order, and this will make the computation more expensive in time (with H = 32, one continuation step costs less than 1 seconds while it takes about 8s with H = 96).

By fixing the imposed pulsation at 3 rad/s, the continuation with respect to the amplitude ($\lambda = F_e$) can reach until 0.0048g with H = 96. This range with the HBM is quite limited comparing with what we are interested in. At higher excitation amplitude and frequency, more oscillations when the free end is "stuck" with the contact points occur, which also challenges the expression of the impact with Fourier series, as shown in Figure 4.6. Physically, the impact forces should never change their signs while the Fourier series of order 96 is not enough to describe the sharp variations.

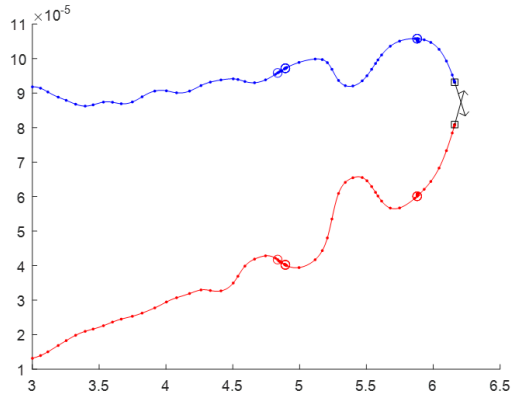

a) H = 32

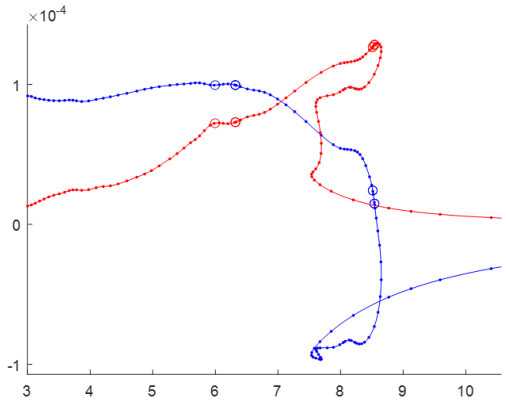

b) H = 64

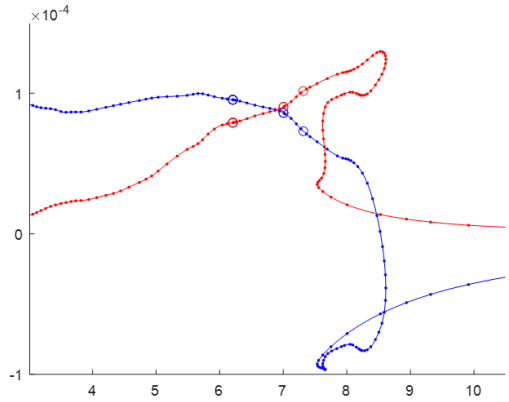

c) H = 96

Figure 4.4. Variation of the amplitude of the first harmonic ($cos(\omega t)$ and $sin(\omega t)$) of the displacement at free end with respect to λ by taking different numbers of harmonics

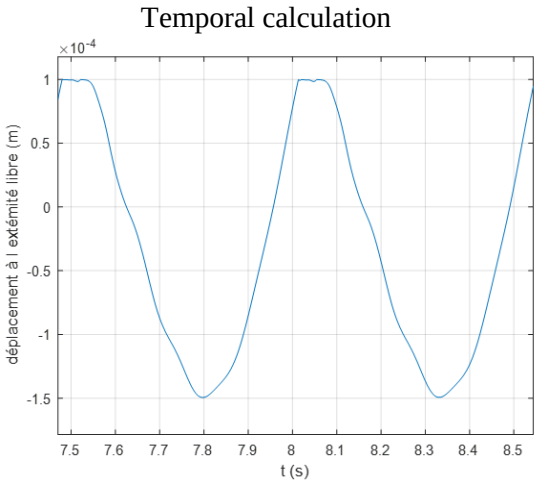

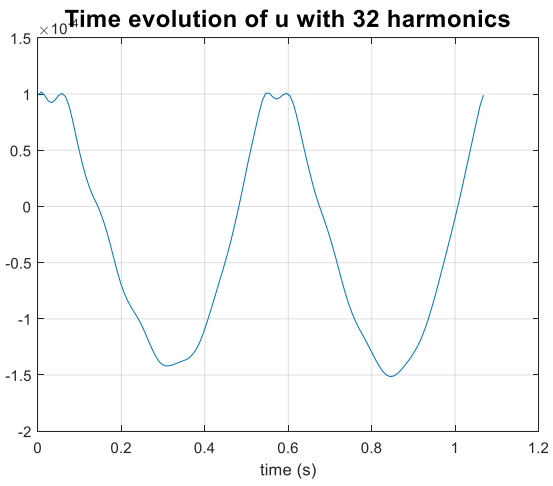

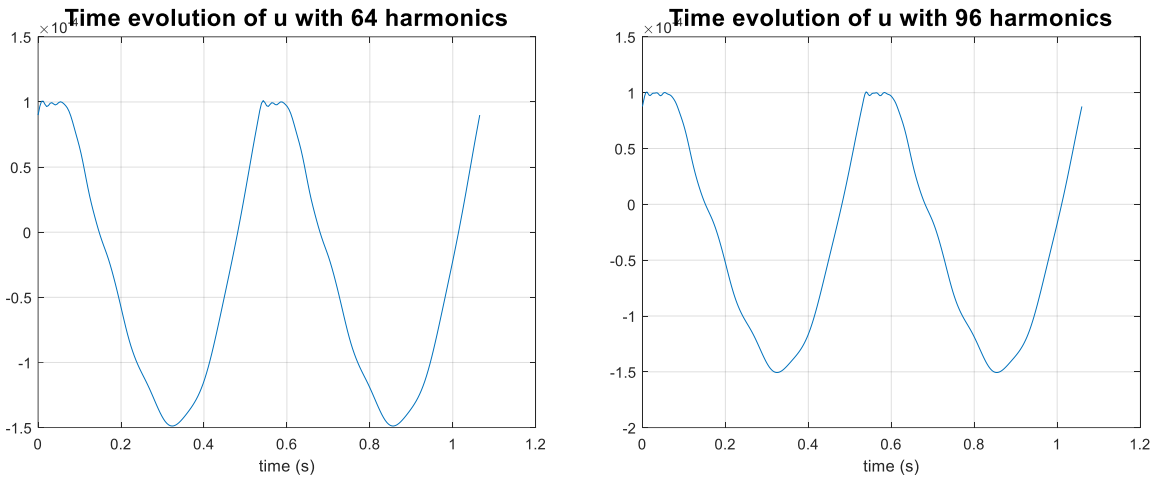

Figure 4.5. Periodic response at the free end in two periods ($\lambda = 5.88$ rad/s) of excitation obtained with temporal calculation and HBM with different numbers of harmonics

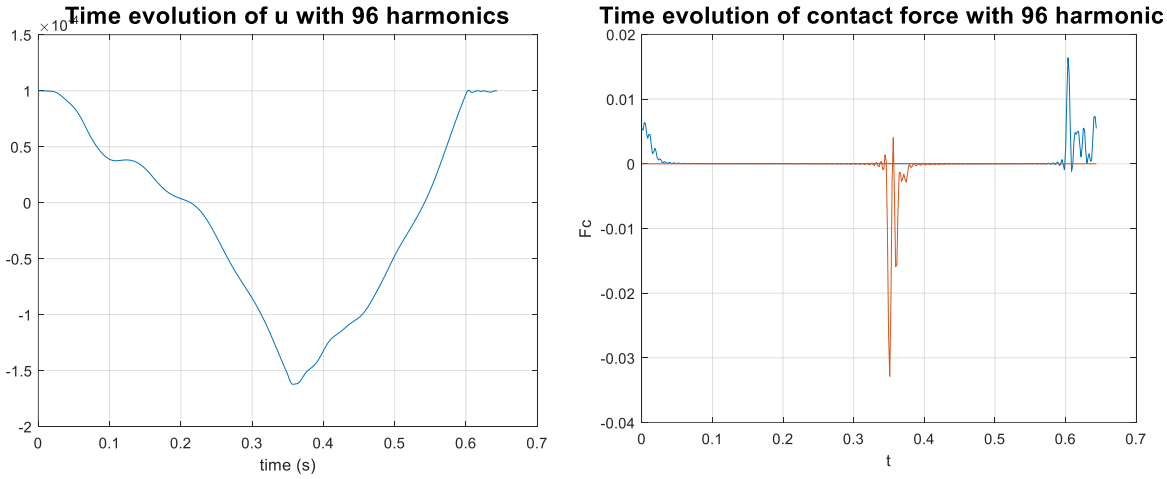

Figure 4.6. Periodic response of displacement and impact force at the free end with $a_{ext} = 0.02\ m/s^2$ and $\lambda = 9.76$ rad/s

4.2.3.2 Analysis with a reduced contact stiffness

The difficulties of the HBM arise from a contact point too rigid, as has been reported in [102][124]. In order to enlarge the study range and better observe the advantages of the HBM, here we take a contact stiffness of 50 times of the bending stiffness of the beam, which is usually the case in the previous studies. A larger clearance is also taken to ease the initialization of the calculation.

The distortion of the resonance peak due to the impact is observed in Figure 4.7. A small contact stiffness is considered as no contact existing, while with a contact stiffness equal to 500 N/m, λ in the range of 13 to 13.8 rad/s corresponds no more to a unique amplitude. These different states resulting from the same external force are critically dependent on the chosen initial conditions. A comparison is conducted between the result of HBM and that of temporal simulation for the case with a still flow. Figure 4.8 represents the evolution with the imposed pulsation of the displacement amplitude at the free end obtained with the temporal calculation, the blue points and red points are solutions with different initial conditions. It is observed that the form of two curves obtained with two methods are coherent except that the HBM result presents only the first harmonic's amplitude while the temporal result presents the norm of all

the harmonics. The HBM has the advantage in finding all the possible responses, including the instable ones, to an external force at the same time. A supplementary analysis of instability, which is more time-consuming, is possible as presented in Figure 4.9, the dashed line represents instable solutions.

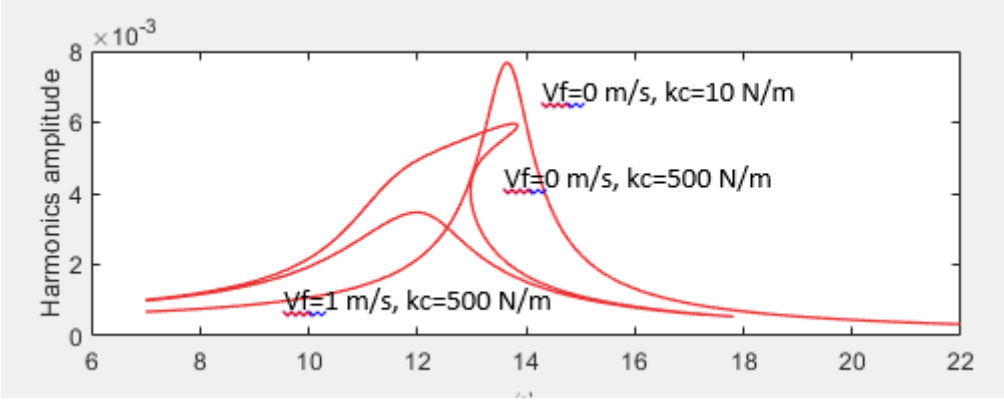

Figure 4.7. Distortion of the resonance peak due to the impacts

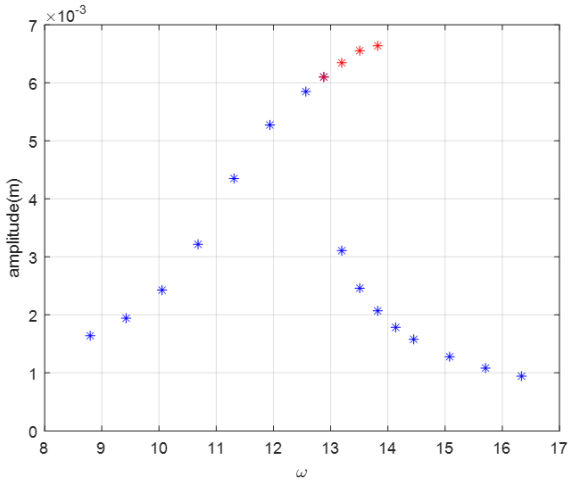

Figure 4.8. Motional spectrum of the displacement at free end with temporal calculation (vf=0 m/s and kc=500 N/m)

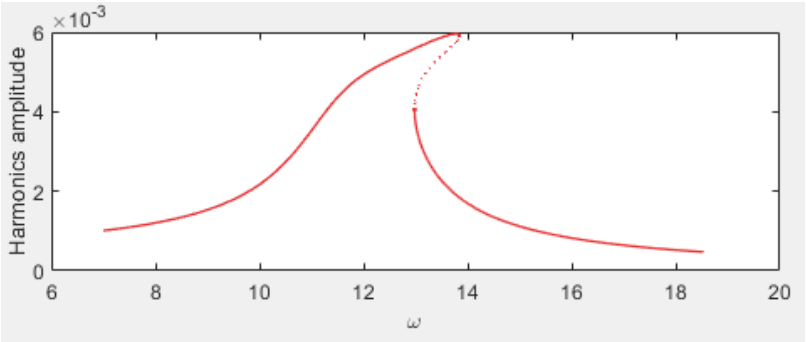

Figure 4.9. Stability analysis of the dynamics of the beam under external force

In this case, the HBM calculation with 32 harmonics is already enough. The computation time to obtain the whole solution branch is much reduced comparing with the temporal calculation. It takes only 5 or 6 iterations for initialization and dozens of steps with each step costing less

than one second, the total calculation time is therefore less than 1 minutes while the temporal calculation costs around 11 seconds for each point and several points to form the curve, with post treatment included it takes about 15 minutes.

a)

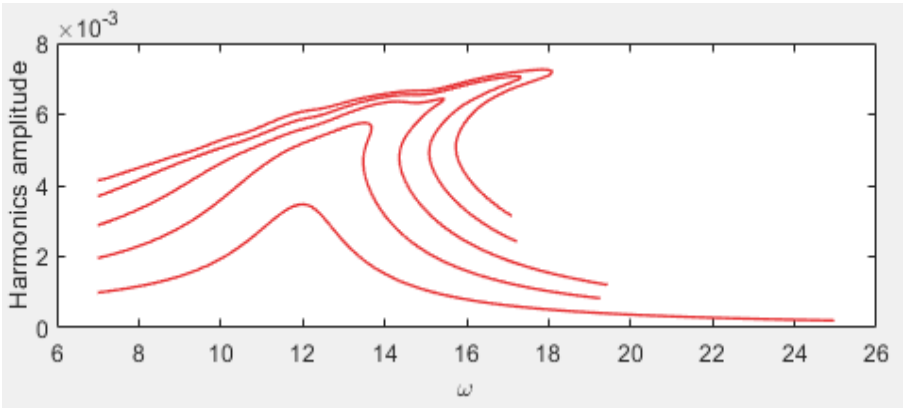

b)

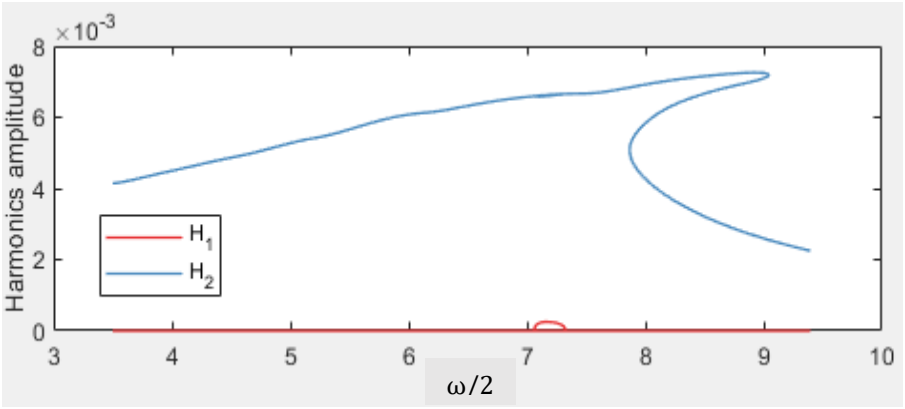

Figure 4.10. Evolution of the harmonics amplitude of the displacement at free end versus imposed pulsation: a) principle harmonics with different a_{ext}; b) H_1 and H_2 denoting respectively the principle harmonics and the sous-harmonics of pulsation $\omega/2$ with $a_{ext} = 0.5\ m/s^2$

The occurrence of the period-doubling bifurcation can be easily observed with the HBM method. The continuation with respect to the imposed pulsation $\lambda = 2\omega$ is performed with different acceleration amplitudes (from $0.1\ \mathrm{m/s^2}$ to $0.5\ \mathrm{m/s^2}$). It is observed from Figure 4.10 that the contacts happen from $0.2\ \mathrm{m/s^2}$ and the first period-doubling bifurcation occurs with $\mathrm{a_{ext}} = 0.5\ \mathrm{m/s^2}$. The bifurcation is observed in the range $\omega = 14.12 \sim 14.66$ rad/s.

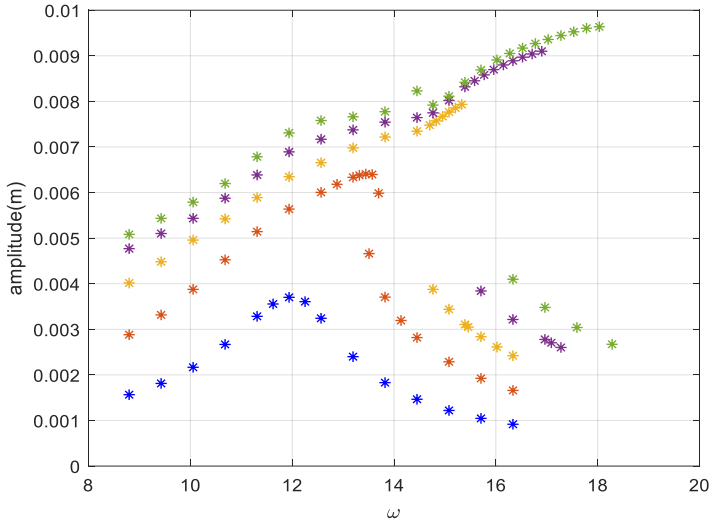

Figure 4.11. Motional spectrum of the displacement at free end with different acceleration amplitude with temporal calculation

Again, the motional spectrum of the displacement at free end obtained with the temporal calculation is presented in Figure 4.11. The curves are of the similar shape as the result of the HBM. A bulge on the curve with $a_{ext} = 0.5\ m/s^2$ is observed, which corresponds to the amplitude of the sous-harmonics. The range of observing the bifurcation is $\omega = 14{,}03 - 14{,}7$ rad/s, which is in good agreement with the result of the HBM. The period-doubling of the displacement can be observed with the two methods, as shown in Figure 4.12.

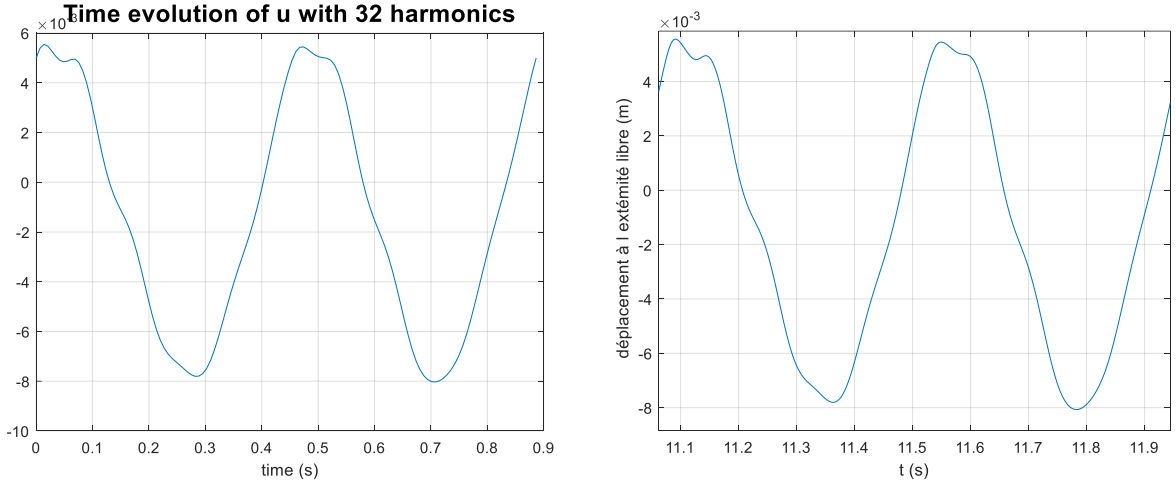

Figure 4.12. Period-doubling of the displacement at free end with $\omega = 14{,}18$ rad/s

4.2.4 Summary

The HBM is an efficient method in finding the periodic solutions of the nonlinear systems in terms of the computation time and data storage. Furthermore, the occurrence of the bifurcation can be easily detected.

However, this method has an outstanding performance for inherently smooth systems, but is less suited to treat nonsmooth nonlinearities like impacts. When it comes to a very rigid contact point, the difficulty in describing the “sticking” contact and the resulting impact force with Fourier series is obvious. What’s more, the calculation with a Fourier expansion of great order

is quite time-consuming. The difficulty of continuation with respect to excitation amplitude limits the range of our study.

In order to study the impact problems, different variations of the classical HBM have been applied in the previous works, such as the method [124] which considers a greater number of harmonics only for nonlinear equations, and the HBM-AFT method [102] which is quite sensitive to the time discretization. But in fact, in these works the ratio between the contact stiffness and the stiffness of the system is often no more than 50. Hereafter, we seek to treat the impact problem of a greater contact stiffness with the formulation relying on the time-integration.

4.3 Global periodic time integration (GPTI)

4.3.1 State of the art

The formulation depending on a time integration algorithm, which is generally limited to a single period, is an alternative to transform the original differential system into a system of algebraic equations, which are then solved by continuation. With these methods, the unknowns in the algebraic system are the values of the original unknown variables at grid points along the periodic orbit. In the following, three methods of this type will be introduced.

The shooting technique [111] seeks periodic solutions by a so-called Boundary-Value Problem (BVP), by which a shooting function to be equal to zero is defined to represent the difference between the initial and final states of one period T. Starting from some assumed initial condition, the motion at T, which can be known in advance (forced oscillations) or an additional unknown to be found (autonomous oscillations, for example in the case of self-excited motions), is obtained by numerical time integration of the equations of motion. Through an iterative procedure to solve the BVP, the initial conditions which satisfy dynamical equilibrium as well as periodicity are found. Peeters et al. [127] employed Newmark's method and a Newton–Raphson iteration scheme to study the nonlinear beams. The symmetries in time and space and a sensitivity analysis were exploited to reduce the computation cost, making the shooting a suitable candidate for addressing large-scale, complex systems. This method can also be applied to study the vibration absorbers [128] and the forced vibrations of rotor systems [129]. A similar approach was undertook by Dimitriadis [130] to study the parametric behavior of limit-cycle oscillations in an aeroelastic system. Shooting is per se limited by the capabilities of time integration algorithms. It can fail for strongly unstable systems, as reported in [111], and it hardly deals with piecewise linear or nonsmooth systems, unless specific time integration techniques or regularization are considered. An additional difficulty with shooting is that the small step sizes that are required for accurate time integration increase the sensitivity to high-order harmonics present in the response [131].

The orthogonal collocation method considers the discrete periodic solution, where the period is divided into $n_{\Delta t}$ time intervals. The steady-state solution is assumed to be a combination of p-order Lagrange polynomials and the discretization of the equation of motion is carried out by the collocation at Gauss points for each interval. Combining with the periodicity condition, the system of N dofs is transformed into an algebraic system comprising $2N(pn_{\Delta t}+1)$ equations that can be solved using a Newton-like approach. This method has been implemented into numerous software, such as AUTO [132] and MATCONT [133]. If the collocation method is accurate and can benefit from adaptive meshing strategies for the time interval [132], the method can become computationally intensive for large finite element models comparing with

the shooting technique. The performances of the HBM and the collocation method for the vibro-impact oscillator (see Figure 4.13(a)) are compared by Karkar [134]. The HBM required about 200 harmonics to obtain a periodic orbit with almost no visible difference with the reference solution and was shown to exhibit the classical Gibbs phenomenon (see Figure 4.13(b)). The orbit obtained with orthogonal collocation in Figure 4.13(c) is smoother and appears to better capture the reference solution, because the continuity of the trajectory is only imposed between two successive time intervals. However, without adaptive meshing strategies, at least 202 intervals were needed to obtain one time interval during the impact time and properly capture this region. For both smooth and nonsmooth systems, he concluded in a better convergence of the HBM compared to orthogonal collocation.

A global periodic time-integration (GPTI) method has been proposed [113],[135] to find the periodic solution in temporally discretized form. The equation of motion discretized with the finite element method can be generally expressed as $\dot{\boldsymbol{Z}} = f(\boldsymbol{Z}, t, \lambda)$, with $\boldsymbol{Z}$ the state vector for each node. Therefore, the global periodic method means an unknown vector which groups the state vector at each time step in one period T, i.e. $\boldsymbol{Z_g} = [\boldsymbol{Z_0}; \boldsymbol{Z_1}; \cdots; \boldsymbol{Z}_{n_{\Delta t}}]$ with $n_{\Delta t}$ the number of time intervals and $\forall k \in [\![0, n_{\Delta t}]\!], \boldsymbol{Z_k} = \boldsymbol{Z}(t_k)$. The system to be solved is therefore written as:

$$R\left(\boldsymbol{Z_g}, T = t_{n_{\Delta t}}, \lambda\right) = \begin{cases} \forall k \in [\![0, n_{\Delta t} - 1]\!], \boldsymbol{Z_{k+1}} = g(\boldsymbol{Z_k}, \dot{\boldsymbol{Z}}_{\boldsymbol{k}}, \dot{\boldsymbol{Z}}_{\boldsymbol{k+1}}, t_k, t_{k+1}) \\ \boldsymbol{Z_0} \quad = \boldsymbol{Z}_{n_{\Delta t}} \end{cases} \tag{4.13}$$

Where g is the function associated with a chosen time integration scheme. This method is not much studied, and we are interested in its performance for the impact problems.

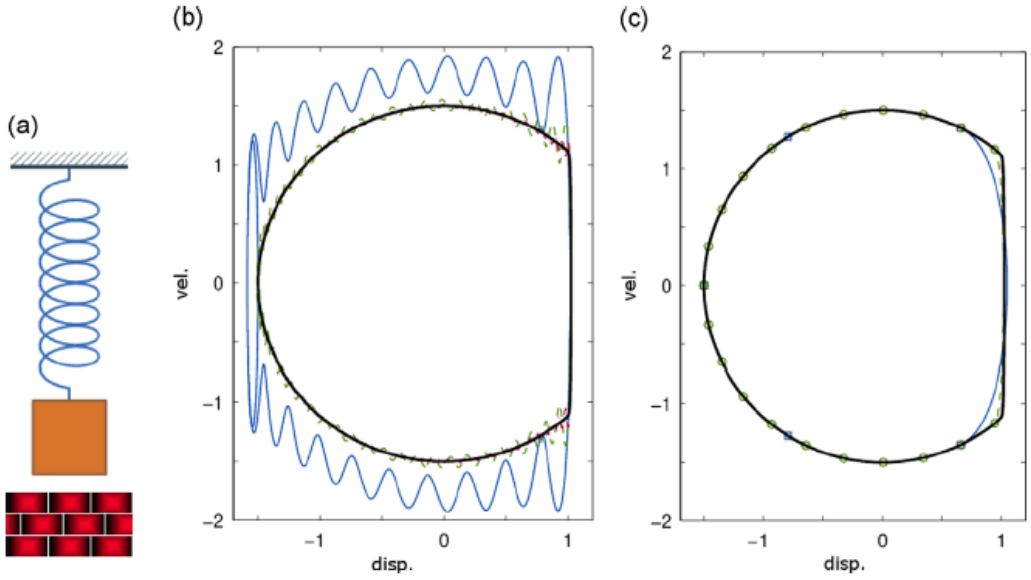

Figure 4.13. (a) Vibro-impact system; (b) phase diagram given by the HB method (blue: H=20; green: H=50, red: H=100; orange: H=200); (c) phase diagram given by orthogonal collocation (blue: $n_{\Delta t}$=16; green: $n_{\Delta t}$=64; red: $n_{\Delta t}$=202; orange: $n_{\Delta t}$=400).

4.3.2 Analysis with vibro-impact problem

In this section, the performance of the GPTI method for the impact problem is evaluated with a vibro-impact system. The clearance between a contact point of stiffness k_c and a system mass-

spring with mass m, spring stiffness k and damping c is d. The equation of motion of the forced system can be written as:

$$m\ddot{x} + c\dot{x} + kx + f_c = f\cos(\omega t) \tag{4.14}$$

with f_c denoting the regularized impact force, of the same expression as equation (4.2). The non-dimensional form of the equation of motion can be expressed as:

$$\tilde{\omega}^2\ddot{\tilde{x}} + 2\xi\tilde{\omega}\dot{\tilde{x}} + \tilde{x} + \frac{\widetilde{k_c}}{2}(\tilde{x} - 1) + \sqrt{[\frac{\widetilde{k_c}}{2}(\tilde{x} - 1)]^2 + \tilde{\varepsilon}} = \alpha\cos(\tau) \tag{4.15}$$

$$\begin{gathered}\tilde{\omega} = \omega/\omega_0\,, \tilde{x} = x/d, \tau = \omega t, \\ \omega_0 = \sqrt{k/m}\,, \xi = c/2\sqrt{mk}\,, \widetilde{k_c} = k_c/k,\ \tilde{\varepsilon} = \varepsilon/d^2k^2\,, \alpha = f/kd\end{gathered} \tag{4.16}$$

At equilibrium point ($\tilde{x} = 0$), the non-dimensional impact force is:

$$\widetilde{f_c} = \frac{\widetilde{k_c}}{2}\left[\left(1 + \frac{4\tilde{\varepsilon}}{\widetilde{k_c}^2}\right)^{\frac{1}{2}} - 1\right] \approx \frac{\tilde{\varepsilon}}{\widetilde{k_c}}$$

By fixing the damping ratio at 5%, the parameter study will be engaged with $\left(\widetilde{k_c}, \tilde{\varepsilon}, \tilde{\omega}, \alpha\right)$. The system is recast into quadratic form to facilitate the continuation. Choosing the excitation pulsation as the continuation parameter, the formulation with Newmark scheme can be written for $\forall n \in [\![1, \mathrm{N}_{sample}]\!]$ as:

$$\begin{cases} x_{n+1} = x_n + hv_n + \dfrac{h^2}{2}[(1-2\beta)a_n + 2\beta a_{n+1}] \\ v_{n+1} = v_n + h[(1-\gamma)a_n + \gamma a_{n+1}] \\ x_{\mathrm{N}_{sample}+1} = x_1, v_{\mathrm{N}_{sample}+1} = v_1 \\ \theta \cdot a_n = -2\xi\omega v_n - x_n - (w_n + r_n) + \alpha\cos[(n-1)h] \\ w_n = \dfrac{k_c}{2}(x_n - 1) \\ r_n^2 = w_n^2 + \varepsilon \\ r_n = z_n^2 \ \text{(to make sure that r is always positive)} \\ \theta = \omega^2 \end{cases} \tag{4.17}$$

Where $h = 2\pi/\mathrm{N}_{sample}$ is the time step. The first four lines are equations corresponding respectively to the time-integration scheme, the periodicity condition and the motion equilibrium. The rest equations are related to the auxiliary unknowns in order to recast the system into quadratic form required for the continuation calculation.

4.3.2.1 Effect of regularization parameter $\tilde{\varepsilon}$

The effect of regularization parameter is firstly studied by fixing $\widetilde{k_c} = 10$, $\alpha = 0.2$. The motional spectrum is obtained by taking different $\tilde{\varepsilon}$ (0.1, 0.05, 0.01, 5.10^{-3}, 10^{-3}, 5.10^{-4}). It is observed in Figure 4.14 that the smaller $\tilde{\varepsilon}$ is, the more evident is the turning point of the distorted resonance peak. However, it takes more steps of continuation in case of smaller $\tilde{\varepsilon}$, i.e. longer calculation time and when $\tilde{\varepsilon}$ becomes too small, the Gibbs phenomenon occurs around the resonance peak. By increasing the sample number, the Gibbs phenomenon can be eliminated, but it does not reduce the continuation steps, as shown in Figure 4.15. A moderate $\tilde{\varepsilon} = 0.005$ can be chosen to have a compromise between the efficiency and the accuracy.

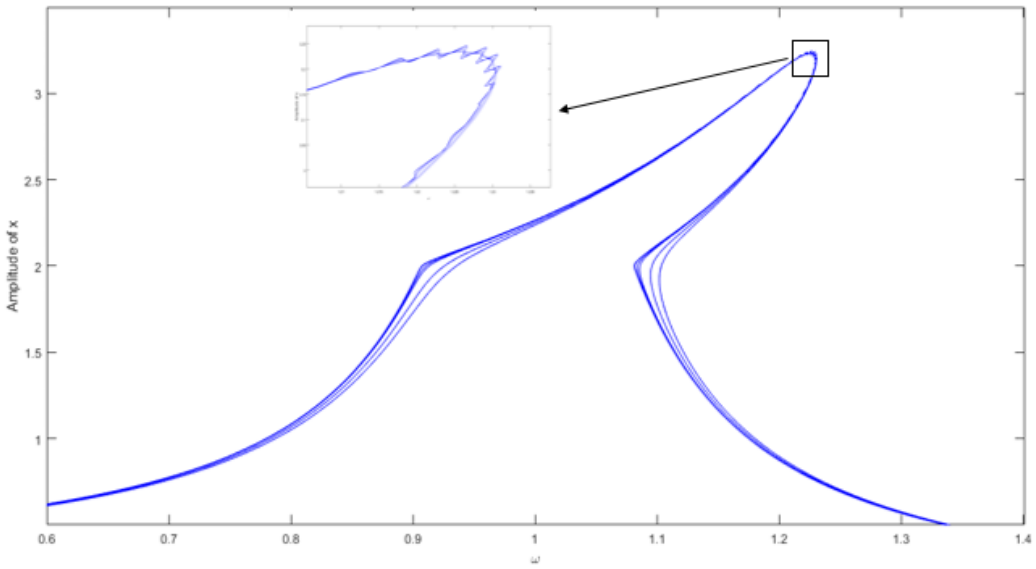

Figure 4.14. Motion spectrum of the oscillator with $\tilde{\varepsilon}$ = 0.1, 0.05, 0.01, 5.10^{-3}, 10^{-3}, 5.10^{-4}

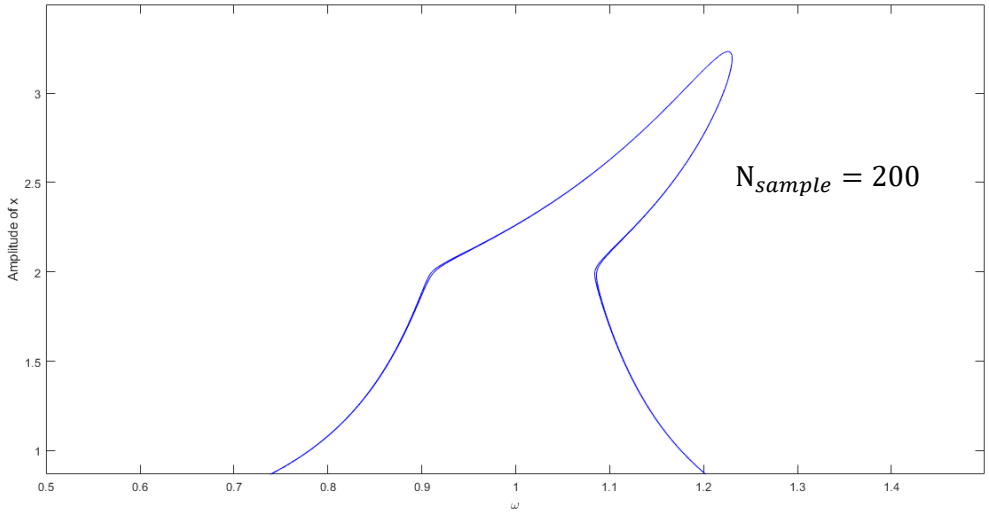

Figure 4.15. Motion spectrum of the oscillator with $\tilde{\varepsilon}$ = 5.10^{-3} by taking 200 time samples

4.3.2.2 Effect of contact stiffness ratio $\widetilde{k_c} = k_c/k$

Taking $N_{sample} = 200$ and $\alpha = 0.2$, $\tilde{\varepsilon} = 0.005$, computations have been performed with different $\widetilde{k_c}$ (5, 10, 20, 30, 50, 100). In order to obtain the motional spectrum in the same range of excitation pulsation, the numbers of continuation steps which determines the calculation time are as listed in Table 4.1. The resultant resonance peaks are as shown in Figure 4.16, the greater the contact stiffness is, the more is the resonance peak distorted. The Gibbs phenomenon is observed with a greater $\widetilde{k_c}$, a smaller time step is then necessary to get rid of it. For example, for the case with $\widetilde{k_c} = 50$, $N_{sample} = 400$ is enough to have the smooth curve. The number of continuation steps is also a little bit increased (from 1360 to 1500).

It is observed in Figure 4.17 that with $\widetilde{k_c}$ becoming more important, the curve of impact force time evolution becomes more and more pointed. Noting that the phase of temporal solution

changes along with the continuation (Figure 4.18), which means that the peak of the contact force moves on the axis τ step by step. The difficulty in continuation will occur in consequence since a small movement results in a sharp change on the value of the force at a certain instance, causing the difficulty of convergence during continuation. In the following, we are interested in the limit on $\widetilde{k_c}$ of this method.

Table 4.1. Continuation steps needed for difference contact stiffness to obtain the motional spectrum

$\widetilde{k_c}$	5	10	20	30	50	100
Continuation steps	320	550	820	1040	1360	2020

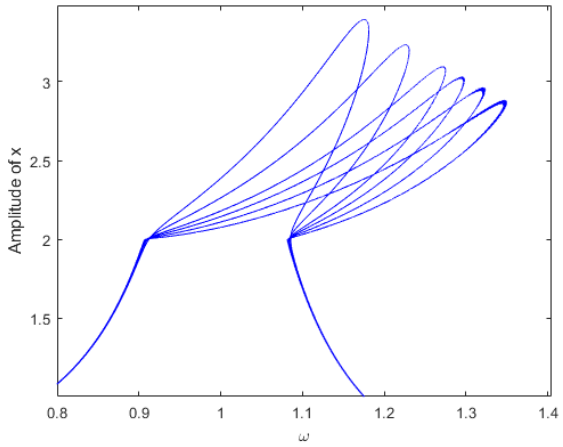

Figure 4.16. Resonance peak with difference contact stiffness $\widetilde{k_c}$ = 5, 10, 20, 30, 50, 100

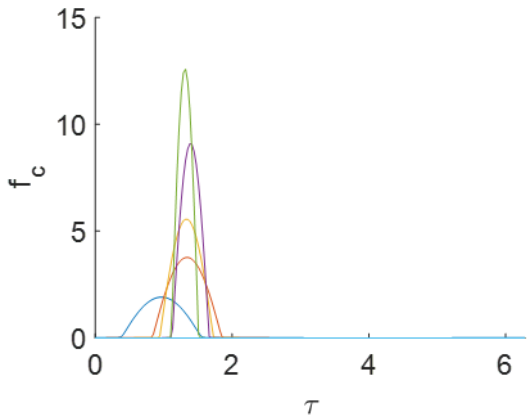

Figure 4.17. Time evolution of impact force with different contact stiffness $\widetilde{k_c}$ = 5, 10, 20, 30, 50, 100

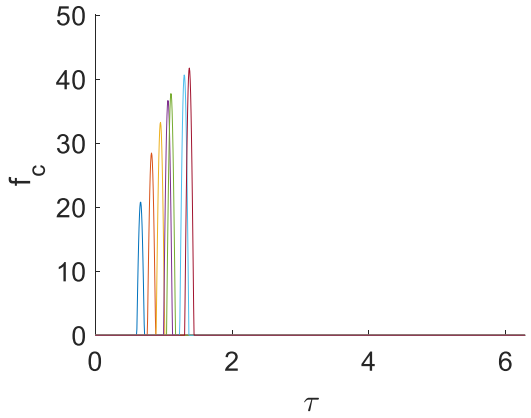

Figure 4.18. Phase of temporal evolution changes along with continuation steps

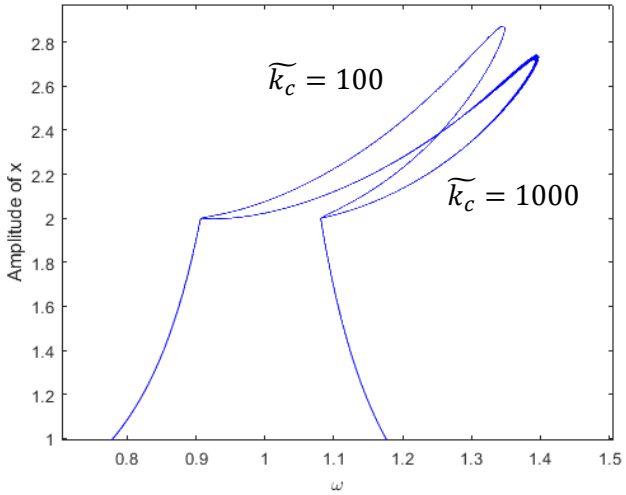

Figure 4.19. Resonance peak with contact stiffness $\widetilde{k_c}$ = 100 and 1000 by taking 500 time samples

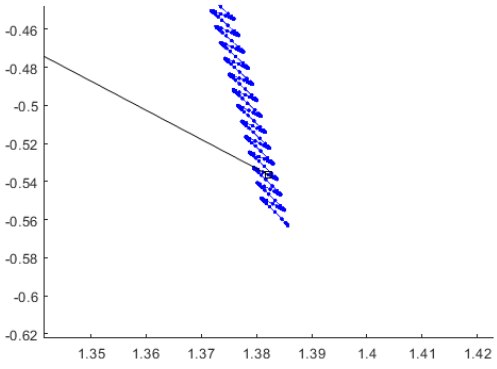

Figure 4.20. Difficulty in continuation for the case when $\widetilde{k_c}$ = 1000 and $N_{sample} = 1000$

In order to have the convergence easier, there is a need to refine the time discretization, i.e. to increase the sample number. However, it is observed that a great sample number results in the necessity of increasing the error tolerance. What's more, it may lead to the difficulty in continuation. Taking the case when $\widetilde{k_c} = 1000$ and $\alpha = 0.2$, we can obtain the spectrum by

taking $N_{sample} = 500$ (see Figure 4.19), while with $N_{sample} = 1000$ the continuation can go no longer further (Figure 4.20). Therefore, the choice of N_{sample} should be carefully made and $\widetilde{k_c} = 1000$ is considered as the limit.

Better performance with an adaptive time stepping

In fact, it is only when the contact happens that we need to refine the time discretization. The formulation with variable time steps is as shown in equation (4.17). By defining a tanh law of variable time steps, as shown in Figure 4.21 for example, when the vibrator comes into contact, the time step is inferior to 0.2 while when the contact does not happen the time step is around 5 times its value. With this law, we arrive at decreasing the sample number so that the need on computation time is decreased (for example, with $N_{sample} = 100$, 720 continuation steps are enough to obtain a curve without the Gibbs phenomenon for $\widetilde{k_c} = 100$). With the variable time steps, the limit on $\widetilde{k_c}$ increases to 5000. When we attempted with the time discretization law allowing to have a greater ratio of time step between the cases without and with contact, which means a sharper slope k_1 of eq. (4.18), difficulty in convergence is observed, more works of optimization should be done in the future.

$$\begin{cases} x_{n+1} = x_n + h_n v_n + \frac{p_n}{2}[(1-2\beta)a_n + 2\beta a_{n+1}] \\ v_{n+1} = v_n + h_n[(1-\gamma)a_n + \gamma a_{n+1}] \\ \theta * a_n = -2\xi\omega v_n - x_n - (w_n + r_n) + \alpha\cos(tau_n) \\ w_n = \frac{k_c}{2}(x_n - 1) \\ r_n^2 = w_n^2 + \varepsilon \\ r_n = z_n^2 \\ \theta = \omega^2 \\ h_n = h_{max}\left(\frac{1}{\pi}c_1 + 0.5\right) \\ c_1 = \tanh(c_2) \\ c_2 = k_1(1-x) + b_1 \\ tau = cumsum(h) \\ tau(N_{sample} + 1) = 2\pi \end{cases} \tag{4.18}$$

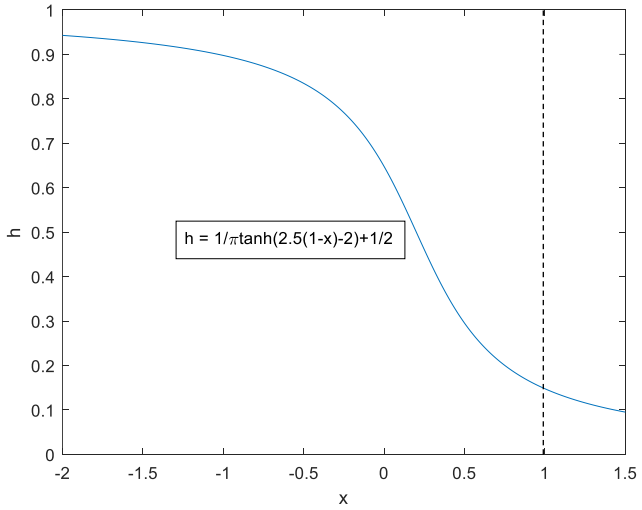

Figure 4.21. tanh law of variable time discretization

4.3.2.3 Effect of excitation amplitude α

The effect of excitation amplitude on the dynamics behavior is studied by fixing $N_{sample} = 200$ and $\tilde{\varepsilon} = 0.005$.

Firstly, the study is carried out with a contact not that rigid, where $\widetilde{k_c} = 10$. The value of α varies (0.2, 0.4, 0.6, 0.8, 0.87). When α is superior to 0.88, the nonlinearity is already not negligible at the equilibrium position of the pseudo-stationary system. In order to avoid the difficulty in initialization, the algorithm for continuation with α should be performed and the solution points are taken as the starting point of the continuation with excitation pulsation. The greater the excitation amplitude is, more continuation steps are necessary to obtain the motional spectrum.

According to Figure 4.22, Figure 4.23 and Figure 4.24, five dynamic behaviors are observed: 1) linear dynamic behavior; 2) one oscillation with one contact during the period, corresponding to the deformed resonance peak and the transition between the behaviors numbered 5 and 3; 3) two oscillations with one contact during the period, corresponding to the transition between the behaviors numbered 2 and 4; 4) two oscillations with two contacts during the period, corresponding to the second peak of the motion spectrum; 5) three oscillations with one contact corresponding to the third peak. The contacts are observed in these figures by the sharp variation of the velocity when the points of the lines are scattered.

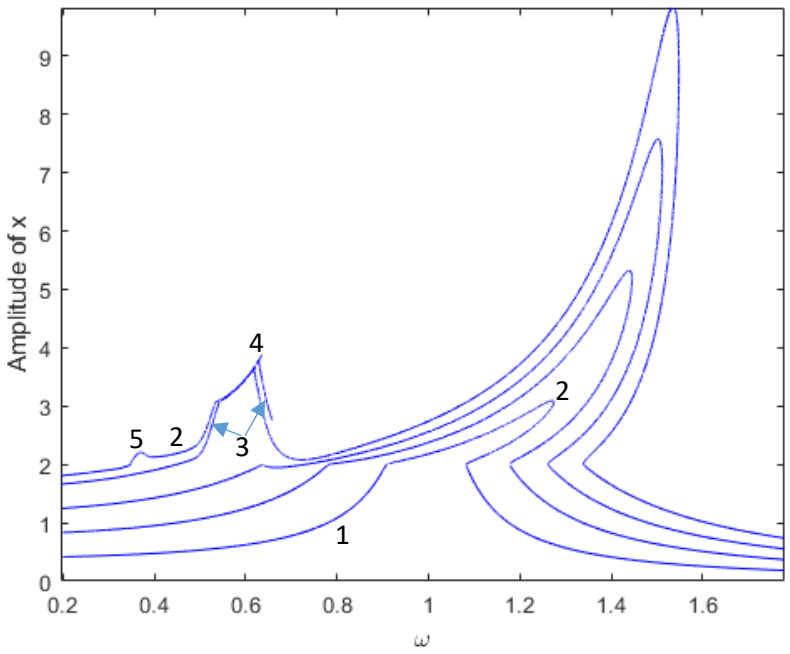

Figure 4.22. Motion spectra with different excitation amplitudes with $\widetilde{k_c} = 10$

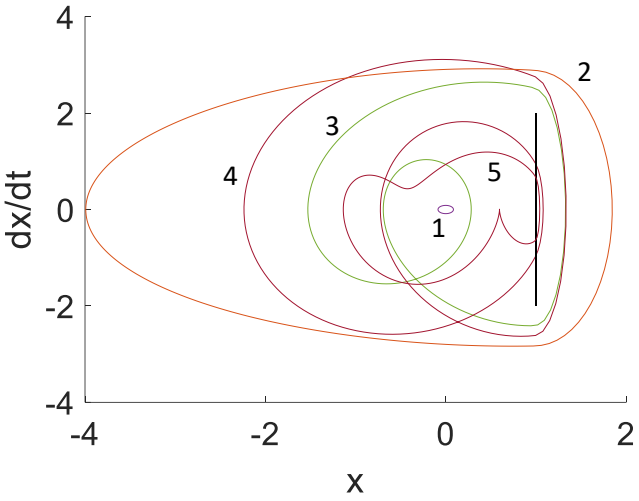

Figure 4.23. Phase diagram corresponding to different regimes

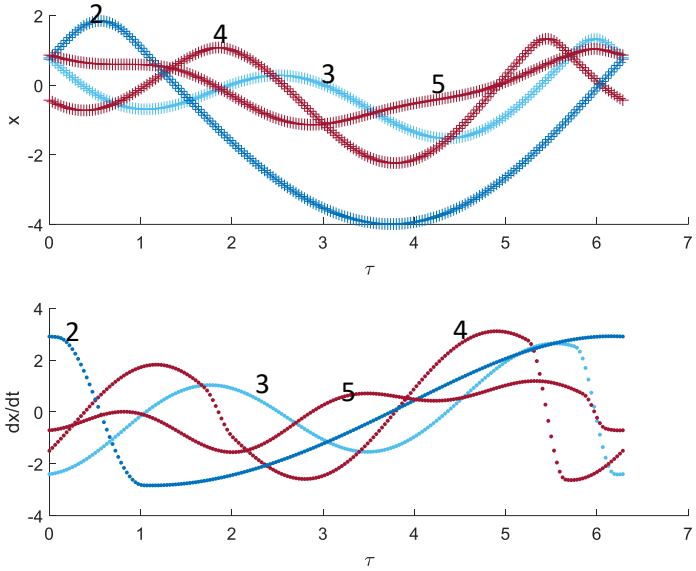

Figure 4.24. Time evolution of displacement and velocity corresponding to different regimes

The study with a quite rigid contact point is in the following presented. Taking $\widetilde{\omega} = 0.2$ for the case $\widetilde{k_c} = 100$, the result of continuation with the excitation amplitude α is as shown in Figure 4.25. At first, no contact happens so the amplitude is proportional to α. The curve becomes flat when the first contact happens (point (a)) and several oscillations during one period are observed. Then the rebound near the contact becomes more important, the second contact occurs (point (b)) and the curve rises again. New rebound arises after the second contact when α becomes greater. With this new rebound becoming more and more important, the third contact happens (point (c)), the curve goes down and then rises. The occurrence of the forth (point (d)) and fifth contact (point (e)) is of the same procedure as that of the third contact, and the separation between the contacts becomes shorter and shorter, resulting in the sticking contact with chatters. Furthermore, when more and more contacts happen, the continuation becomes more and more difficult, the Gibbs phenomenon of the continuation curve becomes more and more evident.

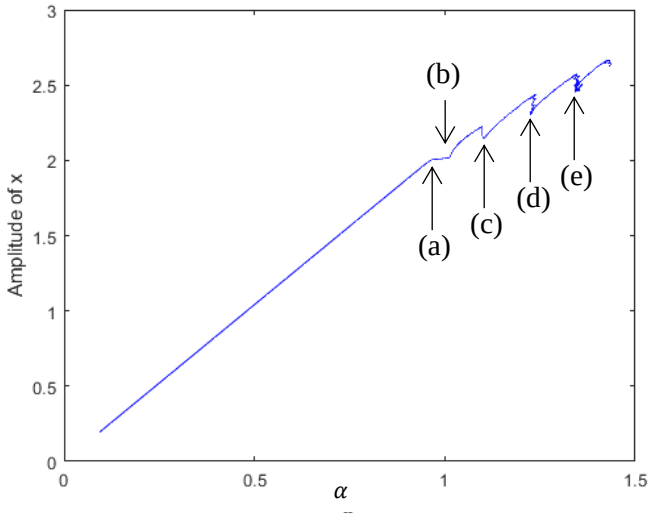

Figure 4.25. Evolution of displacement amplitude with respect to the excitation amplitude for $\widetilde{k_c} = 100$

It allows us to calculate the motion spectrum with a greater excitation by taking the result of continuation with α as the starting point of continuation with $\tilde{\omega}$. The result is as shown in Figure 4.26. The first two curves ($\alpha = 0.8$ and $\alpha = 0.9$) are of the same shape as the case when $\widetilde{k_c} = 10$, the corresponding dynamic behaviors are also the same.

$\alpha = 1$ is the critical condition for the happening of the first contact when the system is pseudo-stationary, i.e. $\tilde{\omega}$ is very small. For $\tilde{\omega}$ inferior to 0.3, the oscillator performs as one contact happens with several oscillations during one period. The smaller $\tilde{\omega}$ is, the longer is the period and therefore, more oscillations induced by the impact can be observed (Figure 4.27(a)). The peak around $\tilde{\omega} = 0.4$ of the motion spectrum shown in Figure 4.26(a) corresponds to two contacts with three oscillations during one period. The transition between this regime and the dynamic behavior with higher $\tilde{\omega}$ is presented as one contact with three oscillations during one period (Figure 4.27(b)). For $\tilde{\omega}$ superior to 0.5, its dynamic behaviors are the same as the preceding cases with smaller α.

When α is greater than 1, it is easy to imagine that the contact is sticking with chatters when the system is pseudo stationary. For example, by taking $\alpha = 1.1$, at very small $\tilde{\omega}$, the temporal displacement of the oscillator is as shown in Figure 4.28. Between $\tilde{\omega} = 0.2$ and 0.33, two contacts happen with several impact-induced waves during one period (Figure 4.29 (a)). The transition between the peak of the motion spectrum at $\tilde{\omega} = 0.33$ and the peak afterwards shown in Figure 4.26 (a) is of the pattern where two contacts with two oscillations are observed during one period (Figure 4.27 (b)). Similar to the case when $\alpha = 1$, the dynamic behavior of two contacts with three oscillations corresponds to the transition between the deformed peak around $\tilde{\omega} = 0.4$ and the small peak around $\tilde{\omega} = 0.5$, after which the oscillation pattern is of no difference from the other curves.

With α =1.2 (see Figure 4.26 (b)), the dynamic response to $\tilde{\omega}$ between 0.33 and 0.46 is similar as that of the case with $\alpha = 1$ and $\tilde{\omega}$ = 0.4 - 0.5, where two contacts are observed with three oscillations. The peak at $\tilde{\omega} = 0.26$ of the motion spectrum is the separating point between the

pattern of three contacts and two contacts. As is always the case, for the transition between $\tilde{\omega} = 0.26$ and 0.33, the greater $\tilde{\omega}$ is, the impact-induced oscillations are observed during one period.

The motion spectrum for α =1.3 is of similar shape as that of α =1.2, except that the peak around $\tilde{\omega} = 0.46$ corresponds to the pattern of two contacts with three oscillations while for $\tilde{\omega}$ from 0.32 to 0.45 four oscillations are observed. The peak at $\tilde{\omega} = 0.3$ corresponds to the occurrence of the third contact and more chatters around the contact point are observed with $\tilde{\omega}$ getting smaller. The peak at $\tilde{\omega} = 0.23$ is the separating point between the pattern with three and four contacts. The interpretation of the curve corresponding to α =1.4 is almost the same except that there is another peak at $\tilde{\omega} = 0.22$ which separates the pattern with four and five successive contacts.

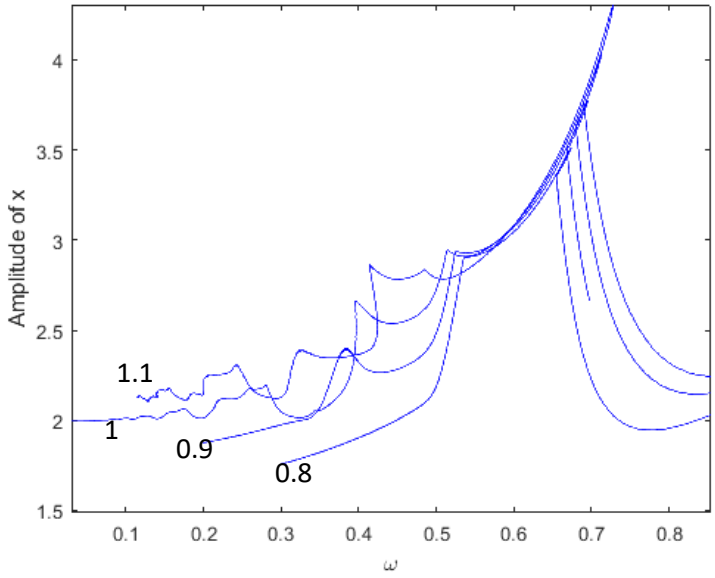

(a) Motion spectra for $\alpha = 0.8, 0.9, 1$ and 1.1

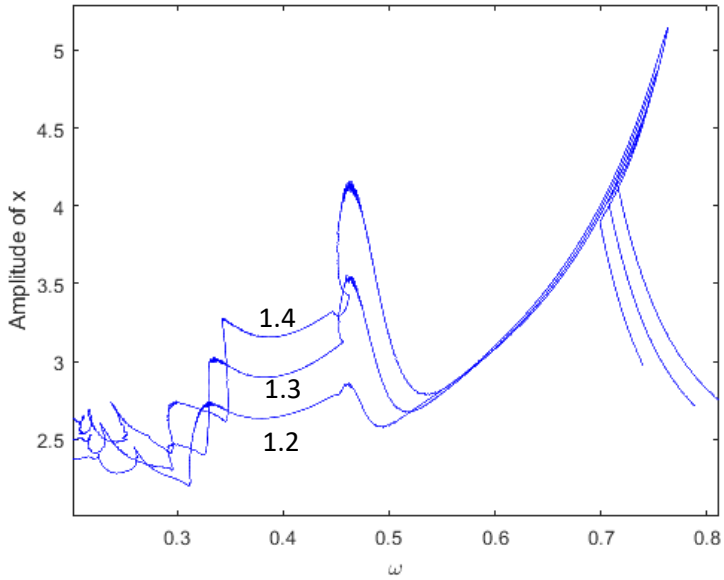

(b) Motion spectra for $\alpha = 1.2, 1.3$ and 1.4

Figure 4.26. Motion spectra for $\widetilde{k_c} = 100$ with different external forces

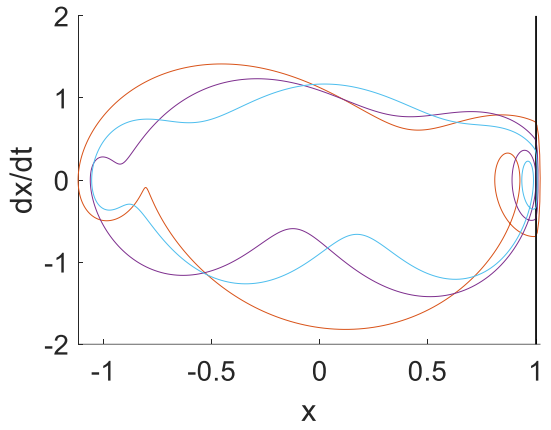

(a) Less oscillations during one period with increasing $\tilde{\omega}$

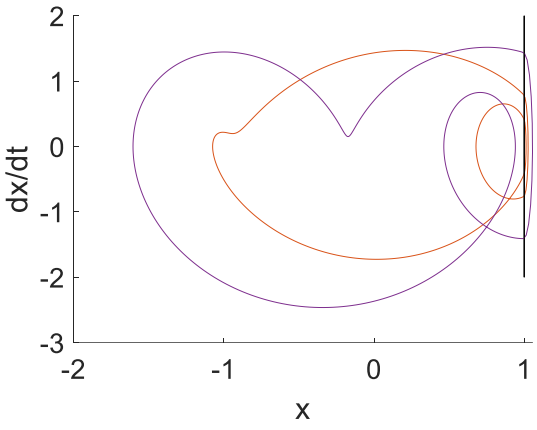

(b) Transition between the patterns from $\tilde{\omega} = 0.4$ to 0.5

Figure 4.27. Phase diagram with $\alpha = 1$

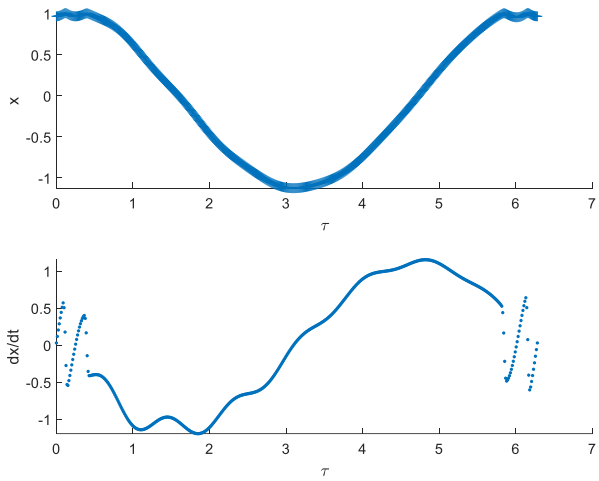

Figure 4.28. Sticking contact of pseudo stationary system

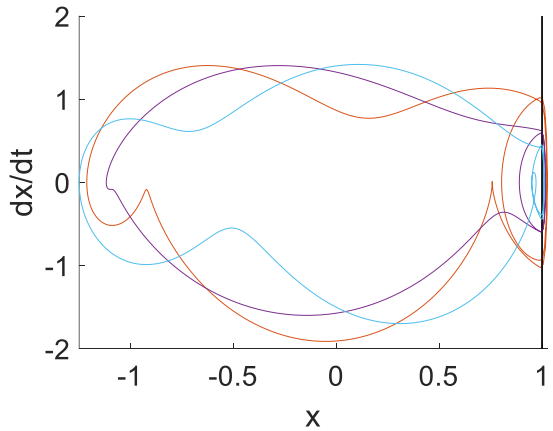

(a) Less oscillations during one period with increasing $\tilde{\omega}$ (from 0.2 to 0.33)

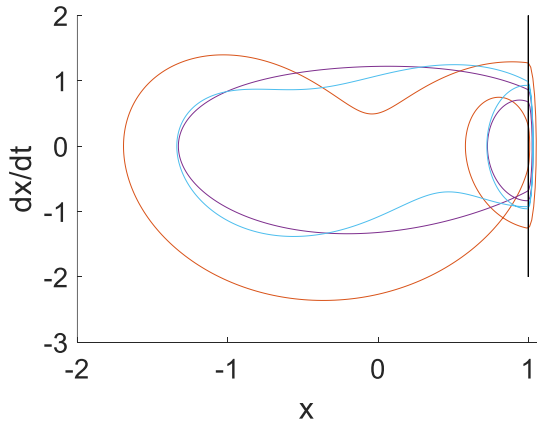

(b) Transition between the patterns from $\tilde{\omega} = 0.33$ to 0.4

Figure 4.29. Phase diagram for $\alpha = 1.1$

4.3.3 Summary

In this section, the performance of the GPTI method is evaluated with the dimensionless vibro-impact system. It can be concluded that this method has the potential to be used for the very rigid contact problems with a temporal discretization well defined. The difficulty in continuation is mainly due to the change of phase, which result in the sharp variation of the impact force. The excitation amplitude is therefore limited due to the occurrence of the "sticking" contacts with chatters, where successive peaks of impact force challenge the numeric convergence.

4.4 Application to the fuel pin

Hereafter, the GPTI method is applied to study the dynamic response of a beam with several contact points under excitation. Similarly as in 4.2.2, there are contact points alternatively at left and right side of the beam, the formulation with Newmark scheme of the vibro-impact problem (4.17) is then modified into:

$$\begin{cases} X_{n+1} = X_n + hV_n + \dfrac{h^2}{2}[(1-2\beta)A_n + 2\beta A_{n+1}] \\ V_{n+1} = V_n + h[(1-\gamma)A_n + \gamma A_{n+1}] \\ X_{\mathrm{N}_{sample}+1} = X_1, V_{\mathrm{N}_{sample}+1} = V_1 \\ \theta \cdot MA_n = -\omega CV_n - KX_n - F_{c,n} + F_e \cos[(n-1)h]\, Q \\ \boldsymbol{F_{c,n}}\left(2c_i|_{i\in[\![1,nc]\!]} - 1\right) = w_n(i) + r_n(i) \quad if\ i\ is\ pair \\ \boldsymbol{F_{c,n}}\left(2c_i|_{i\in[\![1,nc]\!]} - 1\right) = w_n(i) - r_n(i) \quad if\ i\ is\ odd \\ w_n(i) = \dfrac{k_c}{2}\left(X_n\left(2c_i|_{i\in[\![1,nc]\!]} - 1\right) - d\right) \quad if\ i\ is\ pair \\ w_n(i) = \dfrac{k_c}{2}\left(X_n\left(2c_i|_{i\in[\![1,nc]\!]} - 1\right) + d\right) \quad if\ i\ is\ odd \\ r_n^2 = w_n^2 + \varepsilon \\ r_n = z_n^2 \ \text{(to make sure that r is always positive)} \\ \theta = \omega^2 \end{cases} \tag{4.18}$$

Continuation with excitation amplitude has been performed with the representative values of fuel pin ($k_c = 2.46 \times 10^6\ N/m$ and $d = 0.1\ mm$). As can be observed in Figure 4.30, the very small continuation step occurs when α reaches the nonlinear level due to the great value of k_c and the continuation can go no longer further shortly after the first contact happens.

4.4.1 Performance evaluation with less rigid contact points

In order to avoid the difficulty of continuation and to enlarge the study region, a contact stiffness of 3000 N/m is chosen to evaluate the performance of this method, which is not representative of the case of a fuel pin but already enough rigid and a clearance set to be 1 mm. Figure 4.31 presents the motion spectrum of the free end at a relatively high excitation amplitude $a_{ext} = 1.54\ m/s^2$ obtained with one period discretized into 201 time intervals (an odd number of intervals is chosen to avoid the singularity of matrix when performing the Jacobian calculation with *Manlab*). A large number of continuation steps is necessary to obtain the curve (289 continuation steps), which challenges the computation time.

The curve not smooth is verified by arbitrarily choosing the points on this solution branch and comparing the corresponding periodic responses with the results obtained from the direct time-

integration method using the same time interval. Examples are as shown in Figure 4.32 and Figure 4.33, the time evolution of the displacement, the velocity and the impact forces are taken for the comparison and perfect agreement can be observed. Specially, it can be figured out in Figure 4.31 that there exists three periodic solutions with the value of ω taken between 8.71 and 8.93, among which two can be reproduced with direct time-integration by taking different initial conditions and an instable one only identified with the global periodic method. Observing the periodic solutions on the rough plateau of the solution branch of ω between 7.5 and 8.93 (see Figure 4.34), the maximum and minimum displacements of successive solution points are not obtained at the same instance due to the phase variation so that they can fall into the time interval, thus not presented on the curve. The fluctuations of the continuation curve are therefore not caused by the physical phenomenon, but result from the time discretization: the more fine is the discretization during the contact, the less obvious are the fluctuations.

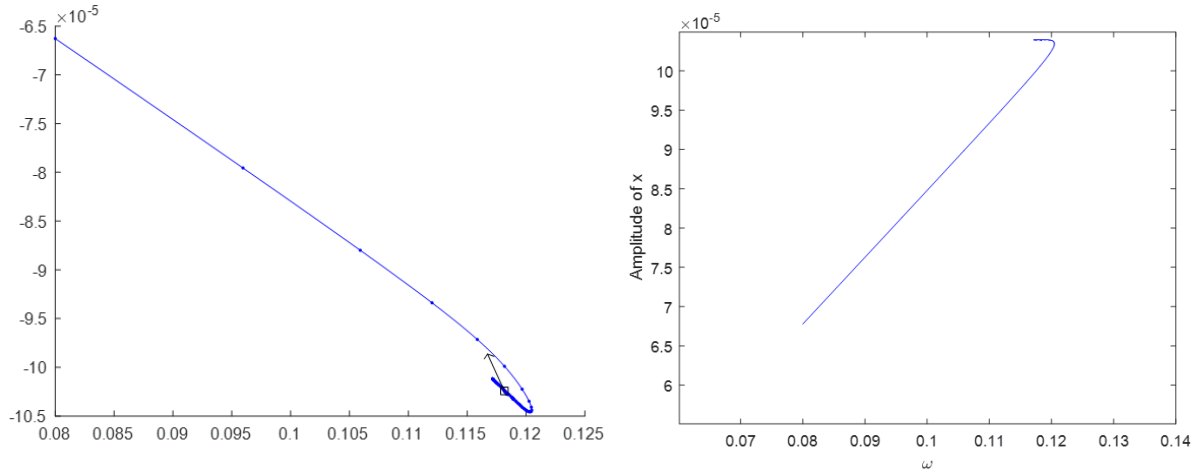

Figure 4.30. Continuation curve with step points and evolution of displacement amplitude at free end with the excitation amplitude for the excitation frequency fixed at 3 Hz

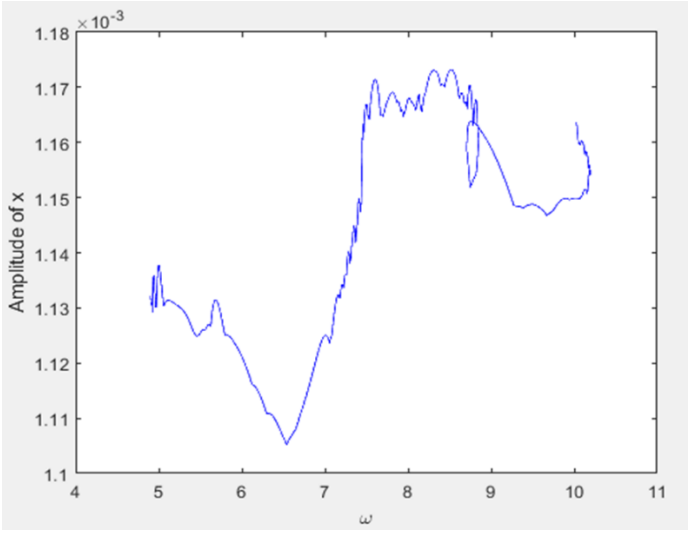

Figure 4.31. Motion spectrum of the displacement at free end with $a_{ext} = 1.54\ m/s^2$

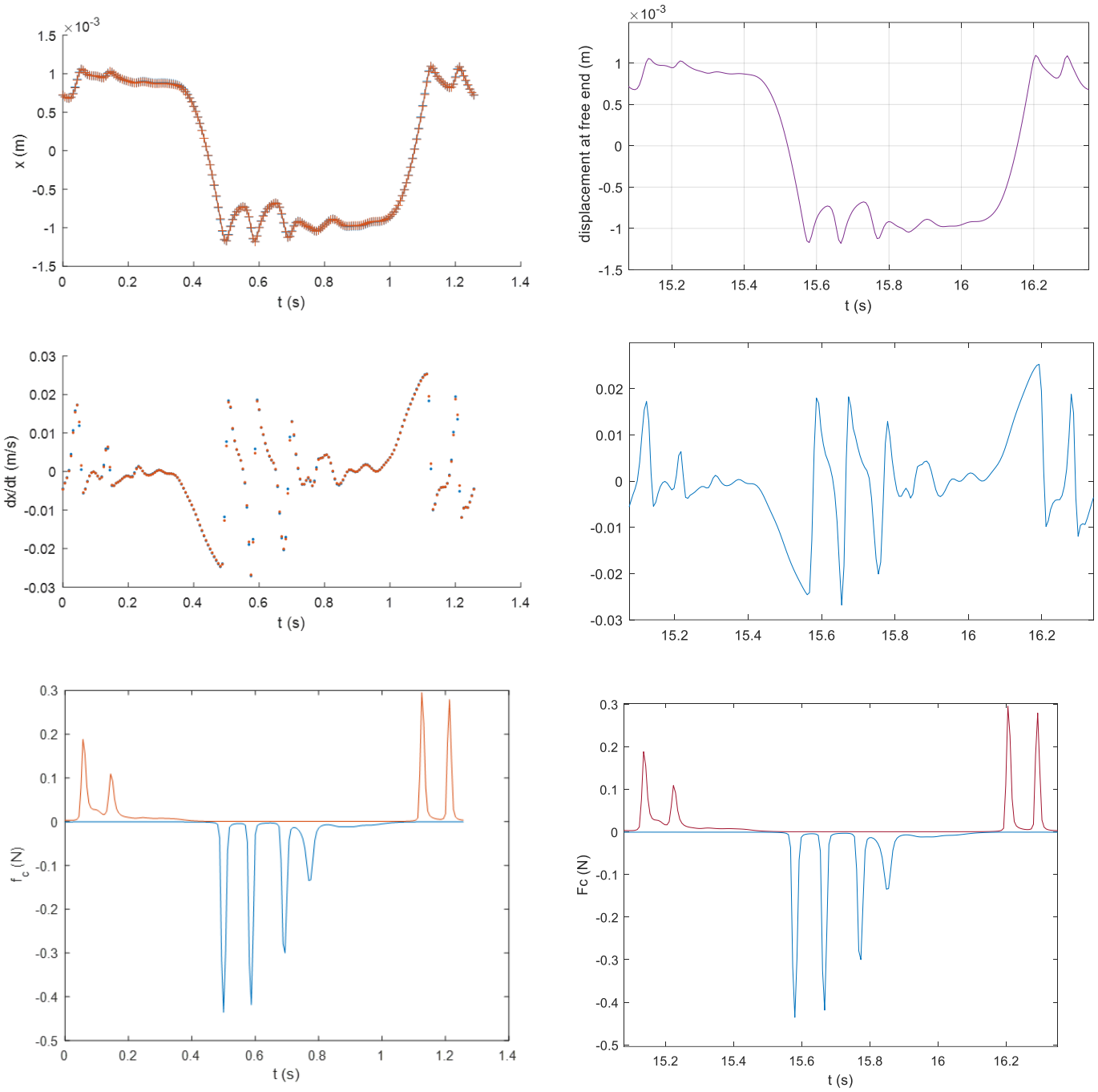

Figure 4.32. Time responses in one period of the displacement and velocity at free end and the impact forces at the first two contact points (counting from the free end) to an excitation of $a_{ext} = 1.54\, m/s^2$ and $\omega = 5\, rad/s$ obtained with the global periodic method (left column) and the direct time-integration method (right column).

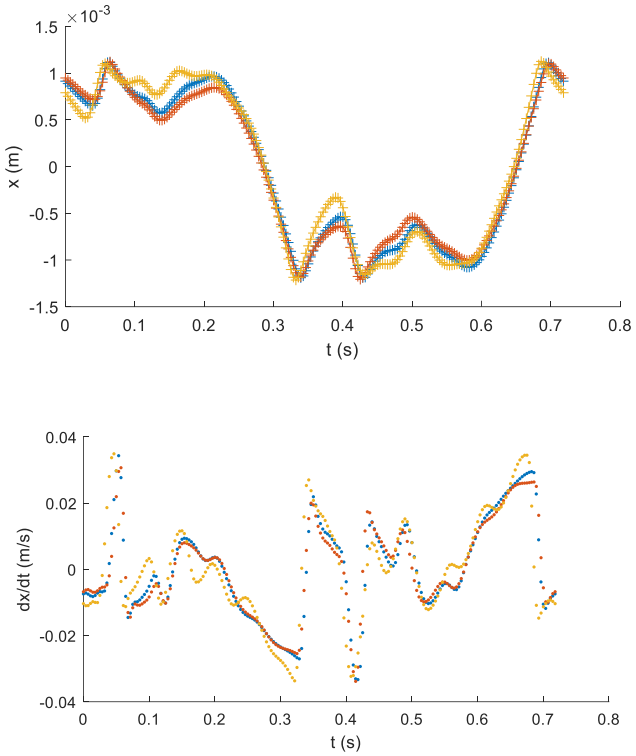
×10^-3
x (m)
t (s)
dx/dt (m/s)
t (s)

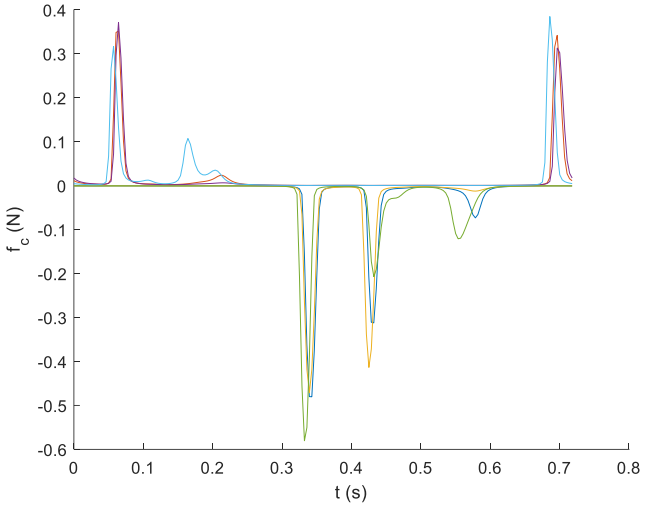
f_c (N)
t (s)

a)

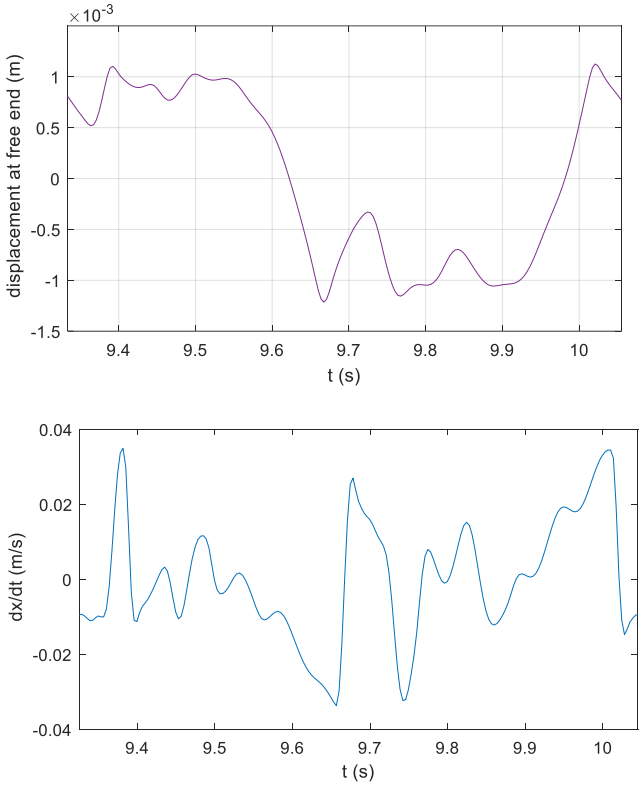
×10^-3
displacement at free end (m)
t (s)
dx/dt (m/s)
t (s)

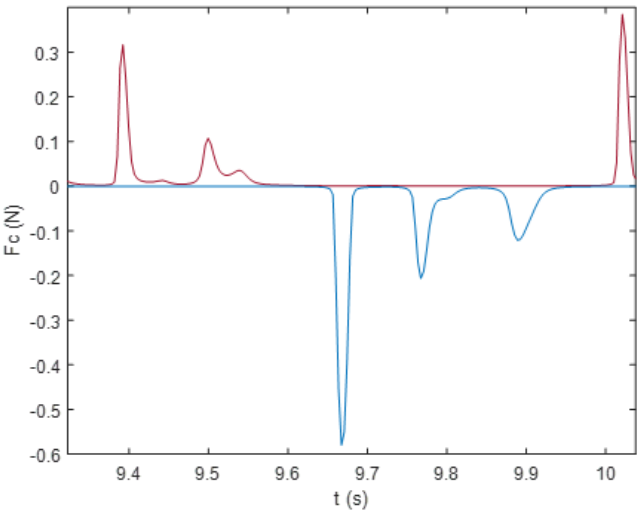
Fc (N)
t (s)

b)

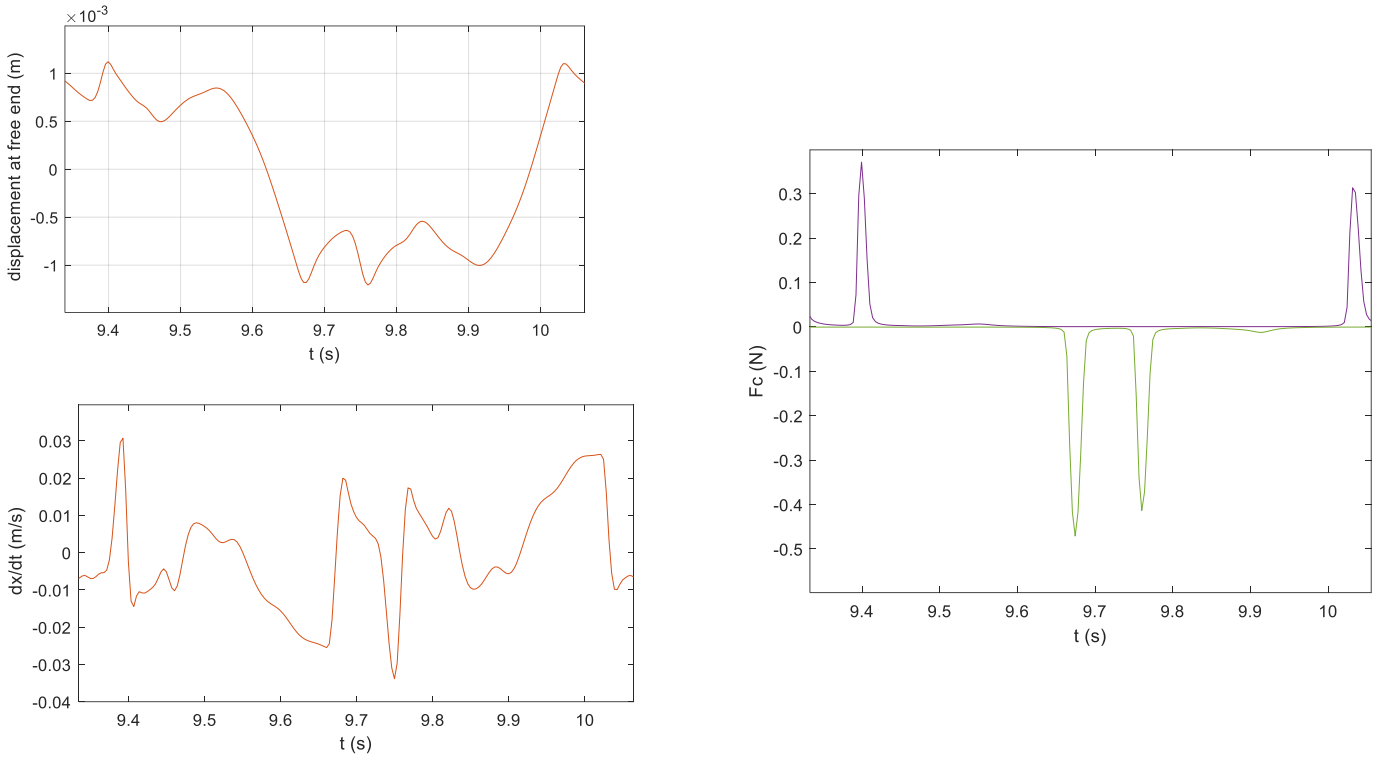

c)

Figure 4.33. Time evolution in one period of the displacement and velocity at free end and the impact forces at the first two contact points (counting from the free end) to an excitation of $a_{ext} = 1.54\ m/s^2$ and $\omega = 8.75\ rad/s$: a) two stable and one instable responses obtained with the global periodic method; b) and c) stable responses obtained with the direct time-integration method using different initial conditions

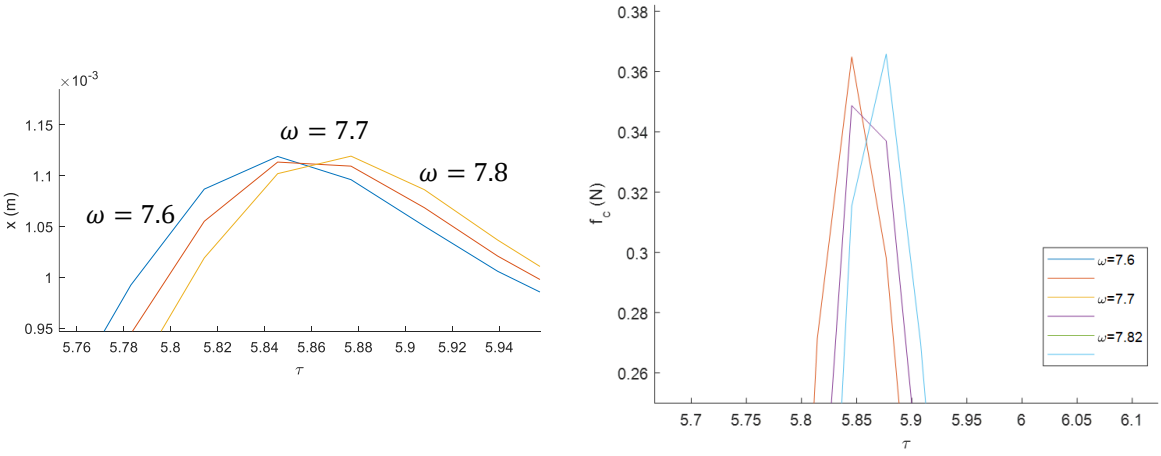

Figure 4.34. Fluctuating displacement amplitude due to rough time discretization

4.4.2 Effect of the contact damper

As noted in the previous section, even with a smaller contact stiffness, the computation is quite demanding in time as a large number of continuation steps is necessary to obtain the motion spectrum. The short arc-length of the continuation is mainly due to the successive impact forces caused by the local chatters and the phase variation along with the continuation. A contact

damper is therefore introduced to calm these chatters. A simple impact law [136], of which the damping coefficient is proportional to the penetration into the contact point, is expressed as:

$$\forall i \in [\![1, nc]\!], F_c(w_{c_i}, \dot{w}_{ci}) = \begin{cases} (k_c(w_{c_i} - d) + c_c\dot{w}_{ci})H(w_{c_i} - d) if\ i\ is\ pair \\ (k_c(w_{c_i} + d) + c_c\dot{w}_{ci})H(-w_{c_i} - d) if\ i\ is\ odd \end{cases}$$
$$c_c = \begin{cases} \eta(w_{c_i} - d) \quad if\ i\ is\ pair \\ -\eta(w_{c_i} - d)\ if\ i\ is\ odd \end{cases} \tag{4.19}$$
$$\eta = \frac{3k_c(1-e)}{2e\dot{w}_{ci,0}}$$

where $w_{c_i} = w(x_{ci})$, $\dot{w}_{ci} = \dot{w}(x_{ci})$ with $\boldsymbol{x_c} = \{x_{c1}, x_{c2}, \cdots, x_{c_{nc}}\}$ the coordinates of the contact points, $H(\cdot)$ is the Heaviside function, $\dot{w}_{ci,0}$ denotes the velocity at the time immediately before impact and e represents the coefficient of restitution. This law can be regularized into:

$$\forall i \in [\![1, nc]\!], F_c(x_{ci})$$
$$= \begin{cases} (k_c + \eta\dot{w}_{ci})\left\{\frac{1}{2}(w_{c_i} - d) + \sqrt{\left[\frac{1}{2}(w_{c_i} - d)\right]^2 + \varepsilon}\right\} if\ i\ is\ pair \\ -(k_c - \eta\dot{w}_{ci})\left\{-\frac{1}{2}(w_{c_i} + d) + \sqrt{\left[\frac{1}{2}(w_{c_i} + d)\right]^2 + \varepsilon}\right\} if\ i\ is\ odd \end{cases} \tag{4.20}$$

The damping coefficient related with the kinetic energy dissipation during the contact can only be determined with the experiments since it depends much on the path of the contact phase. Due to the lack of the experiments, we refer to some previous works, even if not representative, to have an idea of the order of magnitude. Pelloux [92] identified a restitution coefficient of 0.55 in water with his experiments by considering the truncated SUPERPHENIX fuel pin as a Newton's pendulum (see Section 2.1.1). Combining with the computation results in the previous section, which shows that the prior-impact velocity is of the order of 0.01 m/s, the damping coefficient η is of the order of $10k_c$. By supposing $w_c = 1.2 \times 10^{-3}\sin(5t)$ and $\eta = 30k_c$, the non-smooth impact law (4.19) and the regularized impact law (4.20) are as shown in Figure 4.35.

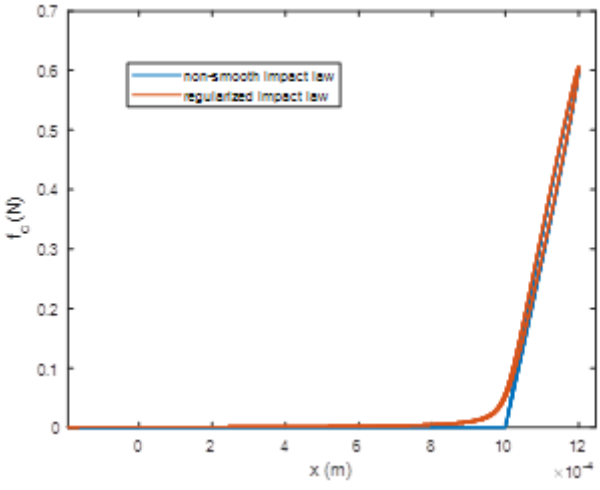

Figure 4.35. Non-smooth and regularized impact law with a contact damper

Figure 4.36 shows the effect of the contact damper on the local chatters and the global vibration by taking different values of η ($30k_c$, $60k_c$, $100k_c$). It is observed that the contact damper does not much influence the global behavior except that the phase is a little bit shifted. As for the local chatters, the effect on the first penetration is not as evident as that on the following vibrations. The impact force peaks, especially those after the first one, become less pointed, which can result in an easier continuation.

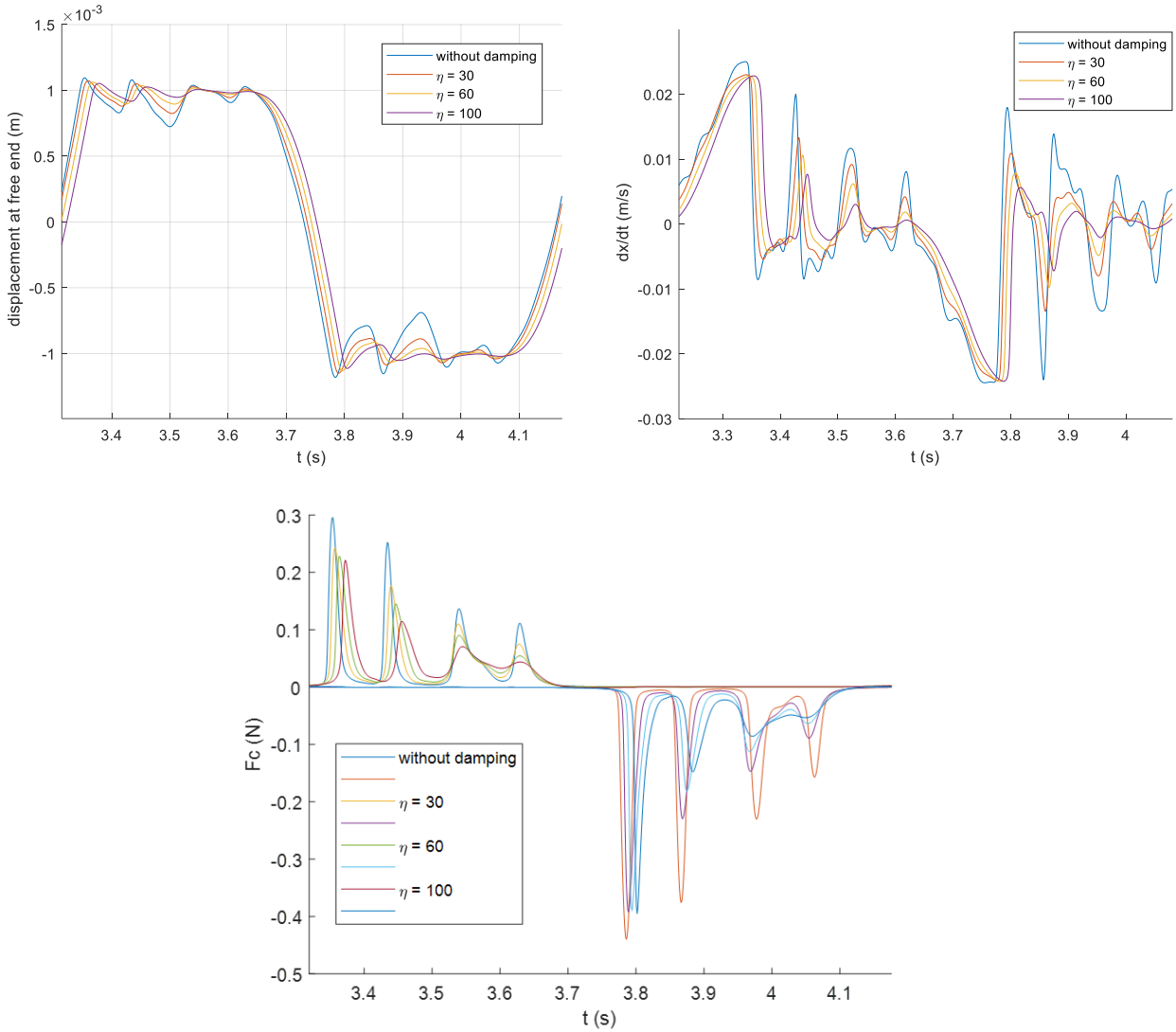

Figure 4.36. Time evolution in one period of the displacement and velocity at free end and the impact forces at the first two contact points (counting from the free end) to an excitation of $a_{ext} = 1.54\, m/s^2$ and $\omega = 7.3\, rad/s$

Taking $\eta = 60k_c$, a continuation with the same parameters as that of Figure 4.31 is carried out. There is a need of less continuation steps (100 continuation steps in place of 289 steps) to obtain the motion spectrum presented in Figure 4.37. The solution branches with and without contact damper are of similar form except that the plateau disappears and no increase is observed at $\omega = 10$. By comparing the periodic responses (see Figure 4.38 and Figure 4.39), the difference does not come from the global behavior but rather from the second chatter at the left contact point (negative displacement and negative impact force), which are of the same order of magnitude as the first chatter when there is no contact damper. Besides, it is noted that the phenomenon of two stable periodic solutions at $\omega = 8.71 - 8.93$ disappears. It is not

surprising as we can see in Figure 4.33 that the difference of the different periodic solutions lies in the local chatters after the first penetration into the contact, which are almost totally damped in this case. Again the fluctuations of the motion spectrum are caused by the phase variation and the time discretization, as has been explained in the previous section.

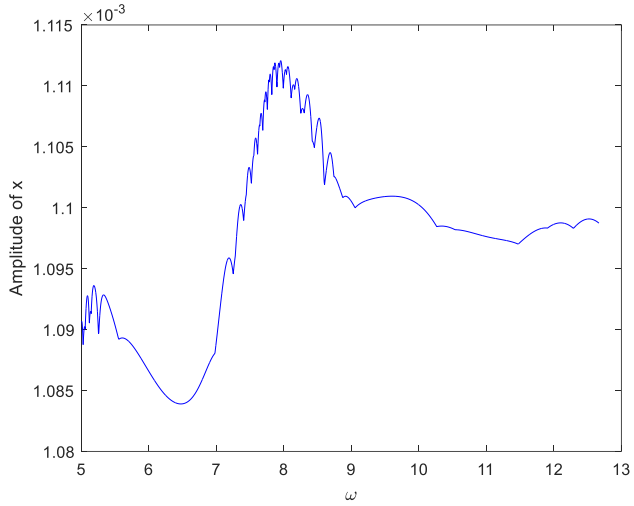

Figure 4.37. Motion spectrum of the displacement at free end with $a_{ext} = 1.54\ m/s^2$ and the damping coefficient $\eta = 60k_c$

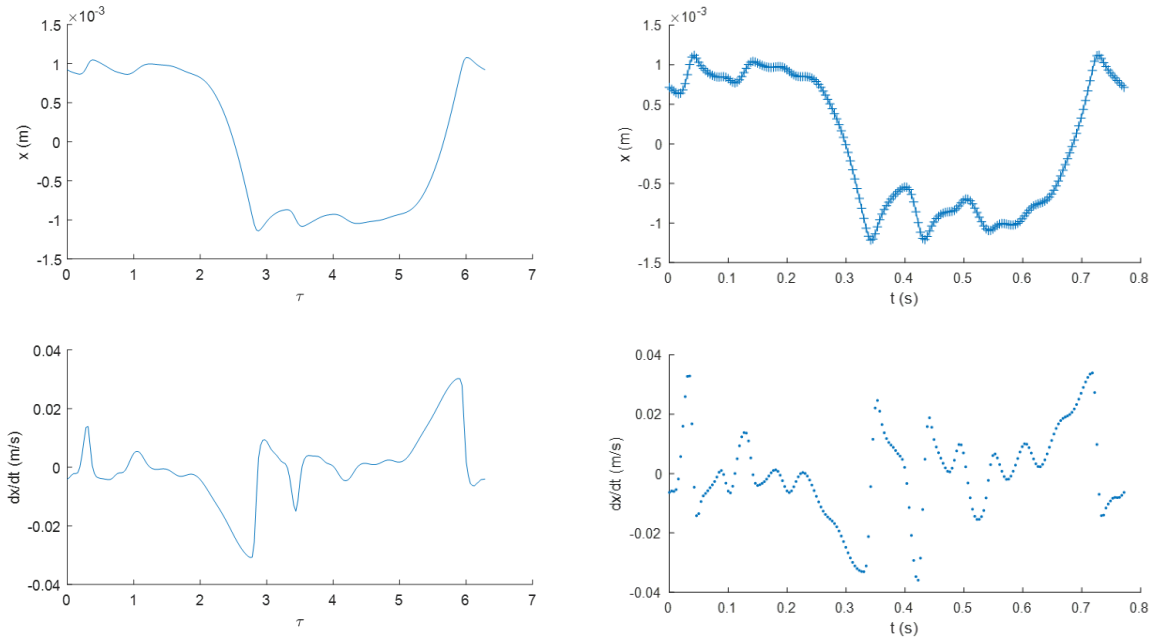

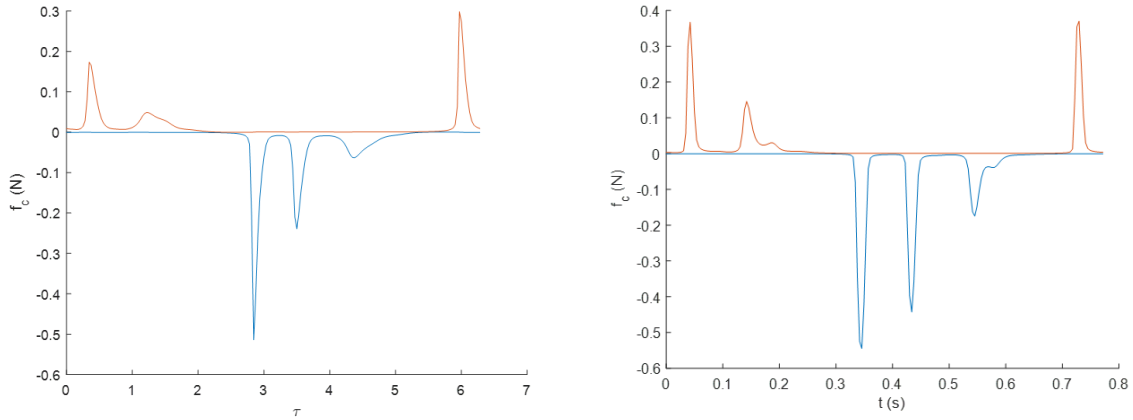

Figure 4.38. Periodic responses with (left column) and without (right column) contact damper at $a_{ext} = 1.54\ m/s^2$ and $\omega = 7.15\ rad/s$

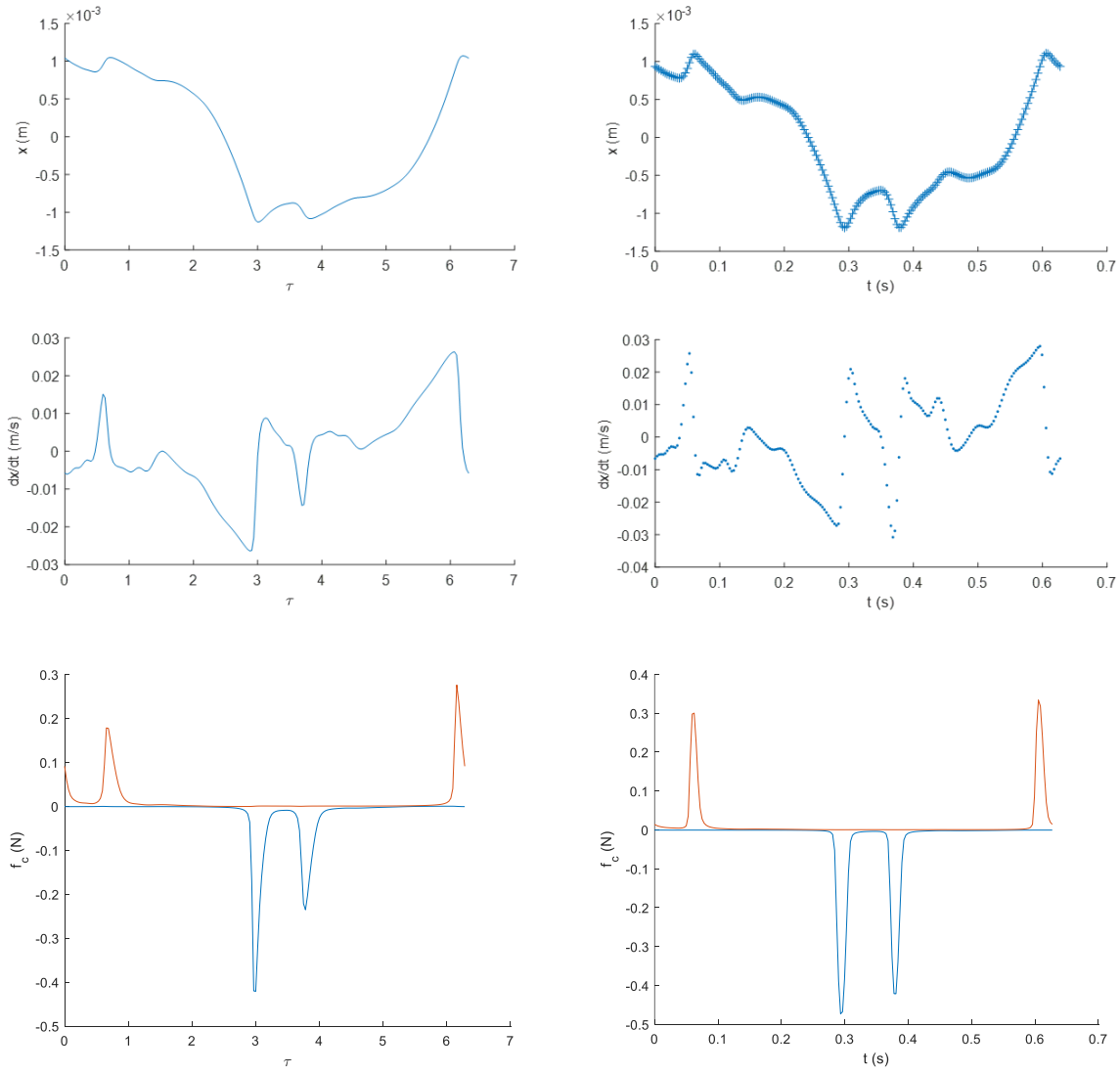

Figure 4.39. Periodic responses with (left column) and without (right column) contact damper at $a_{ext} = 1.54\ m/s^2$ and $\omega = 10\ rad/s$

4.4.3 Global dynamic behavior of fuel pin

The limited capacity of the GPTI method with the very rigid contact points arises from the difficult continuation due to the very pointed peak of impact force, even by adding a contact damper. Regardless of the impact forces, a reduced contact stiffness allows studying the dynamic behavior of the fuel pin without too much changing its global vibration, as can be seen from Figure 4.40. The simulations are performed with the direct time-integration method under the damped contact model, by choosing the real clearance (0.1 mm) and an excitation amplitude of value rather greater than the linear level, the resultant time evolution of the displacement and the velocity at free end present the similar form while the evolution of the impact forces becomes much smoother in terms of a longer contact duration and a smaller impact. Therefore, given the difficulty with the real contact stiffness, it is rather reasonable to study with the reduced contact stiffness of 3000 N/m to have an idea of the global dynamic behavior of the fuel pin.

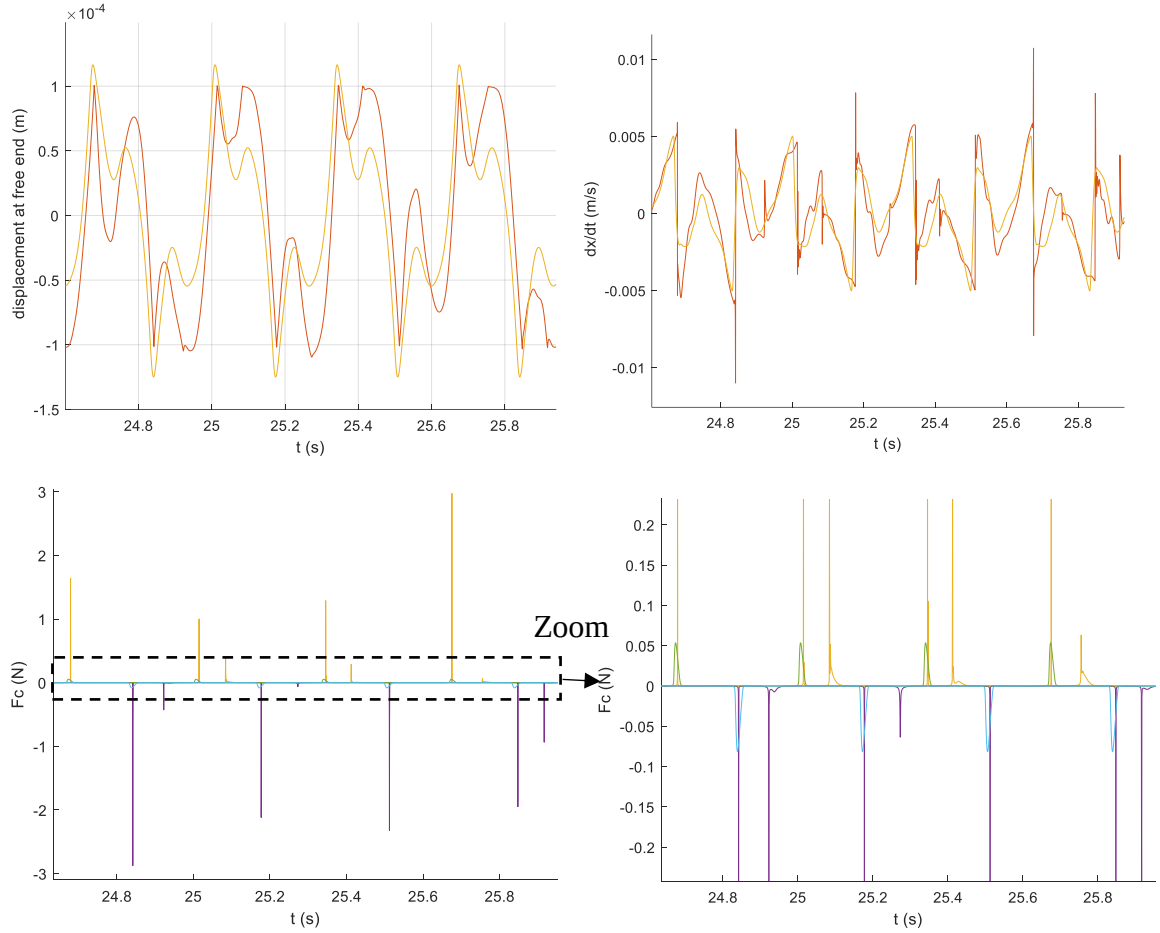

Figure 4.40. Periodic responses of displacement and velocity at free end of the fuel pin with real contact stiffness (red) and reduced $k_c = 3000\ N/m$ (orange) and the corresponding impact forces at the first two contact points (counting from the free end) with $a_{ext} = 0.3\ m/s^2$ and $\omega = 6\pi\ s^{-1}$

Hereafter, the study is carried out by taking the damped impact law with contact stiffness equal to 3000 N/m and a clearance of 0.1mm. Figure 4.41 presents the periodic solution branch of a fixed excitation frequency of 3 Hz. The solution points are in good agreement with the responses obtained with direct time-integration method when the excitation amplitude is inferior to 0.31 m/s^2, and the dynamic behavior is periodic with multiples of the imposed

frequency, as shown in Figure 4.42. However, the solution points with a greater excitation amplitude corresponds no longer with the results of direct time-integration using the same initial condition as previous calculations (see Figure 4.43(a)(b)). It is with another initial condition that we obtain the same results (see Figure 4.43(c)), thus this solution is stable and there should exist another solution branch, which is not obtained with the continuation in Figure 4.41.

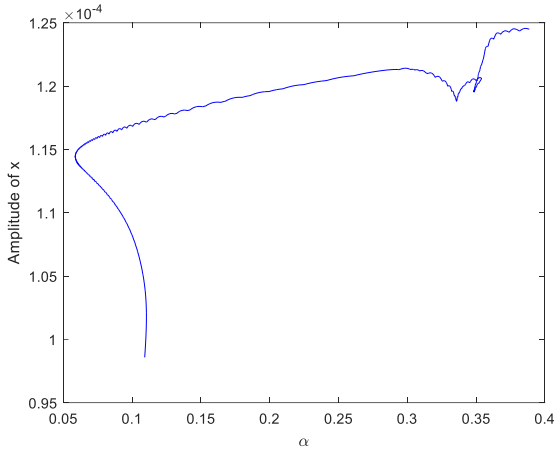

Figure 4.41. Periodic solution branch with respect to excitation amplitude with $\omega = 6\pi\ s^{-1}$

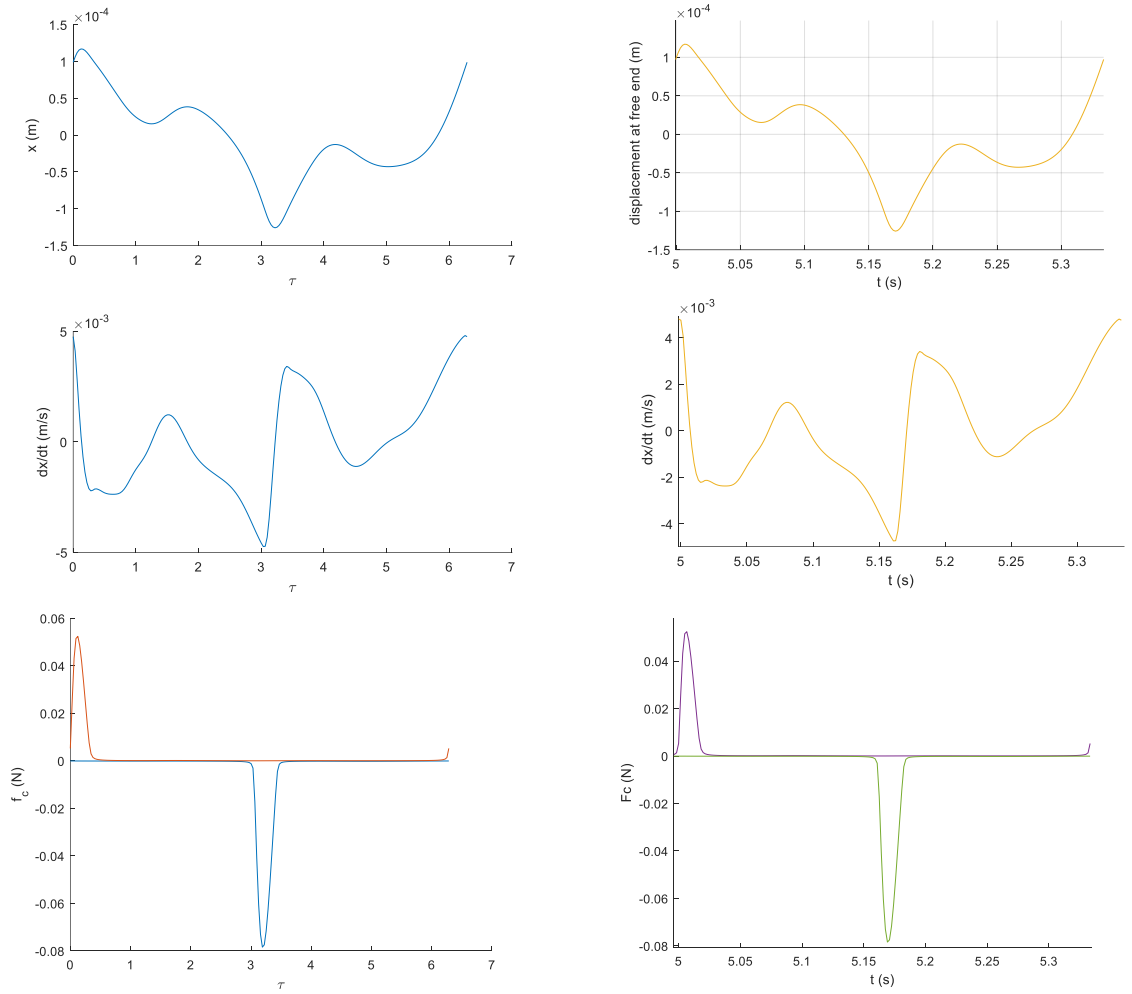

Figure 4.42. Periodic responses obtained with *Manlab* (left column) and with direct time-integration (right column) at $a_{ext} = 0.3\ m/s^2$

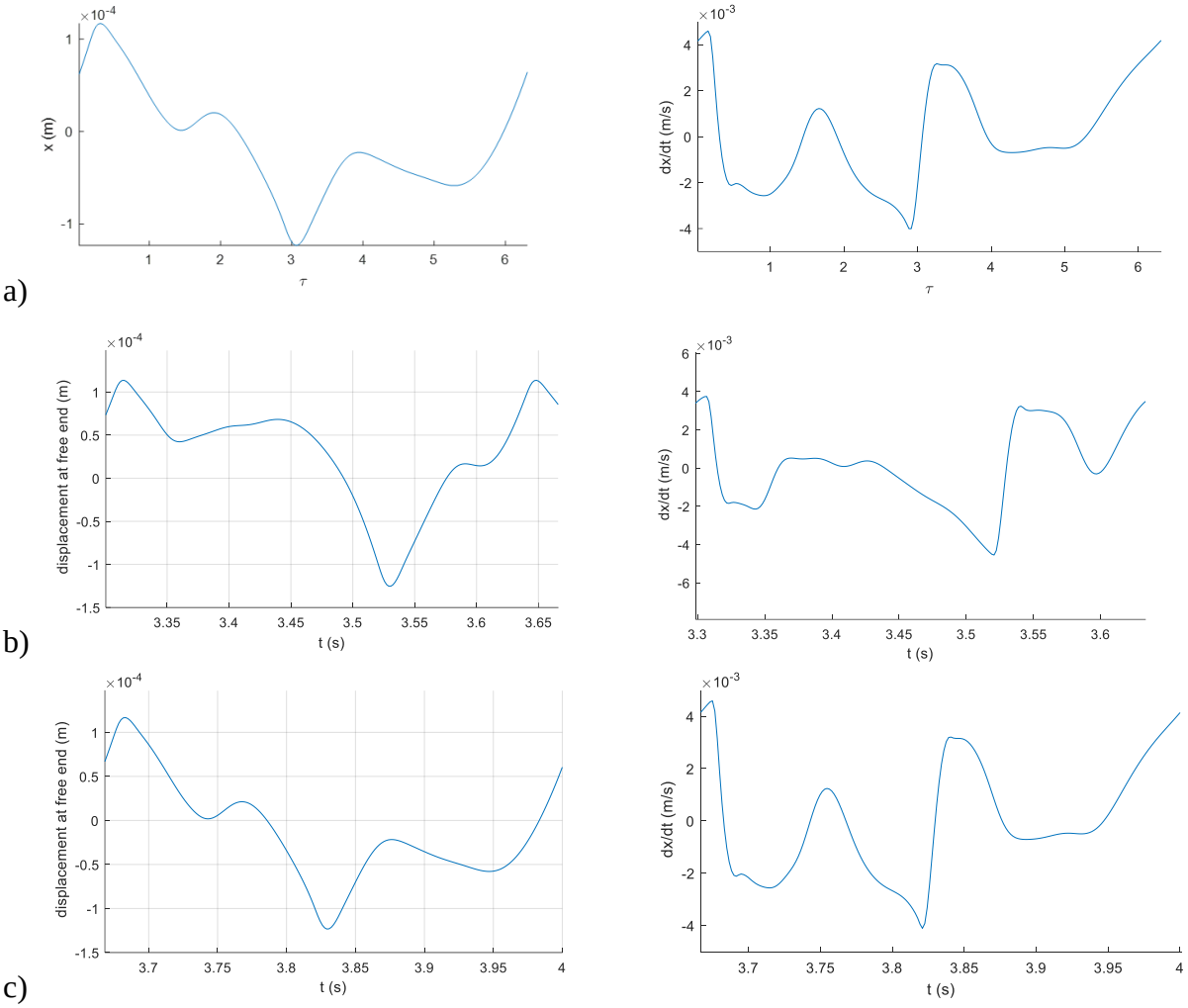

Figure 4.43. Time evolution in one period of the displacement and velocity at free end with $a_{ext} = 0.33\ m/s^2$: a) with the global periodic method; b) and c) stable responses obtained with the direct time-integration method using different initial conditions

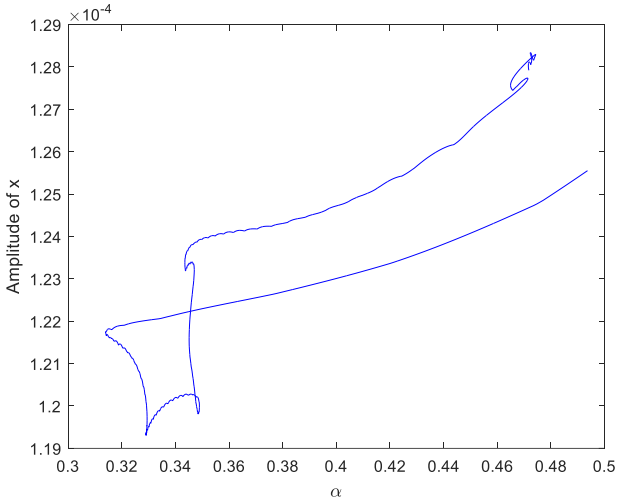

Figure 4.44. Periodic solution branch obtained with another starting point

In order to be able to figure out the period-doubling bifurcation at even greater acceleration amplitude, a calculation in two periods of excitation is carried out (replacing the external force

term in eq. (4.18) by $F_e \cos[2(n-1)h]\,\boldsymbol{Q}$). By taking the periodic solution of Figure 4.43(b) as the starting point of the continuation, a new solution branch is obtained, as presented in Figure 4.44. It is observed that the second stable periodic solution occurs when excitation amplitude equals to 0.31 m/s^2. From this point, there are two paths: one rises smoothly without difficulty of continuation along with the increasing amplitude, however the solution points of which appears to be instable, and the other one descends firstly and then goes up sharply at 0.35 m/s^2, of which the continuation step is much smaller and the solution points appear to be what we are searching for. A stability analysis should be developed as further investigation.

By taking a solution point of Figure 4.41, a solution branch with two-period calculation is as shown in Figure 4.45. With an excitation amplitude between 0.31 m/s^2 and 0.45 m/s^2, the result is the same as the previous simulation, which means the response is still periodic only with the multiples of the excitation frequency. It is when the excitation amplitude is superior to 0.45 m/s^2, the continuation path differs from that obtained with the one-period calculation, of which the solution points are no longer stable. As presented in Figure 4.46, the period-doubling bifurcation is observed, it is evidently a result of the phenomenon of alternative "sticking" contact and rebound as described in Section 3.3.2. Combining with the solution branch in Figure 4.44, another periodic response showing only multiples of the imposed frequency is also stable with this excitation.

It can be also observed in Figure 4.45 that with the amplitude between 0.531 m/s^2 and 0.566 m/s^2, two stable periodic responses exist on this solution branch, to obtain which with direct time-integration method different initial conditions should be taken. One example is presented in Figure 4.47. As presented in Figure 4.48, a third stable periodic solution is observed via the solution branch of Figure 4.44.

Even though the continuation can go further with an amplitude superior to 0.58 m/s^2, it does not reproduce the results from the direct time-integration method, since from this excitation amplitude the dynamic behavior is no longer perfectly periodic.

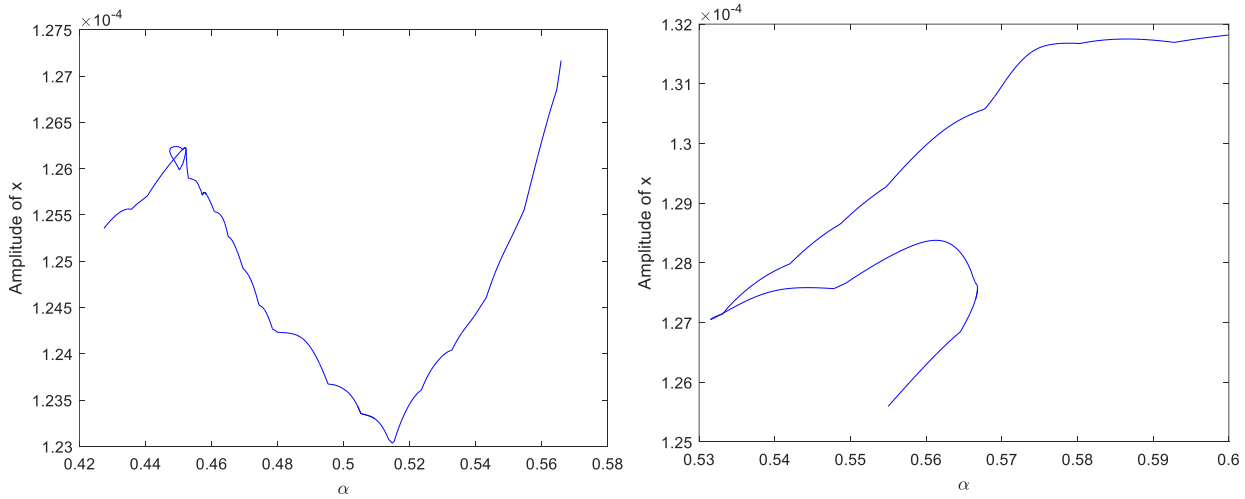

Figure 4.45. Periodic solution branch with respect to excitation amplitude with $\omega = 6\pi\ s^{-1}$

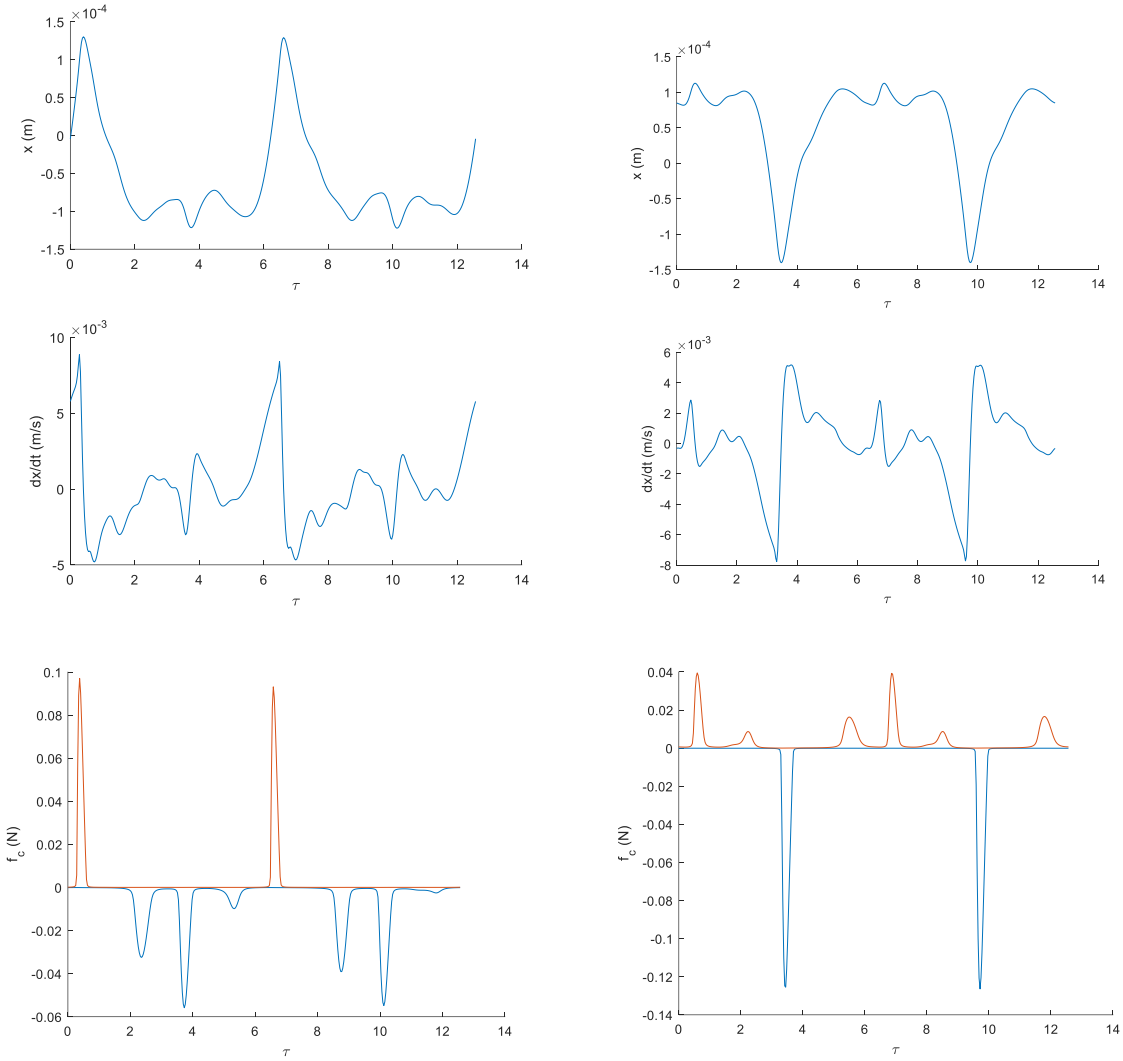

Figure 4.46. Periodic responses on solution branch of Figure 4.45 (left column) and on solution branch of Figure 4.44 (right column) with $a_{ext} = 0.45\ m/s^2$

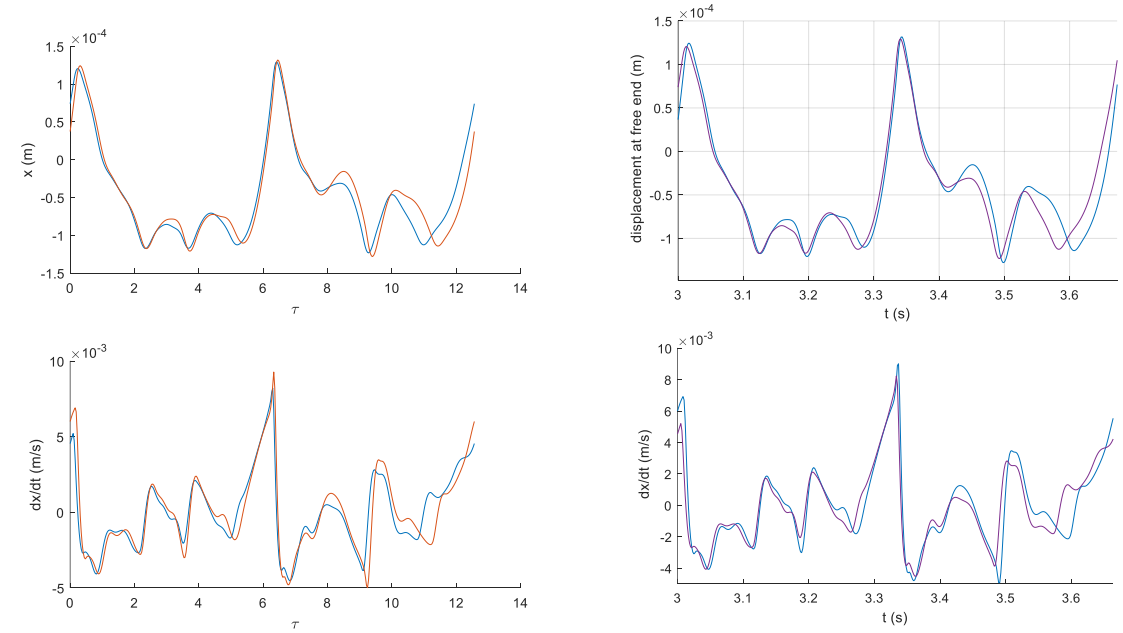

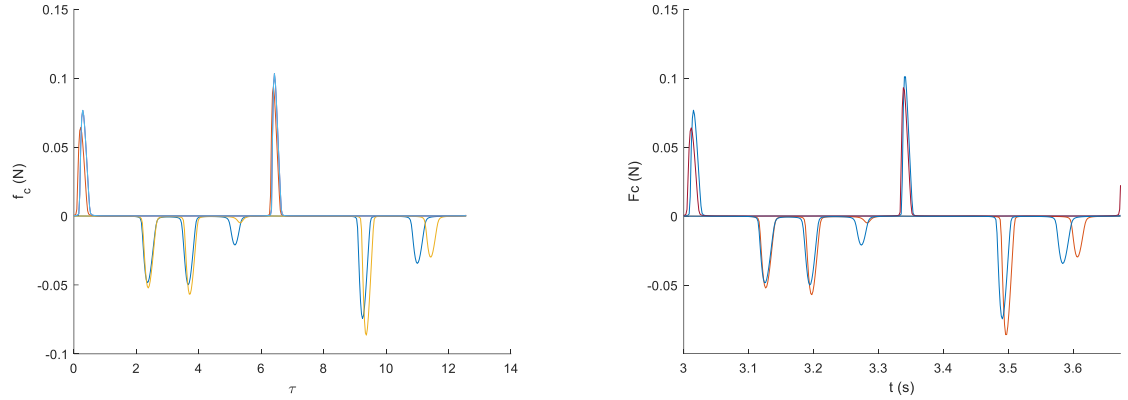

Figure 4.47. Periodic responses obtained with *Manlab* on solution branch of Figure 4.45 (left column) and with direct time-integration (right column) by taking $a_{ext} = 0.56\, m/s^2$

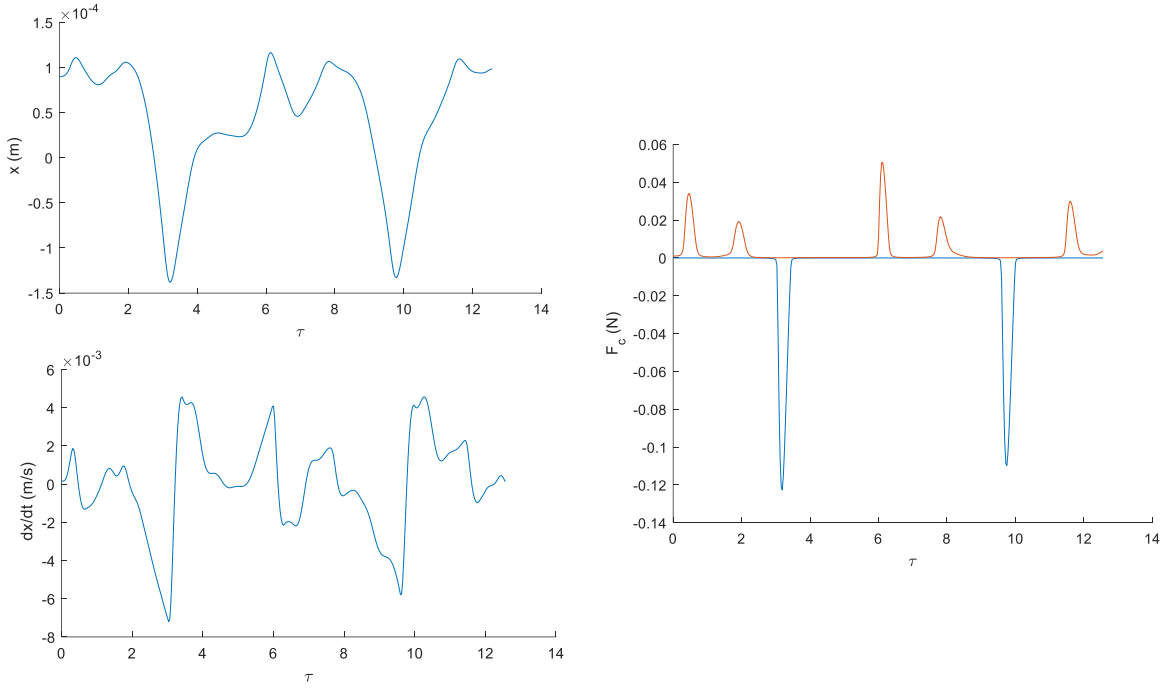

Figure 4.48. Periodic response on solution branch Figure 4.44 with $a_{ext} = 0.56\, m/s^2$

4.5 Conclusion

As it is the steady-state responses of the fuel pin that determine the long-term dynamic behavior, the direct time-integration method is not enough effective in capturing these periodic solutions. The numeric methods for searching directly the periodic dynamic behaviors are therefore of great interest in terms of economizing the computation resources, i.e. the calculation time and the data storage. A literature overview of the two categories of these methods is firstly presented.

Then, the classical frequency-domain method HBM has been applied to study a simplified fuel pin model with only four contact points. The difficulty of describing the sticking contact and the resulting impact forces with the Fourier series has been identified when the contact points are very rigid (with the real contact stiffness). Whereas, a good agreement of the results with the HBM and with the direct time-integration method has been observed in the case with less rigid contact points. Besides, the HBM calculation costs much less time and has the advantage of obtaining all the possible dynamic response on one solution branch, for which it is necessary

to search for different initial conditions with direct time-integration method, and detecting easily the period-doubling bifurcation. However, the range of the excitation amplitude that can be studied with the HBM is limited since when the excitation becomes stronger, the difficulty related with the sticking contact occurs again.

In order to overcome the limitation on the contact stiffness and the study range, we turn to the so-called GPTI method. Since this method is not much studied, its performance with the impact problems is firstly evaluated with a parametric study of the 1-dof vibro-impact system. This method has the potential to study the very rigid contact problems: the limit on the stiffness ratio between the contact point and the system is of 1000 with uniform time steps and of 5000 with adaptive time discretization. The difficulty is mainly due to the change of phase along with the continuation, which results in the sharp variation of the impact force, and is also due to the demanding computation memory. The excitation amplitude is therefore limited due to the occurrence of the "sticking" contacts with chatters, where successive peaks of impact force challenge the numeric convergence.

The GPTI method for problems of multiple dofs with several contact points is then developed and applied to the study of the fuel pin model. In the case with great contact stiffness, the continuation steps become very small shortly after first contact happens and the continuation can go no longer. Again the performance of this method is firstly evaluated with less rigid contact points. The continuation can be carried out in the investigated range of excitation amplitude and frequency. It is verified by comparing the periodic solutions on the continuation branch with the steady-state vibrations obtained with the direct time-integration method and the curve not smooth is caused by the phase variation and the time discretization, which can be eliminated by refining the time intervals. However, the continuation is rather difficult in terms of the short arc-length, which results in a large number of continuation steps, thus demands a large computation time. In order to make the continuation easier, a linear contact damper is introduced, allowing to calm the chatters following the first penetration into the contact point and have the peaks of the impact force less pointed.

In fact, given that even with the effort of introducing a contact damper, the continuation is still difficult for a very rigid contact problem, it is acceptable to study the global dynamic behavior of the fuel pin with a reduced contact stiffness if regardless of the impact forces. The two methods have both their advantages and limits with the impact-related problem. With the continuous solution branch, the GPTI method has the advantage of interpreting easily the change of the periodic patterns, such as the occurrence of the period-doubling phenomenon. The dynamic behavior of the fuel pin with several contact points is so complex that there exists different solution branches for the same excitation, and we are not able to obtain all the possible periodic responses with one continuation computation. Even though the direct time-integration result can be a complementary method of finding the start points of the solution branches, it can never be exhaustive since it is very sensible to the initial condition chosen for a system of complex dynamic behaviors.

In conclusion, both the direct time-integration and the GPTI have the advantages and limits in interpreting the complex dynamic behavior of the fuel pin. The direct time-integration is quite direct and can be applied for any contact rigidity and excitation amplitude, but it is difficult to cover the coexisting regimes led by the nonlinearity as it is sensible to the initial condition. The GPTI method allows in some manner to obtain the coexisting solutions but the complexity of the dynamic response makes it difficult to be exhaustive. Besides, the difficulty with the

continuation leads to a limited range of contact stiffness and excitation amplitude. It has been observed that the complex coexisting regimes differ from one another only in the local behaviors. Introducing a contact damper physically permits some kind of smoothing of the responses, but the difficulty remains and prevents us to think of modeling a complete fuel pin bundle. As a last comment, the mathematically based smoothing method seems necessary if we want to overcome the difficulty caused by the local chatters but up to date there is no mature tool for the study of an industry-scale problem.

Chapter 5 Attempt of a macroscopic model

5.1 Introduction

In section 3.3.3, the model to study the dynamics of a row of six fuel pins does not take into account the modification of the surrounding flow due to the motion of the pins. However, the motion of the fuel pins does have some effects on the surrounding flow, which results in the coupling between the fuel pins. The model is to be improved to take this effect into consideration with the homogenization method. This chapter presents an attempt to build a macroscopic model for the coupled problem with a homogenization method.

The principle of homogenization consists in assimilating the arrangement of structures to a porous medium by using formalisms for changing scales intended for the modeling of these heterogeneous systems. There are mainly two methods: the asymptotic homogenization [137] and the volume averaging method.

In our case, the structure is periodic in the undeformed configuration and the use of the asymptotic expansion method appears to be attractive. This method consists in introducing an asymptotic multi-scale expansion (generally with respect to a ratio of dimensions between the Representative Volume Element - RVE- and the studied domain) in the governing equations of the problem. When making this ratio tends to zero, it leads to a homogenized macroscopic problem for which the homogeneous medium is characterized by the way of problems posed on the RVE. Jacqueline [138] applied this method to model the dynamic behavior of a bundle of 16 PWR assemblies in air (incompressible, irrotational and inviscid flow) under a sinusoidal excitation by considering each assembly as an elementary structure. Under the same assumptions on the flow, Hammami [139] opted for the homogenization to the core of a RAPSODIE core. The homogenized model is 2-dimensional in the cross-section plan of the assemblies and each assembly is considered as a harmonic oscillator. Validated by the experiments, the sensitivity study of the model to the nature of the fluid highlights the need to faithfully describe the evolution of the average pressure surrounding the structures. The adequacy between the proposed model – particularly in water – and the experimental measurements is qualitatively encouraging and represents significant progress for this type of approach. Nevertheless, it is difficult with this method to take into account strong non linearities due for example to the important convective transport effect [143] and the use of averaging method is then envisaged.

The averaging method aims at transforming by an averaging operator the local equations on the microscopic scale where the material appears as a juxtaposition of distinct phases, to a global equation at the macroscopic scale, which is characterized by a RVE. This method was firstly introduced to model the porous medium [140], such as sedimentary rocks, aquifers or concretes and cements. It was then adapted to the turbulent flow [141]. The method was applied by Sigrist and Broc [142] and Ricciardi [89] for the seismic analysis of PWR cores. They assimilated each fuel assembly to a porous medium and proposed a local averaging method aiming at modeling the displacements of the assemblies in interaction with an axial turbulent flow. Their formalism has the particularity of using spatial filters to describe the effects of turbulence and those related to the porous scale: the flow within the assemblies is modeled using the LES model [49]. The fluid-structure interaction for different core prototypes is simulated numerically and compared to vibration measurements obtained on equivalent scale models. However, the distance between assemblies is considered constant over time and limits the field of application of the method to

overall movements. Gineau [143] applied a 2-dimensional model in the cross-section plan to study the vibratory response of the bundles of cylindrical tubes and hexagonal tubes in the laminar flow. Even though the particularly important confinement in the hexagonal configuration gives rise to a coupling of modes which is difficult to reproduce by the homogenized model, the multi-scale approach implemented remains a good compromise between the cost of the numerical realizations and the expected agreement with the references. This method is limited to the case where the structural displacements are small enough to be always limited in their associated RVEs which are independent of space and time.

In our studied case, the relative displacements of the fuel pins should be modeled to take the impacts between them into account. What's more, their displacements under external loads can be relatively high. Basing on the existing methods, modifications should be made to remove the restriction on the vibratory amplitude. In this case, in order to preserve an individual description for each fuel pin, it would be necessary to envisage the deformable and mobile RVEs. The originality of the approach resides in the fact that the RVE (volume and geometry) to which the averaging operators will be applied will be considered depending on space and time to follow the overall motion of the pins.

5.2 Modified averaging method

The model to study the dynamic behavior of a row of six fuel pins, taking the coupling between them into account, is developed based on the volume averaging method. The idea is to assimilate the row of beams immersed in an axial flow as pores regularly distributed inside the studied domain, as is shown in Figure 5.1. The method consists in space averaging the governing equation of fluid on the RVE, which is defined to be composed of a section of beam (orange part) and the surrounding fluid (blue part), so that the equivalent porous fluid characterized by the averaged properties could be defined and be coupled with the motion equation of the beam by the hydraulic forces model proposed by Paidoussis [58].

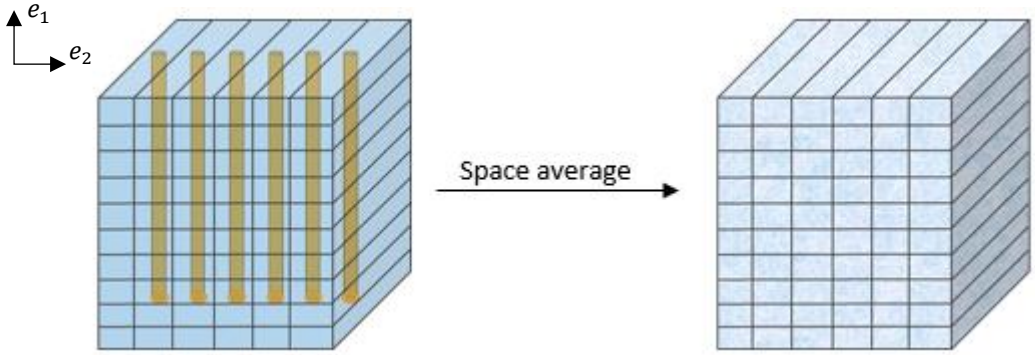

Figure 5.1. Principal idea of porous method

5.2.1 Spatial averaging theorems

For purposes of averaging, some notations should be defined. The RVE is denoted by $\Omega(\boldsymbol{x},t) = \Omega_s(\boldsymbol{x},t) \cup \Omega_f(\boldsymbol{x},t)$ with Ω_s and Ω_f representing respectively the structure and the fluid domain. Its centroid is marked by the system of variables $(\boldsymbol{x},t)$. Let us note the components of $\boldsymbol{x} = x_1\boldsymbol{e_1} + x_2\boldsymbol{e_2} + x_3\boldsymbol{e_3}$, where (x_1,x_2,x_3) are the coordinates on the orthogonal basis $(\boldsymbol{e_1}, \boldsymbol{e_2}, \boldsymbol{e_3})$. A local coordinate system $(\boldsymbol{\xi},t)$ of which the axes are parallel with $\boldsymbol{x}$ marks the relative position of a point with respect to the centroid of the RVE. The RVE is characterized by the macroscopic

properties, which are spatial averages defined either on the total volume V_t or on the fluid volume V_f. The notations are defined as:

$$\begin{aligned}\overline{\boldsymbol{\varphi}}(\boldsymbol{x},t) &= \frac{1}{V_t}\int_{\Omega_f(\boldsymbol{x},t)} \boldsymbol{\varphi}(\boldsymbol{x}+\boldsymbol{\xi},t)dV_\xi \\ \underline{\boldsymbol{\varphi}}(\boldsymbol{x},t) &= \frac{1}{V_f}\int_{\Omega_f(\boldsymbol{x},t)} \boldsymbol{\varphi}(\boldsymbol{x}+\boldsymbol{\xi},t)\ dV_\xi\end{aligned} \tag{5.1}$$

$$\beta(\boldsymbol{x},t) = \frac{V_f}{V_t} = \frac{\overline{\boldsymbol{\varphi}}}{\underline{\boldsymbol{\varphi}}} \tag{5.2}$$

with β denoting the porosity, defined as the fluid fraction in the control volume.

The averaging of the equations governing microscopic phenomena requires the application of permutation theorems between the volume integral and partial derivations in order to obtain the formulation of the equivalent macroscopic problem. As explained above, in order to be able to model the relatively great displacements, the RVE are defined to be deformable and mobile. Basing on the Leibniz integral rule and the divergence theorems, two permutation theorems over a space-and time-dependent volume are as follows (see Appendix B for the proof):

$$\begin{aligned}&\frac{1}{V_t}\int_{\Omega_f(\boldsymbol{x},t)} div\boldsymbol{\varphi}(\boldsymbol{x}+\boldsymbol{\xi},t)\ dV_\xi \\ &\quad= div\left(\frac{1}{V_t}\int_{\Omega_f(\boldsymbol{x},t)}\boldsymbol{\varphi}(\boldsymbol{x}+\boldsymbol{\xi},t)dV_\xi\right)+\frac{1}{V_t}\nabla V_t\cdot\left(\frac{1}{V_t}\int_{\Omega_f(\boldsymbol{x},t)}\boldsymbol{\varphi}(\boldsymbol{x}+\boldsymbol{\xi},t)dV_\xi\right) \\ &\quad-\frac{1}{V_t}\oint_{\partial\Omega_f(\boldsymbol{x},t)}(\boldsymbol{n}\cdot\nabla\boldsymbol{\xi})\cdot\boldsymbol{\varphi}(\boldsymbol{x}+\boldsymbol{\xi},t)dS_\xi\end{aligned} \tag{5.3}$$

$$\begin{aligned}&\frac{1}{V_t}\int_{\Omega_f(\boldsymbol{x},t)}\frac{\partial\boldsymbol{\varphi}(\boldsymbol{x}+\boldsymbol{\xi},t)}{\partial t}dV_\xi \\ &\quad=\frac{\partial}{\partial t}\left(\frac{1}{V_t}\int_{\Omega_f(\boldsymbol{x},t)}\boldsymbol{\varphi}dV_\xi\right)+\frac{1}{V_t}\frac{\partial V_t}{\partial t}\left(\frac{1}{V_t}\int_{\Omega_f(\boldsymbol{x},t)}\boldsymbol{\varphi}dV_\xi\right) \\ &\quad-\frac{1}{V_t}\oint_{\partial\Omega_f(\boldsymbol{x},t)}(\boldsymbol{v_b}\cdot\boldsymbol{n})\boldsymbol{\varphi}\,dS_\xi\end{aligned} \tag{5.4}$$

Where $\partial\Omega_f$ denotes the border of the domain Ω_f, $\boldsymbol{n}$ is its outward-pointing unit normal vector and $\boldsymbol{v_b}$ is it velocity. Particularly in our case, $\partial\Omega_f$ can be decomposed into two parts: the fluid-structure interface A_s and the fluid-fluid interface A_f defined by the boundary of RVE. At any instance t, the position of the structure $\boldsymbol{u}$ is independent of the RVE, thus we have on A_s:

$$\nabla\boldsymbol{\xi} = -\boldsymbol{I} \tag{5.5}$$

Therefore, equations (5.3) is rewritten into:

$$\frac{1}{V_t}\int_{\Omega_f(\boldsymbol{x},t)} div\boldsymbol{\varphi}(\boldsymbol{x}+\boldsymbol{\xi},t)\,dV_\xi = div\overline{\boldsymbol{\varphi}} + \frac{1}{V_t}\nabla V_t\cdot\overline{\boldsymbol{\varphi}} + \frac{1}{V_t}\oint_{A_s(\boldsymbol{x},t)} \boldsymbol{n}\cdot\boldsymbol{\varphi}(\boldsymbol{x}+\boldsymbol{\xi},t)\,dS_\xi - \frac{1}{V_t}\oint_{A_f(\boldsymbol{x},t)} (\boldsymbol{n}\cdot\nabla\boldsymbol{\xi})\cdot\boldsymbol{\varphi}(\boldsymbol{x}+\boldsymbol{\xi},t)dS_\xi \tag{5.6}$$

5.2.2 Space-averaging of the Navier-Stokes equations

Since the RVE Ω is deformable and mobile, the microscopic observation volume $d\Omega$ is therefore temporally variable. This results in the necessity of the arbitrary lagrangian eulerian (ALE) description of fluid. The flow is classically considered to be Newtonian, incompressible and viscous, the Navier-Stokes equations in ALE form are:

$$div\boldsymbol{v} = 0 \tag{5.7}$$

$$\rho_f\frac{\partial\boldsymbol{v}}{\partial t} + \rho_f[(\boldsymbol{v}-\widehat{\boldsymbol{v}})\cdot\nabla]\boldsymbol{v} = div\boldsymbol{\sigma_f} + \rho_f\boldsymbol{g} \tag{5.8}$$

Where $\boldsymbol{v}$ and $\widehat{\boldsymbol{v}}$ are respectively the velocity of fluid and of the microscopic observation volume $d\Omega$ in laboratory reference, ρ_f is the density of fluid and $\boldsymbol{\sigma_f}$ denotes the Cauchy stress tensor. Since the fluid is supposed to be Newtonian and incompressible, the Cauchy stress tensor is expressed as:

$$\boldsymbol{\sigma_f} = -p\boldsymbol{I} + \mu(\nabla\boldsymbol{v} + \nabla^T\boldsymbol{v}) \tag{5.9}$$

Where p denotes the pressure, μ refers to the viscosity and $\boldsymbol{I}$ is the identity tensor.

The spatial averaging theorems are applied on the (5.7) and (5.8) to obtain the governing equations of the equivalent fluid in the RVE. Firstly, the averaged continuity equation is expressed as:

$$div(\overline{\boldsymbol{v}}) + \frac{1}{V_t}\nabla V_t\cdot\overline{\boldsymbol{v}} + \frac{1}{V_t}\oint_{A_s(x,t)} \boldsymbol{v}(\boldsymbol{x}+\boldsymbol{\xi},t)\cdot\boldsymbol{n}\,dS_\xi - \frac{1}{V_t}\oint_{A_f(x,t)} (\boldsymbol{n}\cdot\nabla\boldsymbol{\xi})\boldsymbol{v}(\boldsymbol{x}+\boldsymbol{\xi},t)dS_\xi = 0 \tag{5.10}$$

The momentum equation (5.6) is averaged term by term:

$$\frac{1}{V_t}\int_{\Omega_f}\rho_f\frac{\partial\boldsymbol{v}}{\partial t}d\Omega = \rho_f\left(\frac{\partial\overline{\boldsymbol{v}}}{\partial t} + \frac{1}{V_t}\frac{\partial V_t}{\partial t}\overline{\boldsymbol{v}} - \frac{1}{V_t}\oint_{A_s(\boldsymbol{x},t)}(\boldsymbol{v_b}\cdot\boldsymbol{n})\boldsymbol{v}\,dS_\xi - \frac{1}{V_t}\oint_{A_f(\boldsymbol{x},t)}(\boldsymbol{v_b}\cdot\boldsymbol{n})\boldsymbol{v}\,dS_\xi\right) \tag{5.11}$$

$\widehat{\boldsymbol{v}} = \boldsymbol{v_b}$ on the boundaries A_s and A_f. The second term can be separated into two parts:

$$\frac{1}{V_t}\int_{\Omega_f}\rho_f[(\boldsymbol{v}-\widehat{\boldsymbol{v}})\cdot\nabla]\boldsymbol{v}dV_\xi = \frac{1}{V_t}\rho_f\left(\int_{\Omega_f} div(\boldsymbol{v}\otimes\boldsymbol{v})d\Omega - \int_{\Omega_f}(\widehat{\boldsymbol{v}}\cdot\nabla)\boldsymbol{v}dV_\xi\right) \tag{5.12}$$

The two terms can be simplified as following:

$$\frac{1}{V_t}\rho_f \int_{\Omega_f} div(\boldsymbol{v}\otimes\boldsymbol{v})d\Omega = \rho_f\left[div\left(\frac{1}{V_t}\int_{\Omega_f}\boldsymbol{v}\otimes\boldsymbol{v}dV_\xi\right)+\frac{1}{V_t}\nabla V_t\cdot\left(\frac{1}{V_t}\int_{\Omega_f}\boldsymbol{v}\otimes\boldsymbol{v}dV_\xi\right)+\frac{1}{V_t}\oint_{A_s(\boldsymbol{x},t)}(\boldsymbol{v}\cdot\boldsymbol{n})\,\boldsymbol{v}dS_\xi-\frac{1}{V_t}\oint_{A_f(\boldsymbol{x},t)}(\boldsymbol{n}\cdot\boldsymbol{\nabla\xi})\cdot(\boldsymbol{v}\otimes\boldsymbol{v})\,dS_\xi\right] \tag{5.13}$$

$$\frac{1}{V_t}\rho_f\int_{\Omega_f}(\widehat{\boldsymbol{v}}\cdot\nabla)\boldsymbol{v}dV_\xi=\rho_f\frac{1}{V_t}\int_{\Omega_f}\nabla\boldsymbol{v}\cdot\widehat{\boldsymbol{v}}dV_\xi=\rho_f\frac{1}{V_t}\left(\int_{\partial\Omega_f}\boldsymbol{v}(\widehat{\boldsymbol{v}}\cdot\boldsymbol{n})dS_\xi-\int_{\Omega_f}\boldsymbol{v}div\widehat{\boldsymbol{v}}dV_\xi\right) \tag{5.14}$$

Since the fluid is viscous, its velocity on A_s is equal to that of A_s, the third term in eq. (5.13) and the third term in eq. (5.11) are equal:

$$\frac{1}{V_t}\oint_{A_s(\boldsymbol{x},t)}(\boldsymbol{v}\cdot\boldsymbol{n})\,\boldsymbol{v}dS_\xi=\frac{1}{V_t}\oint_{A_s(\boldsymbol{x},t)}(\boldsymbol{v_b}\cdot\boldsymbol{n})\boldsymbol{v}\,dS_\xi$$

According to the turbulence model, velocity can be divided into a spatial average and a fluctuation $\boldsymbol{v}'$:

$$\boldsymbol{v}=\frac{1}{V_f}\int_{\Omega_f}\boldsymbol{v}dV_\xi+\boldsymbol{v}'=\underline{\boldsymbol{v}}+\boldsymbol{v}' \tag{5.15}$$

By substituting (5.15) into $\frac{1}{V_t}\int_{\Omega_f}\boldsymbol{v}\otimes\boldsymbol{v}d\Omega$, we obtain:

$$\begin{aligned}\frac{1}{V_t}\int_{\Omega_f}\boldsymbol{v}\otimes\boldsymbol{v}dV_\xi&=\frac{1}{V_t}\int_{\Omega_f}(\underline{\boldsymbol{v}}\otimes\underline{\boldsymbol{v}})dV_\xi+\frac{1}{V_t}\int_{\Omega_f}\boldsymbol{v}'\otimes\boldsymbol{v}'dV_\xi\\&=\beta(\boldsymbol{x},t)(\underline{\boldsymbol{v}}\otimes\underline{\boldsymbol{v}})+\beta(\boldsymbol{x},t)\underline{\boldsymbol{v}'\otimes\boldsymbol{v}'}\end{aligned} \tag{5.16}$$

The Reynolds tensor corresponds to the turbulence effect:

$$\boldsymbol{\sigma_{Re}}=\rho_f\underline{\boldsymbol{v}'\otimes\boldsymbol{v}'} \tag{5.17}$$

Classically, it is modeled by the turbulent viscosity model proposed by Smagorinsky [49]:

$$\boldsymbol{\sigma_{Re}}=-\frac{2}{3}\rho_f k_T\boldsymbol{I}+\mu_T(\nabla\underline{\boldsymbol{v}}+\nabla^T\underline{\boldsymbol{v}}) \tag{5.18}$$

As a result, equation (5.13) is simplified into

$$\frac{1}{V_t}\rho_f \int_{\Omega_f} div(\boldsymbol{v}\otimes\boldsymbol{v})d\Omega$$
$$= \rho_f \left[div\left(\beta(\underline{\boldsymbol{v}}\otimes\underline{\boldsymbol{v}})\right) + \frac{1}{V_t}\nabla V_t \cdot \left(\beta(\underline{\boldsymbol{v}}\otimes\underline{\boldsymbol{v}})\right) + \frac{1}{V_t}\oint_{A_s(\boldsymbol{x},t)} (\hat{\boldsymbol{v}}\cdot\boldsymbol{n})\boldsymbol{v}\, dS_\xi \right. \quad (5.19)$$
$$\left. - \frac{1}{V_t}\oint_{A_f(\boldsymbol{x},t)} (\boldsymbol{n}\cdot\boldsymbol{\nabla\xi})\cdot(\boldsymbol{v}\otimes\boldsymbol{v})\, dS_\xi \right] + div(\beta\boldsymbol{\sigma_{Re}}) + \frac{1}{V_t}\nabla V_t(\beta\boldsymbol{\sigma_{Re}})$$

In consequence, the left hand of the equivalent momentum equation is:

$$\frac{1}{V_t}\int_{\Omega_f}\left\{\rho_f\frac{\partial\boldsymbol{v}}{\partial t} + \rho_f[(\boldsymbol{v}-\hat{\boldsymbol{v}})\cdot\nabla]\boldsymbol{v}\right\}dV_\xi$$
$$= \rho_f\left(\frac{\partial\overline{\boldsymbol{v}}}{\partial t} + \frac{1}{V_t}\frac{\partial V_t}{\partial t}\overline{\boldsymbol{v}} - \frac{1}{V_t}\oint_{A_f(\boldsymbol{x},t)}(\hat{\boldsymbol{v}}\cdot\boldsymbol{n})\boldsymbol{v}\, dS_\xi + div\left(\beta(\underline{\boldsymbol{v}}\otimes\underline{\boldsymbol{v}})\right)\right. \quad (5.20)$$
$$+ \frac{1}{V_t}\nabla V_t\left(\beta(\underline{\boldsymbol{v}}\otimes\underline{\boldsymbol{v}})\right) - \frac{1}{V_t}\oint_{A_f(\boldsymbol{x},t)}(\boldsymbol{n}\cdot\boldsymbol{\nabla\xi})\cdot(\boldsymbol{v}\otimes\boldsymbol{v})\, dS_\xi$$
$$\left. - \frac{1}{V_t}\int_{\partial\Omega_f}\boldsymbol{v}(\hat{\boldsymbol{v}}\cdot\boldsymbol{n})dS_\xi + \frac{1}{V_t}\int_{\Omega_f}\boldsymbol{v}div\hat{\boldsymbol{v}}dV_\xi\right) + div(\beta\boldsymbol{\sigma_{Re}}) + \frac{1}{V_t}\nabla V_t(\beta\boldsymbol{\sigma_{Re}})$$

The right hand of the averaged momentum equation is

$$\frac{1}{V_t}\int_{\Omega_f}(div\boldsymbol{\sigma_f} + \rho_f\boldsymbol{g})dV_\xi$$
$$= div(\overline{\boldsymbol{\sigma_f}}) + \frac{1}{V_t}\nabla V_t\cdot\overline{\boldsymbol{\sigma_f}} + \frac{1}{V_t}\oint_{A_s(\boldsymbol{x},t)}\boldsymbol{\sigma_f}\cdot\boldsymbol{n}\, dS_\xi \quad (5.21)$$
$$- \frac{1}{V_t}\oint_{A_f(\boldsymbol{x},t)}(\boldsymbol{n}\cdot\boldsymbol{\nabla\xi})\cdot\boldsymbol{\sigma_f}dS_\xi + \beta\rho_f\boldsymbol{g}$$

From the equations (5.10), (5.20) and (5.21), besides the terms with the macroscopic properties, there exists still many terms (in blue), especially those on the fluid-fluid boundary A_f, difficult to be dealt with. In order to obtain the equivalent fluid model, hypothesis need to be made to simplify the equations and also to make appear the information of the structure positions.

5.2.3 Hypothesis

In order to establish equivalent governing equations, we make the following assumptions: the fluid (in this case water) is classically assumed to be viscous, incompressible and Newtonian. Gravity effects are negligible compared to the inertial and viscous forces. As classically assumed in slender body theory, the sections of the rods do not deform. Turbulent kinetic energy is assumed to be negligible in comparison with the turbulent diffusion.

The studied system is made up of a row of N identical beams, and their individual movements make the system pseudo-periodic. In order to preserve an individual description for each fuel pin, the homogenized problem will be solved on a set of discrete volumes. The study domain is divided into N non-material control volumes hereinafter and each volume boundary is assumed

to be located on the midpoint between neighboring beams, as presented in Figure 5.2, to never have the beams exceeding the corresponding RVE during their motion.

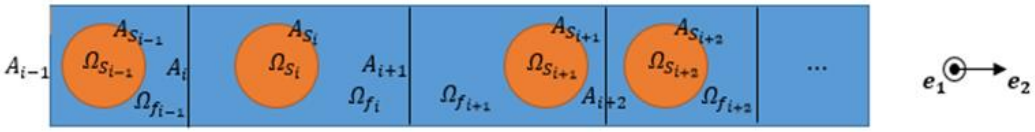

Figure 5.2. Horizontal section of the studied case

All the hypotheses are recapitulated below:

H1 The fluid is Newtonian, incompressible and viscous.

H2 The sections of beams are not deformable and the fluid cannot enter into the structure.

H3 Turbulent kinetic energy is assumed to be negligible in comparison with the turbulent diffusion. The turbulent viscosity is supposed to be constant in time and space and it is much more important than the dynamic viscosity.

H4 The displacement of the beam is considered to be only in the plan $(\boldsymbol{e_1}, \boldsymbol{e_2})$. They can be considered as the Bernoulli beam and their rotation is very small: $\frac{\partial u_i}{\partial x_1} = O(10^{-3})$, with u_i the position of the centroid of the i[th] beam.

H5 The configuration is infinitely periodic in direction $\boldsymbol{e_3}$, i.e. no exchange between the rows.

H6 The left and right boundaries are supposed to be located at the midpoints of adjacent beams. The position on the $\boldsymbol{e_2}$ axis of the fluid surfaces A_f of the control volume are noted A_i and therefore can be expressed as:

$$A_i = \begin{cases} 0 & i = 1 \\ \dfrac{u_i + u_{i-1}}{2} & 2 \leq i \leq N \\ N \cdot P & i = N+1 \end{cases} \tag{5.22a}$$

with P the pitch of the beams at $t = 0$. To make the gradient terms meaningful, the continuous $\Omega(\boldsymbol{x}, t)$ coherent with the discrete ones should also be defined with the interpolation between the discrete RVEs, as shown in Figure 5.3.

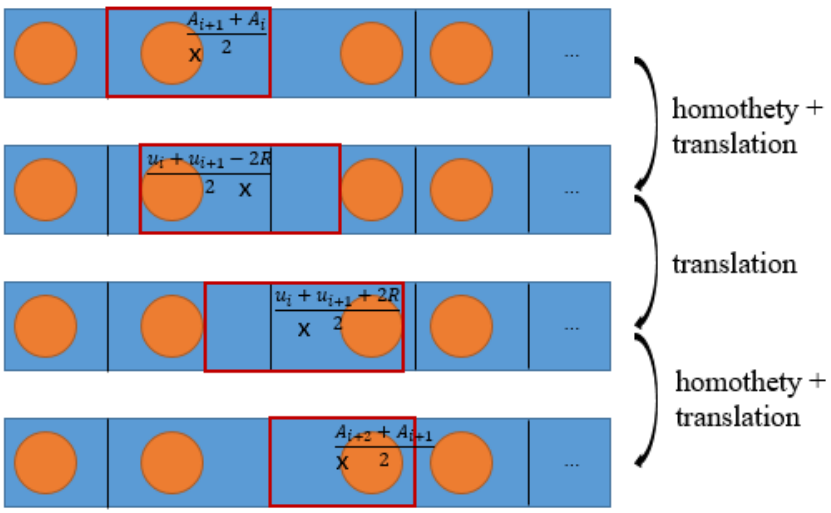

Figure 5.3. Continuous $\Omega(\boldsymbol{x},t)$ (horizontal section marked by the red case) defined with the interpolation between the discrete RVEs of which the centroid is noted by a cross

The domain is therefore described as $\Omega(\boldsymbol{x},t)=\{(\boldsymbol{x}+\boldsymbol{\xi},t)|\boldsymbol{\xi}\in\left[-\frac{h}{2},\frac{h}{2}\right]\times\left[A_{f2}^{-}-x_2,A_{f2}^{+}-x_2\right]\times[-\frac{P}{2},\frac{P}{2}]\}$, with A_f^- and A_f^+ being piecewise linear functions with respect to x_2. h is the thickness of the control volume in the $\boldsymbol{e_1}$ direction and is chosen small compared the other dimensions. The segments corresponds respectively to the three processes presented in Figure 5.3, thus for $\forall i\in[1,N+1]$, they are expressed as:

For $\frac{A_{i+1}+A_i}{2}\leq x_2<\frac{u_i+u_{i+1}-2R}{2}$,

$$A_{f2}^{-}(\boldsymbol{x},t)=\frac{\left(x_2-\frac{A_{i+1}+A_i}{2}\right)(u_i-R)+\left(\frac{u_i+u_{i+1}-2R}{2}-x_2\right)A_i}{\frac{u_i+u_{i+1}-2R}{2}-\frac{A_{i+1}+A_i}{2}}$$

$$A_{f2}^{+}(\boldsymbol{x},t)=\frac{(x_2-\frac{A_{i+1}+A_i}{2})(u_{i+1}-R)+(\frac{u_i+u_{i+1}-2R}{2}-x_2)A_{i+1}}{\frac{u_i+u_{i+1}-2R}{2}-\frac{A_{i+1}+A_i}{2}}$$

For $\frac{u_i+u_{i+1}-2R}{2}\leq x_2\leq\frac{u_i+u_{i+1}+2R}{2}$,

$$A_{f2}^{-}(\boldsymbol{x},t)=\frac{(x_2-\frac{u_i+u_{i+1}-2R}{2})(u_i+R)+(\frac{u_i+u_{i+1}+2R}{2}-x_2)(u_i-R)}{2R}$$

$$A_{f2}^{+}(\boldsymbol{x},t)=\frac{(x_2-\frac{u_i+u_{i+1}-2R}{2})(u_{i+1}-R)+(\frac{u_i+u_{i+1}+2R}{2}-x_2)(u_{i+1}+R)}{2R}\qquad(5.22b)$$

For $\frac{u_i+u_{i+1}+2R}{2}<x_2\leq\frac{A_{i+2}+A_{i+1}}{2}$,

$$A_{f2}^{-}(\boldsymbol{x},t)=\frac{(x_2-\frac{u_i+u_{i+1}+2R}{2})A_{i+1}+(\frac{A_{i+2}+A_{i+1}}{2}-x_2)(u_i+R)}{\frac{A_{i+2}+A_{i+1}}{2}-\frac{u_i+u_{i+1}+2R}{2}}$$

$$A_{f2}^{+}(\boldsymbol{x},t)=\frac{(x_2-\frac{u_i+u_{i+1}+2R}{2})A_{i+2}+(\frac{A_{i+2}+A_{i+1}}{2}-x_2)(u_{i+1}+R)}{\frac{A_{i+2}+A_{i+1}}{2}-\frac{u_i+u_{i+1}+2R}{2}}$$

R is the radius of the beam. The domain is discretized into $\Omega_{j,i} = \Omega(\boldsymbol{x}_{j,i}, t)$ with $\boldsymbol{x}_{j,i} = ((j + \frac{1}{2})h, \frac{A_{i+1}+A_i}{2}(x_{1j,i}), 0)$, the left and right boundaries are denoted as $A_{j,i}$ and $A_{j,i+1}$. The notations j and i indicates respectively the discretization in direction $\boldsymbol{e_1}$ and $\boldsymbol{e_2}$. We suppose that $h \ll P$.

5.2.4 Attempts of simplifications

Firstly, the hypothesis H2 imposes the simplification for each $\Omega_{j,i}$:

$$\oint_{A_{S_{j,i}}} \boldsymbol{n} \cdot \boldsymbol{v}\, dS_\xi = 0 \tag{5.23}$$

With the definition (5.22b) of $\Omega(\boldsymbol{x}, t)$, and the evolution of its boundary with respect to $\boldsymbol{x}$ (the term $\boldsymbol{n} \cdot \nabla \boldsymbol{\xi}$ in eq. (5.10), eq. (5.20) and eq. (5.21)) can be calculated. On the boundaries normal to $\boldsymbol{e_1}$ and $\boldsymbol{e_3}$, its value is zero since $\Omega(\boldsymbol{x}, t)$ is not deformable in these two directions. Therefore, we have:

$$\frac{1}{V_t}\oint_{A_f} (\boldsymbol{n} \cdot \nabla \boldsymbol{\xi}) \cdot \boldsymbol{\varphi} dS_\xi = \frac{1}{V_t}\oint_{A_{f2}^-} (\boldsymbol{n} \cdot \nabla \boldsymbol{\xi}) \cdot \boldsymbol{\varphi} dS_\xi + \frac{1}{V_t}\oint_{A_{f2}^+} (\boldsymbol{n} \cdot \nabla \boldsymbol{\xi}) \cdot \boldsymbol{\varphi} dS_\xi \tag{5.24}$$

With the hypothesis H4, particularly for $\Omega_{j,i}$:

$$(\boldsymbol{n} \cdot \nabla \boldsymbol{\xi})|_{A_{j,i}} = \left(-\frac{1}{2}\left(\frac{\partial u_{i-1}}{\partial \xi_1} + \frac{\partial u_i}{\partial \xi_1}\right), -\left.\frac{\partial A_{f2}^-}{\partial x_2}\right|_{x_2 = x_{2j,i}} + 1{,}0 \right) \tag{5.25a}$$

$$(\boldsymbol{n} \cdot \nabla \boldsymbol{\xi})|_{A_{j,i+1}} = \left(\frac{1}{2}\left(\frac{\partial u_i}{\partial \xi_1} + \frac{\partial u_{i+1}}{\partial \xi_1}\right), \left.\frac{\partial A_{f2}^+}{\partial x_2}\right|_{x_2 = x_{2j,i}} - 1{,}0 \right) \tag{5.25b}$$

Since $h \ll P$ (from H6), eq. (5.25a) and (5.25b) is supposed to be constant and equal to the value at half height ($\xi_1 = 0$). Therefore, we can define a new macroscopic property by area averaging:

$$\frac{1}{S_{A_{j,i}}}\oint_{A_{j,i}} \boldsymbol{\varphi} dS_\xi = \boldsymbol{\varphi}_{A_{j,i}} \tag{5.26}$$

Again with the hypothesis H4 of small rotations, we suppose that their surface is equal to their projection on the plan $(\boldsymbol{e_1}, \boldsymbol{e_3})$, i.e. $S_{A_{j,i}} \approx S_{A_{j,i+1}} \approx h \cdot P$, and by multiplying with the width defined at half height $l_{j,i} = (A_{j,i+1} - A_{j,i})\big|_{x = x_{1j,i}}$, the total volume can be obtained.

In conclusion, the continuity equation (5.10) can be simplified into:

$$div(\beta \underline{\boldsymbol{v}}) + \frac{1}{V_t}\nabla V_t \cdot \beta \underline{\boldsymbol{v}} - \frac{1}{l_{j,i}}\left((\boldsymbol{n} \cdot \nabla \boldsymbol{\xi})|_{A_{j,i}} \cdot \boldsymbol{v}_{A_{j,i}} + (\boldsymbol{n} \cdot \nabla \boldsymbol{\xi})|_{A_{j,i+1}} \cdot \boldsymbol{v}_{A_{j,i+1}}\right) = 0 \tag{5.27}$$

Where $\frac{1}{V_t}\nabla V_t = \frac{1}{l_{j,i}}\nabla l_{j,i}$ and $(\boldsymbol{n} \cdot \nabla \boldsymbol{\xi})|_{A_{j,i}}$ are functions dependent on u_{i-1}, u_i and u_{i+1}.

As for the left hand of the momentum equation (5.20), since with hypothesis H4 $\hat{\boldsymbol{v}}$ is only in the direction $\boldsymbol{e_2}$, $\hat{\boldsymbol{v}} \cdot \boldsymbol{n}$ is not equal to zero only on the boundaries $A_{j,i}$ and $A_{j,i+1}$. According to the definition in H6:

$$-\frac{1}{V_t}\oint_{A_f} (\hat{\boldsymbol{v}} \cdot \boldsymbol{n})\boldsymbol{v}\, dS_\xi = \frac{1}{l_{j,i}}\left(\frac{\dot{u}_{i-1} + \dot{u}_i}{2}\boldsymbol{v}_{A_{j,i}} - \frac{\dot{u}_i + \dot{u}_{i+1}}{2}\boldsymbol{v}_{A_{j,i+1}}\right) \tag{5.28}$$

Similarly, the term concerning the evolution of the boundary of the RVE can be written as:

$$-\frac{1}{V_t}\oint_{A_f(\boldsymbol{x},t)}(\boldsymbol{n}\cdot\boldsymbol{\nabla\xi})\cdot(\boldsymbol{v}\otimes\boldsymbol{v})\,dS_\xi = -\frac{1}{l_{j,i}}\left((\boldsymbol{n}\cdot\nabla\boldsymbol{\xi})|_{A_{j,i}}\cdot\frac{1}{S_{A_{j,i}}}\oint_{A_{j,i}}(\boldsymbol{v}\otimes\boldsymbol{v})dS_\xi + (\boldsymbol{n}\cdot\nabla\boldsymbol{\xi})|_{A_{j,i+1}}\cdot\frac{1}{S_{A_{j,i+1}}}\oint_{A_{j,i+1}}(\boldsymbol{v}\otimes\boldsymbol{v})dS_\xi\right) \tag{5.29}$$

Recalling the turbulence model, this time the volume average is replaced by an area average, thus on boundary $A_{j,i}$, $\boldsymbol{v}=\left(\frac{1}{S_{A_{j,i}}}\oint_{A_{j,i}}\boldsymbol{v}dS_\xi\right)+\boldsymbol{v}'$:

$$\frac{1}{S_{A_{j,i}}}\oint_{A_{j,i}}(\boldsymbol{v}\otimes\boldsymbol{v})dS_\xi = \left(\frac{1}{S_{A_{j,i}}}\oint_{A_{j,i}}\boldsymbol{v}dS_\xi\right)\otimes\left(\frac{1}{S_{A_{j,i}}}\oint_{A_{j,i}}\boldsymbol{v}dS_\xi\right)+\frac{1}{S_{A_{j,i}}}\oint_{A_{j,i}}(\boldsymbol{v}'\otimes\boldsymbol{v}')dS_\xi \tag{5.30}$$

$$\begin{aligned}\boldsymbol{\sigma_{Re}}|_{A_{j,i}} &= \rho_f\frac{1}{S_{A_{j,i}}}\oint_{A_{j,i}}(\boldsymbol{v}'\otimes\boldsymbol{v}')dS_\xi \\ &= -\frac{2}{3}\rho_f k_T\boldsymbol{I}+\mu_T(\nabla\frac{1}{S_{A_{j,i}}}\oint_{A_{j,i}}\boldsymbol{v}dS_\xi+\nabla^T\frac{1}{S_{A_{j,i}}}\oint_{A_{j,i}}\boldsymbol{v}dS_\xi)\end{aligned} \tag{5.31}$$

As a result, substituting eq. (5.30) and eq. (5.31) into eq. (5.29), and with H3 we have:

$$\begin{aligned}-\frac{1}{V_t}\oint_{A_f(\boldsymbol{x},t)}(\boldsymbol{n}\cdot\boldsymbol{\nabla\xi})\cdot(\boldsymbol{v}\otimes\boldsymbol{v})\,dS_\xi &= -\frac{1}{l_{j,i}}\Big\{(\boldsymbol{n}\cdot\nabla\boldsymbol{\xi})|_{A_{j,i}}\cdot\left[\left(\boldsymbol{v}_{A_{j,i}}\otimes\boldsymbol{v}_{A_{j,i}}\right)+\mu_T\left(\nabla\boldsymbol{v}_{A_{j,i}}+\nabla^T\boldsymbol{v}_{A_{j,i}}\right)\right] \\ &+(\boldsymbol{n}\cdot\nabla\boldsymbol{\xi})|_{A_{j,i+1}}\cdot\left[\left(\boldsymbol{v}_{A_{j,i+1}}\otimes\boldsymbol{v}_{A_{j,i+1}}\right)+\mu_T\left(\nabla\boldsymbol{v}_{A_{j,i+1}}+\nabla^T\boldsymbol{v}_{A_{j,i+1}}\right)\right]\Big\}\end{aligned} \tag{5.32}$$

Since $\hat{\boldsymbol{v}}$ and $\boldsymbol{v}$ are both constant and equal to the velocity of the structure, $\oint_{A_s}(\hat{\boldsymbol{v}}\cdot\boldsymbol{n})\boldsymbol{v}\,dS_\xi=0$. The term is then simplified as (5.28):

$$\begin{aligned}-\frac{1}{V_t}\int_{\partial\Omega_f}\boldsymbol{v}(\hat{\boldsymbol{v}}\cdot\boldsymbol{n})dS_\xi &= -\frac{1}{V_t}\oint_{A_s}(\hat{\boldsymbol{v}}\cdot\boldsymbol{n})\boldsymbol{v}\,dS_\xi-\frac{1}{V_t}\oint_{A_f}(\hat{\boldsymbol{v}}\cdot\boldsymbol{n})\boldsymbol{v}\,dS_\xi \\ &= \frac{1}{l_{j,i}}\left(\frac{\dot{u}_{i-1}+\dot{u}_i}{2}\boldsymbol{v}_{A_{j,i}}-\frac{\dot{u}_i+\dot{u}_{i+1}}{2}\boldsymbol{v}_{A_{j,i+1}}\right)\end{aligned} \tag{5.33}$$

The last term to be explained in (5.20) is $\frac{1}{V_t}\int_{\Omega_f}\boldsymbol{v}\cdot div\hat{\boldsymbol{v}}dV_\xi$. According to the definition of the boundary positions in H5, $\hat{\boldsymbol{v}}$ inside the RVE should also be a piecewise linear function with respect to ξ_2:

$$div\hat{\boldsymbol{v}} = \begin{cases}\dfrac{\dot{u}_i-\dot{u}_{i-1}}{u_i-u_{i-1}-2R}\left(x_{1j,i}+\xi_1,t\right) & if\ \dfrac{u_{i-1}+u_i}{2}\left(x_{1j,i}+\xi_1\right)\le\xi_2+x_{2j,i}<u_i\left(x_{1j,i}+\xi_1\right)-R \\ 0 & if\ u_i\left(x_{1j,i}+\xi_1\right)-R\le\xi_2+x_{2j,i}\le u_i\left(x_{1j,i}+\xi_1\right)+R \\ \dfrac{\dot{u}_{i+1}-\dot{u}_i}{u_{i+1}-u_i-2R}\left(x_{1j,i}+\xi_1,t\right) & if\ u_i\left(x_{1j,i}+\xi_1\right)+R\le\xi_2+x_{2j,i}<\dfrac{u_{i+1}+u_i}{2}\left(x_{1j,i}+\xi_1\right)\end{cases} \tag{5.34}$$

Again with the hypothesis $h\ll P$, it is supposed that the variation of $div\hat{\boldsymbol{v}}$ with respect to ξ_1 is negligible in $\Omega_{j,i}$. With an assumption quite strong as below:

$$\frac{1}{V_t}\int_{\Omega_f} \boldsymbol{v} div\hat{\boldsymbol{v}} dV_\xi$$

$$\begin{aligned}
&= \frac{1}{l_{j,i}}\left(\int_{\frac{u_{i-1}+u_i}{2}(x_{1j,i})}^{u_i(x_{1j,i})-R} div\hat{\boldsymbol{v}}\frac{1}{S_{A_{j,i}}}\oint_{A_{j,i}} \boldsymbol{v} dS_\xi\, d\xi_2\right. \\
&\left. + \int_{u_i(x_{1j,i})+R}^{\frac{u_{i+1}+u_i}{2}(x_{1j,i})} div\hat{\boldsymbol{v}}\frac{1}{S_{A_{j,i+1}}}\oint_{A_{j,i+1}} \boldsymbol{v} dS_\xi\, d\xi_2\right) \\
&= \frac{1}{l_{j,i}}\theta_1(\boldsymbol{x}_{j,i}, t, u_{i-1}, u_i)\boldsymbol{v}_{A_{j,i}} + \frac{1}{l_{j,i}}\theta_2(\boldsymbol{x}_{j,i}, t, u_i, u_{i+1})\boldsymbol{v}_{A_{j,i+1}}
\end{aligned} \tag{5.35a}$$

$$\begin{aligned}
\theta_1(\boldsymbol{x}_{j,i}, t, u_{i-1}, u_i) &= \begin{cases} 0 & if\ u_i - u_{i-1} - 2R = 0 \\ \frac{\dot{u}_i - \dot{u}_{i-1}}{2}(x_{1j,i}) & if\ not \end{cases} \\
\theta_2(\boldsymbol{x}_{j,i}, t, u_i, u_{i+1}) &= \begin{cases} 0 & if\ u_{i+1} - u_i - 2R = 0 \\ \frac{\dot{u}_{i+1} - \dot{u}_i}{2}(x_{1j,i}) & if\ not \end{cases}
\end{aligned} \tag{5.35b}$$

Similarly, the term of the right hand of the momentum equation (5.21) can be simplified as:

$$-\frac{1}{V_t}\oint_{A_f} (\boldsymbol{n}\cdot\boldsymbol{\nabla\xi})\cdot\boldsymbol{\sigma_f} dS_\xi$$

$$\begin{aligned}
&= -\frac{1}{l_{j,i}}\left((\boldsymbol{n}\cdot\nabla\boldsymbol{\xi})|_{A_{j,i}}\cdot\frac{1}{S_{A_{j,i}}}\oint_{A_{j,i}}\boldsymbol{\sigma_f} dS_\xi + (\boldsymbol{n}\cdot\nabla\boldsymbol{\xi})|_{A_{j,i+1}}\right. \\
&\left.\cdot\frac{1}{S_{A_{j,i+1}}}\oint_{A_{j,i+1}}\boldsymbol{\sigma_f} dS_\xi\right)
\end{aligned} \tag{5.36}$$

By substituting eq. (5.28), eq. (5.32), eq. (5.33) and eq. (5.34) into eq. (5.20) and by replacing eq. (5.9) and eq. (5.36) into eq. (5.21), with the hypothesis that the dynamic viscosity is much lower than the turbulent viscosity, the equivalent momentum equation expressed with the macroscopic properties is as below:

$$\begin{aligned}
&\rho_f\left(\frac{\partial(\beta\underline{\boldsymbol{v}})}{\partial t} + \frac{1}{V_t}\frac{\partial V_t}{\partial t}(\beta\underline{\boldsymbol{v}}) + div\left(\beta(\underline{\boldsymbol{v}}\otimes\underline{\boldsymbol{v}})\right) + \frac{1}{V_t}\nabla V_t\left(\beta(\underline{\boldsymbol{v}}\otimes\underline{\boldsymbol{v}})\right)\right) \\
&\quad + div\left(\beta\mu_T(\nabla\underline{\boldsymbol{v}} + \nabla^T\underline{\boldsymbol{v}})\right) + \frac{1}{V_t}\nabla V_t\left(\beta\mu_T(\nabla\underline{\boldsymbol{v}} + \nabla^T\underline{\boldsymbol{v}})\right) \\
&\quad + \frac{\rho_f}{l_{j,i}}\left\{\left[(\dot{u}_{i-1} + \dot{u}_i)\boldsymbol{v}_{A_{j,i}} - (\dot{u}_i + \dot{u}_{i+1})\boldsymbol{v}_{A_{j,i+1}}\right] - (\boldsymbol{n}\cdot\nabla\boldsymbol{\xi})|_{A_{j,i}}\right. \\
&\quad \cdot\left[\left(\boldsymbol{v}_{A_{j,i}}\otimes\boldsymbol{v}_{A_{j,i}}\right) + \mu_T\left(\nabla\boldsymbol{v}_{A_{j,i}} + \nabla^T\boldsymbol{v}_{A_{j,i}}\right)\right] - (\boldsymbol{n}\cdot\nabla\boldsymbol{\xi})|_{A_{j,i+1}} \\
&\quad \cdot\left[\left(\boldsymbol{v}_{A_{j,i+1}}\otimes\boldsymbol{v}_{A_{j,i+1}}\right) + \mu_T\left(\nabla\boldsymbol{v}_{A_{j,i+1}} + \nabla^T\boldsymbol{v}_{A_{j,i+1}}\right)\right] \\
&\quad \left. + \theta_1(\boldsymbol{x}_{j,i}, t, u_{i-1}, u_i)\boldsymbol{v}_{A_{j,i}} + \theta_2(\boldsymbol{x}_{j,i}, t, u_i, u_{i+1})\boldsymbol{v}_{A_{j,i+1}}\right\} \\
&\quad = -\nabla\overline{p} - \frac{1}{V_t}\frac{\partial V_t}{\partial t}\overline{p} + \frac{1}{l_{j,i}}\left((\boldsymbol{n}\cdot\nabla\boldsymbol{\xi})|_{A_{j,i}}\cdot p_{A_{j,i}} + (\boldsymbol{n}\cdot\nabla\boldsymbol{\xi})|_{A_{j,i+1}}\cdot p_{A_{j,i+1}}\right) \\
&\quad + \beta\rho_f\boldsymbol{g} + \boldsymbol{F_{structure\to fluide}}
\end{aligned} \tag{5.37}$$

Where $\frac{1}{V_t}\frac{\partial V_t}{\partial t} = \frac{\dot{u}_{i+1}-\dot{u}_{i-1}}{u_{i+1}-u_{i-1}}(x_{1j,i})$ is a function dependent on u_{i-1} and u_{i+1}.

The last term represents the structure body force acting on the fluid and thus allows the coupling between the fluid and the structure:

$$\boldsymbol{F}_{\boldsymbol{structure\rightarrow fluide}} = \frac{1}{V_t}\oint_{A_s(\boldsymbol{x},t)} \boldsymbol{\sigma_f}\cdot\boldsymbol{n}\, dS_\xi \tag{5.38}$$

Recalling the model proposed by Paidoussis for the hydraulic forces (1.13) – (1.16):

$$\boldsymbol{F}_{\boldsymbol{structure\rightarrow fluide}} = -\frac{1}{S_{j,i}}(\boldsymbol{F_A}+\boldsymbol{F_N}+\boldsymbol{F_L}) \tag{5.39}$$

$$\begin{aligned}\boldsymbol{F_A} = -m_f\Bigg[&\frac{\partial}{\partial t}\left(\dot{u}_i(x_{1j,i})-\underline{v}_{2j,i}\right)+2\underline{v}_{1j,i}\frac{\partial}{\partial\xi_1}\left(\dot{u}_i(x_{1j,i})-\underline{v}_{2j,i}\right)\\&+\underline{v}_{1j,i}{}^2\frac{\partial^2 u_i}{\partial\xi_1{}^2}(x_{1j,i})\Bigg]\boldsymbol{e_2}\\ \boldsymbol{F_N} = -\Bigg[&\frac{1}{2}\rho D\underline{v}_{1j,i}C_N\left(\dot{u}_i(x_{1j,i})-\underline{v}_{2j,i}+\underline{v}_{1j,i}\frac{\partial u_i}{\partial\xi_1}(x_{1j,i})\right)\\&+\frac{1}{2}\rho D C_D\left(\dot{u}_i(x_{1j,i})-\underline{v}_{2j,i}\right)\Bigg]\boldsymbol{e_2}\\ \boldsymbol{F_L} = &\frac{1}{2}\rho D\underline{v}_{1j,i}{}^2C_T\boldsymbol{e_1}+\frac{1}{2}\rho D\underline{v}_{1j,i}{}^2C_T\frac{\partial u_i}{\partial\xi_1}(x_{1j,i})\boldsymbol{e_2}\end{aligned} \tag{5.40}$$

where $S_{j,i} = l_{j,i}\cdot P$.

In conclusion, the variables in the equivalent governing equations of the fluid are:

- The volume averaging velocity of fluid $\underline{\boldsymbol{v}}$ (in $\boldsymbol{e_1}$ and $\boldsymbol{e_2}$)
- The area averaging velocity of fluid on the moving boundaries $\boldsymbol{v}_{A_{j,i}}$ and $\boldsymbol{v}_{A_{j,i+1}}$
- The volume averaging pressure of fluid $\overline{p}$
- The area averaging pressure on the moving boundaries $p_{A_{j,i}}$ and $p_{A_{j,i+1}}$
- The displacement of the beam u_{i-1}, u_i and u_{i+1}

For a layer with N beam sections in a row, there are 3N equations for fluid, coupling with N equations for 7N-1 (2N for $\underline{\boldsymbol{v}}$, 2($N$-1) for $\boldsymbol{v}_{A_{j,i}}$, N for $\overline{p}$, N+1 for $p_{A_{j,i}}$ and N for u_i) unknowns. By building a relationship between the volume averaging properties and the area averaging ones, the problem can be closed. Gineau [143] in her work applied the co-located finite volume method and thus established the relationship by equating their integrals on the boundary. This idea can be reused in our further study.

5.3 Discussion

In this chapter, we aim at constructing an improved model which takes into consideration the coupling between the fuel pins by the flow between them. In order to avoid the large number of degrees of freedom necessary in a CFD calculation, the space averaging method is adopted to build a global model characterized by the macroscopic properties.

There are already many existing works [89],[142],[143] utilizing this idea and obtaining good agreements between the simulation results and the experiments. However, these methods need to be modified since in our studied case, the relative displacements of the fuel pins should be modeled to be able to take the impacts between them into account. What's more, their displacements under external loads can be relatively large. As a result, in order to preserve an

individual description for each fuel pin, it would be necessary to use the deformable and mobile RVEs.

The work is started with a theoretical work on the modified spatial averaging theorem for the RVEs of which the volume is space-dependent. Then, it is applied on the local Navier-Stokes equations in ALE form to obtain the equivalent governing equations for fluid. There exists many new terms involving the deformability of the RVEs, which accounts for the exchanges between them. These terms make appear the macroscopic properties defined by the area averaging. The problem can be closed by establishing the relationships between the area averaging properties and the volume averaging ones.

In the process of transforming the local governing equations to the global ones, many hypothesis have been made, some can be quite strong (the one used to treating the space-dependent velocity of the observation volume) and risk to lose too much accuracy. Therefore, the verification of the resulting macroscopic model is necessary. There are mainly two ways, either by the experiments or by the accurate CFD calculations, which makes up a prospective for this part of work.

Conclusion and perspectives

This chapter is a recapitulation of the work presented in this document. The main outcomes of the PhD are presented and a discussion will be opened on perspectives.

Conclusion

This thesis work makes up a part of the risk analysis for the design of ASTRID reactor. When there is an external load, such as an earthquake, the fuel pins will collide with the wrapper tube and among themselves, challenging the integrity of cladding. For this safety concern, we search to describe accurately the dynamic responses of the fuel pins to an excitation. Special concern is paid on two physical phenomena quite complex: the strong non-linearity induced by the impacts and also the fluid structure interaction.

In fact, the aspect of numerous potential impacts in air has been studied both experimentally and numerically in the thesis work by T. Catterou, our goal is thus to take the fluid aspect into consideration. The first effort was to incorporate the fluid-elastic forces, basing on the widely used expression proposed by Paidoussis, into the structure model. Therefore, many parameters related to the hydraulic forces and the impact law are to be determined by the experiments. Inspired by the experiences from the previous tests, a new bench, named as CARNEAR, allowing to carry out the sweep sine excited experiments under different flow velocity with one single fuel pin and a row of fuel pins are designed. A guaranteed measurement with fast camera is anticipated to record the temporal history of motion. Even though the existence of spacer wire complicates the flow pattern and thus arises the difficulty in the investigation of local effects, the global parameters lumping the effects of different physics can be determined with the modal analysis. Besides, it can give an experimental basis to validate the modeling. Unfortunately, we were not able to perform the experiments as a result of the budget limitation and the difficulty arising from the health crisis.

The model taking the aforementioned physical phenomena into consideration by the Paidoussis's expression of the hydraulic forces and a penetration impact law is then exploited with the implicit Newmark scheme combining the Newton-Raphson iteration with a convergence criterion on force. Due to the lack of experiments, an estimation of the coefficients has been performed by a parametric study of their effects based on the previous theoretical and experimental outcomes. The phenomenal analyses on the nonlinear responses of the fuel pin have been performed. It is found that the global dynamic behavior of the fuel pin under excitation is relatively simple in our studied range and the complexity is mainly due to the local chatters in much smaller time scale. Different nonlinear vibration patterns, of multiples of imposed frequency and of period-doubling, have been identified. The former one corresponds to the "sticking" contact, and the latter one identifying the sub-harmonics corresponds to the alternative "sticking" contact and simple "rebound". The chaotic response has been figured out as the random alternation. The mixing of different sub-harmonics is also observed to be another source of the transition to the chaos. Besides, the nonlinearity of the system of a row of fuel pins is observed to be weaker, even with a greater number of contact points. It is possibly due to the greater space for the vibration.

The nonlinearity can lead to coexisting vibration regimes, it is difficult to for the direct time-integration to fully cover the possible outcomes since the different initial conditions are to be searched. The periodic dynamic response searching methods, well known for the good

performance with the smooth nonlinearity in terms of economizing the computation resources and good agreement with the reference, are applied to address this problem. Their performance with impact problems are evaluated before applying the full fuel pin model.

The first evaluation is on the classical frequency-domain method HBM, of the high order purely frequency-based type, with a simplified fuel pin model with only four contact points. A good agreement with the direct time-integration method is obtained in the case with less rigid contact points, costing less time and detecting easily the period-doubling bifurcation points. This observation is coherent with the previously reported work as their studied range of the stiffness ratio between the contact and the system is less than 100. The difficulty of describing the sticking contact and the resulting impact forces with the Fourier series has been identified when the contact points are very rigid. This also results in a quite limited range of the excitation amplitude that can be studied.

In order to overcome these limitations, we turn to the so-called global periodic time integration (GPTI) method, which consists in searching for the state vector for each node at each time step in one period. Since this method is not much studied, its performance with the impact problems is firstly evaluated with a parametric study of the 1-dof vibro-impact system and is found to have the potential to study the very rigid contact problems: the limit on the stiffness ratio between the contact point and the system is of 1000 with uniform time steps and of 5000 with adaptive time discretization. The difficulty is mainly due to the change of phase along with the continuation, which results in the sharp variation of the impact force. The excitation amplitude is therefore limited due to the occurrence of the "sticking" contacts, where successive peaks of impact force challenge the numeric convergence.

Since it appears to have a better performance than the HBM, the GPTI method for problems of multiple dofs with several contact points is then developed and applied to the study of the fuel pin model. The verification is performed with less rigid contact points by comparing the periodic solutions on the continuation branch with the steady-state vibrations obtained with the direct time-integration method. The continuation is be performed in our interested range but is rather difficult in terms of the short arc-length, which results in a large number of continuation steps, thus demands a large computation memory. A linear contact damper, allowing to calm the chatters following the first penetration into the contact point and have the peaks of the impact force less pointed, makes the continuation easier.

The GPTI method is still not applicable to a very rigid contact problem even with the effort of introducing a contact damper, as the impact forces are still too pointed to have an easy continuation. In fact, it is acceptable to study the global dynamic behavior of the fuel pin with a reduced contact stiffness if regardless of the impact forces. With the continuous solution branch, the global periodic time integration method has the advantage of interpreting easily the change of the periodic patterns, such as the occurrence of the period-doubling phenomenon. The dynamic behavior of the fuel pin with several contact points is so complex that there exists different solution branches for the same excitation. Not like the study of the systems with less complex dynamics, we are not able to obtain all the possible periodic responses with one continuation computation. Even though the direct time-integration result can be a complementary method of finding the start points of the solution branches, it can never be exhaustive since it is very sensible to the initial condition chosen for a system of complex dynamic behaviors. Therefore, the periodic searching method and the direct time-integration

method are both limited in interpreting the dynamic behavior of the fuel pin when it becomes complex.

The model used above is more suited to the study of a single fuel pin, in order to be able to simulate the coupling motion of several fuel pins, an improved model, characterized by the macroscopic properties is proposed basing on the space averaging method. Overcoming the limits of the existing methods, modifications have been made to allow modelling the relatively big displacements of the fuel pins and their relative displacements by considering the deformable and mobile RVEs. The verification of the hypothesis used for deriving this model needs further investigation.

Perspectives

Many perspectives are opened as a result of this PhD thesis either for experiments, or the modeling and the associated numerical methods.

First of all, the experiments anticipated in CARNEAU are expected to be realized to the model parameters and offer a validation of the proposed models and the numeric methods.

As for the global periodic time integration method, it should be optimized in terms of its functionality. The associated stability analysis and the detection of the bifurcation point for the other solution branches are anticipated. And optimization for the initialization and the compression of the number of variables for a shorter computation time.

It was shown in the work of Catterou that global dynamics of systems with impacts are affected greatly by the configuration. The continuation with respect to the related parameters, such as the clearance can be carried out with the existing method. This suggests the investigation of a coupled problem whose objective is to model long-term behavior with evolving gaps due to the contacts or the irradiation.

In fact, part of the difficulty with the rigid impact problems arises from the fact that we are simulating simultaneously two physical phenomena of very different time scales: the global vibration and the local chatters induced by the impacts. An existing idea is to model the global vibration with an appropriate shock law which does not describe the penetrations in detail but only presents the sticking or the rebound.

The model taking the coupling between adjacent fuel pins into account is to be implemented. The verification of the model by either the experiments or the accurate CFD simulations is also necessary. It can be exploited with both the traditional time-integration approach and the periodic searching method. Therefore, the coupling effect can be evaluated by comparing with the results from the former model.

Appendix A

The discretization of the equation (3.17) is accomplished with the Bernoulli beam element. Using N uniform finite elements, the length of which is $l = L/N$. The coordinates of the nodes are x_i $(i = 1, \dots, N+1)$. For each node, there are two degrees of freedom: displacement w (or deflection) and rotation $\varphi = \partial w/\partial x$. On each element, the displacement can be represented by:

$$w(x) = w_1 N_1(x) + \varphi_1 N_2(x) + w_2 N_3(x) + \varphi_2 N_4(x) = \boldsymbol{N^t q}$$

Where the shape functions N_i $(i = 1, \dots, 4)$ are Hermite polynomials of third order. In vector form, the shape functions are written as:

$$\boldsymbol{N}(\xi) = \begin{bmatrix} (1-\xi)^2\left(\frac{1}{4}\xi + \frac{1}{2}\right) \\ \frac{1}{8}l(1-\xi)^2(1+\xi) \\ (1+\xi)^2\left(\frac{1}{2} - \frac{1}{4}\xi\right) \\ \frac{1}{8}l(1+\xi)^2(\xi-1) \end{bmatrix}, \text{ with } \xi = \frac{2x - x_n - x_{n+1}}{l}$$

It is associated with the degrees of freedom of the element:

$$\boldsymbol{q}^T = [w_1, \varphi_1, w_2, \varphi_2]$$

For each element, there are stiffness matrices associated with the structure, the added mass, the gravity and the viscous forces:

$$\boldsymbol{K_e = K_s^e + K_{iner,f}^e + K_{grav,1}^{ie} - K_{grav,2}^e - K_{drag}^{ie} - K_{v,1}^{ie} + K_{v,2}^e}$$

Respectively,

$$\int_0^L (EIw''\delta w'')dx = \bigcup_{ie=1}^{N} \delta \boldsymbol{q}^T \left(\int_{-1}^{1} \boldsymbol{N}'' EI \boldsymbol{N}''^T d\xi \right) \boldsymbol{q} = \bigcup_{ie=1}^{N} \delta \boldsymbol{q}^T \boldsymbol{K_s^e q}$$

$$\int_0^L \chi \rho A U^2 w'' \delta w \, dx = \bigcup_{ie=1}^{N} \delta \boldsymbol{q}^T \left(\int_{-1}^{1} \boldsymbol{N} \chi \rho A U^2 \boldsymbol{N}''^T d\xi \right) \boldsymbol{q} = \bigcup_{ie=1}^{N} \delta \boldsymbol{q}^T \boldsymbol{K_{iner,f}^e q}$$

$$\int_0^L (m - \rho A) g (L - x) w'' \delta w dx = (m - \rho A) g \sum_{n=1}^{N} \int_{x_n}^{x_{n+1}} (L - x) w'' \delta w dx$$

$$= \bigcup_{ie=1}^{N} \delta \boldsymbol{q}^T \left(\int_{-1}^{1} 2(m - \rho A) g \left(N - ie + \frac{1-\xi}{2} \right) \boldsymbol{N} \boldsymbol{N}''^T d\xi \right) \boldsymbol{q} = \bigcup_{ie=1}^{N} \delta \boldsymbol{q}^T \boldsymbol{K_{grav,1}^{ie} q}$$

$$\int_0^L (m - \rho A) g w' \delta w dx = \bigcup_{ie=1}^{N} \delta \boldsymbol{q}^T \left(\int_{-1}^{1} (m - \rho A) g \boldsymbol{N} \boldsymbol{N}'^T dx \right) \boldsymbol{q} = \bigcup_{ie=1}^{N} \delta \boldsymbol{q}^T \boldsymbol{K_{grav,2}^e q}$$

$$\int_0^L \frac{1}{2} \rho D^2 U^2 C_b w'' \delta w \, dx = \bigcup_{ie=1}^{N} \delta \boldsymbol{q}^T \left(\int_{-1}^{1} \boldsymbol{N} \frac{1}{2} \rho D^2 U^2 C_b \boldsymbol{N}''^T d\xi \right) \boldsymbol{q} = \bigcup_{ie=1}^{N} \delta \boldsymbol{q}^T \boldsymbol{K_{drag}^{ie} q}$$

$$\int_0^L \frac{1}{2} \rho_f D U^2 C_T \left(1 + \frac{D}{D_h}\right) (L - x) w'' \delta w dx = \frac{1}{2} \rho_f D U^2 C_T \left(1 + \frac{D}{D_h}\right) \sum_{n=1}^{N} \int_{x_n}^{x_{n+1}} (L - x) w'' \delta w dx$$

$$= \bigcup_{ie=1}^{N} \delta \boldsymbol{q}^T \left(\int_{-1}^{1} \rho_f D U^2 C_T \left(1 + \frac{D}{D_h}\right) \left(N - ie + \frac{1-\xi}{2} \right) \boldsymbol{N} \boldsymbol{N}''^T d\xi \right) \boldsymbol{q} = \bigcup_{ie=1}^{N} \delta \boldsymbol{q}^T \boldsymbol{K_{v,1}^{ie} q}$$

$$\int_0^L \left[\frac{1}{2}\rho DU^2 C_N + \frac{1}{2}\rho_f DU^2 C_T \frac{D_h}{D}\right] w'\delta w dx = \bigcup_{ie=1}^{N} \delta \boldsymbol{q}^T \left(\int_{-1}^{1} \left[\frac{1}{2}\rho DU^2 C_N + \frac{1}{2}\rho_f DU^2 C_T \frac{D_h}{D}\right] \boldsymbol{N}\boldsymbol{N}'^T d\xi\right) \boldsymbol{q}$$

$$= \bigcup_{ie=1}^{N} \delta \boldsymbol{q}^T \boldsymbol{K}_{\boldsymbol{v,2}}^{\boldsymbol{e}} \boldsymbol{q}$$

$$\boldsymbol{K}_{\boldsymbol{s}}^{\boldsymbol{e}} = \frac{EI}{l^3}\begin{bmatrix} 12 & 6l & -12 & 6l \\ 6l & 4l^2 & -6l & 2l^2 \\ -12 & -6l & 12 & -6l \\ 6l & 2l^2 & -6l & 4l^2 \end{bmatrix}, \boldsymbol{K}_{\boldsymbol{iner,f}}^{\boldsymbol{e}} = \frac{-\chi\rho AU^2}{30l}\begin{bmatrix} 36 & 33l & -36 & 3l \\ 3l & 4l^2 & -3l & -l^2 \\ -36 & -3l & 36 & -33l \\ 3l & -l^2 & -3l & 4l^2 \end{bmatrix}$$

$$\boldsymbol{K}_{\boldsymbol{grav,1}}^{\boldsymbol{ie}} = \frac{1}{30}(m-\rho A)g \cdot \left((ie-N)\begin{bmatrix} 36 & 33l & -36 & 3l \\ 3l & 4l^2 & -3l & -l^2 \\ -36 & -3l & 36 & -33l \\ 3l & -l^2 & -3l & 4l^2 \end{bmatrix} + \begin{bmatrix} -33 & -27l & 33 & -6l \\ -3l & -3l^2 & 3l & 0 \\ 3 & -3l & -3 & 6l \\ 0 & l^2 & 0 & -l^2 \end{bmatrix}\right)$$

$$\boldsymbol{K}_{\boldsymbol{grav,2}}^{\boldsymbol{e}} = \frac{1}{60}(m-\rho A)g\begin{bmatrix} -30 & 6l & 30 & -6l \\ -6l & 0 & 6l & -l^2 \\ -30 & -6l & 30 & 6l \\ 6l & l^2 & -6l & 0 \end{bmatrix}, \boldsymbol{K}_{\boldsymbol{drag}}^{\boldsymbol{ie}} = \frac{-\rho D^2 U^2 C_b}{60l}\begin{bmatrix} 36 & 33l & -36 & 3l \\ 3l & 4l^2 & -3l & -l^2 \\ -36 & -3l & 36 & -33l \\ 3l & -l^2 & -3l & 4l^2 \end{bmatrix}$$

$$\boldsymbol{K}_{\boldsymbol{v,1}}^{\boldsymbol{ie}} = \frac{1}{60}\rho_f DU^2 C_T\left(1+\frac{D}{D_h}\right)\cdot\left((ie-N)\begin{bmatrix} 36 & 33l & -36 & 3l \\ 3l & 4l^2 & -3l & -l^2 \\ -36 & -3l & 36 & -33l \\ 3l & -l^2 & -3l & 4l^2 \end{bmatrix} + \begin{bmatrix} -33 & -27l & 33 & -6l \\ -3l & -3l^2 & 3l & 0 \\ 3 & -3l & -3 & 6l \\ 0 & l^2 & 0 & -l^2 \end{bmatrix}\right)$$

$$\boldsymbol{K}_{\boldsymbol{v,2}}^{\boldsymbol{e}} = \frac{1}{120}\left[\rho DU^2 C_N + \rho_f DU^2 C_T \frac{D}{D_h}\right]\begin{bmatrix} -30 & 6l & 30 & -6l \\ -6l & 0 & 6l & -l^2 \\ -30 & -6l & 30 & 6l \\ 6l & l^2 & -6l & 0 \end{bmatrix}$$

The damping matrices associated with the added mass and the viscous forces for each element is expressed as:

$$\boldsymbol{C}_{\boldsymbol{e}} = \boldsymbol{C}_{\boldsymbol{v}}^{\boldsymbol{e}} + \boldsymbol{C}_{\boldsymbol{iner,f}}^{\boldsymbol{e}}$$

Respectively,

$$\int_0^L \left(\frac{1}{2}\rho_f DUC_N + \frac{1}{2}\rho_f DC_D\right)\dot{w}\delta w dx = \bigcup_{ie=1}^{N} \delta \boldsymbol{q}^T \left(\int_{-1}^{1} \left(\frac{1}{2}\rho_f DUC_N + \frac{1}{2}\rho_f DC_D\right)\boldsymbol{N}\boldsymbol{N}^T d\xi\right)\dot{\boldsymbol{q}} = \bigcup_{ie=1}^{N} \delta \boldsymbol{q}^T \boldsymbol{C}_{\boldsymbol{v}}^{\boldsymbol{e}} \dot{\boldsymbol{q}}$$

$$\int_0^L 2\chi\rho AU\dot{w}'\delta w\, dx = \bigcup_{ie=1}^{N} \delta \boldsymbol{q}^T \left(\int_{-1}^{1} \boldsymbol{N} 2\chi\rho AU \boldsymbol{N}'^T d\xi\right)\dot{\boldsymbol{q}} = \bigcup_{ie=1}^{N} \delta \boldsymbol{q}^T \boldsymbol{C}_{\boldsymbol{iner,f}}^{\boldsymbol{e}} \dot{\boldsymbol{q}}$$

$$\boldsymbol{C}_{\boldsymbol{iner,f}}^{\boldsymbol{e}} = \frac{\chi\rho AU}{30}\begin{bmatrix} -30 & 6l & 30 & -6l \\ -6l & 0 & 6l & -l^2 \\ -30 & -6l & 30 & 6l \\ 6l & l^2 & -6l & 0 \end{bmatrix}, \boldsymbol{C}_{\boldsymbol{v}}^{\boldsymbol{e}} = \left(\frac{1}{2}\rho_f DUC_N + \frac{1}{2}\rho_f DC_D\right)\frac{l}{420}\begin{bmatrix} 156 & 22l & 54 & -13l \\ 22l & 4l^2 & 13l & -3l^2 \\ 54 & -6l & 156 & -22l \\ -13l & -3l^2 & -22l & 4l^2 \end{bmatrix}$$

And the mass matrix for each element is written as:

$$\int_0^L (m+\chi\rho A)\ddot{w}\delta w\, dx = \bigcup_{ie=1}^{N} \delta \boldsymbol{q}^T \left(\int_{-1}^{1} \boldsymbol{N}(m+\chi\rho A)\boldsymbol{N}^T d\xi\right)\ddot{\boldsymbol{q}} = \bigcup_{ie=1}^{N} \delta \boldsymbol{q}^T \boldsymbol{M}_{\boldsymbol{e}} \ddot{\boldsymbol{q}}$$

$$\boldsymbol{M}_{\boldsymbol{e}} = \frac{(m+\chi\rho A)l}{420}\begin{bmatrix} 156 & 22l & 54 & -13l \\ 22l & 4l^2 & 13l & -3l^2 \\ 54 & -6l & 156 & -22l \\ -13l & -3l^2 & -22l & 4l^2 \end{bmatrix}$$

The boundary condition is accounted on the N[th] element by the matrices expressed as follows:

$$\int_0^L \delta w\left(\chi_e(m+f\chi\rho A)\frac{\partial^2 w}{\partial t^2}\right)\delta(x-L)dx = \delta \boldsymbol{q}^T \left(\int_{-1}^{1} \boldsymbol{N}\chi_e(m+f\chi\rho A)\delta(\xi-1)\boldsymbol{N}^T d\xi\right)\ddot{\boldsymbol{q}} = \delta \boldsymbol{q}^T \boldsymbol{M}_{\boldsymbol{B}} \ddot{\boldsymbol{q}}$$

$$\int_0^L \delta w \left(\chi_e f \chi \rho A U \frac{\partial^2 w}{\partial t \partial x} + \left(\frac{1}{2} \rho D U C_N \overline{\chi_e} - f \chi \rho A U \right) \frac{\partial w}{\partial t} \right) \delta(x - L) dx$$

$$= \delta \boldsymbol{q}^T \left[\int_{-1}^{1} \boldsymbol{N} \chi_e f \chi \rho A U \delta(\xi - 1) \boldsymbol{N}'^T d\xi + \int_{-1}^{1} \boldsymbol{N} \left(\frac{1}{2} \rho D U C_N \overline{\chi_e} - f \chi \rho A U \right) \delta(\xi - 1) \boldsymbol{N}^T d\xi \right] \dot{\boldsymbol{q}}$$

$$= \delta \boldsymbol{q}^T \boldsymbol{C_B} \dot{\boldsymbol{q}}$$

$$\int_0^L \delta w \left(\left[-f \chi \rho A U^2 + \frac{1}{2} \rho D U^2 C_T \frac{D}{D_h} \chi_e - \chi_e (m - \rho A) g + \frac{1}{2} \rho D U^2 C_N \overline{\chi_e} \right] \frac{\partial w}{\partial x} \right) \delta(x - L) dx$$

$$= \delta \boldsymbol{q}^T \left(\int_{-1}^{1} \boldsymbol{N} \left[-f \chi \rho A U^2 + \frac{1}{2} \rho D U^2 \left(C_T \frac{D}{D_h} \chi_e + C_N \overline{\chi_e} \right) - \chi_e (m - \rho A) g \right] \delta(\xi - 1) \boldsymbol{N}'^T d\xi \right) \boldsymbol{q}$$

$$= \delta \boldsymbol{q}^T \boldsymbol{K_B} \boldsymbol{q}$$

$$\boldsymbol{M_B} = \chi_e (m + f \chi \rho A) \frac{1}{2} \begin{bmatrix} 0 & 0 & 0 & 0 \\ 0 & 0 & 0 & 0 \\ 0 & 0 & 1 & 0 \\ 0 & 0 & 0 & 0 \end{bmatrix}$$

$$\boldsymbol{C_B} = \chi_e f \chi \rho A U \frac{1}{2} \begin{bmatrix} 0 & 0 & 0 & 0 \\ 0 & 0 & 0 & 0 \\ 0 & 0 & 0 & 1 \\ 0 & 0 & 0 & 0 \end{bmatrix} + \frac{1}{2} \left(\frac{1}{2} \rho D U C_N \overline{\chi_e} - f \chi \rho A U \right) \begin{bmatrix} 0 & 0 & 0 & 0 \\ 0 & 0 & 0 & 0 \\ 0 & 0 & 1 & 0 \\ 0 & 0 & 0 & 0 \end{bmatrix}$$

$$\boldsymbol{K_B} = \left[-f \chi \rho A U^2 + \frac{1}{2} \rho D U^2 \left(C_T \frac{D}{D_h} \chi_e + C_N \overline{\chi_e} \right) - \chi_e (m - \rho A) g \right] \frac{1}{2} \begin{bmatrix} 0 & 0 & 0 & 0 \\ 0 & 0 & 0 & 0 \\ 0 & 0 & 0 & 1 \\ 0 & 0 & 0 & 0 \end{bmatrix}$$

The matrices for the whole beam is constructed by assembling the elementary matrices described above. As shown in Figure A.1, the boundary condition at $x = 0$ is translated by imposing $w_1 = 0$ and $\varphi_1 = 0$ at node x_1, thus the first two rows and the first two columns of the complete matrix are removed (in grey).

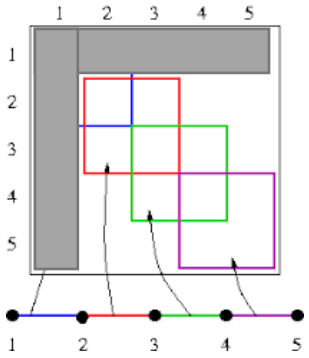

Figure A.1. Assemblage of elementary matrices

The vector for each element corresponding to the external force is written as:

$$\int_0^L F_{ext} \delta w dx = \bigcup_{ie=1}^{N} \delta \boldsymbol{q}^T \int_{-1}^{1} F_{ext}(x,t) \boldsymbol{N} d\xi = \bigcup_{ie=1}^{N} \delta \boldsymbol{q}^T \boldsymbol{F_e}$$

If the external force is uniformly distributed, thus,

$$\boldsymbol{F_e} = F_{ext}(t) \boldsymbol{Q_e} = F_{ext}(t) \frac{l}{2} \begin{bmatrix} 1 \\ \frac{l}{6} \\ 1 \\ -\frac{l}{6} \end{bmatrix}$$

The procedure of assemblage of the elementary vector $\boldsymbol{Q_e}$ is similar to that of the matrices.

If the external forces F_{c_i} $(i \in [\![1, nc]\!])$ are concentrated at certain points, which for simplification are supposed to coincide with the nodes localized at $\boldsymbol{x_c} = \{x_{c1}, x_{c2}, \cdots, x_{c_{nc}}\}$, then $\boldsymbol{F_c}$ is a vector with $(2c_i - 1)^{th}$ element equal to F_{c_i} and others equal to 0.

Finally, we obtain the following general form of the second order ordinary differential equation:

$$(\boldsymbol{M_s} + \boldsymbol{M_f})\ddot{\boldsymbol{X}} + \boldsymbol{C_f}\dot{\boldsymbol{X}} + (\boldsymbol{K_s} + \boldsymbol{K_f})\boldsymbol{X} + \boldsymbol{F_c} = F_{ext}(t)\boldsymbol{Q}$$

$$\boldsymbol{X}^T = [\, w_2 \; \varphi_2 \; \dots \; w_{N+1} \; \varphi_{N+1}]$$

Appendix B

Let Ω_0 be the reference configuration, of which the centroid is the origin of the coordinates η_i of the deformable and moving domain $\Omega_{\boldsymbol{x},t}$ with $\boldsymbol{x}$ defining its centroid and t the time. The local coordinates relative to $\boldsymbol{x}$ in $\Omega_{\boldsymbol{x},t}$ are marked by ξ_i. We now consider a mapping $\psi_{\boldsymbol{x},t}$ which at time t associates to a point $\boldsymbol{\eta} \in \Omega_0$ a point $\boldsymbol{\xi} \in \Omega_{\boldsymbol{x},t}$ such that:

$$\begin{aligned} \psi_{\boldsymbol{x},t}\colon \Omega_0 &\to \Omega_{\boldsymbol{x},t} \\ \boldsymbol{\eta} &\to \boldsymbol{\xi} = \psi_{\boldsymbol{x},t}(\boldsymbol{\eta}) \end{aligned} \tag{B.1}$$

The Jacobian matrix of $\psi_{\boldsymbol{x},t}$ is denoted by $\boldsymbol{J}_{\boldsymbol{x},t} = \nabla_{\boldsymbol{\eta}}\psi_{\boldsymbol{x},t}$ and $J_{\boldsymbol{x},t}$ its determinant. The instantaneous velocity of $\Omega_{\boldsymbol{x},t}$ denoted as $\hat{\boldsymbol{v}}$ is defined as:

$$\hat{\boldsymbol{v}}(\boldsymbol{\xi}, t) = \frac{\partial \psi_{\boldsymbol{x},t}}{\partial t}(\boldsymbol{\eta}) \tag{B.2}$$

The proof of the averaging theorem associated with divergence eq. (5.3) is as following, here we adopt the Einstein notations:

$$\begin{aligned} &\frac{\partial}{\partial x_i}\int_{\Omega_{\boldsymbol{x},t}} \varphi_i(\boldsymbol{x}+\boldsymbol{\xi}, t)\, dV_\xi \\ &\quad= \lim_{\Delta x_i \to 0} \frac{1}{\Delta x_i}\left(\int_{\Omega_{\boldsymbol{x}+\Delta x_i \boldsymbol{e_i},t}} \varphi_i\big(\boldsymbol{x}+\Delta x_i \boldsymbol{e_i} + \psi_{\boldsymbol{x}+\Delta x_i \boldsymbol{e_i},t}(\boldsymbol{\eta}), t\big) dV_\xi \right. \\ &\quad\left. - \int_{\Omega_{\boldsymbol{x},t}} \varphi_i\left(\boldsymbol{x}+\psi_{\boldsymbol{x},t}(\boldsymbol{\eta}), t\right) dV_\xi \right) \\ &\quad= \int_{\Omega_0} \lim_{\Delta x_i \to 0} \frac{1}{\Delta x_i}\Big(\varphi_i\big(\boldsymbol{x}+\Delta x_i \boldsymbol{e_i} + \psi_{\boldsymbol{x}+\Delta x_i \boldsymbol{e_i},t}(\boldsymbol{\eta}), t\big) J_{\boldsymbol{x}+\Delta x_i \boldsymbol{e_i},t} \\ &\quad- \varphi_i\left(\boldsymbol{x}+\psi_{\boldsymbol{x},t}(\boldsymbol{\eta}), t\right) J_{\boldsymbol{x},t}\Big)\, dV_\eta = \int_{\Omega_0} \frac{\partial}{\partial x_i}\Big(\varphi_i\left(\boldsymbol{x}+\psi_{\boldsymbol{x},t}(\boldsymbol{\eta}), t\right) J_{\boldsymbol{x},t}\Big)\, dV_\eta \end{aligned} \tag{B.3}$$

$$\begin{aligned} &\int_{\Omega_0} \frac{\partial}{\partial x_i}\Big(\varphi_i\left(\boldsymbol{x}+\psi_{\boldsymbol{x},t}(\boldsymbol{\eta}), t\right) J_{\boldsymbol{x},t}\Big)\, dV_\eta \\ &\quad= \int_{\Omega_{\boldsymbol{x},t}} \frac{\partial \varphi_i}{\partial (x+\xi)_j}\left(\delta_{ji} + \frac{\partial \psi_{\boldsymbol{x},t_j}}{\partial x_i}\right) dV_\xi + \int_{\Omega_{\boldsymbol{x},t}} \varphi_i(\boldsymbol{x}+\boldsymbol{\xi}, t)\frac{1}{J_{\boldsymbol{x},t}}\frac{\partial J_{\boldsymbol{x},t}}{\partial x_i} dV_\xi \end{aligned} \tag{B.4}$$

Since when we observe the local phenomena in $\Omega_{\boldsymbol{x},t}$, $\boldsymbol{x}$ is fixed, therefore inside the integral $\nabla_{\boldsymbol{x}+\boldsymbol{\xi}} = \nabla_{\boldsymbol{\xi}}$. And with the following process we obtain the so-called Abel's formula:

$$\frac{\partial J_{\boldsymbol{x},t}}{\partial x_i}=\begin{vmatrix} \frac{\partial}{\partial x_i}\frac{\partial \xi_1}{\partial \eta_1} & \frac{\partial}{\partial x_i}\frac{\partial \xi_1}{\partial \eta_2} & \frac{\partial}{\partial x_i}\frac{\partial \xi_1}{\partial \eta_3} \\ \frac{\partial \xi_2}{\partial \eta_1} & \frac{\partial \xi_2}{\partial \eta_2} & \frac{\partial \xi_2}{\partial \eta_3} \\ \frac{\partial \xi_3}{\partial \eta_1} & \frac{\partial \xi_3}{\partial \eta_2} & \frac{\partial \xi_3}{\partial \eta_3} \end{vmatrix}+\begin{vmatrix} \frac{\partial \xi_1}{\partial \eta_1} & \frac{\partial \xi_1}{\partial \eta_2} & \frac{\partial \xi_1}{\partial \eta_3} \\ \frac{\partial}{\partial x_i}\frac{\partial \xi_2}{\partial \eta_1} & \frac{\partial}{\partial x_i}\frac{\partial \xi_2}{\partial \eta_2} & \frac{\partial}{\partial x_i}\frac{\partial \xi_2}{\partial \eta_3} \\ \frac{\partial \xi_3}{\partial \eta_1} & \frac{\partial \xi_3}{\partial \eta_2} & \frac{\partial \xi_3}{\partial \eta_3} \end{vmatrix}+\begin{vmatrix} \frac{\partial \xi_1}{\partial \eta_1} & \frac{\partial \xi_1}{\partial \eta_2} & \frac{\partial \xi_1}{\partial \eta_3} \\ \frac{\partial \xi_2}{\partial \eta_1} & \frac{\partial \xi_2}{\partial \eta_2} & \frac{\partial \xi_2}{\partial \eta_3} \\ \frac{\partial}{\partial x_i}\frac{\partial \xi_3}{\partial \eta_1} & \frac{\partial}{\partial x_i}\frac{\partial \xi_3}{\partial \eta_2} & \frac{\partial}{\partial x_i}\frac{\partial \xi_3}{\partial \eta_3} \end{vmatrix} \tag{B.5}$$

with the chain rule, we have:

$$\frac{\partial}{\partial x_i}\frac{\partial \xi_k}{\partial \eta_l}=\frac{\partial \frac{\partial \xi_k}{\partial x_i}}{\partial \xi_k}\frac{\partial \xi_k}{\partial \eta_l}$$

Therefore (B.5) can be calculated term by term and gives:

$$\frac{\partial J_{\boldsymbol{x},t}}{\partial x_i}=\left(\frac{\partial}{\partial \xi_1}\frac{\partial \xi_1}{\partial x_i}+\frac{\partial}{\partial \xi_2}\frac{\partial \xi_2}{\partial x_i}+\frac{\partial}{\partial \xi_3}\frac{\partial \xi_3}{\partial x_i}\right)J_{\boldsymbol{x},t}=J_{\boldsymbol{x},t}\nabla_{\boldsymbol{\xi}}\cdot\frac{\partial \psi_{\boldsymbol{x},t}}{\partial x_i} \tag{B.6}$$

Substituting (B.6) into (B.4), we can obtain:

$$\begin{aligned}
&\int_{\Omega_{\boldsymbol{x},t}}\frac{\partial \varphi_i}{\partial (x+\xi)_j}\left(\delta_{ji}+\frac{\partial \psi_{\boldsymbol{x},t_j}}{\partial x_i}\right)dV_\xi+\int_{\Omega_{\boldsymbol{x},t}}\varphi_i(\boldsymbol{x}+\boldsymbol{\xi},t)\frac{1}{J_{\boldsymbol{x},t}}\frac{\partial J_{\boldsymbol{x},t}}{\partial x_i}dV_\xi \\
&\quad=\int_{\Omega_{\boldsymbol{x},t}}\frac{\partial \varphi_i}{\partial \xi_j}\delta_{ji}dV_\xi+\int_{\Omega_{\boldsymbol{x},t}}\left(\frac{\partial \varphi_i}{\partial \xi_j}\frac{\partial \psi_{\boldsymbol{x},t_j}}{\partial x_i}+\varphi_i\nabla_{\boldsymbol{\xi}}\cdot\frac{\partial \psi_{\boldsymbol{x},t}}{\partial x_i}\right)dV_\xi \\
&\quad=\int_{\Omega_{\boldsymbol{x},t}}\frac{\partial \varphi_i}{\partial \xi_i}dV_\xi+\int_{\Omega_{\boldsymbol{x},t}}\left(\nabla_{\boldsymbol{\xi}}\varphi_i\cdot\frac{\partial \psi_{\boldsymbol{x},t}}{\partial x_i}+\varphi_i\nabla_{\boldsymbol{\xi}}\cdot\frac{\partial \psi_{\boldsymbol{x},t}}{\partial x_i}\right)dV_\xi \\
&\quad=\int_{\Omega_{\boldsymbol{x},t}}\frac{\partial \varphi_i}{\partial \xi_i}dV_\xi+\int_{\Omega_{\boldsymbol{x},t}}\nabla_{\boldsymbol{\xi}}\left(\varphi_i\otimes\frac{\partial \psi_{\boldsymbol{x},t}}{\partial x_i}\right)dV_\xi \\
&\quad=\int_{\Omega_{\boldsymbol{x},t}}\frac{\partial \varphi_i}{\partial \xi_i}dV_\xi+\int_{\partial\Omega_{\boldsymbol{x},t}}\left(\frac{\partial \boldsymbol{\xi}}{\partial x_i}\cdot\boldsymbol{n}\right)\varphi_i dV_\xi
\end{aligned} \tag{B.7}$$

Combining (B.3) with (B.7), we finally obtain the permutation rule of integral and divergence for obtaining the theorem (5.3):

$$div\int_{\Omega_{\boldsymbol{x},t}}\boldsymbol{\varphi}(\boldsymbol{x}+\boldsymbol{\xi},t)dV_\xi=\int_{\Omega_{\boldsymbol{x},t}}div\boldsymbol{\varphi}(\boldsymbol{x}+\boldsymbol{\xi},t)dV_\xi+\int_{\partial\Omega_{\boldsymbol{x},t}}(\nabla_x\boldsymbol{\xi}\cdot\boldsymbol{n})\cdot\boldsymbol{\varphi}dV_\xi \tag{B.8}$$

The permutation rule for obtaining the theorem (5.4) is the famous Reynolds transport equation. The proof is similar as the previous one.

$$\begin{aligned}\frac{\partial}{\partial t}\int_{\Omega_{\boldsymbol{x},t}}\boldsymbol{\varphi}(\boldsymbol{x}+\boldsymbol{\xi},t)dV_\xi \\ &= \lim_{\Delta t\to 0}\frac{1}{\Delta t}\left(\int_{\Omega_{\boldsymbol{x},t+\Delta t}}\boldsymbol{\varphi}\big(\boldsymbol{x}+\psi_{\boldsymbol{x},t+\Delta t}(\boldsymbol{\eta}),t+\Delta t\big)dV_\xi\right. \\ &\left.-\int_{\Omega_{\boldsymbol{x},t}}\boldsymbol{\varphi}\left(\boldsymbol{x}+\psi_{\boldsymbol{x},t}(\boldsymbol{\eta}),t\right)dV_\xi\right) \\ &= \int_{\Omega_0}\lim_{\Delta t\to 0}\frac{1}{\Delta t}\Big(\boldsymbol{\varphi}\big(\boldsymbol{x}+\psi_{\boldsymbol{x},t+\Delta t}(\boldsymbol{\eta}),t+\Delta t\big)J_{\boldsymbol{x},t+\Delta t} \\ &-\boldsymbol{\varphi}\left(\boldsymbol{x}+\psi_{\boldsymbol{x},t}(\boldsymbol{\eta}),t\right)J_{\boldsymbol{x},t}\Big)dV_\eta = \int_{\Omega_0}\frac{\partial}{\partial t}\Big(\boldsymbol{\varphi}\left(\boldsymbol{x}+\psi_{\boldsymbol{x},t}(\boldsymbol{\eta}),t\right)J_{\boldsymbol{x},t}\Big)dV_\eta\end{aligned} \tag{B.9}$$

$$\begin{aligned}&\int_{\Omega_0}\frac{\partial}{\partial t}\Big(\boldsymbol{\varphi}\left(\boldsymbol{x}+\psi_{\boldsymbol{x},t}(\boldsymbol{\eta}),t\right)J_{\boldsymbol{x},t}\Big)dV_\eta \\ &\qquad=\int_{\Omega_{\boldsymbol{x},t}}\left(\frac{\partial\boldsymbol{\varphi}}{\partial t}+\frac{\partial\boldsymbol{\varphi}}{\partial\boldsymbol{\xi}}\frac{\partial\psi_{\boldsymbol{x},t}}{\partial t}\right)dV_\xi+\int_{\Omega_{\boldsymbol{x},t}}\boldsymbol{\varphi}(\boldsymbol{x}+\boldsymbol{\xi},t)\frac{1}{J_{\boldsymbol{x},t}}\frac{\partial J_{\boldsymbol{x},t}}{\partial t}dV_\xi\end{aligned} \tag{B.10}$$

With the Euler expansion formula, which is obtained with the similar process as in (B.4) and (B.5):

$$\frac{\partial J_{\boldsymbol{x},t}}{\partial t}=\left(\frac{\partial}{\partial\xi_1}\frac{\partial\psi_{\boldsymbol{x},t_1}}{\partial t}+\frac{\partial}{\partial\xi_2}\frac{\partial\psi_{\boldsymbol{x},t_2}}{\partial t}+\frac{\partial}{\partial\xi_3}\frac{\partial\psi_{\boldsymbol{x},t_3}}{\partial t}\right)J_{\boldsymbol{x},t}=J_{\boldsymbol{x},t}\nabla_{\boldsymbol{\xi}}\cdot\frac{\partial\psi_{\boldsymbol{x},t}}{\partial t}=J_{\boldsymbol{x},t}\nabla_{\boldsymbol{\xi}}\cdot\hat{\boldsymbol{v}} \tag{B.11}$$

As a result,

$$\begin{aligned}\int_{\Omega_0}\frac{\partial}{\partial t}\Big(\boldsymbol{\varphi}\left(\boldsymbol{x}+\psi_{\boldsymbol{x},t}(\boldsymbol{\eta}),t\right)J_{\boldsymbol{x},t}\Big)dV_\eta &= \int_{\Omega_{\boldsymbol{x},t}}\frac{\partial\boldsymbol{\varphi}}{\partial t}dV_\xi+\int_{\Omega_{\boldsymbol{x},t}}\big(\nabla_{\boldsymbol{\xi}}\boldsymbol{\varphi}\cdot\hat{\boldsymbol{v}}+\boldsymbol{\varphi}\nabla_{\boldsymbol{\xi}}\cdot\hat{\boldsymbol{v}}\big)dV_\xi \\ &= \int_{\Omega_{\boldsymbol{x},t}}\frac{\partial\boldsymbol{\varphi}}{\partial t}dV_\xi+\int_{\Omega_{\boldsymbol{x},t}}\nabla_{\boldsymbol{\xi}}(\boldsymbol{\varphi}\otimes\hat{\boldsymbol{v}})dV_\xi=\int_{\Omega_{\boldsymbol{x},t}}\frac{\partial\boldsymbol{\varphi}}{\partial t}dV_\xi+\int_{\partial\Omega_{\boldsymbol{x},t}}(\hat{\boldsymbol{v}}\cdot\boldsymbol{n})\boldsymbol{\varphi}dV_\xi\end{aligned} \tag{B.12}$$

The permutation rule of integral and divergence for obtaining the theorem (5.4) is therefore:

$$\frac{\partial}{\partial t}\int_{\Omega_{\boldsymbol{x},t}}\boldsymbol{\varphi}(\boldsymbol{x}+\boldsymbol{\xi},t)dV_\xi=\int_{\Omega_{\boldsymbol{x},t}}\frac{\partial\boldsymbol{\varphi}}{\partial t}dV_\xi+\int_{\partial\Omega_{\boldsymbol{x},t}}(\hat{\boldsymbol{v}}\cdot\boldsymbol{n})\boldsymbol{\varphi}dV_\xi \tag{B.13}$$

Bibliography

[1] T. Beck, V. Blanc, J.-M. Escleine et al., *Conceptual design of ASTRID fuel subassemblies*, Nuclear Engineering and Design 315, p. 51-60, (2017).

[2] T. Catterou, *Étude numérique et expérimentale du comportement dynamique non linéaire d'un réseau de tubes avec jeux - application aux faisceaux d'aiguilles combustibles RNR*, PhD thesis, (2018).

[3] M. Fadaee, S. D. Yu, *Modeling large number of rod-to-rod and rod-to-rigid surface frictional contact*, Nucl. Eng. Des. 330, p. 87–96, (2018).

[4] M. Hassan, R. Rogers, *Friction modelling of preloaded tube contact dynamics*, Nucl. Eng. Des. 235, (2005).

[5] G. Gilardi, I. Sharf, *Literature survey of contact dynamics modelling*, Mech. Mach. Theory 37, p. 1213–1239, (2002).

[6] M. Jean, *The non-smooth contact dynamics method*, Comput. Methods Appl. Mech. Eng. 177, p. 235–257, (1999).

[7] V. Acary. *Energy conservation and dissipation properties of time-integration methods for the nonsmooth elastodynamics with contact*, Report. INRIA, (2014).

[8] W. Goldsmith, *Impact: The Theory and Physical Behaviour of Colliding Solids*, E. Arnold, London, (1960).

[9] C. M. Donahue, C. M. Hrenya, A. P. Zelinskaya et al., *Newton's cradle undone: Experiments and collision models for the normal collision of three solid spheres*, Physics of Fluids, (2008).

[10] A. Millard, R. Roche, *Elementary solutions for the propagation of ovalization along straight pipes and elbows*. Int. J. Press. Vessels Pip. 16, p. 101–129, (1984).

[11] H. Hertz, D. E. Jones et G. A. Schott, Miscellaneous papers. Cornell University Library, London : Macmillan, New York, Macmillan et co., (1896).

[12] T. Catterou, V. Blanc, G. Ricciardi et al., *Non-linear damping of sodium fast reactor fuel pins: Experimental analysis and numerical modelisation*, Nuclear Engineering and Design 364, (2020).

[13] T.H. Lee, *Nonlinear dynamic analysis of a stacked fuel column subjected to boundary motion*, Nuclear Engineering and Design 32 (3), p. 337-350, (1975).

[14] W.-S. Choi, D.-O. Kim, K.-B. Park, J.-M. Noh, W.-J. Lee, *Evaluation on the behavior of stacked blocks subject to a harmonic excitation*, 17th International Conference on Nuclear Engineering (2009).

[15] J. Delannoy, M. Amabili, B. Matthews, B. Painter, K. Karazis, *Non-linear damping identification in nuclear systems under external excitation*, ASME International Mechanical Engineering Congress and Exposition (2015).

[16] J. Delannoy, M. Amabili, B. Matthews, B. Painter, K. Karazis, *Identification of non-linear damping of nuclear reactor components in case of one-to-one internal resonance*, ASME International Mechanical Engineering Congress and Exposition (2016).

[17] G. Ferrari, P. Balasubramanian, S. Le Guisquet, L. Piccagli, K. Karazis, B. Painter, M. Amabili, *Non-linear vibrations of nuclear fuel rods*, Nuclear Engineering and Design 338, p. 269-283, (2018).

[18] M.H. Fontana, P.A. Gnadt, T.S. Kress, R.E. MacPherson, L.F. Parsly, J.L. Wantland, *Effect of inlet blockages in 19-rod simulated LMFBR fuel subassemblies*, Trans Amer Nucl Soc, 345-347, (1973).

[19] R. Berger, J. Lapie, *CFNa II - Détection d'ébullition par allalyse des bruits de température,* Compte rendu d'essais du 25 Juin et du J Juillet 75, C.E.A., (1975).

[20] C. Piettre, *Compte rendu des essais GR19 BP,* C.E.A., (1985).

[21] C. Piettre, B. Rameau, *ECONA. Grappe à profil axial de flux constant. Annexes du compte rendu des essais de convection naturelle simple phase et d'ebullition. Tome 2,* C.E.A. , (1987).

[22] F. Namekawa, A. Ito, K. Mawatari, *Buoyancy effects on wire-wrapped rod bundle heat transfer in an LMFBR fuel assembly,* AlChESymposium Series Niagra Falls, pp. 128-133, (1984)..

[23] B. Rameau, *FETUNA GR 91 - Resultats d'essais et interpretation à l'aide du code,* CEA., (1982)

[24] E. H. Novendstern, *Turbulent flow pressure drop model for fuel rod assemblies utilizing a helical wire-wrap spacer system,* Nuclear Engineering and Design 22(1), p. 28–42, (1972).

[25] K. Rehme, *Pressure-drop correlations for fuel-elements spacers*, Nuclear Technology 17(1), p. 15–23, (1973).

[26] S. K. Cheng and N. E. Todreas, *Hydrodynamic models and correlations for bare and wire-wrapped hexagonal rod bundles – bundle friction factors, subchannel friction factors and mixing parameters,* Nuclear Engineering and Design 92(2), p. 227–251, (1986).

[27] S. K. Chen, N. E. Todreas, and N. T. Nguyen, *Evaluation of existing correlations for the prediction of pressure drop in wire-wrapped hexagonal array pin bundles*, Nuclear Engineering and Design 267, p. 109–131, (2014).

[28] M.H. Chun, K.W. Seo, *An experimental study and assessment of existing friction factor correlations for wire-wrapped fuel assemblies,* Annals of nuclear energy 28, p. 1683-1695, (2001).

[29] Choi et al., *Measurement of pressure drop in a full-scale fuel assembly of a liquid metal reactor,* Journal of pressure vessel technology 125, p. 233-238, (2003).

[30] G. Kennedy, K. Van Tichelen, J. Pacio, I. Di Piazza, H. Uitslag-Doolaard, *Thermal-Hydraulic Experimental Testing of the MYRRHA Wire-Wrapped Fuel Assembly*, Nuclear Technology, 206, p. 179-190, (2020).

[31] R.M. Roidt, M.D. Carelli, R.A. Markley, *Experimental investigations of the hydraulic field in wire-wrapped LMFBR core assemblies*, Nuclear Engineering and Design 62, p. 295-321, (1980).

[32] T. Nguyen, N. Goth, P. Jones, S. Lee, R. Vaghetto, Y. Hassan, *PIV measurements of turbulent flows in a 61-pin wire-wrapped hexagonal fuel bundle,* International Journal of Heat and Fluid Flow 65, p. 47-59, (2017).

[33] B. MAYS, R. B. JACKSON, *Thermal Hydraulic Computational Fluid Dynamics Simulations and Experimental Investigation of Deformed Fuel Assemblies,* AREVA Federal Services/U.S. Department of Energy, (2017).

[34] M. Martin, D. Leonard, R. B. Jackson, K. M. Steer, *CFD Verification and Validation of Wire-Wrapped Pin Assemblies,* Nuclear Technology 206, p. 1325-1336, (2020).

[35] F. E. Dunn, D. Hahn, H. Jeong, K. Ha, J. E. Cahalan, *Whole Core Sub-Channel Analysis for LMR Passive Safety Analysis*, 14th Pacific Basin Nuclear Conference, (2004).

[36] K. L. Basehore, N. E. Todreas, *SUPERENERGY-2: A Multiassembly Steady-State Computer Code for LMFBR Core Thermal-hydraulic Analysis*, PNL-3379. Pacific Northwest Laboratory, Richland, WA, (1980).

[37] C. W. Stewart, C. L. Wheeler, R. J. Cena et al., *COBRA-IV: the Model and the Method*, BNWL-2214, Pacific Northwest Laboratory, (1979).

[38] H. Ninokata, A. Efthimiadis, N. E. Todreas, *Distributed resistance modeling of wire-wrapped rod bundles*, Nucl. Eng. Des. 104, p. 93–102, (1987).

[39] H. Y. Jeong, K. S. Ha, W. P Chang et al., *Modeling of flow blockage in a liquid metalcooled reactor subassembly with a subchannel analysis code*, Nucl. Technol. 149 (1), p. 71–87, (2005).

[40] D. Wilcox, *Reassessment of the scale determining equation for advanced turbulence models*, AIAA Journal 26, p. 1299, (1988).

[41] F. R. Menter, *Two-Equation Eddy-Viscosity Turbulence Models for Engineering Applications*, AIAA Journal 32(8), p. 1598–1605, (1994).

[42] I. Ahmad, K.-Y. Kim, *Flow and convective heat transfer analysis using rans for a wire-wrapped fuel assembly*, Journal of Mechanical Science and Technology 20(9), p. 1514–1524, (2006).

[43] J. De Ridder, *Computational Analysis of Flow-Induced Vibrations in Fuel Rod Bundles of Next Generation Nuclear Reactors*, PhD thesis, (2015).

[44] K. Natesan, T. Sundararajan, A. Narasimhan, K. Velusamy, *Turbulent flow simulation in a wire-wrap rod bundle of an LMFBR*, Nuclear Engineering and Design 240 (5), p. 1063-1072, (2010).

[45] S. Rolfo, C. P´eniguel, M. Guillaud, D. Laurence, *Thermal-hydraulic study of a wire spacer fuel assembly*, Nuclear Engineering and Design 243, p. 251–262, (2012).

[46] R. Gajapathy, K. Velusamy, P. Selvaraj, P. Chellapandi, *CFD investigation of effect of helical wire-wrap parameters on the thermal hydraulic performance of 217 fuel pin bundle*, Annals of Nuclear Energy 77, p. 498–513, (2015).

[47] N. G. Rasu, K. Velusamy, T. Sundararajan, P. Chellapandi, *Simultaneous development of flow and temperature fields in wire-wrapped fuel pin bundles of sodium cooled fast reactor*, Nuclear Engineering and Design 267, p. 44–60, (2014).

[48] J.-H. Jeong, J. Yoo, K.-L. Lee, K.-S. Ha, *Three-dimensional flow phenomena in a wire-wrapped 37-pin fuel bundle for SFR*, Nuclear Engineering and Technology 47(5), p. 523–533, (2015).

[49] J. Smagorinsky. *General Circulation Experiments with the Primitive Equations. I. The Basic Experiment*, Monthly Weather Review 91, p. 99–164, (1963).

[50] P. F. Fischer, J. Lottes, , A. Siegel, P. Palmiotti, *Large eddysimulation of wire-wrapped fuel pins I: Hydrodynamics in a periodic array*, Proc. of M and C + SNA 2007, (2007).

[51] A. Saxena, *Thermal-hydraulic numerical simulation of fuel sub-assembly for Sodium-cooled Fast Reactor*, PhD thesis, (2014).

[52] M. P. Paidoussis, *Dynamics of flexible slender cylinders in axial flow. Part 1: Theory*, Journal of Fluid Mech 26, p. 717–736, (1966).

[53] M. J. Lighthill, *Note on the swimming of slender fish*, Journal of Fluid Mechanics 9(2), p. 305-317, (1960).

[54] G. Taylor, *Analysis of the swimming of long and narrow animals*, Proc Roy Soc Lond A – Math Phys Sci 214, p. 158–183, (1952).

[55] M. P. Paidoussis, *Dynamics of cylindrical structures subjected to axial flow*. Journal of Sound Vib 29, p. 365–385, (1973).

[56] M. P. Païdoussis, M. Pettigrew, *Dynamics of flexible cylinders in axisymetrically confined axial flow*, Journal of Applied Mechanics, (1979).

[57] S. Chen, M. Wamnsganss, *Parallel-flow-induced vibration of fuel rods*. Nuclear Engineering and Design, (1972).

[58] M. P. Paisoussis, *Fluid-Structure Interactions: slender structures and axial flow: Vol 2*, Academic Press, (2016).

[59] M. P. Paidoussis, *Dynamics of cylindrical structures in axial flow: A review*, Journal of Fluid Mech 107, (2021).

[60] L. Divaret, O. Cadot, P. Moussou, O. Doaré, *Normal forces exerted upon a long cylinder oscillating in an axial flow*. J. Fluid Mech. 752, p. 649–669, (2014).

[61] A. Joly, N. de B. de Chassey, A. Martin, O. Cadot, L. Pastur, P. Moussou, *Direct measurement of steady fluid forces upon a deformed cylinder in confined axial flow*, J. Fluids Struct. 104, (2021).

[62] S. Ersdal, O. M. Faltinsen, *Normal forces on cylinders in near-axial flow*, J. Fluids Struct. 22, p. 1057–1077, (2006).

[63] W. R. Hawthorne, *The early development of the Dracone flexible barge*, Proc. Inst. Mech. Eng. 175, p. 52–83, (1961).

[64] J. L. Lopes, M. P.Païdoussis, C. Semler, *Linear and nonlinear dynamics of cantilevered cylinders in axial flow. Part 2: The equations of motion*. J. Fluids Struct. 16, p. 715–737, (2002).

[65] M. P. Païdoussis, E. Grinevich, D. Adamovic, C. Semler, *Linear and nonlinear dynamics of cantilevered cylinders in axial flow. Part 1: Physical dynamics*, J. Fluids Struct. 16, p. 691–713, (2002).

[66] M. J. Hannoyer, M. P. Païdoussis, *Instabilities of tubular beams simultaneously subjected to internal and external axial flows*, ASME J. Mech. Des. 100, p. 328–336, (1978).

[67] C. Semler, J.-L. Lopes, N. Augu, M. P. Païdoussis, *Linear and nonlinear dynamics of cantilevered cylinders in axial flow. Part 3: Nonlinear dynamics*. J. Fluids Struct. 16, p. 739–759, (2002).

[68] E. de Langre, M. P. Païdoussis, O. Doaré, Y. Modarres-Sadeghi, *Flutter of long flexible cylinders in axial flow*, J. Fluid Mech. 571, 371–389, (2007).

[69] Z. G. Liu, Y. Liu, J. Lu, *Numerical simulation of the fluid–structure interaction for an elastic cylinder subjected to tubular fluid flow*, Comput. & Fluids 68, p. 192–202, (2012).

[70] Y. Modarres-Sadeghi, M. P. Païdoussis, C. Semler, E. Grinevich, *Experiments on vertical slender flexible cylinders clamped at both ends and subjected to axial flow*. Phil. Trans. R. Soc. A 366, p. 1275–1296, (2008).

[71] E. Ter Hofstede, S. Kottapalli, A. Shams, *Numerical prediction of flow induced vibrations in nuclear reactor applications*, Nucl. Eng. Des. 319, p.81–90, (2017).

[72] E. Lillberg, K. Angele, G. Lundqvist, N. Edh, *Tailored experiments for validation of CFD with FSI for nuclear reactor applications*, NURETH16, (2015).

[73] D. De Santis, A. Shams, *Numerical modeling of flow induced vibration of nuclear fuel rods*, Nucl. Eng. Des. 320, p. 44–56, (2017).

[74] Z. Y. Lu, C. W. Wong, Y. Zhou, *Turbulence intensity effect on the axial-flow-induced vibration of an elastic cylinder*, J. Fluids Struct. 99, p. 103-144, (2020).

[75] S. S. Chen, *Vibration of nuclear fuel bundles*, Nucl. Eng. Des. 35, p. 399–422, (1975).

[76] M. P. Païdoussis, S. Suss, *Stability of a cluster of flexible cylinders in bounded flow*, J. Appl. Mech. 44, p. 401–408, (1977).

[77] M. P. Païdoussis, *The dynamics of clusters of flexible cylinders in axial flow: Theory and experiments*, J. Sound Vib. 65, p. 391–417, (1979).

[78] W. H. Lin, *Hydrodynamic forces on multiple circular cylinders oscillating in a viscous incompressible fluid*, Z. Angew. Math. Mech. 67, p. 487–501, (1987).

[79] M. P. Païdoussis, J.O. Gagnon, *Experiments on the vibration of cylinders in axial flow: modal and spectral characteristics*, J. Sound Vib. 96, p. 341–352, (1984).

[80] J. O. Gagnon, M. P. Païdoussis, *Fluid coupling characteristics and vibration of cylinder clusters in axial flow. Part I: Theory*. J. Fluids Struct. 8, p. 257–291, (1994a).

[81] J. O. Gagnon, M. P. Païdoussis, *Fluid coupling characteristics and vibration of cylinder clusters in axial flow. Part II: Experiments*. J. Fluids Struct. 8, p. 293–324, (1994b).

[82] M. P. Païdoussis, L. R. Curling, *An analytical model for vibration of clusters of flexible cylinders in turbulent axial flow*, J. Sound Vib. 98, p. 493–517, (1985).

[83] L. R. Curling, M. P. Paidoussis, Analyses for random flow-induced vibration of cylindrical structures subjected to turbulent axial flow, J. Sound Vib. 264, p. 795–833, (2003).

[84] L. R. Curling, M. P. Paidoussis, *Measurements and characterization of wall-pressure fluctuations on cylinders in a bundle in turbulent axial flow. Part 1: spectral characteristics*. J. Sound Vib. 157, p. 405–433, (1992a).

[85] L. R. Curling, M. P. Paidoussis, *Measurements and characterization of wall-pressure fluctuations on cylinders in a bundle in turbulent axial flow. Part 2: temporal characteristics*. J. Sound Vib. 157, p. 435–449, (1992b).

[86] Z. G. Liu, Y. Liu, J. Lu, *Numerical simulation of the fluid–structure interaction of two simple fuel assemblies*. Nucl. Eng. Des. 258, p. 1–12, (2013).

[87] J. De Ridder, J. Degroote, K. Van Tichelen, J. Vierendeels, *Predicting modal characteristics of a cluster of cylinders in axial flow : from potential flow solutions to coupled CFD–CSM calculations*, J. Fluids Struct. 74, p. 90-110, (2017).

[88] D. De Santis, S. Kottapalli, A. Shams, *Numerical simulations of rod assembly vibration induced by turbulent axial flows*, Nucl. Eng. Des. 335, p. 94–105, (2018).

[89] G. Ricciardi, S. Bellizzi, B. Collard, B. Cochelin, *Modelling Pressurized Water Reactor cores in terms of porous media*, Journal of Fluids and Structures 25, p. 112–133, (2009).

[90] G. Ricciardi, *Hydraulic coupling of fuel assemblies under axial flow, confinement effect*, Nucl. Eng. Des. 326, p. 190-201, (2018).

[91] G. Ricciardi, *Fluid-structure interaction modelling of a PWR fuel assembly subjected to axial flow*, J. Fluids Struct. 62, p. 156-171, (2016).

[92] G. Pelloux, *Manuscrit de fin d'étude - Contribution à l'étude des conséquences d'un séisme sur les aiguilles combustible du coeur du réacteur à neutrons rapides SUPERPHENIX 1. Modélisation et calcul dynamique d'une rangée d'aiguille et mise au point d'une maquette d'essai*, CEA Cadarache, (1992).

[93] G. Meynier, A. Courtial, G. Siffre, *Compte rendu d'essais de choc sur maquette de faisceau combustible SPX1*, Note technique CEA, (Oct. 1989).

[94] A. Roubaud, P. Bernard, Y. Thiebaut et al., *Compte rendu des essais de remise en service du banc BELIER*, Note technique CEA., (Oct. 1993).

[95] P. Fardeau, *Compte rendu d'essais de choc sur maquette de faisceau combustible PHENIX*, (Oct. 1995).

[96] J. C. Flamand, J. C. Maguin, A. Mattei, J. Rigaudeau, J. C. Leroux, *Influence of axial coolant flow on fuel assembly damping for the response to horizontal seismic loads*, 11th International Conference on Structural Mechanics in Reactor Technology (SMiRT 11), (1991).

[97] B. Collard, S. Pisapia, S. Bellizzi, F. Witters, *PWR fuel assembly modal testing and analysis*, Proceedings of the ASME 2003 Pressure Vessels and Piping Conference, p. 147–152, (2003).

[98] P. Moussou, , A. Guilloux, E. Boccaccio, G. Ricciardi, *Fluid Damping in Fuel Assemblies*, Proceedings of the ASME 2017 Pressure Vessels and Piping Conference, (2017).

[99] G. Ricciardi, E. Boccaccio, *Modelling of the flow induced stiffness of a PWR fuel assembly*, Nuclear Engineering and Design 282, p. 8–14, (2015).

[100] S. Clement, *Mise en oeuvre expérimentale et analyse vibratoire non-linéaire d'un dispositif à quatre maquettes d'assemblage combustibles sous écoulement axial*, PhD Thesis, (2014).

[101] B. De Pauw, W. Weijtjens, S. Vanlanduit, K. Van Tichelen, F. Berghmans, *Operational modal analysis of flow-induced vibration of nuclear fuel rods in a turbulent axial flow*, Nuclear Engineering and Design 284, p. 19-26, (2015).

[102] R. Alcorta, *Prediction of non-linear responses and bifurcations of impacting systems: Contribution to the understanding of steam-generator vibrations*, PhD thesis, (2021).

[103] N. Mureithi, M. P. Païdoussis, S. Price, *The post-Hopf-bifurcation response of a loosely supported cylinder in an array subjected to cross-flow. Part II: theoretical model and comparison with experiments*, Journal of Fluids and Structures 8(7), p. 853–876, (1994).

[104] H. B. Khenous, P. Laborde, Y. Renard, *Comparison of two approaches for the discretization of elastodynamic contact problems*, Comptes Rendus Mathematique 342.10, p. 791-796, (2006).

[105] T. Thenint, *Etude d'un système non linéaire à chocs sous excitation large bande : application à un tube de générateur de vapeur*, PhD thesis, (2011).

[106] V. F. Siniavskii, V. S. Fedotovskii, A. B. Kukhtin, *Oscillation of a Cylinder in a Viscous Liquid*, Prikladnaia Mekhanika 16, p. 62-67, (1980).

[107] S. F. Hoerner, *Fluid-Dynamic Drag: Practical Information on Aerodynamic Drag and Hydrodynamic Resistance*, (1965).

[108] C. R. Ortloff, J. Ives, *On the dynamic motion of a thin flexible cylinder in a viscous stream*, Journal of Fluid Mechanics 38, p. 713-720, (1969).

[109] A. H. Nayfeh, D. T. Mook, *Nonlinear Oscillations*, Wiley Series in Nonlinear Science, (1979).

[110] B. Cochelin, C. Vergez, *A high order purely frequency-based harmonic balance formulation for continuation of periodic solutions*, Journal of Sound and Vibration 324, p. 243–262, (2009).

[111] R. Seydel, *Practical Bifurcation and Stability Analysis*, Springer, (2010).

[112] B. Cochelin, N. Damil, M. Potier-ferry, *Asymptotic-numerical methods and Pade approximants for non-linear elastic structures*, International Journal for Numerical Methods in Engineering 37 (7), p. 1187–1213, (1994).

[113] L. Guillot, *On a quadratic formalism for the continuation of the solutions of dynamical systems and their bifurcations - Applications to reed instruments*, PhD thesis, (2020).

[114] N. M. Krylov, N. N. Bogoliubov, *Introduction to Non-Linear Mechanics, Volume 11*, Princeton University Press, (1950).

[115] M. S. Nakhla, J. Vlach, *A piecewise harmonic balance technique for determination of periodic response of nonlinear systems*, IEEE Transactions on Circuit Theory 23, p. 85–91, (1976).

[116] Z. K. Peng, Z. Q. Lang, S. A. Billings, G. R. Tomlinson, *Comparisons between harmonic balance and nonlinear output frequency response function in nonlinear system analysis*, Journal of Sound and Vibration 311, p. 56–73, (2008).

[117] S. L. Lau, Y. K. Cheung, *Amplitude incremental variational principle for nonlinear vibration of elastic systems*, ASME Journal of Applied Mechanics 28, p. 959–964, (1981).

[118] C. Pierre, A. A. Ferri, E. H. Dowell, *Multi-harmonic analysis of dry friction damped systems using an incremental harmonic balance method*, Journal of Applied Mechanics 52 (4), p. 958-964, (1985).

[119] A. A. Ferri, E. H. Dowell, *Frequency domain solutions to multi-degree-of-freedom, dry friction damped systems*, Journal of Sound and Vibration 124, p. 207–224, (1988).

[120] T. M. Cameron, J. H. Griffin, *An alternating frequency/time domain method for calculating the steady-state response of nonlinear dynamic systems*, Journal of Applied Mechanics 56 (1), p. 149–154, (1989).

[121] S. Navicet, C. Pierre, F. Thouverez, L. Jéséquel, *A dynamic Lagrangian frequency-time method for the vibrations of dry-friction-damped systems*, Journal of Sound and Vibration 265, p. 201–219, (2003).

[122] B. Troyanovsky, *Frequency Domain Algorithms for Simulating Large Signal Distortion in Semiconductor Devices*, PhD Thesis, (1997).

[123] S. Karkar, B. Cochelin, C. Vergez, *A high-order, purely frequency based harmonic balance formulation for continuation of periodic solutions: The case of non-polynomial nonlinearities*, Journal of Sound and Vibration 332, p. 968-977, (2013).

[124] E. H. Moussi, S. Bellizzi, B. Cochelin, I. Nistor, *Nonlinear normal modes of a two degrees-of-freedom piecewise linear system*, Mechanical Systems and Signal Processing 64–65, p. 266–281, (2015).

[125] A. Grolet, F. Thouverez, *On a new harmonic selection technique for harmonic balance method*, Mechanical Systems and Signal Processing 30, p. 43–60, (2012).

[126] E. J. Doedel, Lecture notes on numerical analysis of nonlinear equations, in: B. Krauskopf, H. M. Osinga, J. Galán-Vioque (Eds.), *Numerical Continuation Methods for Dynamical Systems*, Springer, The Netherlands, (2007).

[127] M. Peeters, R. Viguié, G. Sérandour, G. Kerschen, J. C. Golinval, *Nonlinear normal modes, part II: toward a practical computation using numerical continuation techniques*, Mechanical Systems and Signal Processing 23 (1), p. 195–216, (2009).

[128] Y. S. Lee, G. Kerschen, A. F. Vakakis, P. Panagopoulos, L. Bergman, D. M. McFarland, *Complicated dynamics of a linear oscillator with a light, essentially nonlinear attachment*, Physica D:Nonlinear Phenomena 204 (1–2), p. 41–69, (2005).

[129] P. Sundararajan, S. T. Noah, *Dynamics of forced nonlinear systems using shooting/arc-length continuation method—application to rotor system*s, Journal of Vibration and Acoustics 119 (1), p. 9–20, (1997).

[130] G. Dimitriadis, *Shooting-based complete bifurcation prediction for aeroelastic systems with freeplay*, Journal of Aircraft 48 (6), p. 1864–1877, (2011).

[131] L. Renson, G.Kerschen, B.Cochelin, *Numerical computation of nonlinear normal modes in mechanical engineering*, Journal of Sound and Vibration 364, p. 177–206, (2016).

[132] E. J. Doedel, R. C. Paffenroth, A. R. Champneys, T. F. Fairgrieve, Y. A. Kuznetsov, B. E. Oldeman, B. Sandstede, X. J. Wang, *Auto2000: Continuation and bifurcation software for ordinary differential equations*, Available via ⟨http://cmvl.cs.concordia.ca/⟩, (2000).

[133] A. Dhooge, W. Govaerts, Y. A. Kuznetsov, *Matcont: a matlab package for numerical bifurcation analysis of odes*, ACM Transactions on Mathematical Software 29 (2), p. 141–164, (2003).

[134] S. Karkar, B. Cochelin, C. Vergez, *A comparative study of the harmonic balance method and the orthogonal collocation method on stiff nonlinear systems*, Journal of Sound and Vibration 333(12), p. 2554–2567, (2014).

[135] R. Arquier, S. Bellizzi, R. Bouc, B. Cochelin. *Two methods for the computation of nonlinear modes of vibrating systems at large amplitudes*. Computers and Structures 84 (24-25), p.1565-1576, (2006).

[136] K. Ye, L. Li, H. Zhu, *A modified Kelvin impact model for pounding simulation of base-isolated building with adjacent structures*, Earthq. Eng. Eng. Vib. 8, p. 433–446, (2009a).

[137] A. Bensoussan, J. L. Lions, G. Papanicolaou, *Asymptotic analysis for periodic structures*, Amsterdam, North-Holland, (1978).

[138] E. Jaquelin, D. Brochard, C. Trolliat, L. Jezequel, *Homogenisation of non-linear array of confined beams*, Nuclear Engineering and Design 165(1-2), p. 213-223, (1996).

[139] L. Hammami, *Contribution à l'étude de l'interaction fluide-structure dans les faisceaux de tube par une technique d'homogénéisation*, PhD thesis, (1990).

[140] S. Whitaker, *Advances in theory of fluid motion in porous media*, Ind. Engng Chem. 61, p. 14-28, (1969).

[141] M. D. Lemos, *Turbulence in Porous Media: Modeling and application*, Elsevier, (2006).

[142] J. Sigrist, D. Broc, *Dynamic analysis of a tube bundle with fluid-structure interaction modeling using a homogeneisation method*, Computer Methods in Applied Mechanics and Engineering 197, p. 1080-1099, (2008).

[143] A. N. Gineau, *Modélisation multi-échelle de l'interaction fluide-structure dans les systèmes tubulaires*, PhD thesis, (2015).

List of figures

List of tables